UNIVERSITY OF CALIFORNIA, SAN DIEGO

Mechanical performance, constitutive response, and fragmentation of tailored mesostructured aluminum-based compacts

A dissertation submitted in partial satisfaction of the

requirements for the degree of Doctor of Philosophy

in

Materials Science and Engineering

by

Andrew Martin Marquez

Committee in charge:

Professor Marc A. Meyers, Chair
Professor Olivia Graeve
Professor Vlado Lubarda
Professor Vitali Nesterenko
Professor Jan Talbot

2017

The Dissertation of Andrew Martin Marquez is approved, and is acceptable in quality and form for publication on microfilm and electronically:

_____

_____

_____

_____

_____

Chair

University of California, San Diego

2017

TABLE OF CONTENTS

LIST OF FIGURES

LIST OF TABLES

ACKNOWLEDGEMENTS

I would like to gratefully acknowledge my advisor, Professor Marc Meyers, for his intellectual guidance and financial support. I am grateful to all of my coauthors, collaborators, and colleagues who have contributed to the success of my work, especially Keyur Karandikar, Melisa Ribero, Zezhou Li, Tarah Sullivan, Jerry Jung, Andrei Pissarenko, Christopher Braithwaite, Kenneth Vecchio, David Gibbins, Nick Krywopusk and Timothy Weihs.

I would also like to thank all of my friends and family for their continued encouragement and support throughout my education, especially my parents, Annette and Rolando, and my fiancée, Corina De Pablo. Financial support is key to the success of this work. The work presented in this dissertation was supported principally by a Multi-University Research Initiative through the Office of Naval Research (N00014-07-1-0740).

Chapter 3 and 4, in part, are published as "Fragmentation and constitutive response of tailored mesostructured aluminum compacts." Journal of Applied Physics, vol 119, p. 145903, 2016. A. Marquez, C. Braithwaite, T. Weihs, N. Krywopusk, D. Gibbins, K. Vecchio, and M. Meyers. The dissertation author is the first author of this work.

Chapter 4, in part, is submitted for publication as "Fragmentation and mechanical performance of tailored nickel-aluminum laminate compacts." A. Marquez, Z. Li, C. Braithwaite, T. Weihs, N. Krywopusk, D. Gibbins, and M. Meyers. The dissertation author is the first author of this work.

VITA

2017 Ph.D. Materials Science and Engineering

University of California, San Diego, La Jolla, CA

Dissertation: Mechanical performance, constitutive response and fragmentation of tailored mesostructured aluminum-based compacts

Advisor: Professor Marc A. Meyers

2011 M.S. Materials Science and Engineering

University of California, San Diego, La Jolla, CA

2010 B.S. Mechanical and Materials Science Engineering

University of California, Irvine, Irvine, CA

PUBLICATIONS

Marquez AM, Ribero Vairo MS, Benson DJ, Braithwaite CH, Weihs TP, Krywopusk NM, Gibbins DJ, Meyers MA. Fragmentation simulation of tailored mesostructured aluminum compacts. International Journal of Impact Engineering, in preparation, 2017.

Jung JY, Pissarenko A, Trikanad AA, Restrepo D, Marquez AM, Gonzalez D, Naleway SE, Meyers MA, Zavattieri, McKittrick J, A nose-like damper on the head? Mechanical functions of the skull bone features in woodpeckers. Journal of the Mechanical Behavior of Biomedical Materials, in preparation, 2017.

Marquez AM, Li Z, Braithwaite CH, Weihs TP, Krywopusk NM, Gibbins DJ, Vecchio KS, Meyers MA. Fragmentation and mechanical performance of tailored nickel-aluminum laminate compacts. Materials Science and Engineering-A, in preparation, 2017.

Marquez AM, Braithwaite CH, Weihs TP, Krywopusk NM, Gibbins DJ, Vecchio KS, Meyers MA. Fragmentation and constitutive response of tailored mesostructured aluminum compacts. Journal of Applied Physics, vol 119, p.145903, 2016.

ABSTRACT OF THE DISSERTATION

Mechanical performance, constitutive response and fragmentation of tailored mesostructured aluminum-based compacts

by

Andrew Martin Marquez

Doctor of Philosophy in Materials Science and Engineering

University of California, San Diego, 2017

Professor Marc André Meyers, Chair

The fragmentation and constitutive response of tailored aluminum-based compacts is examined under dynamic conditions. Mesostructured Al compacts having interfaces between the powders (with sizes of 40, 100, and 400 μm) with controlled strengths were produced by swaging. Nickel-aluminum compacts were also produced and

studied because the Ni-Al system is an optimum model system to investigate exothermic reactions initiated by dynamic events, such as ballistic impact.

In order to obtain a fundamental quantitative understanding of the process the fragmentation of pre-compacted powders is essential for the modeling of the energetics and kinetics of exothermic reactions. Thus, in this work the Mott theory was extended by incorporating fracture toughness. The fracture toughness and yield stress are used to calculate fragment sizes in a variety of particle sizes and geometries which are compared with experimental results.

The fragmentation generated in the explosively-driven rings expanded at a velocity of approximately 100 m/s was captured by high-speed photography. The fragment size distributions obtained varied widely and correlated with the interfacial strength of the compacts as well as with powder size. Finite element simulations were also conducted to help better understand the influence of material properties on fragmentation. Experimental results and finite element simulations both confirm that the modified Mott theory, which incorporates fracture toughness, can successfully calculate fragment size.

CHAPTER 1: INTRODUCTION AND OBJECTIVES

1.1 Motivation

In this thesis, the fragmentation and constitutive responses of tailored mesostructured aluminum-based compacts, including powder consolidated reactive Ni-Al, were studied numerically, or chemically, or both facets under a quasi-static or dynamic loading condition. There were three key points that we were working to reach by studying these materials through this range of methods: (1) To investigate the mechanical performance of the tailored mesostructured aluminum-based compacts under quasi-static and dynamic loading conditions; (2) To tailor the fragmentation response of aluminum and nickel-aluminum compacts by changing interface cohesion between the particles; (3) To characterize and predict fragmentation with a modified Mott theory that incorporates fracture toughness and yield strength.

The central motivation for these points of research is also three-fold. The first is that there is currently a great deal of interest in the use of powdered metallic materials for applications where reactivity of these materials can be utilized. One such application is in reactive munitions casings where it has been proven that utilizing reactive materials can double the lethal radii of conventional warheads [1]. Next is that the addition of metals, such as aluminum, to energetic materials has been shown to be effective in increasing the blast characteristics of formulations [2]. Lastly, the nickel/aluminum system was selected for study because it is one of the more commonly used reactive materials for areas utilizing exothermic reactions initiated by dynamic events such as in the aerospace industry. The system is also well known for combustion synthesis, which also uses the

exothermic heat of reactive materials but to generate a large degree of releasing heat and sustain the self-propagating high temperature reactions [3]. The mechanism also came to be known as self-sustaining high temperature synthesis (SHS) [4].

The promising features of using reactive materials and combustion synthesis reactions are the high reaction speed and the resulting strong exotherms. It was discovered with reactive systems, the speed of reactions could be up to 10^7-10^9 times quicker than diffusion controlled reactions [5]. Combustion synthesis was initially developed for the purpose of welding train tracks in 1899. It was based upon the use of German chemist Hans Goldschmidt's invention called thermite reactions. The basic theory behind the Goldschmidt process for welding and repairing train tracks was the use of a reduction process and an intensive exothermic heat for melting and creating iron fillings through the damaged portion of the train tracks. Through the utilization of the thermite process, train tracks were capable of being repaired in only a matter of minutes. The exothermic chemical reaction is best described with: $Fe_2O_3+Al \rightarrow 2Fe+Al_2O_3+Heat$ (Figure 1.1) [6]. The exothermic heat generated a dramatically large temperature increase that was so strong that it could melt iron and almost instantaneously fix any broken railroad.

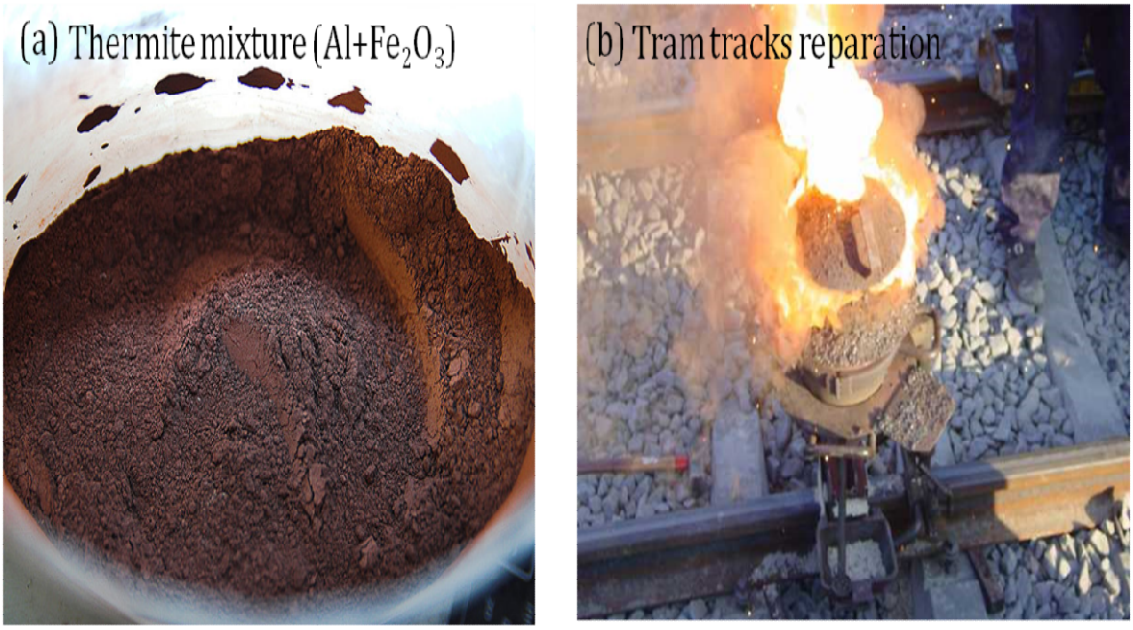

Figure 1.1: (a) Photograph of a thermite mixture, (b) photograph of a thermite process being used to fix a railroad [6].

Figure 1.2 represents both an industrial utilization (Figure 1.2(a)) and a scientific research outcome (Figure 1.2(b)) with combustion synthesis. Figure 1.2(a) demonstrates the industrial utilization of a self-propagating reaction to connect a copper heat sink to a heat withstanding printed circuit board [7]. The images of SHS disks of TiC in Figure 1.2(b) depicts from left to right the development from ignition to reaction propagation through combustion synthesis of the self-propagating high-temperature synthesis compacted and hot-pressed titanium carbides [8]. The SHS mechanism of a combustion synthesis could be used to create large melting temperature, great strength and hardness materials as detailed in the thorough studies conducted by Naresh Thadhani in 1993 [9].

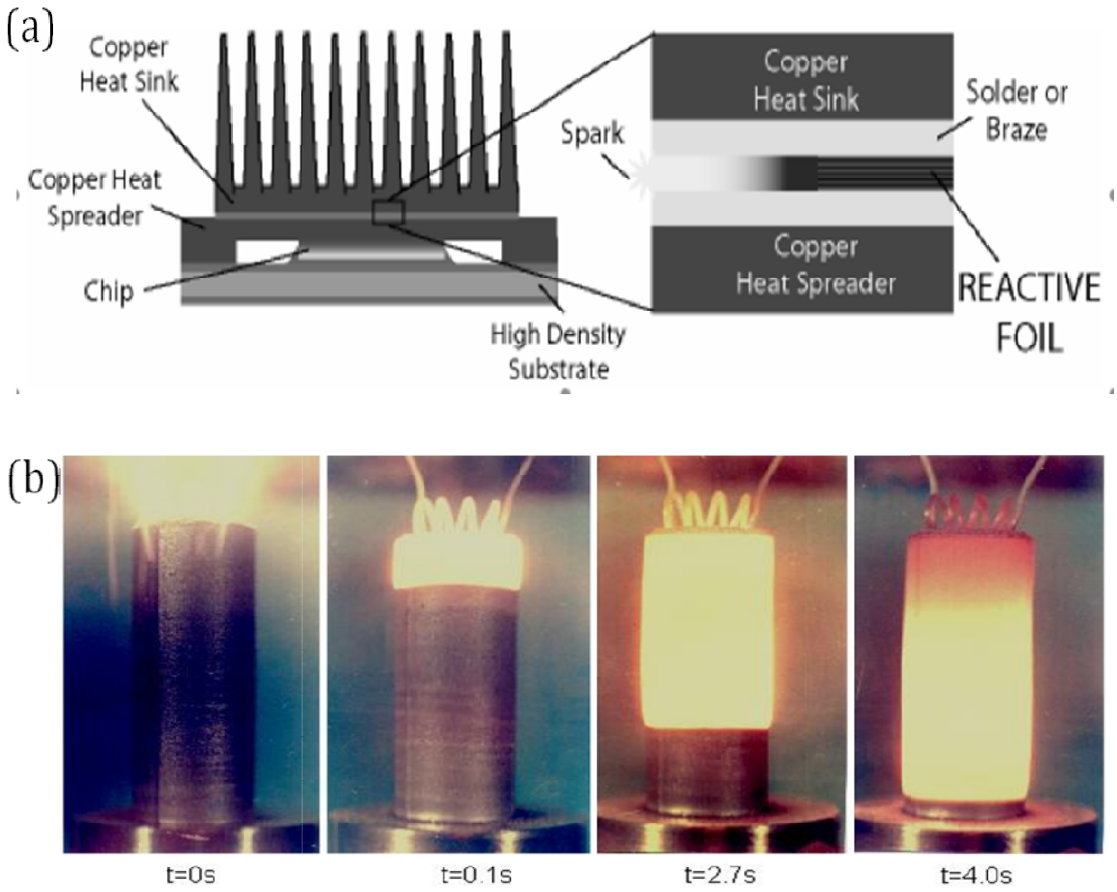

Figure 1.2: Combustion synthesis being used for **(**a) melting solder to connect a copper heat sink to a printed circuit board; (b) create SHS disks of TiC [8].

1.2 Introduction to dynamic testing of materials

Materials react to external forces in a number of ways including dislocation generation and motion, mechanical twinning, phase transformation, or fracture. The dynamic behavior of materials is frequently described by physical based constitutive equations that link stress, strain, and typically temperature or deformation history. There are a wide range of equations that have been proposed and successfully used to describe the dynamic behavior of materials. Table 1.1 shows a list of some of the well known physical based constitutive equations for dynamic behavior. [10] Among the variety of

methods used to study dynamic properties of materials at high strain rates the most well known are the Hopkinson bar and the expanding ring test.

Table 1.1: Widely known physically based constitutive equations for dynamic behavior [10]

Litonski	1977	$\tau = B(\gamma_0 + \gamma_p)^n (1 - aT)\left[1 + b\left(\frac{d\gamma}{dt}\right)\right]^m$
Johnson-Cook	1983	$\sigma = (\sigma_0 + B\varepsilon^n)\left[1 + C\ln\frac{\dot{\varepsilon}}{\dot{\varepsilon}_0}\right]\left[1 - \left(\frac{T - T_r}{T_m - T_r}\right)^m\right]$
Klopp	1985	$\tau = \tau_0\left(\frac{\gamma}{\gamma_0}\right)^n \left(\frac{T}{T_r}\right)^{-\nu} \left(\frac{\dot{\gamma}_p}{\dot{\gamma}_0}\right)^m \Rightarrow \tau = \tau_0\left(\frac{\dot{\gamma}}{\dot{\gamma}_0}\right)^{1/M} \left(1 + \frac{\gamma}{\gamma_0}\right)^m \exp(-\lambda\Delta T)$
Meyers	1994	$\sigma = (\sigma_0 + B\varepsilon^n)\left[1 + C\log_{10}\frac{\dot{\varepsilon}}{\dot{\varepsilon}_0}\right]\left(\frac{T}{T_r}\right)^{-\lambda}$ $\sigma = (\sigma_0 + B\varepsilon^n)\left[1 + C\log_{10}\frac{\dot{\varepsilon}}{\dot{\varepsilon}_0}\right] e^{-\lambda(T - T_r)}$
Andrade	1994	$\sigma = (\sigma_0 + B\varepsilon^n)\left[1 + C\log\frac{\dot{\varepsilon}}{\dot{\varepsilon}_0}\right]\left[1 - \left(\frac{T - T_r}{T_m - T_r}\right)^m\right] H(T)$ $H(T) = \frac{1}{1 - \left\{1 - \left[(\sigma_f)_{rec}/(\sigma_f)_{def}\right]\right\} u(T)}; \quad u(T) = \begin{cases} 0 & for \quad T < T_c \\ 1 & for \quad T > T_c \end{cases}$

The Hopkinson pressure bar was first suggested by Bertram Hopkinson in 1914. [11] It was initially utilized as a way to measure stress pulse propagation in a metal bar. In the initial setup of the experiment a single bar is struck by a bullet or gun-cotton detonation. H. Kolsky developed Hopkinson's method in 1949 through integrating innovations with cathode ray oscilloscopes and electrical condenser units to measure the propagation of pressure pulses in the bars on either side of the sample. [12] The basic setup of Kolsky's method, where two Hopkinson bars are used in series to determine stress and strain, would continue to be used in the subsequent refinements to the Hopkinson bar arrangement up to the modern version.

The standard compression setup is known as a split-Hopkinson pressure bar. It essentially is made up of a striker, an incident bar and a transmission bar. The process of testing begins when the striker bar impacts onto the incident bar, an elastic stress wave is created and travels through the incident bar. Once the wave arrives at the specimen/incident bar boundary, a part of the wave is bounced back as a result of the impedance difference amid the sample and the bar and some of the wave is absorbed through the sample that applies a load to the sample and ultimately through the transmission bar, as a transmitted wave. [13] The elastic strains related to the stress waves are recorded by strain gages applied to the sides of the incident and transmission bars. The recorded data are extrapolated to find the axial strain rate and stress of the sample.

For the retrieval of accurate dynamic material data from a sample tested with the split-Hopkinson pressure bar, the sample must to undergo almost uniform deformation. The distribution of stress throughout the sample needs to almost uniform as well, this is characteristically known as dynamic stress equilibrium. Under these conditions, the stress and strain data of a sample can be averaged throughout a sample's volume to estimate the response of a material. In addition, to increase the ease of fitting effects of the strain rate within models of a material, the preference is that every split-Hopkinson pressure bar experiment should be conducted as close to a strain rate that is constant as possible. The difference between machines that test quasi-statically, in which the rigidity of the machine is usually significantly greater compared to a sample and the conditions of testing are simply manipulated through adjusting the motion of the machine, and a split-Hopkinson pressure bar is that there is much less rigidity in their loading bars. The

conditions of testing of a split-Hopkinson pressure bar sample directly relate to the incident bar loading and the response of a sample. Based on the response of a sample, the loading history should be modified in order for a sample to deform with the preferred conditions of loading.

The incident pulse has a trapezoidal profile and the length is the same as the time it would take a longitudinal elastic bar wave to travel round-trip along a striker bar. For the size of the incident pulse, it is dependent on the starting speed of the striker bar, and the time is plainly related to the length of the striker bar. Putting a thin disc that can deform plastically, otherwise known as a pulse shaper, on the end of the incident bar that is impacted allows for the shape of the incident wave to be adjusted with the specific selection of the proportions and material of the disc. [14-19] By utilizing these well-developed methods, the wave of loading could be customized specifically to the preferred loading rate, size and length. Then waves of loading are created along an incident bar with respect to the preferred conditions of testing and desired response of a sample that are critically required to obtain suitable data from an experiment.

Performing a tension test with the split-Hopkinson pressure bar is difficult because there are a various techniques to apply load and to affix a sample on to an incident and transmission bar. Tension testing with a split-Hopkinson bar started with a design in 1960 by J. Harding. [20] His setup required utilizing an empty load bar that was attached on to a yoke along with placing the sample, which is threaded, within the empty load bar. The tensile pulse was produced through a blow to the empty load bar using a ram and then the first compression wave would bounce back acting in a tensile form from the free side. T. Nicholas achieved the next advance with tension testing with a split-

Hopkinson bar by utilizing a classic compression arrangement but with samples that were threaded on the incident as well as the transmission sides, then a combination collar was secured to a sample. [21] A sample was required to be tightly secured to both the incident and transmission end so that it could avoid the first compression pulse. Nicholas technique generated a compression pulse first through impacting the incident side with a ram; however as the compression pulse arrived at a sample, there was no load applied to the threading on the sample. This compression pulse was expected to go throughout the combination collar then bounce back from the free side creating tension, a tensile pulse ideally then pulls on the sample after that. In 1984 the last development in the loading method for tension testing with a split-Hopkinson bar was developed by Ogawa. [22] This setup utilized an empty striker to create a force on an extension, which was threaded on both sides of the incident bar. The thrust on the striker was provided by through the use of a gas gun or driven disk. A sample would once be secured on both an incident and transmission bar again with threads. Figure 1.3 below is an illustration of the setup by Ogawa.

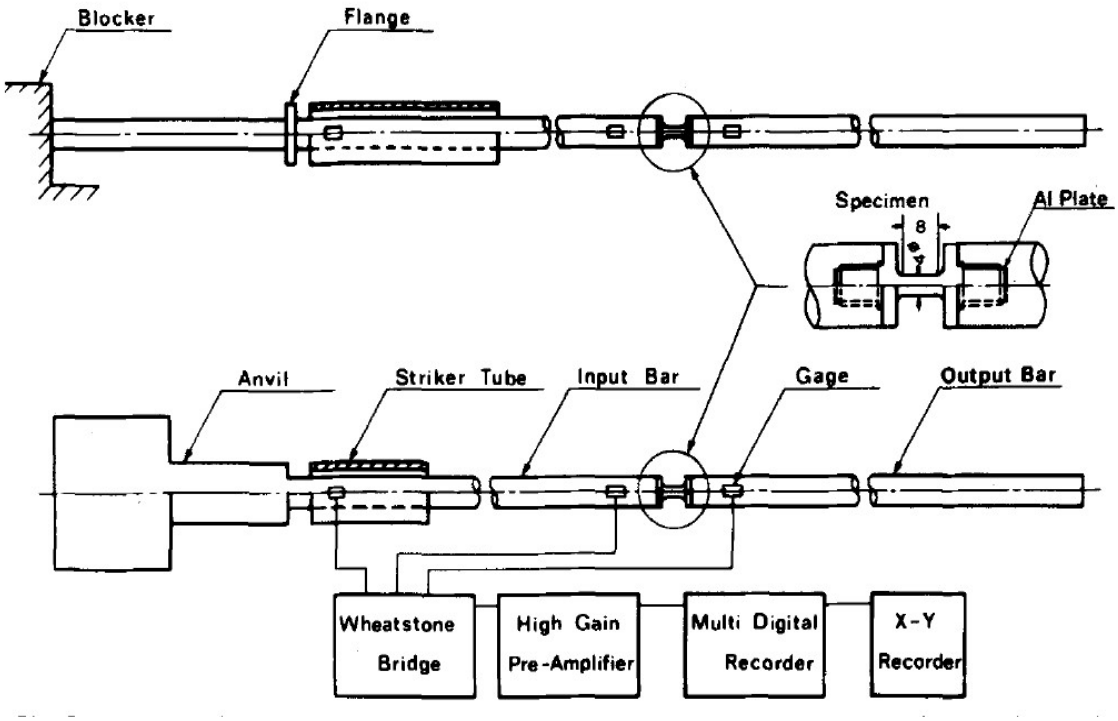

Figure 1.3: Tension test setup for split-Hopkinson bar [22].

As was the case in testing through tension, an assortment of techniques for attaching a sample and applying a load exists for testing in torsion with the split-Hopkinson bar. The first technique for producing load in torsion, known as the stored-torque method, requires fastening the area around the center of an incident bar then torque is created on an end that is free. Figure 1.4 shows an illustration of the setup for this method. [23] A torque is kept along the area linking the fastener and the wheel that applies load through initially tightly securing the fastener and then rotating the wheel for loading with the use of a hydraulically powered system of wires and pulleys. As soon as the fastener is let loose a wave of torsion transmits in the direction of the sample, and an unloading wave travels back in the direction of the wheel. A drawing of the

characteristics, which illustrates the transmission of the elastic pulses through the bars, is provided in Figure 1.4. As the unloading wave arrives at the greater diameter area, some of the wave bounces back and transmits in the direction of the sample. The rotary motion linked to the reflected pulse is in a reverse bearing compared to the pulse linked to the loading wave at the start. As a result, as soon as the reflected wave hits the sample, there is a decrease in the strain rate. The difference in diameters is intended to cause a decrease by a factor of 10 in the velocity of rotary motion. Adjusting the position of the fastener can change the extent of the high-rate deformation.

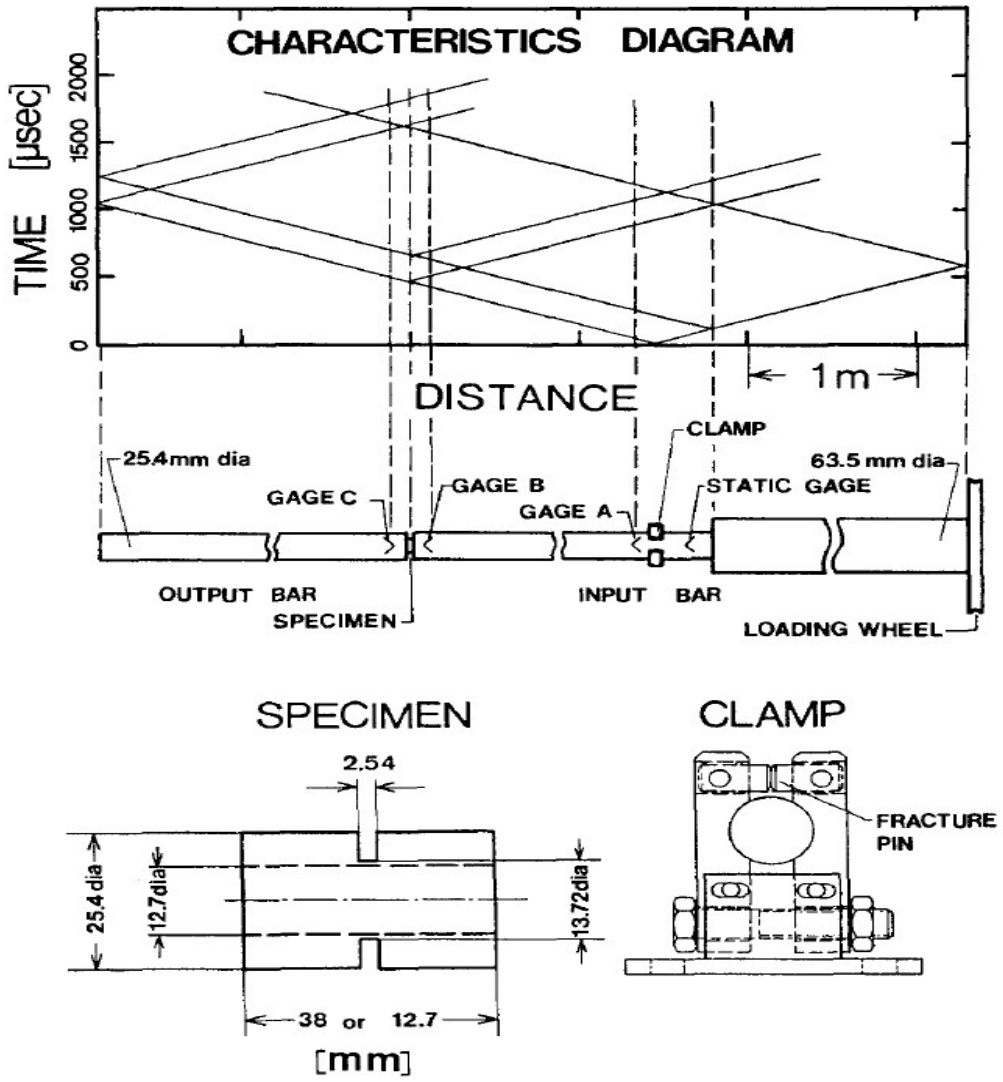

Figure 1.4: Torsion test setup for split-Hopkinson bar [23].

A different method for loading called the explosive-loading technique utilizes explosives put on the end of an incident bar that is free to generate the incident wave. The explosive-loading technique is especially susceptible to error due to the fact that every explosive is required to generate an equivalent pulse on the incident bar (to generate pure torsion without bending) and they all need to be set off at the same time. Also it is improbable that explosive-loading will generate undisturbed incident waves, which could

create irregular strain rates during an experiment. However, the explosive-loading technique has the benefit of a little rise time when measured against the stored-torque technique. Due to continual load be applied into the plastic range, the distribution of strain in the thin-wall cylinder could sometimes not maintain homogeneity. In some instances, based on the material being tested, shear bands could possibly develop that entirely surround the thin-wall cylinder. In instances where the strain does not maintain homogeneity, analysis of data from the strain gages is drastically distorted due to the fact that the strain rate and, consequently, the strain that are extracted from the strain-gage data are average numbers determined with the supposition that the deformation maintains homogeneity. When shear bands form, they cannot be discovered until a quantity of deformation that is plastic has amassed. The occurrence of shear bands on a thin-wall cylindrical sample is simple to identify by engraving small axial lines in the interior face of the sample prior to applying a load. When strain stays homogenous during the process of deformation, following an experiment, every line emerges skewed according to the angle of shear inside the gage piece of a sample, but stays as a straight line as well as axial within the flange section. A skewed portion inside the gage section is a sign that the strain is nonhomogeneous. If non-uniform strain occurs, such as with a shear band, the engravings depart noticeably from lines that are straight. Figure 1.5 from the ASM handbook demonstrates through photographs this technique of detecting shear bands. [24]

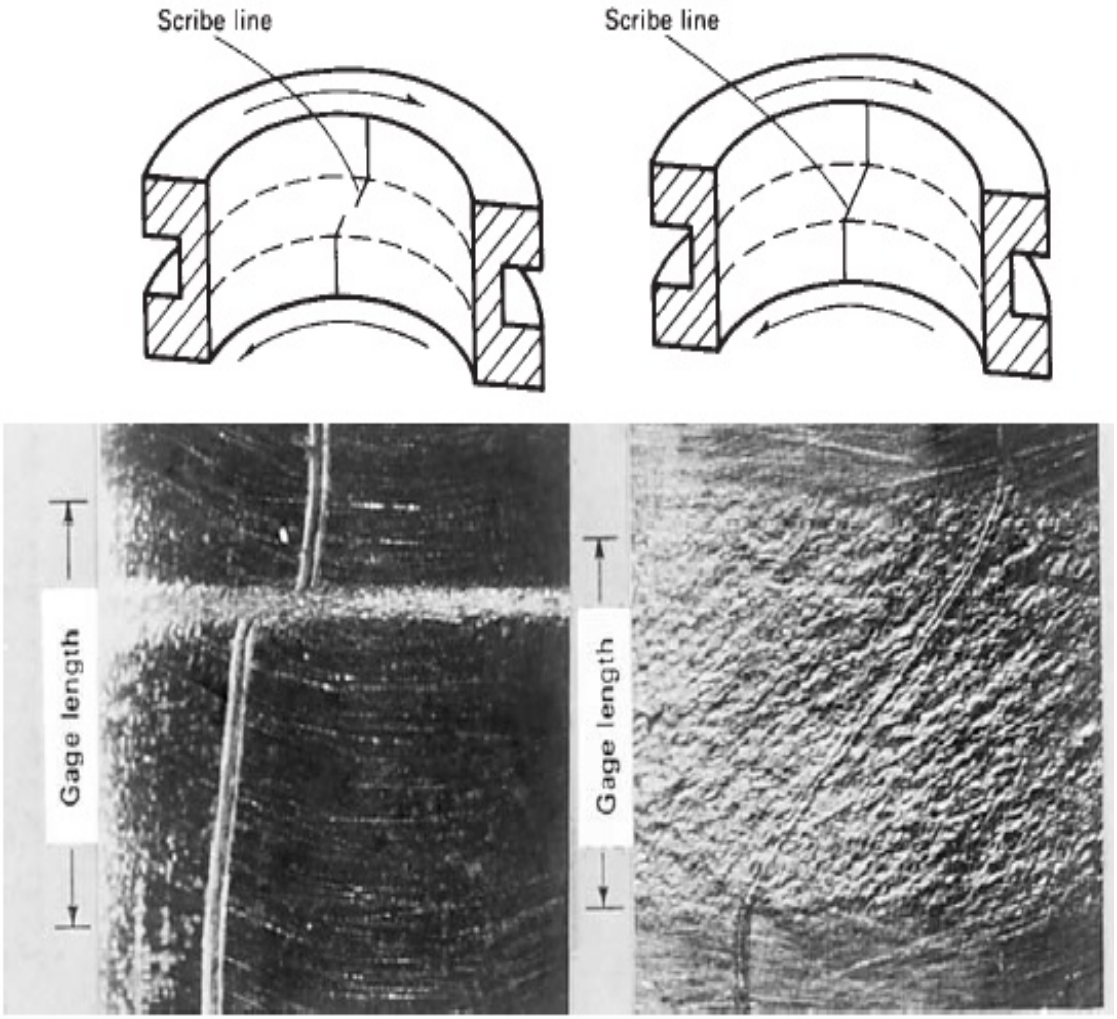

Figure 1.5: Scribed lines within the gage length of a specimen used to detect shear bands [24].

Another dynamic testing technique that has met with substantial success is the expanding ring technique. The expanding ring technique was introduced by Johnson, Stein and Davis in 1962. [25] The way that the technique is setup involves a steel cylinder that has a core, in which an explosive is detonated. A shock wave travels outward and enters the metal ring, propelling it in a trajectory with an expanding radius. By measuring the velocity history of the expanding ring by laser interferometry, one

could resolve the curve of stress-strain for this specimen at a particular strain rate. Figure 1.6 shows illustrations of an expanding ring test setup.

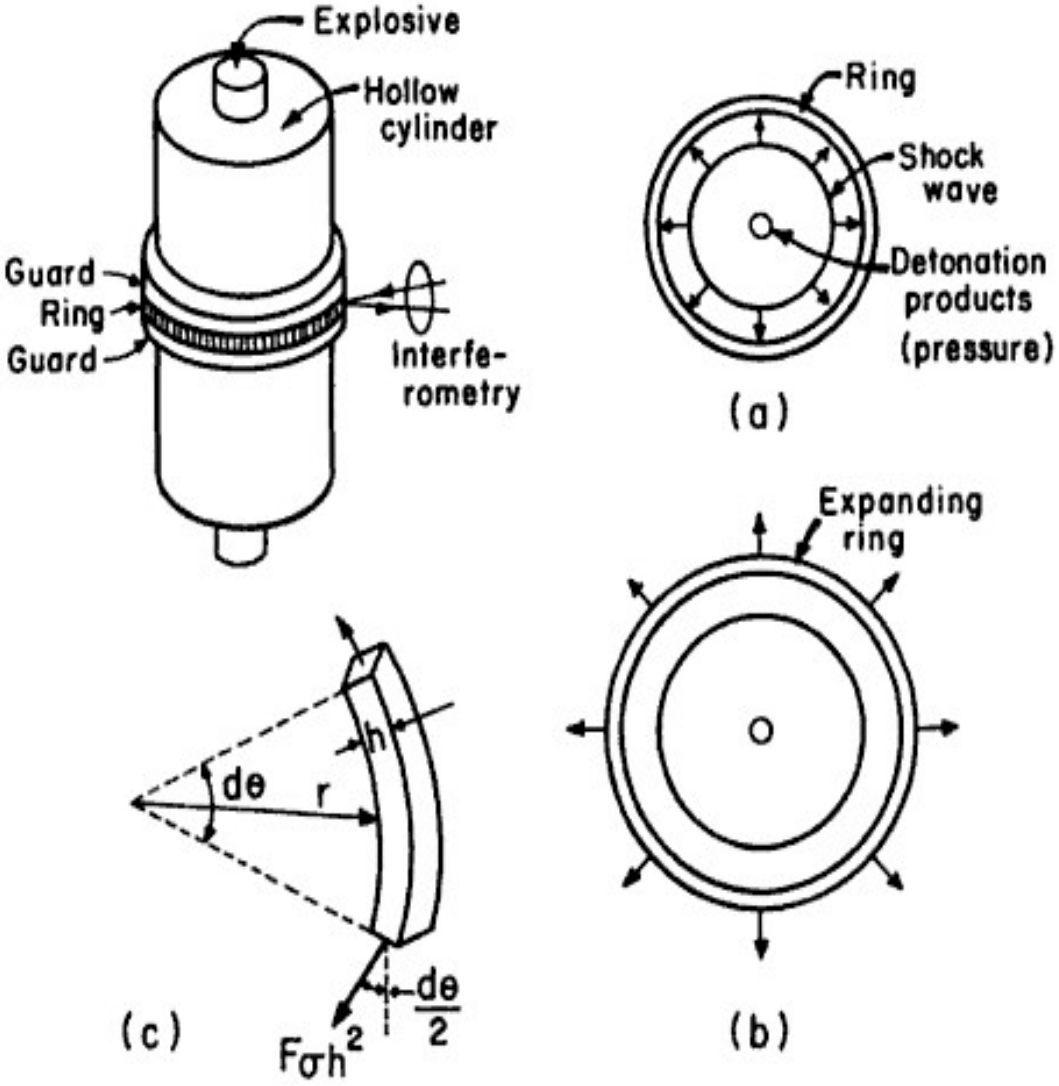

Figure 1.6: Illustration of expanding ring experiment setup – (a) shock wave emitting as a result of pressure from detonation products within hollow cylinder, (b) pressure causing expanding ring to deform, (c) schematic of fragment from expanding ring experiment.

Laser interferometry is based on interference fringes that appear when different laser beams interact. [26-30]Laser is a highly coherent (phased-in) monochromatic light

beam. If two beams are either offset (having the same wavelength) or have slightly different wavelengths, interference patterns will occur. The wavelength of lasers is determined by the source and is of the order of 500 nanometers (0.5 μm). The displacement interferometer, which uses the Michelson interferometer principle[31-35], is explained in Figure 1.7. When the free surface (reflecting) moves to the right, the reflected beam is displaced. This reflected beam is represented by the discontinuous line. The reflected beam is later juxtaposed to a reference beam that continues unchanged. At every displacement of the mirror by λ/x, the crest of the reflected wave is displaced by 2λ/x. When the reflected wave is displaced λ/2 (mirror displaced λ/4), the reference and reflected beams cancel each other totally, and an interference fringe is generated. [36]

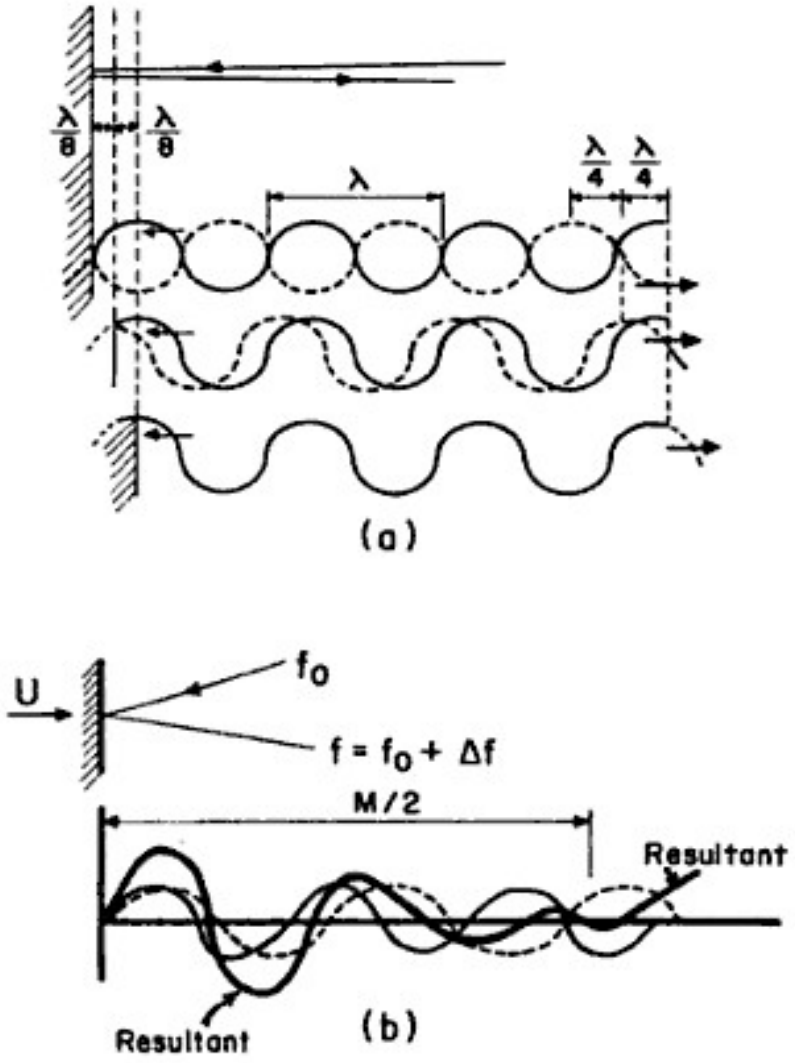

Figure 1.7: (a) The Michelson interferometer principle, (b) the theory of displacement interferometry.

Even though one experiment gives a string of data points, solely a single data point for each strain-rate value can be attained. Due to this fact, several experiments performed at different starting strain rates are necessary to characterize material performance for circumstances of constant strain rate. A number of methods could be utilized to contrast the starting strain rate applied to a specimen; i.e. changing (1) quantity of charges utilized, (2) span of inner opening in center, and (3) the entire diameter of the

ring and core setup. Varying any of the described factors changes the starting disconnection speed of the ring and consequently the strain rate and maximum displacement. Symmetrical extension of thin rings or round shells provides a way to generate homogeneous deformation of a sample, circumventing the issue of wave propagation. Providing that symmetrical grown and ring disconnection is accomplished and confirmed, and the kinematics of the growing ring is recorded with suitable precision, dynamic uniaxial stress-strain data can be calculated. [37]

The fragmentation of solids in dynamic loading is a subject of great importance, primarily in military applications, where the aim is to tailor the fragment size for high-explosive projectiles [38]. Following the classic studies by Mott and coworkers [39-46] in the early 1940s, starting with the report by Mott and Linfoot [39] as part of the Allied war effort, a vast number of experiments were performed in this domain to predict and control fragmentation. The contribution by Grady in this domain expands the original Mott ideas in a remarkable manner. [47] The primary motivation was to tailor the fragmentation response of aluminum by changing the interface cohesion between particles. Two variables were changed for this purpose. The first variable changed was the particle size; three different conditions of aluminum compacts were used: 40 μm aluminum particles, 100 μm aluminum particles, and 400 μm aluminum particles. The other variable changed was the strength of the interface. The strength of the interface was changed through the unique sample processing technique called swaging. The constitutive response of the materials was analyzed using mechanical techniques like the split-Hopkinson pressure bar. The fragmentation of the tailored aluminum compacts was observed using a specifically designed setup of the expanding ring technique that allows

for high speed photography of the fragmentation of rings and soft capture of the fragments. The fragments were analyzed post-fracture with scanning electron microscopy. Simulations of the fragmentation process in the expanding ring technique were conducted using a finite-element analysis program.

CHAPTER 2: BACKGROUND

2.1 Fragmentation theories

The statistical issues that control the fragmentation of a body are completely determined even to this day. A principal concern among the number of aims is the calculation of the size division of fragments consequential from a fragmentation occurrence. A stimulating methodology to the quandary has essentially been to explore the statistically mainly random means of separating a particular topology to a group of distinct entities. The described method for statistical fragmentation has been generally characterized as geometric fragmentation.

2.1.1 Lineau theory

As mentioned in the introduction, Mott pursued a theoretical explanation of the division of fragments during a fragmenting cylinder occurrence. He was influenced through the current work at the time by C.C. Lineau whose theoretical efforts were fundamental to geometric fragmentation. [48] Lineau thought of the basic occurrence of an extended piece like a glass dowel or a elongated wire undertaking pressure, which results in several divisions of the piece. When every spot on the piece is just as prone as each other to break, then the quandary is regarded as statistically correct. A model for this occurrence is setup as an infinite one-dimensional part, or row, wherein fractures are initiated with equivalent likelihood at any spot on the row, illustrated by Figure 2.1.

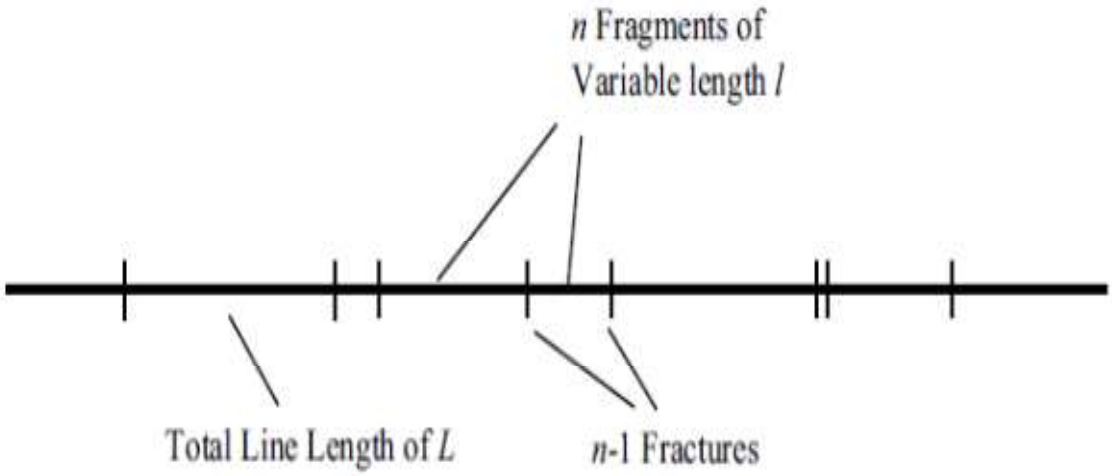

Figure 2.1: (a) Line of total length L segmented into fragments of variable length l by n - 1 fractures [48].

Consider the row wherein fractures are initiated at random to be of length L. [49] The average distance amid fractures λ or equally the rate of recurrence of fractures over a unit of length h_o=1/λ describe the statistical division. The indiscriminate division of spots on a row is characterized by Poisson statistics. When a random section l of the row is observed then the likelihood of discovering n spots (breaks) inside the section l is prescribed by:

$$P(n,l) = \frac{(l/\lambda)^n e^{-l/\lambda}}{n!} \tag{1}$$

The likelihood of discovering zero breaks inside the section l is:

$$P(0,l) = e^{-l/\lambda} \tag{2}$$

, then the likelihood of discovering a single break inside the succeeding length addition dl is:

$$P(1, dl) = (1/\lambda)dl \tag{3}$$

The likelihood of fragments of length *l* inside an addition *dl* is prescribed by:

$$f(l)dl = P(0, l)P(1, dl) = (1/\lambda)e^{-l/\lambda}dl \tag{4}$$

, where:

$$f(l) = (1/\lambda)e^{-l/\lambda} \tag{5}$$

describes a fragment length probability density distribution. The integral of $f(l)$ is:

$$F(l) = 1 - e^{-l/\lambda} \tag{6}$$

, which describes a cumulative fragment distribution.

When there exists a division of N_o fragments corresponding with these statistical assertions, the resulting analytic expression:

$$N(l) = N_o e^{-l/\lambda} \tag{7}$$

will characterize the cumulative allotment of fragments greater than span *l*. Allocating a density per unit length to the one-dimensional part it is viable to show that the cumulative mass fraction of fragments is specified through the expression:

$$P(0, l) = e^{-l/\lambda} \tag{8}$$

This expression is a more commonly used experimental description.

2.1.2 Mott and Mott-Linfoot theories

In 1943, N.F. Mott and E.H. Linfoot [39] utilized the previous study of Lineau [48] and advanced his random geometric fragmentation concepts in search of a practical fragment size distribution expression for the explanation of fragmenting munitions. They

realized the Lineau method was acceptable because fragment munitions data accessible at the moment was discovered to plot relatively linear in a log value against the cube root of the fragment mass depiction. They reasoned that due to the fact $m^{1/3}$ is proportional to a length span of the fragment then the equivalent indiscriminate variable depicted with a Lineau one-dimensional model worked in a multidimensional fragmentation occurrence. While studying fragments in the existing data, they found that a considerable fraction kept interior and exterior faces of the initial munitions casing. The observation led to a suggestion that in the fragmentation of an areal region the more suitable length amount would be comparative to $m^{1/2}$. Therefore a graph of log number against $m^{1/2}$ ought to present a superior assessment of the fragment distribution statistics. Following the description of the previous Lineau distribution, the fragment cumulative probability distribution that Mott and Linfoot proposed is prescribed by:

$$F(m) = 1 - e^{-(m/\mu)^{1/2}} \tag{9}$$

wherein the characteristic mass μ is the distribution scale parameter. The probability density distribution is prescribed as follows:

$$f(m) = \frac{1}{2\mu}\left(\frac{m}{\mu}\right)^{-1/2} e^{-(m/\mu)^{1/2}} \tag{10}$$

For almost seventy years the Mott and Linfoot distribution has been used successfully in a range of forms to systematize and evaluate enormous amounts of exploding munitions fragmentation data. Mott devoted a great deal of his consequent work to validating the two previous functional forms.

In their early attempts to substantiate their theories, Mott and Linfoot utilized an especially practical geometric representation. Their basis for this model was the statistical separation of a plane by an indiscriminate array of perpendicular and parallel lines. It was assumed that the separation of the lines in the different directions was independently determined by the Lineau distribution. Thus:

$$f_x(x) = \frac{1}{x_o} e^{-x/x_0}, \tag{11}$$

, where:

$$f_y(y) = \frac{1}{y_o} e^{-y/y_0} \tag{12}$$

where the variation of the standard separation or frequency of lines in the perpendicular and parallel orientation was permissible. One can easily observe the described straightforward geometric representation could logically reproduce the numerical performance of discharging munitions. The indiscriminate lines compare to experiential vertical and horizontal cracks, and then the fraction x_0/y_0 suggests a lengthened character or feature proportion of discharging munitions fragments as shown in Figure 2.2.

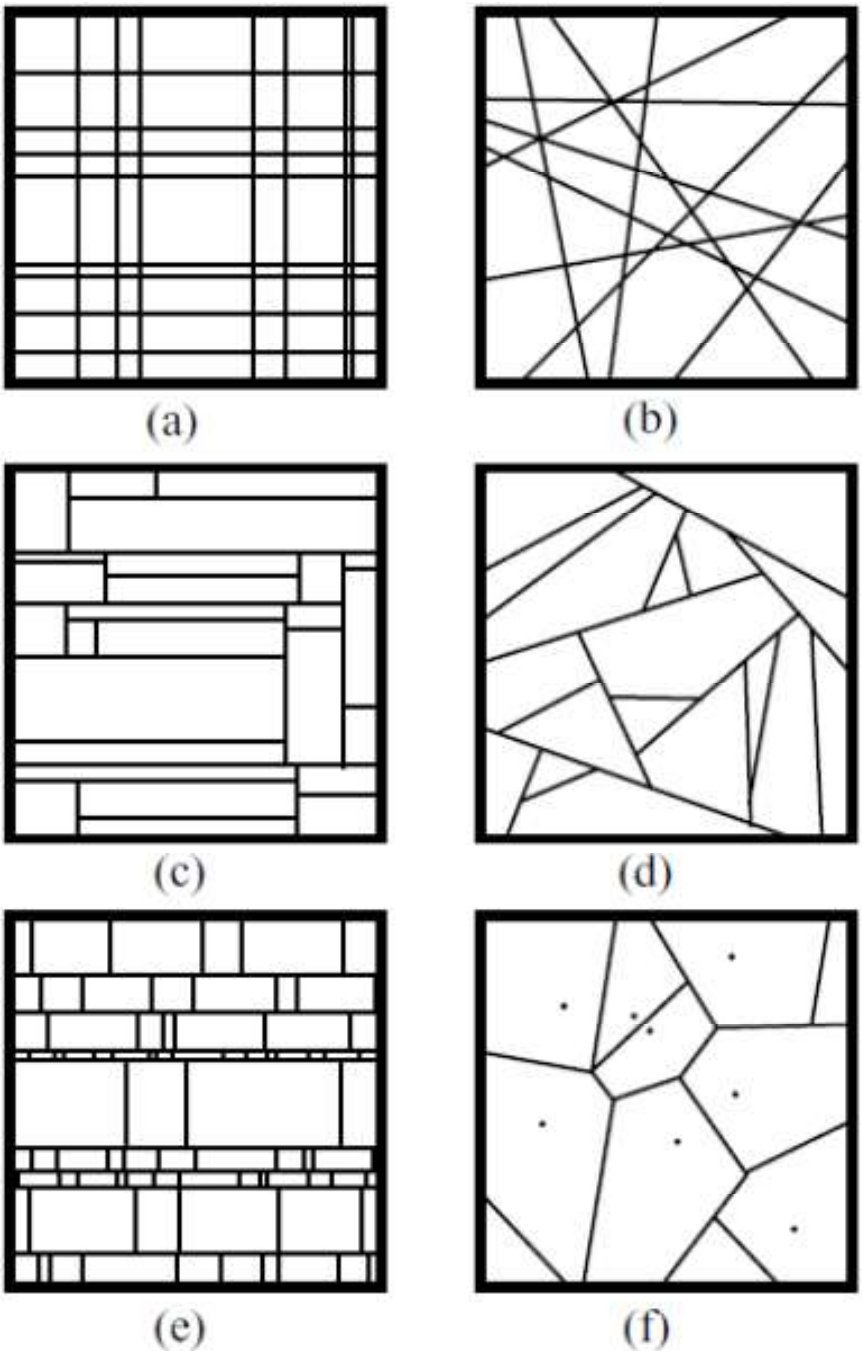

Figure 2.2: Illustrations of the geometric random fragmentation algorithms investigated by Mott and others [38].

However, Mott[41, 45, 46, 50] found through the subsequent process the prescribed division does not fit closely to the relations in Equation 9 and Equation 10

theorized by Mott and Linfoot.[39] Nevertheless, when effectively generalized, it is possible to show that this geometric algorithm approximates fairly closely the numerical depiction of a biaxial division of expanding munitions.

The probability density distribution considering fragment span and thickness is subsequently given using a combination with Equation 11 and Equation 12:

$$f(x,y) = \frac{1}{x_0 y_0} e^{-x/x_0 - y/y_0} \tag{13}$$

Mott and Linfoot[39] continued to solve for the fragment size distribution utilizing the next method: Consider $z = \sqrt{xy}$, where *xy* represents the fragment region, to offer the quantification of a fragment dimension. Then a collective representation for fragments with area greater than *z* is given by the integral term:

$$1 - F(z) = \iint_{xy>z^2} \frac{1}{x_0 y_0} e^{-x/x_0 - y/y_0} dx dy \tag{14}$$

The double integral over area is represented by:

$$\frac{1}{x_0 y_0} \int_0^\infty e^{-x/x_0} \left[\int_{z^2/x}^\infty e^{-y/y_0} dy \right] dx \tag{15}$$

which reduces simply to:

$$\frac{1}{x_0} \int_0^\infty e^{-\frac{1}{x_0}\left(x + \frac{x_0 z^2}{y_0\, x}\right)} dx \tag{16}$$

Through the modification of *x*:

$$x = z\sqrt{\frac{x_0}{y_0}\eta} \tag{17}$$

the expression changes to:

$$\frac{z}{\sqrt{x_0 y_0}} \int_0^\infty e^{-\frac{z}{\sqrt{x_0 y_0}}\left(\eta + \frac{1}{\eta}\right)} d\eta \tag{18}$$

Once the characteristic length $z_0 = \sqrt{x_0 y_0}$ is introduced and the additional change of variable $\eta = e^{\theta}$ is made then the integral becomes:

$$\frac{z}{z_0} \int_{-\infty}^{\infty} e^{-\frac{z}{z_0}\left(e^{\theta}+e^{-\theta}\right)} e^{\theta} d\theta \tag{19}$$

which can then change as an integral of the hyperbolic function:

$$2\frac{z}{z_0} \int_{0}^{\infty} e^{-2\frac{z}{z_0}\cosh} \cosh\theta \, d\theta \tag{20}$$

Mott and Linfoot[39] recognized the solution of the integral as an adapted Bessel equation. The integral solving to adapted Bessel functions of integer order [51] yields:

$$K_n(u) = \int_{0}^{\infty} e^{-u\cosh} \cosh n\theta \, d\theta \tag{21}$$

to an adapted Bessel function on an order of *n*. Therefore, it provides a cumulative probability distribution for fragment magnitude *z*:

$$F(z) = 1 - 2\frac{z}{z_0} K_1(2z/z_0) \tag{22}$$

It is possible to determine the probability density distribution from $dF(z)/dz = f(z)$ in combination with an adapted Bessel equation expression [51]:

$$\frac{d}{du}\left(uK_1(u)\right) = -uK_0(u) \tag{23}$$

or:

$$f(z) = 4\frac{z}{z_0^2} K_0(2z/z_0) \tag{24}$$

It is also enlightening to observe a different key approach. Equation 13 can be used to set up again with the probability density distribution considering fragment span

and thickness. There is one conversion with the probability distribution *g(a,r)* on a fragment region:

$$a = xy \tag{25}$$

also a fragment aspect relation:

$$r = x/y \tag{26}$$

needs to be determined.

The differential invariant:

$$f(x,y)dxdy = g(a,r)dadr$$

converts to:

$$dxdy = \left|\frac{\partial(x,y)}{\partial(a,r)}\right| dadr$$

for a differential factor under the transformation Jacobian [52].

A converted probability density expression subsequently becomes:

$$g(a,r) = f\big(x(a,r), y(a,r)\big) \left|\frac{\partial(x,y)}{\partial(a,r)}\right| \tag{27}$$

Once the Jacobian is calculated through Equation 25 and Equation 26:

$$\left|\frac{\partial(x,y)}{\partial(a,r)}\right| = \frac{1}{2} r^{-1} \tag{28}$$

that results in:

$$g(a,r) = \frac{1}{2x_0 y_0} \frac{1}{r} e^{-\left(\frac{1}{x_0}\sqrt{ar} + \frac{1}{y_0}\sqrt{a/r}\right)} \tag{29}$$

which is the probability density distribution in a fragment region and aspect ratio.

Then in order to find a probability density distribution on region *h(a)*, regardless of aspect ratio, the solution must be found for the integral over all *r*:

$$h(a) = \frac{1}{2x_0y_0}\int_0^{\infty}\frac{1}{r}e^{-\left(\frac{1}{x_0}\sqrt{ar}+\frac{1}{y_0}\sqrt{a/r}\right)}dr \tag{30}$$

The integration variable can be changed through $r = (x_0/y_0)e^{2\eta}$ that gives:

$$h(a) = \frac{2}{a_0}\int_0^{\infty} e^{-2\sqrt{\frac{a}{a_0}}\cos} \quad d\eta \tag{31}$$

where $a_0 = x_0y_0$. From the common integral expression for an adapted Bessel function of Equation 21 there is:

$$h(a) = \frac{2}{a_0}K_0\left(2\sqrt{a/a_0}\right) \tag{32}$$

This distribution relation of fragment region is correspondent to the development by Mott and Linfoot[39] inside Equation 24 if the conversion $a = z^2$ is executed.

The collective distribution function in fragment region *H(a)* is numerically found by an integration of Equation 32 and the relation $K_1'(u) = -K_0(u)$ [51]:

$$H(a) = 1 - 2\sqrt{a/a_0}\,K_1\left(2\sqrt{a/a_0}\right) \tag{33}$$

The distribution of density in Equation 29 can be developed more to gain the probability density expression on aspect ratio *k (r)* regardless of fragment dimension. When executing the integral on fragment region:

$$k(r) = \frac{1}{2x_0y_0}\int_0^{\infty}\frac{1}{r}e^{-\left(\frac{\sqrt{r}}{x_0}+\frac{1}{y_0r}\right)\sqrt{a}}da \tag{34}$$

with the transformation:

$$\xi = \left(\frac{\sqrt{r}}{x_0}+\frac{1}{(y_0\sqrt{r})}\right)\sqrt{a}$$

it is found that:

$$k(r) = \frac{1}{r_0}\frac{1}{(1+r/r_0)^2}\int_0^\infty \xi e^{-\xi} d\xi \tag{35}$$

where $r_0 = x_0/y_0$. Therefore:

$$k(r) = \frac{1}{r_0}\frac{1}{(1+r/r_0)^2} \tag{36}$$

gives the probability density distribution on fragment aspect ratio.

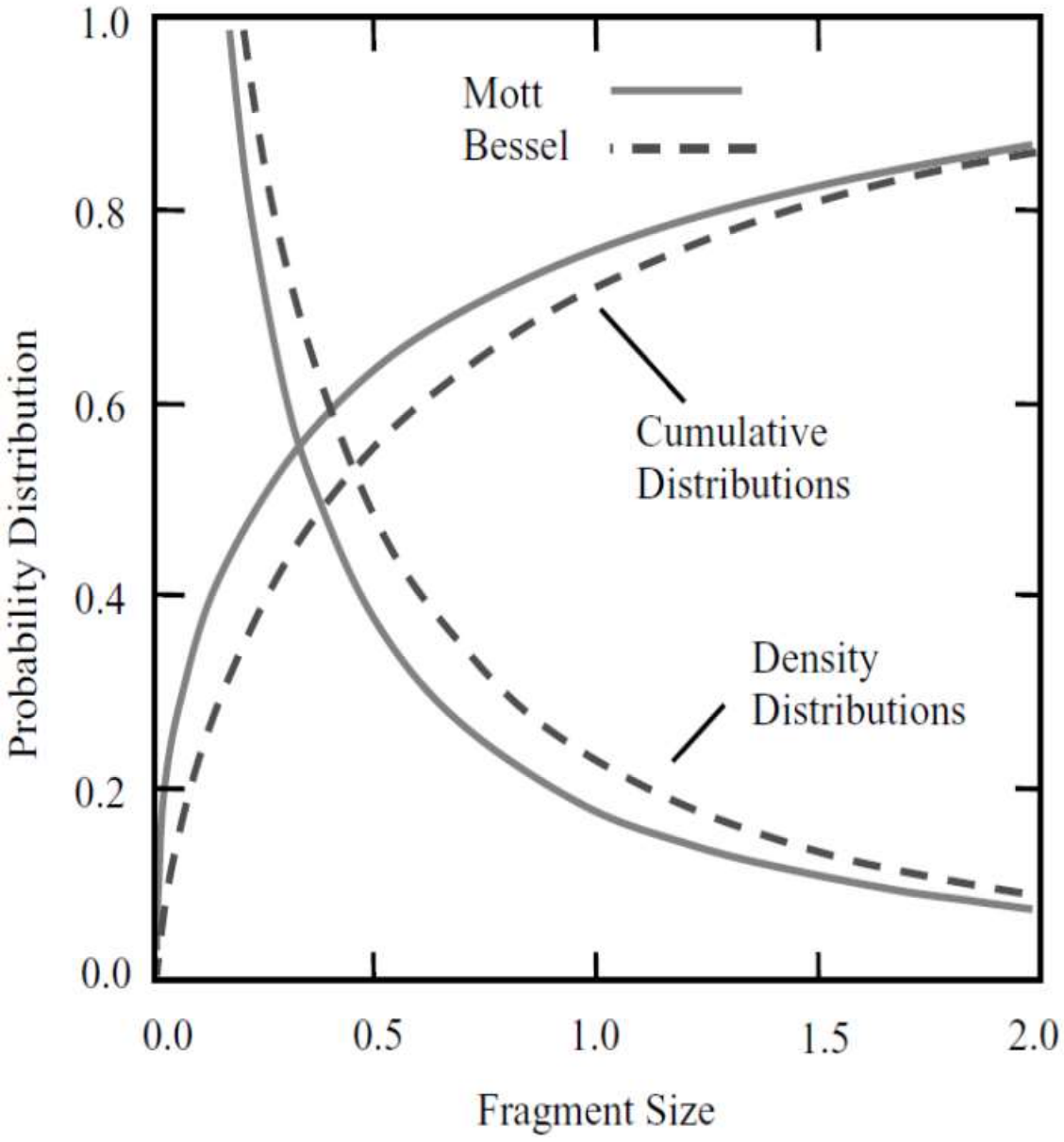

Figure 2.3: A comparison between the Mott distribution and the Bessel fragment size (area) distribution resulting from the random Lineau placement of vertical and horizontal lines on the surface [47].

The density and cumulative probability distributions with indiscriminate orthogonal lines geometric fragmentation set up is evaluated for a Mott distribution in Figure 2.3 having each of the distributions being normalized to unity. The evaluation discloses variations, which were discovered by Mott and Linfoot, being unsuccessful in

yielding a validation they were looking for. A distribution variance of five is calculated (by the second moment around the average) with a Mott distribution Equation 10 that is considerably larger than the variance of three equated with a Bessel distribution in Equation 32. A greater amount of mutually undersized and big fragments would be predicted by the Mott distribution.

Then Mott and Linfoot[39] attempted to solve the geometric fragmentation quandary when direction along with position of lines in a region is an indiscriminate variable as shown in Figure 2.2b. However, they were not able to establish the distribution of size for this fragmentation algorithm with the exception of the diminutive fragment maximum that was in agreement to a projected reliance of fragment quantity comparative with a second root of the fragment area. The calculations performed by computer with the described geometric fragmentation approach [53] imply sensible concurrence to a Mott distribution on an entire array of fragment dimensions. Through a process of trying to solve the geometric quandary of indiscriminately directed perpendicular and parallel lines followed by an expansion to arbitrarily directed lines that are illustrated through Figure 2.2b, Mott and Linfoot implicitly discovered a resultant distribution of fragment range had to in all probability rely on the approach selected in indiscriminately dividing a region.

2.1.3 Mott cylindrical segmentation theory

If the distribution of fragment size developed for the indiscriminate geometric fragmentation method is based on which fragmentation algorithm, then evidently an algorithm that best accurately reproduces the incident for study should be anticipated to

provide a higher quality approximation of the numerical characteristics desired. The previous approach estimates sensibly any perpendicular cracks and succeeding surrounding disintegration found during a munition fragmentation occurrence. The closeness compared to the area in interest probably directed Mott toward determining the last geometric fragmentation method to examine.

The last algorithm is shown if Figure 2.2e. The process begins with marking indiscriminately placed parallel lines, after which every parallel band is segmented using an indiscriminately placed perpendicular line such that the standard spacing between each band is comparative to the thickness of that band. While attempting to find the solution to the distribution of size in the set up, Mott additionally altered the functional form directing the indiscriminate positioning of parallel lines and perpendicular line sections.

It is discovered in solving to find a fragment magnitude distribution of the geometric approach, using a Lineau distribution of perpendicular lines and parallel line sections, the algorithm won't be maintainable as well as the final distribution won't converge. Mott most likely discovered the problem so this finding could have possibly influenced his choice of a distribution form dissimilar from the Lineau type. It's just as probable the choice had not been capricious and had been spurred through physical concepts materializing in these additional physically-rooted hypotheses beginning to be utilized.

Either way, by attempting to solve the other geometric fragmentation model put forth by Mott, it is found to be apparent the probability density distribution of fragments in a sectional area will not merely be gained through mixing the pair of linear distributions like the operation performed on the preceding examination. In the beginning

it becomes obligatory to involve numeral distributions due to complexities when normalizing a probability distribution. It is important to understand initially when provided the probability density distribution through fragment spans *f(x)*, an entire distance *dL* of fragments with a span *x* inside addition *dx* becomes simply:

$$dL = xdN = N_0 x f(x) dx \tag{37}$$

or:

$$L = N_0 \int_0^\infty x f(x) dx = N_0 \langle x \rangle \tag{38}$$

where $\langle x \rangle$ represents an anticipated figure of *x* while N_0 represents the overall fragment amount. Under a Lineau distribution like prescribed in (2.11) an anticipated figure becomes simply $\langle x \rangle = L/N_0 = x_0$.

With the geometric fragmentation algorithm shown in Figure 2.2e the area is prescribed with equivalent thickness and length *L*. Now take into consideration a single band with thickness *y*. An amount of divisions or fragments inside the single band with span *x*, inside addition *dx*, becomes basically:

$$dN_x = N_{xo} \frac{1}{x_0} e^{-x/x_0} dx = \frac{L}{x_0^2} e^{-x/x_0} dx \tag{39}$$

assuming there is a Lineau distribution of fragment spans. Likewise, an amount of bands with thickness, *y* with addition *dy* becomes:

$$dN_y = \frac{L}{y_0^2} e^{-y/y_0} dy \tag{40}$$

Therefore, the amount of fragments with span *x* as well as thickness *y* inside each region (letting $L^2 = 1$) becomes purely the following result:

$$dN = dN_x dN_y = \frac{1}{x_0^2 y_0^2} e^{-x/x_0 - y/y_0} dx dy \tag{41}$$

Then Mott continued to supplement the geometric fragmentation algorithm by assuming inside a band with thickness *y* a standard fragment span becomes relative to *y* such as:

$$x_0 = py \tag{42}$$

Mott proposed this figure *p* would generally be 5 considering the munitions fragments from which he was provided a chance at examining. His proposition was evidently spurred by the study of fragments collected through some cylindrical munition fragmentation occurrence wherein the type of fracturing corresponds from a large amount of stretched out fragments. A resultant fragment number distribution is consequently:

$$dN = \frac{1}{p^2 y_0^2 y^2} e^{-y/y_0 - x/py} dxdy \tag{43}$$

Once again there is a change of variables:

$$a = xy, \quad r = x/y \tag{44}$$

with a Jacobian:

$$\left|\frac{\partial(x,y)}{\partial(a,r)}\right| = 1/2r \tag{45}$$

that leads to a number distribution:

$$dN = \frac{1}{2p^2 y_0^2} \frac{1}{a} e^{-\sqrt{\frac{a}{ry_0^2}} - r/p} da\, dr \tag{46}$$

of fragment region *a* and aspect ratio *r*. Then the numeral distribution with respect to fragment area is found with an integral:

$$\frac{dN}{da} = n(a) = \frac{1}{2p^2 y_0^2} \frac{1}{a} \int_0^\infty e^{-\sqrt{\frac{a}{ry_0^2}} - r/p} dr \tag{47}$$

or, with use of the variable change $r = p\eta$:

$$n(a) = \frac{1}{2py_0^2}\frac{1}{a}\int_0^\infty e^{-\sqrt{\frac{a}{py_0^2\sqrt{\eta}}}\frac{1}{}-\eta}\, d\eta \qquad (48)$$

However, the integral within Equation 48 is unfortunately not finite. A brief assessment with this distribution will demonstrate a boundless numeral density distribution when the region *a* and aspect ratio *r* grows smaller. Therefore, the especially logical statistical fragmentation geometry, after being merged with a Lineau (Poisson) placement of all the breaks, results in this imprecise fragment distribution. Even though it is not overtly addressed through the papers by Mott he had to of followed the same line of reasoning and come across an identical predicament.

2.1.4 Grady-Kipp theory

In 1985 D.E. Grady and M.E. Kipp [53] developed a different model and rationalization based on distributions of fragment dimensions examined within munitions fragmentation. Grady and Kipp began by suggesting that if it is possible to represent fragmentation in munitions through mechanism-independent statistical means then conceivably fragment mass, in contrast with fragment magnitude (regarded as $m^{1/2}$ or $m^{1/3}$ for the Mott-Linfoot development), is the further suitable indiscriminate figure. Grady and Kipp followed this suggestion by proposing also each mass of a fragment is distributed in fragment amount based on the Poisson process, which parallels earlier developments of Lineau that were first described.

Based on these suggestions, utilizing fragment mass as an indiscriminate scalar variable, the indiscriminate breakup observed with mass will be comparable as a single-dimension Lineau setup. So the fractures positioned indiscriminately throughout a scalar

assessment with mass will determine any fragmentation. Then the Poisson variable can be determined from the breaks that will provide the collective fragment probability distribution:

$$F(m) = 1 - e^{-m/\mu} \tag{49}$$

as well as the density distribution:

$$f(m) = \frac{1}{\mu} e^{-m/\mu}. \tag{50}$$

Unlike the Mott-Linfoot distribution, the Grady-Kipp distribution maintains an identical linear exponential practical format considering area as well as volume division.

Grady and Kipp [53] also attempted to justify the fragment distribution theories they developed with geometric fragmentation techniques. However, computing capabilities available at the time did not restrict them to only geometries that had analytic solutions. Figures 2.2c and 2.2d illustrate the algorithms they attempted to utilize. Their approach used this procedure: First some spot is chosen randomly in a single region. An indiscriminate perpendicular or parallel path in Figure 2.2c or indiscriminate random path in Figure 2.2d is then selected and a streak sketched through the spot and stopped once it reached the region border. Another spot is chosen at random then an indiscriminate streak once more sketched halving the secondary region inside where the spot landed. The method is reiterated successively so that a required amount of fragmentation was attained.

Soon they discovered the distributions based on using parallel and perpendicular streaks, and indiscriminately directed streaks, succeeding partitioning geometric progressions merged into linear-exponential distributions observed with Equation 49 and

Equation 50 with satisfactory statistics of fragments in the geometric fragmentation for a region. After thorough consideration they understood the geometric process starts reproducing the Poisson sectioning of a scalar region or volume. Therefore, this concurrence will be anticipated.

This linear exponential (Poisson) density and cumulative distribution is demonstrated in Figure 2.4, where it is shown to be much different compared to a Mott distribution. A considerably more expansive Mott distribution demonstrates variation that factors five times greater compared to a Poisson distribution.

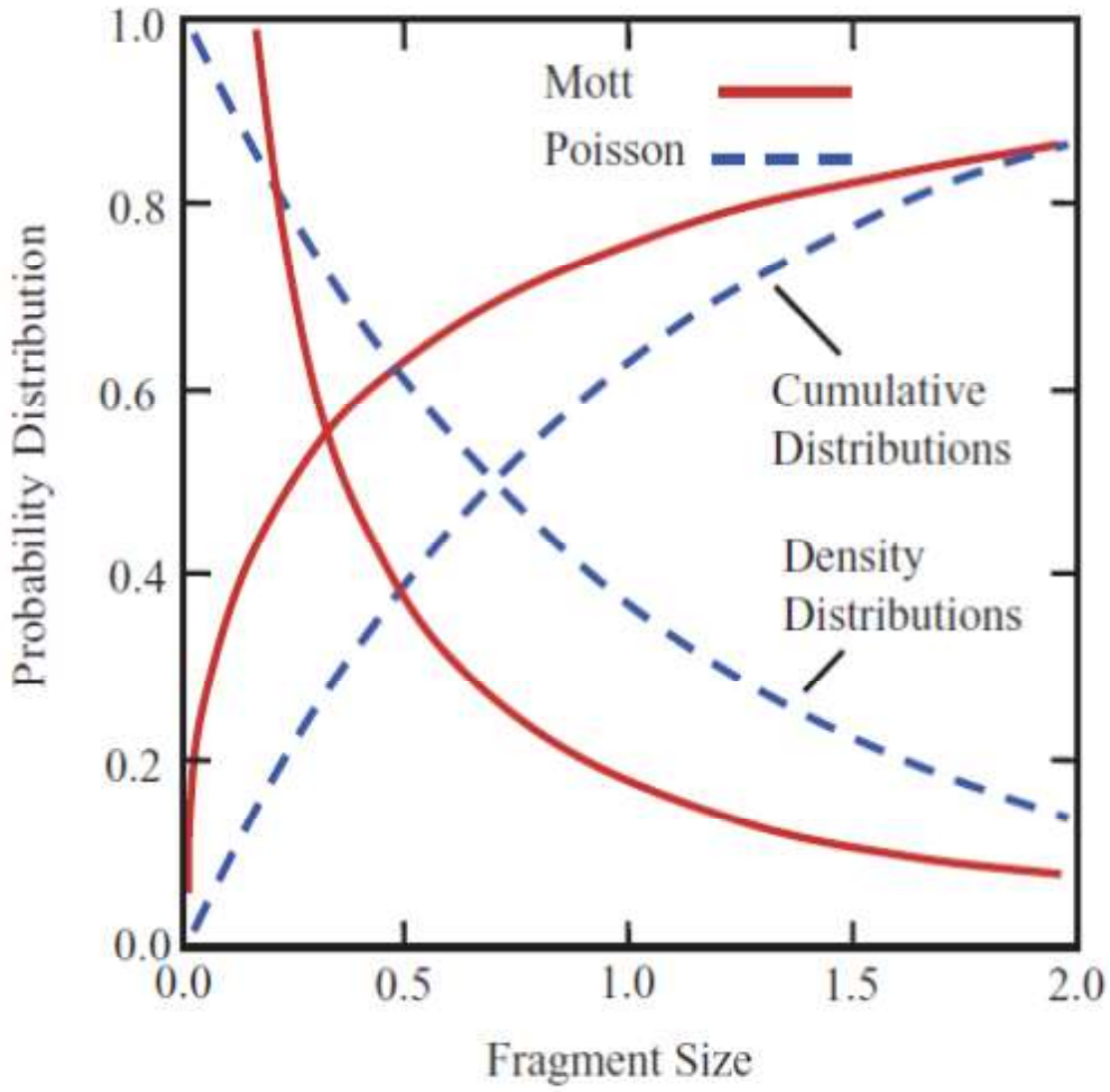

Figure 2.4: A comparison between the Mott distribution and the Exponential, or Poisson, fragment size (area) distribution resulting from the random segmentation of the surface [31].

Based on the significant disparity among an exponential distribution and a Mott distribution demonstrated through Figure 2.4, as well as the long history of agreement in describing munitions fragmentation data, one would be inclined to query how it would be possible for the exponential distribution to become utilized for any suitable demonstration. So they [53] put forth this subsequent idea to maintain their exponential

distribution. Through all of these numerical fragmentation quandaries addressed so far, numerical uniformity in an area of fragmentation has been basically presupposed. Specifically, typical fragment magnitude saw no change from end until end inside an area under examination. During an actual function unvarying and homogenous breakup will not typically be attained. Usually, the intricacy in an apparatus geometry as well as forceful pressure causes an amount of rupture to change within an area and also as a result the typical fragment magnitude is dependent on location. Any uniform expansions of a spherical shell or a uniformly expanding ring are special experimental geometries that nearly attain homogeneous fragmentation. However, the majority of experimental geometries actually undergo inhomogeneous fragmentation.

The linear exponential distribution that follows the Poisson method within a scalar mass area:

$$f(m) = \frac{1}{\mu} e^{-m/\mu} \tag{51}$$

which was proposed by Grady and Kipp in 1985, made the assumption there was numerical uniformity using a standard mass μ that was unvarying for an area under examination. Another distribution having a dissimilar average fragment size can be expressed just as well using a distribution with the form of Equation 51. A juxtaposition of this pair of distributions will not be represented with a linear exponential distribution. Actually this distribution is characterized through a bi-linear structure:

$$f(m) = \frac{g_1}{\mu_1} e^{-m/\mu_1} + \frac{g_2}{\mu_2} e^{-m/\mu_2} \tag{52}$$

where g_1 and g_2 represent the numeral proportions for each of the particular homogeneous distributions, then μ_1 and μ_2 represent each of the respective mean

fragment masses. Essentially every numerically inhomogeneous distribution can be represented by the Poisson combination [54]:

$$f(m) = \sum_1^n \frac{g_i}{\mu_i} e^{-m/\mu_i} \tag{53}$$

It is possible to demonstrate every Poisson combination version for any fragment distribution maintains greater variance compared to any numerically uniform linear exponential expression with an equal distribution. So then it would be informative to examine a comparison of the bi-linear distribution with Equation 52 and the Mott distribution, normalizing a Mott distribution with a standard fragment mass $x = m/\mu$:

$$f(x) = \frac{1}{\sqrt{2x}} e^{-\sqrt{2x}} \tag{54}$$

and likewise the bi-linear distribution with $x = m/\mu$ and $\mu = g_1\mu_1 + g_2\mu_2$:

$$f(x) = \frac{g_1}{\alpha_1} e^{-x/\alpha_1} + \frac{g_2}{\alpha_2} e^{-x/\alpha_2} \tag{55}$$

where $\alpha_1 = \mu_1/\mu$ and $\alpha_2 = \mu_2/\mu$.

Then limit an integral for this distribution as well as an initial moment for unity with Equation 55:

$$g_1 + g_2 = 1 \tag{56}$$

$$\alpha_1 g_1 + \alpha_2 g_2 = 1 \tag{57}$$

The second and third distribution moments, which are equivalent to the distribution variance as well as offset, could as well become equivalent for any respective moments with a Mott distribution that gives:

$$2(g_1\alpha_1^2 + g_2\alpha_2^2) = 6 \tag{58}$$

$$6(g_1\alpha_1^3 + g_2\alpha_2^3) = 90 \tag{59}$$

specifically constricting all four constants for this bi-linear distribution. An evaluation with Mott and bi-linear distributions, which in point of fact are complementary collective distributions, having the similar distribution moments is illustrated in Figure 2.5. Even though prominent visual differences can be seen, the bi-linear distribution begins demonstrating significant aspects with a Mott distribution. These distributions can be evaluated through a semi-logarithmic expression where one exponential or Poisson distribution is depicted linear in a graph. Improved concurrence could, evidently, result when additional expressions become involved with a Poisson combination depiction.

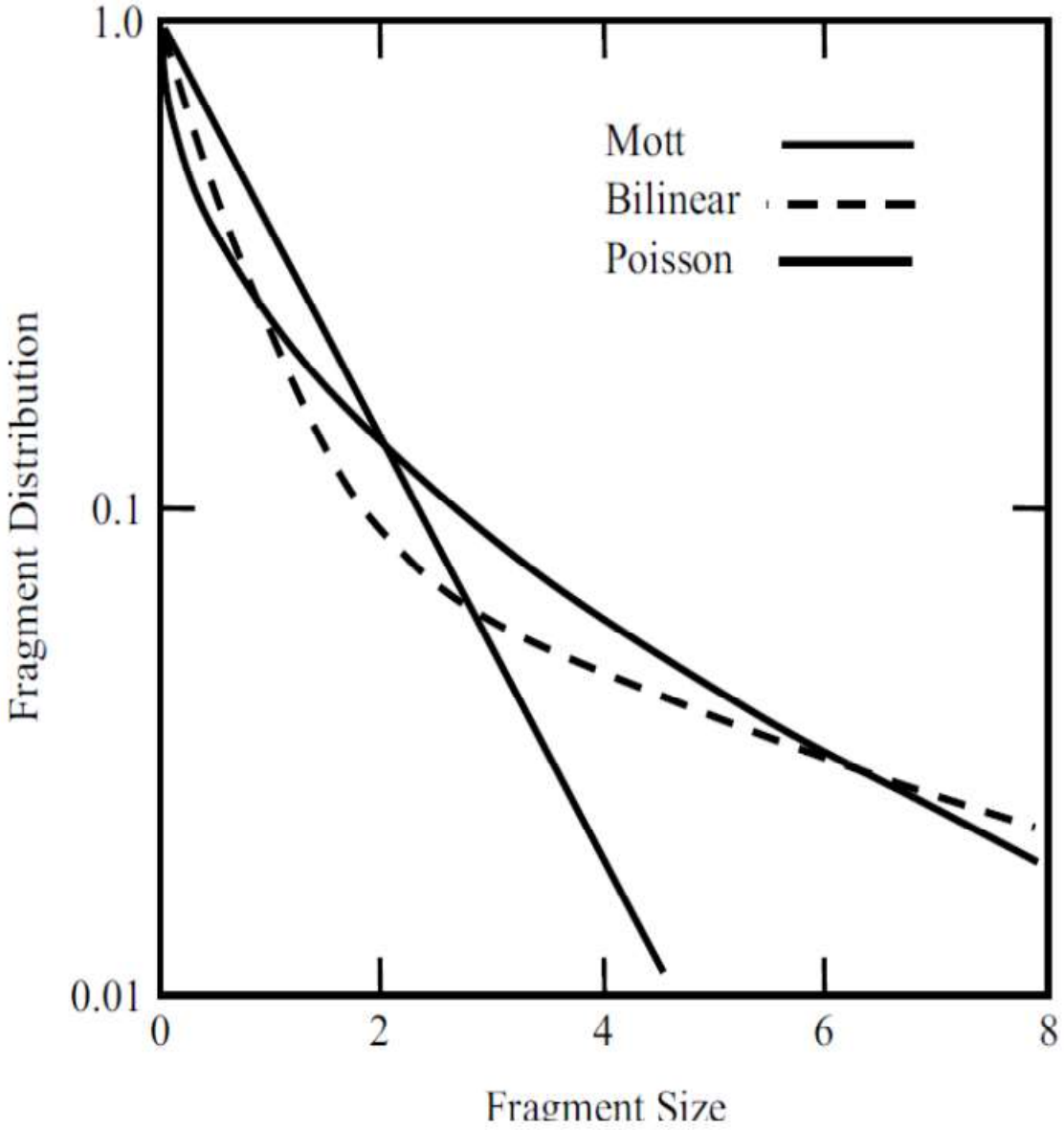

Figure 2.5: Comparison of the Mott and Poisson fragment size complementary cumulative distribution with a bilinear (Poisson mixture) distribution approximation [31].

2.1.5 Voronoi-Dirichlet theory

The current review of indiscriminate geometric fragmentation is incomplete with no discussion about a Voronoi-Dirichlet expression [55]. This process of indiscriminate division for a region has been given a great deal more attention in a wider range of

literature.[56-60] The distributions produced from this construction were suggested as functions for a distribution of galactic material throughout space [61] as well as creation of geological column shaped formations [62].

This method of construction with a couple dimensions is depicted through Figure 2.2f. Similar to a Grady-Kipp set up, this process starts through an indiscriminate numerically uniform distribution of spots in an area, or inside a volume when considering a three-dimensional region. Then the space will be divided randomly through the utilization of perpendicular bisecting lines or surfaces as seen in Figure 2.2f. Also, the space is randomly divided by the reciprocal (or dual) Delauney construction [63] employed through the joining, with lines or surfaces, the points of each Voronoi-Dirichlet cell.

There has not been any direct determination of the analytic expressions of fragment size distributions attained through a Voronoi-Dirichlet set up. A computational finding of the resulting fragment size distributions has been extensively sought after [64]. However, an analytic relation that successfully reproduced the computational distributions has been found through intuitive techniques [61].

The analytic distributions as well as the methods of establishing these distributions both maintain some concern for developing arithmetical splintering with geometric processes. In the mid 1960s, Kiang was the first to consider the one-dimensional Voronoi-Dirichlet set ups, wherein the spots are positioned inidscriminately throughout a bar, like the Poisson method. Afterwards a degenerate vertical bisector, or middle, for every couple of spots would be found. A Voronoi-Dirichlet distribution in a row can be considered therefore a dual of the previously considered Lineau distribution,

or a degenerate Delauney distribution as well. Contrary to the Lineau distribution wherein indiscriminate spots in a row are regarded as cracks or breakage, for a Voronoi-Dirichlet distribution the indiscriminate spots will be considered as in a way the center in fragments having breaks developing in midpoints.

In order to find the fragment magnitude distribution of a one-dimensional Voronoi-Dirichlet distribution, the following process must be utilized. Firstly, the possibility for discovering a span *l* linking a couple of Poisson spots is expressed through a Lineau distribution:

$$f(l)dl = \frac{1}{\lambda} e^{-l/\lambda} \tag{60}$$

Then the possibility for locating a couple of spots with span l_1 that is contiguous to a couple of spots with length l_2 becomes the multiplication:

$$f(l_1)f(l_2)dl_1dl_2 = \frac{1}{\lambda^2} e^{-(l_1+l_2)/\lambda} dl_1dl_2 \tag{61}$$

Utilizing the transformation:

$$L = (l_1 + l_2)/2 \tag{62}$$

$$\xi = (l_1 - l_2)/2 \tag{63}$$

provides the distribution:

$$f(L) = \frac{1}{\lambda^2} \int_{-L}^{L} e^{-2L/\lambda} d\xi \tag{64}$$

in which *L* represents a span linking the centers between a couple of spots. Through integration it is possible to attain the Voronoi-Dirichlet distribution for fragments in a row:

$$f(L) = \frac{2}{\lambda} \left(\frac{2L}{\lambda}\right) e^{-2L/\lambda} \tag{65}$$

A comparison between the single dimension Voronoi distribution Equation 65 with a Lineau, or Poisson, distribution is shown in Figure 2.6 below.

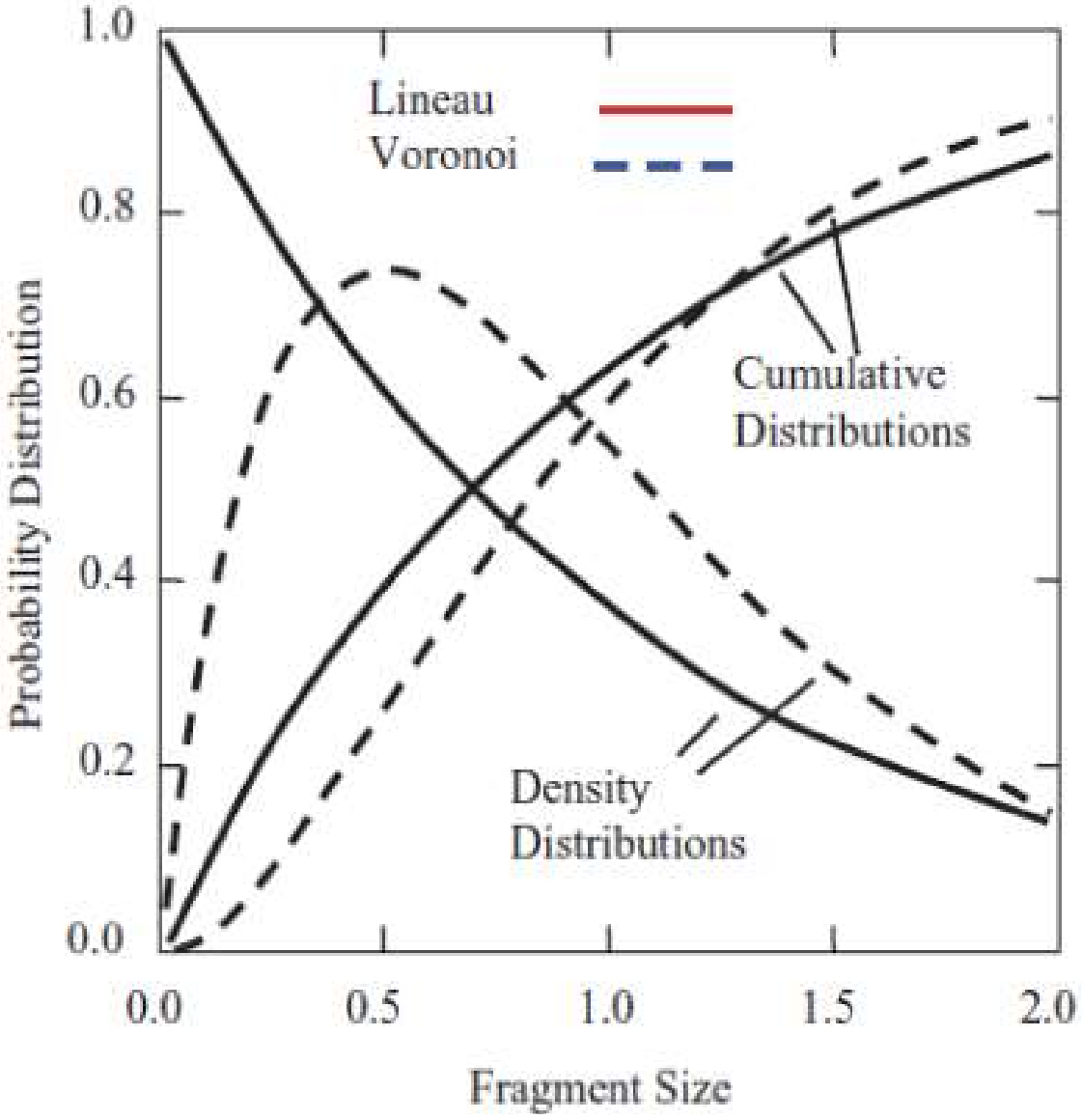

Figure 2.6: A comparison of the one-dimensional Voronoi distribution and the Lineau, or Poisson, fragment length distribution resulting from the random segmentation of the line according to the respective algorithms [31].

Mott made a last endeavor to validate with geometric techniques his projected $m^{1/2}$ distribution. Based upon some thin, stretched out and sliver-framed fragments that

were collected out of discharged munitions experiments Mott deduced the rupture observed with end-detonated metallic casings having a cylindrical evenness will actually arise from longitudinal oriented fractures containing sporadic fracture stemming as well as fracture juncture, which resulted with these experimental fragments. Then Mott went on to propose the statistical algorithm shown in Figure 2.2e that was evaluated previously utilizing a Lineau distribution with all streaks as well as streak sections. In order to indiscriminately allocate all perpendicular as well as parallel streak aspects in a plane Mott used a one-dimensional Voronoi-Dirichlet distribution described previously instead of the Lineau distribution utilized in his prior geometric pursuits. He could have made this selection for one of two reasons. He could have performed the analysis utilizing the Lineau distribution, as attempted previously, and discovered that a suitable solution could not be attained. On the other hand, ideas he developed in his later work may have also had an influence on his choice, particularly, his idea of physics with breakage relations prohibiting an adjacent nearness with parallel cracks thereby limiting a range with tinier fragments. It is observed that the Voronoi-Dirichlet distribution offers a better numerical limitation constricting an occurrence with adjacent parallel cracks with consequently an amount of tinier fragments.

Based on the process discussed beforehand, while utilizing a Voronoi-Dirichlet distribution with Equation 65 to verify the indiscriminate position of perpendicular streaks and streak sections, this subsequent magnitude distribution of fragment area will be attained:

$$f(a) = \frac{2}{a_0}\frac{1}{\sqrt{4a/a_0}}\int_0^{\infty}\left(\xi\sqrt{4a/a_0} - 1\right)(1 + 1/\xi^2)e^{-\xi\sqrt{4a/a_0}-1/\xi^2}d\xi \qquad (66)$$

This correlation relates with the distribution offered from Mott and the distinction is found with distribution figure $\lambda = \sqrt{a/a_0}$ utilized whenever $a_0 = py_0^2$. A consequent collective distribution results as follows:

$$F(a) = \sqrt{4a/a_0}\int_0^{\infty}(1 + 1/\xi^2)\, e^{-\xi\sqrt{4a/a_0}-1/\xi^2} d\xi \qquad (67)$$

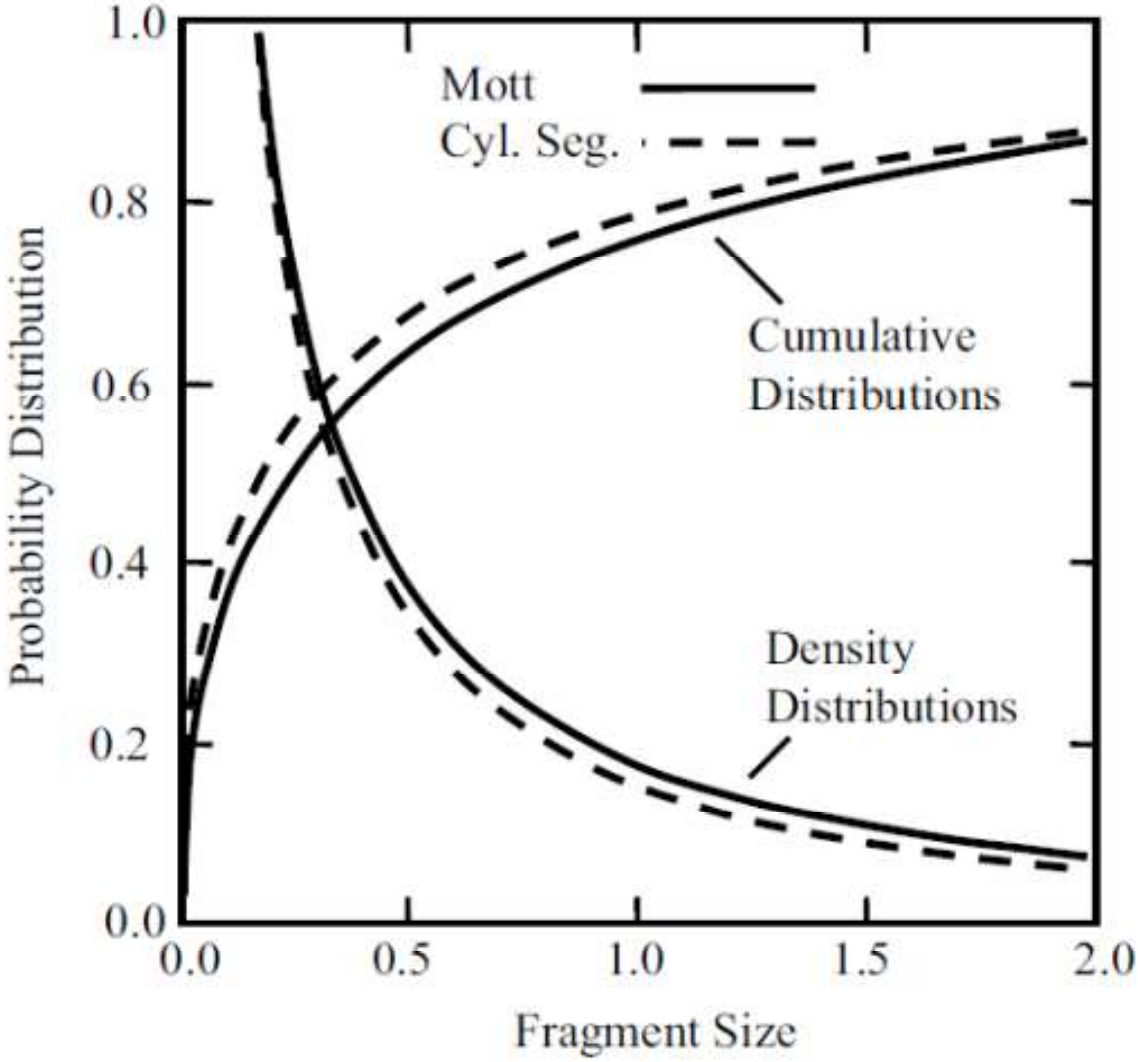

Figure 2.7: A comparison of the cumulative and density fragment size distributions from the Mott distribution and the geometric cylinder segmentation distribution [31].

This graph within Figure 2.7 shows a comparison between the Mott distribution and a circular division method projected from Mott utilizing a Voronoi technique with indiscriminately allocating all dividing streaks as well as streak sections. Figure 2.7 relates with Figure 2.4 wherein a comparison of a Mott distribution to an indiscriminate perpendicular as well as parallel streak process is shown. One last evaluation will be illustrated with the figure below that shows how density distributions coming out of either method proposed from Mott compare to a Mott distribution through the wide range variety in fragment magnitudes. One noteworthy observation about these two algorithms is that they have a tendency to bestride the Mott-Linfoot projected distribution, either one containing correspondingly greater or lesser variation.

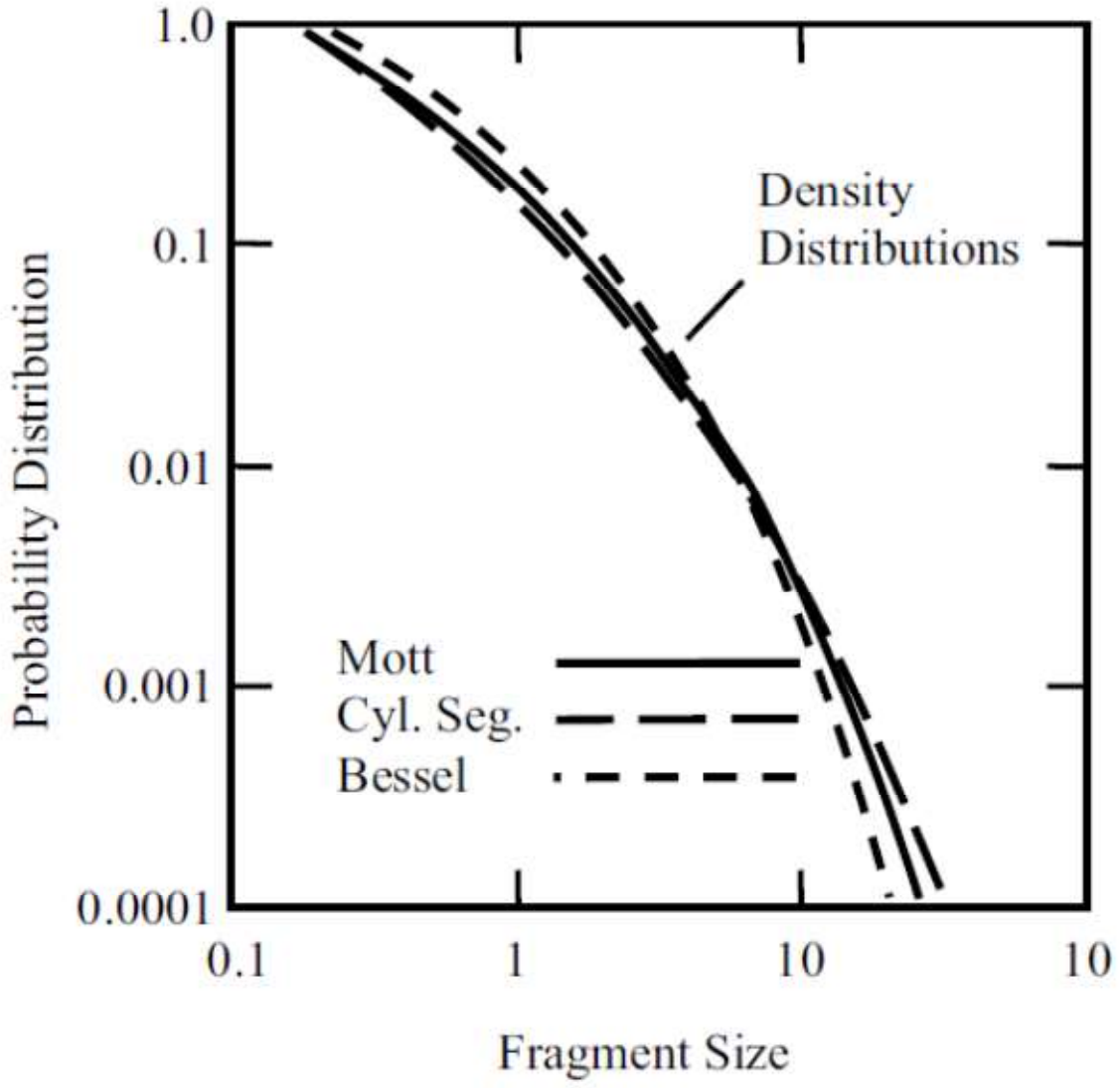

Figure 2.8: A comparison of the probability density fragment distributions from the Mott distribution, the geometric cylinder segmentation distribution, and the geometric random horizontal and vertical lines (Bessel) distribution. Approximately 95% of the fragment area (mass) is included in the range of the plotted distributions [31].

2.2 Mechanical and chemical properties

2.2.1 Young's modulus

Young's modulus represents elastic properties of materials. The linear portion of a stress-strain curve shows that a material is stretched or constrained as a tension or

compression progresses (see Fig. 2.9). This elastic property was experimentally demonstrated by Robert Hooke in 1678 [65]. The elastic stress-strain behavior can be easily presented in mathematical form called Young's modulus or the elastic modulus (E):

$$E = \frac{\sigma}{\varepsilon} \tag{68}$$

where E is the Young's modulus, σ is an applied stress (engineering stress), and ε is the normal strain. The material property can be altered by porosities, cracks, and inclusions in the materials.

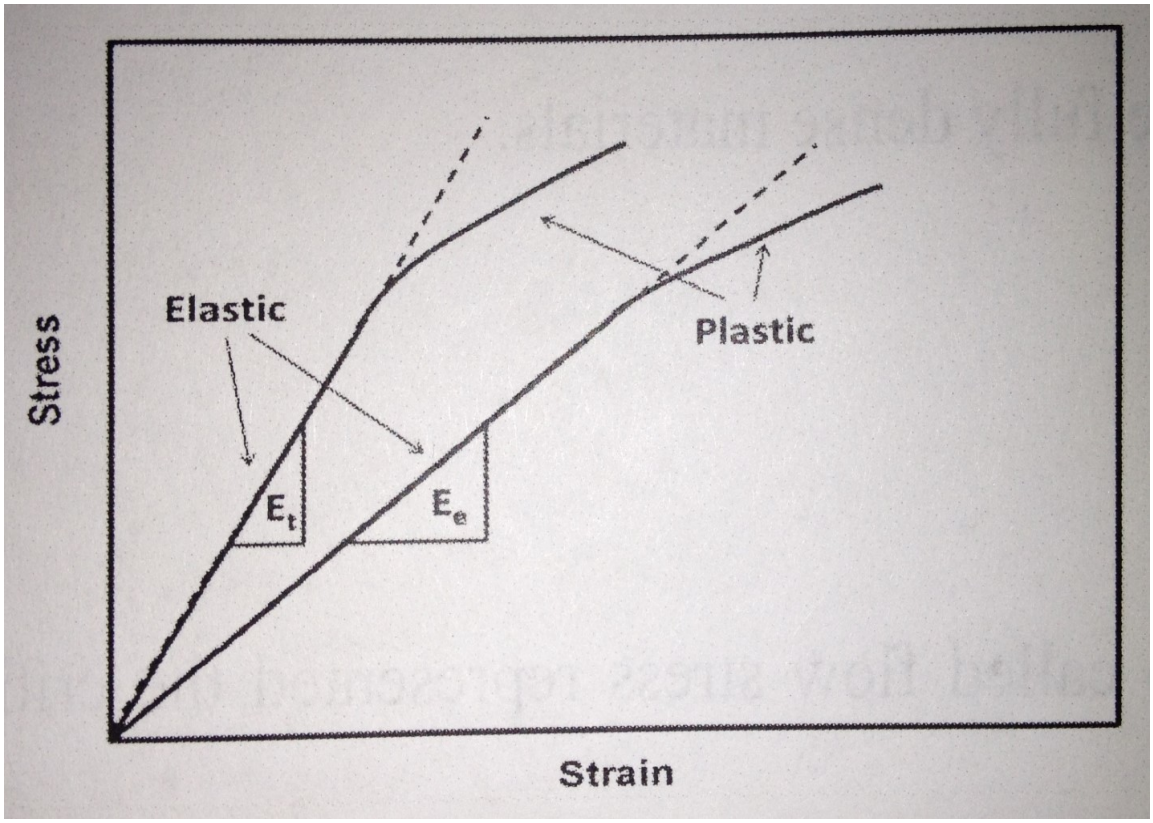

Figure 2.9: Stress vs. strain curves (for metals).

For instance, materials with a sufficient amount of porosities such as ceramics have a distinct elastic modulus from fully dense bulks. Wachtman [66] and MacKenzie [67] characterized this by the mathematical expression:

$$E = E_o(1 - f_1 p + f_2 p^2) \tag{69}$$

where f_1 and f_2 are equal to 1.9 and 0.9 for spherical voids, and p is the porosity. If the material is compacted with several constituents, the law of mixtures can be applied, which is presented as the equation:

$$E = E_A(1 - f_B) + E_B f_B \tag{70}$$

here E_A and E_B are the Young's modulus of mixtures, and f_B is the fraction of the component B. The pre-existing cracks also dominated the elastic behavior of materials. O'Connell and Budiansky proposed an estimation [68]:

$$\frac{E}{E_o} = 1 - \frac{16(10-3v)(1-v^2)}{45(2-v)} f_S \tag{71}$$

where f_s is defined as the volume fraction of cracks (the number of cracks per unit volume, N, multiplied by the cube of the mean crack radius, a^3, and v is Poisson's ratio of materials, which is a different value from the fully dense materials.

2.2.2 Yield stress

Yield stress is also called flow stress represents the critical stress, which allows the materials to start plastically deforming. This irreversible plastic deformation is due to the slide of glide planes, dislocation movement, and void accumulation. Based on different manufacturing processes, materials with similar compositions may have different yield stresses (see Fig. 2.10). AISI 1040 steels have different flow stresses due

to many factors such as crystal sizes, different phases, or dispersions. Based on different quenching and tempering processes, the phases and grain sizes of the steel are manipulated, hence the mechanical properties vary by the manufacturing processes of the steel. Parabolic work-hardening curves clearly show in the stress-strain plot following the elastic stress-strain curves in Figure 2.10. This work hardening behavior can be written as follow (Ludwik-Hollomon equation):

$$\sigma = \sigma_o + K\varepsilon^n \tag{72}$$

where σ_o is the yield stress, K is a constant, and the exponent n is the material constant.

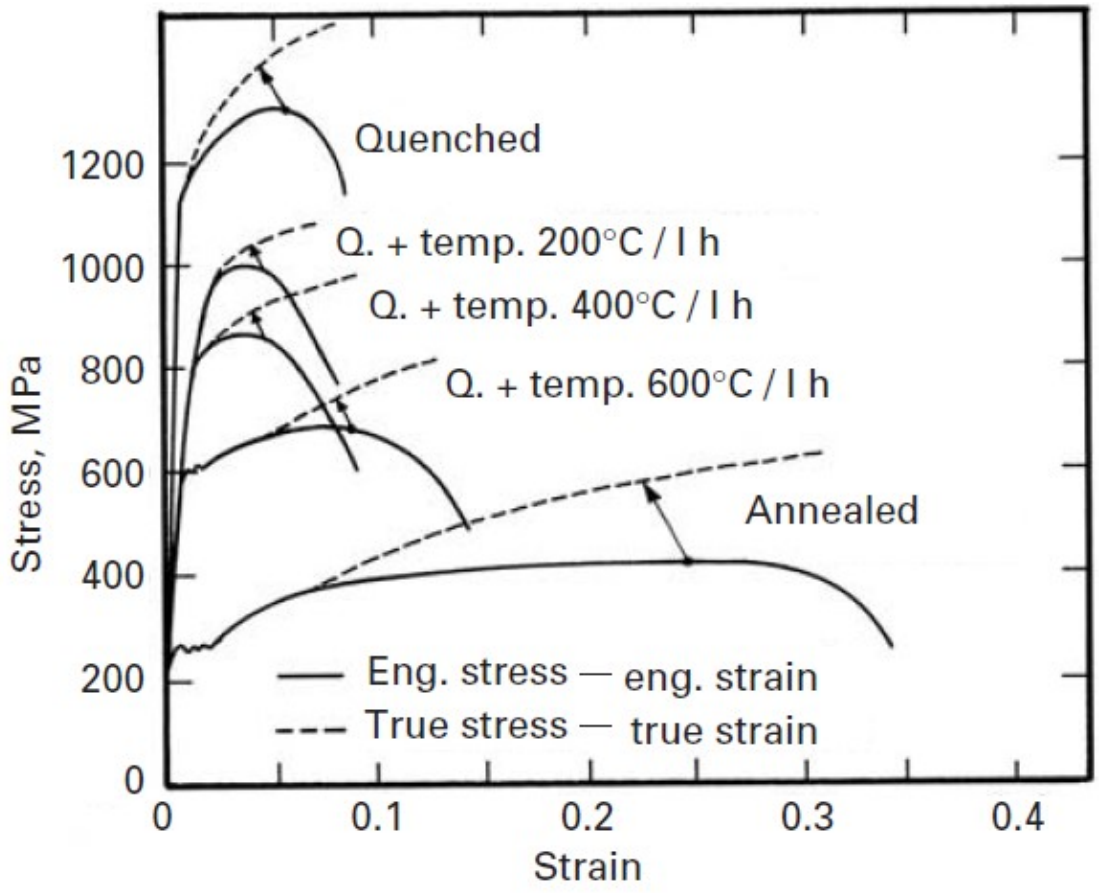

Figure 2.10: Stress-strain curves for AISI 1040 steel subjected to different heat treatments.

Other than the intrinsic factors of materials which were mentioned above, the test environments can also play an important role. Strain rates and temperatures are often considered factors in influencing plastic behaviors. The stress-strain constitutive equation incorporating strain rate and thermal activity effects is called the Johnson-Cook equation:

$$\sigma = (\sigma_o + K\varepsilon^n)\left(1 + C\ln\frac{\dot{\varepsilon}}{\dot{\varepsilon_o}}\right)\left[1 - \left(\frac{T-T_r}{T_m-T_r}\right)^m\right] \quad (73)$$

where the K, n, and m are material parameters, T_r and T_m are the reference temperature and melting temperature respectively, and $\dot{\varepsilon_o}$ is the reference strain rate. This equation was commonly used to predict large-scale deformations. Nevertheless the constitutive equations incorporating microstructural elements such as grain sizes, dislocation interactions and dynamics are also used to provide stress-strain behavior computationally. The Zerilli-Armstrong equation [69] is one of these constitutive equations. The basic idea behind this equation is to develop a computational method to represent the mechanical response of materials from low to high temperatures and from low strain rates (~10^{-5} s^{-1}) to extremely high strain rates (~10^9 s^{-1}).

2.2.3 Strain rate dependence

A high strain rate test applied on the material can present totally distinct stress-strain behavior compared to a low strain rate test. Strain rate sensitivities can vary broadly depending on materials [70]. Figure 2.11 shows nanocrystalline Ni tested under a range of strain rates from 3x10^{-4} to 3x10^{-1} s^{-1}. The yield stress increases as the strain rate increases [71]. A quantitatively analytical method for characterizing this strain rate dependence of different composites is the strain rate sensitivity parameter m, defined as:

$$\sigma = \sigma_o + K\varepsilon^n \tag{74}$$

where the τ is the yield stress, and the $\dot{\varepsilon}$ is the strain rate. It is commonly seen that materials with small grains have a higher strain rate sensitivity value due to grain boundary (GB) deformation mechanisms such as grain boundary migration, grain boundary sliding, or grain boundary dislocation nucleation [72]. The strain rate sensitivity can also be altered by external properties of materials such as dimensions (see Fig. 2.12), porosities, or inclusions.

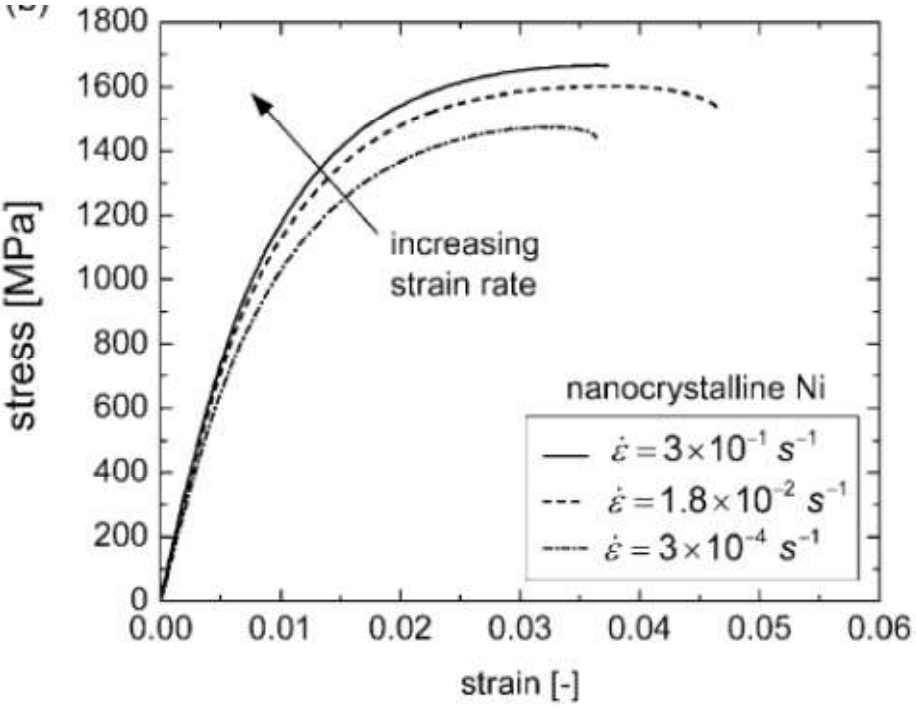

Figure 2.11: Nanocrystalline Ni tested utilizing different tensile strains: 3 x 10^{-4}, 3 x 10^{-2}, 3 x 10^{-1} s^{-1}[49].

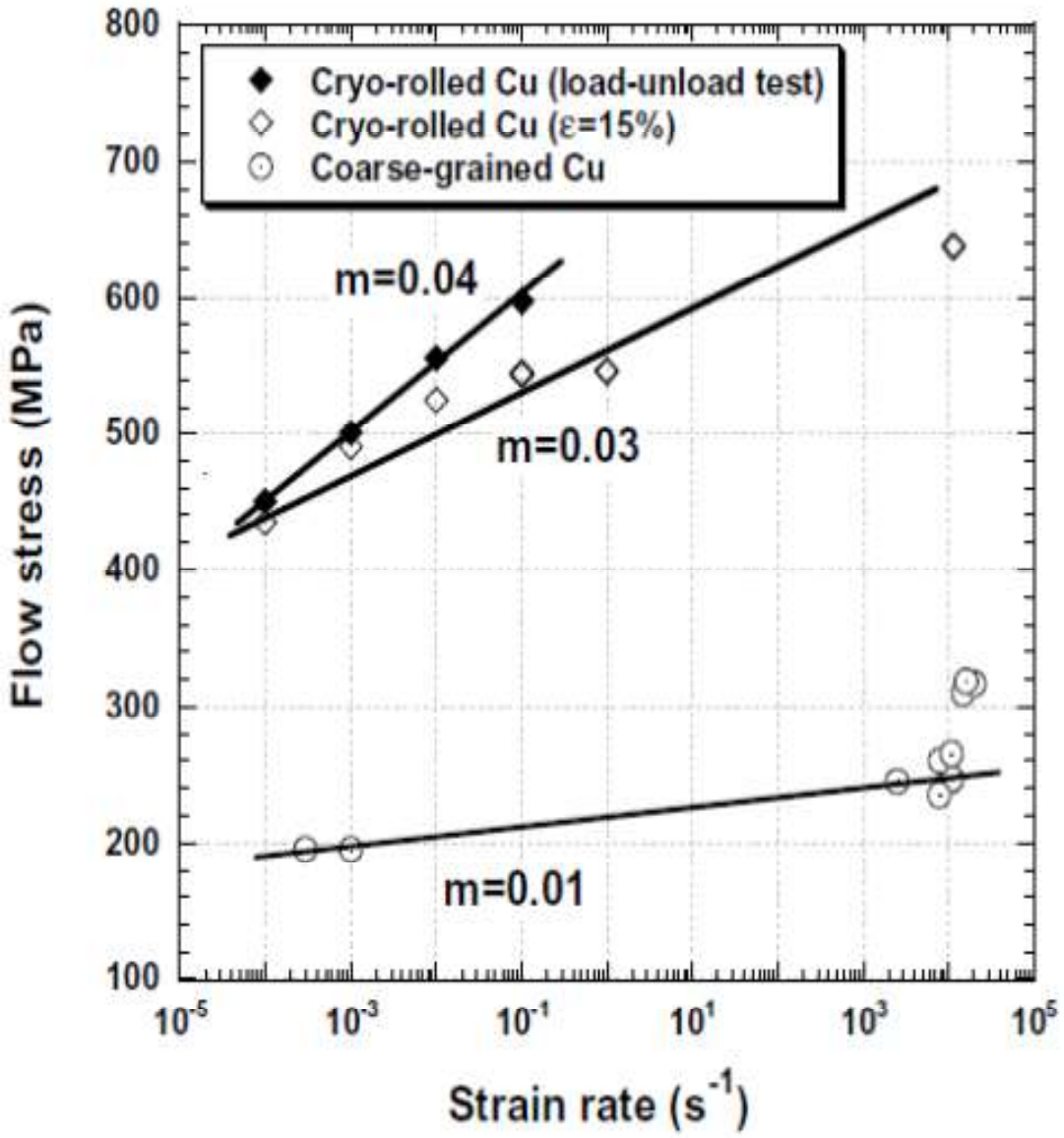

Figure 2.12: Nanocrystalline strain rate sensitivities from different thicknesses of Cu.

Here the *m* value is not always positively proportional to the increases of strain rates. Materials such as titanium alloys (Ti-6%, Al-4%, V), iron-based alloys, aluminum alloys, and some ceramics have super-plastic mechanical properties. Superplastic materials can be stretched extensively, and can reach extremely high strains without

failure. These materials become more stretchable under high strain rate tests [65] which give a negatively proportional value of m.

2.2.4 Strengthening mechanisms

In order to satisfy the specific requirements for each application, materials must have adequate mechanical strength and flexibility. There are numerous methods to strengthen materials. For instance, inclusion strengthening is known as the easiest way to obtain strong and ductile materials by mixing two or more elements with high strengths or good ductility. Aluminum based alloys are of inclusion hardening materials. These alloys usually include hard and high strength materials such as Ti, W, or Ni added and dispersed in a soft and ductile Al matrix. In this case, the hard and high strength materials support the alloy to sustain high stress, while the ductile Al matrix keeps the flexibility.

Multi-elemental compounds have mechanical properties integrated all of adding materials. There is a mathematical method to predict the mechanical properties of these alloys, which is called the law of mixtures [65] or the additive rule [73], shown as the following equation:

$$E = E_a \times f_a + E_b \times f_b + E_c \times f_c \ldots \quad (75)$$

where E represents the elastic modulus (or hardness, yield stress, etc.), f is the volumetric fraction of the material, a, b, and c are symbols corresponding to each element. However, the law of mixtures can only provide an uncertain evaluation which can be easily altered by extrinsic properties, for example porosity and inclusion morphology [74].

The intermetallic reaction is one of the strengthening mechanisms. Most of the intermetallic products have relatively high strength compared to the soft matrix [73]. Intermetallics perform as the hard and high strength inclusions, nevertheless these phases generated by an exothermic reaction help to eliminate the porosity and increase the bonding strength between different elements.

Other strengthening factors such as dispersions, phase changes (martensite), and grain sizes also play important roles in strengthening mechanisms of materials. However these factors are not the major subjects in our study, therefore we are not going to discuss those in this section.

CHAPTER 3: EXPERIMENTAL METHODS

3.1 Swaging (powder consolidated cylinders)

Swaging is a standard forging process where a rapidly rotating die uniformly reduces the diameter of a tube or rod by cold working, illustrated in Figure 3.1(a). Aluminum powders of approximate sizes 40, 100, and 400 μm were compacted into tubes of 304 stainless steel in an Instron 5582 and then swaged, this process is depicted in Figure 3.1(b). The swaging was conducted with a Fenn 5F swager connected to a rack-and-pinion mechanism (Fig. 3.1(c)). Tight fitting 12.7mm rods of Al 6061 were secured in the center of the tubes prior to swaging and then machined out later along with the stainless steel jackets to generate hollow cylinders with 30mm OD and 22mm ID that could be cut into rings with a 4 mm thickness, which are shown in Figure 3.1(d). In the case of the 100 μm powder, the center rod was also varied in size to 18.8 mm or removed to observe the effect of different degrees of compaction. As the compaction increases one expects better mechanical properties [75]. Additionally, nickel-aluminum powders of approximate sizes 355-500 μm were compacted into tubes of AISI 304 stainless steel in an Instron 5582 and then were swaged to a smaller diameter using a Fenn 5F swager. The center rod was also varied in size between 12.7 mm and 18.8 mm or removed to observe the effect of different degrees of compaction. As the compaction increases it would be expected to find more adhesion between the individual particles [22] caused by the greater degree of plastic deformation. The addition of the core creates an increase in the degree of plastic deformation for a certain fraction of densification because the particles are not only brought together but also there is significant interparticle shear and breaking of surface oxides.

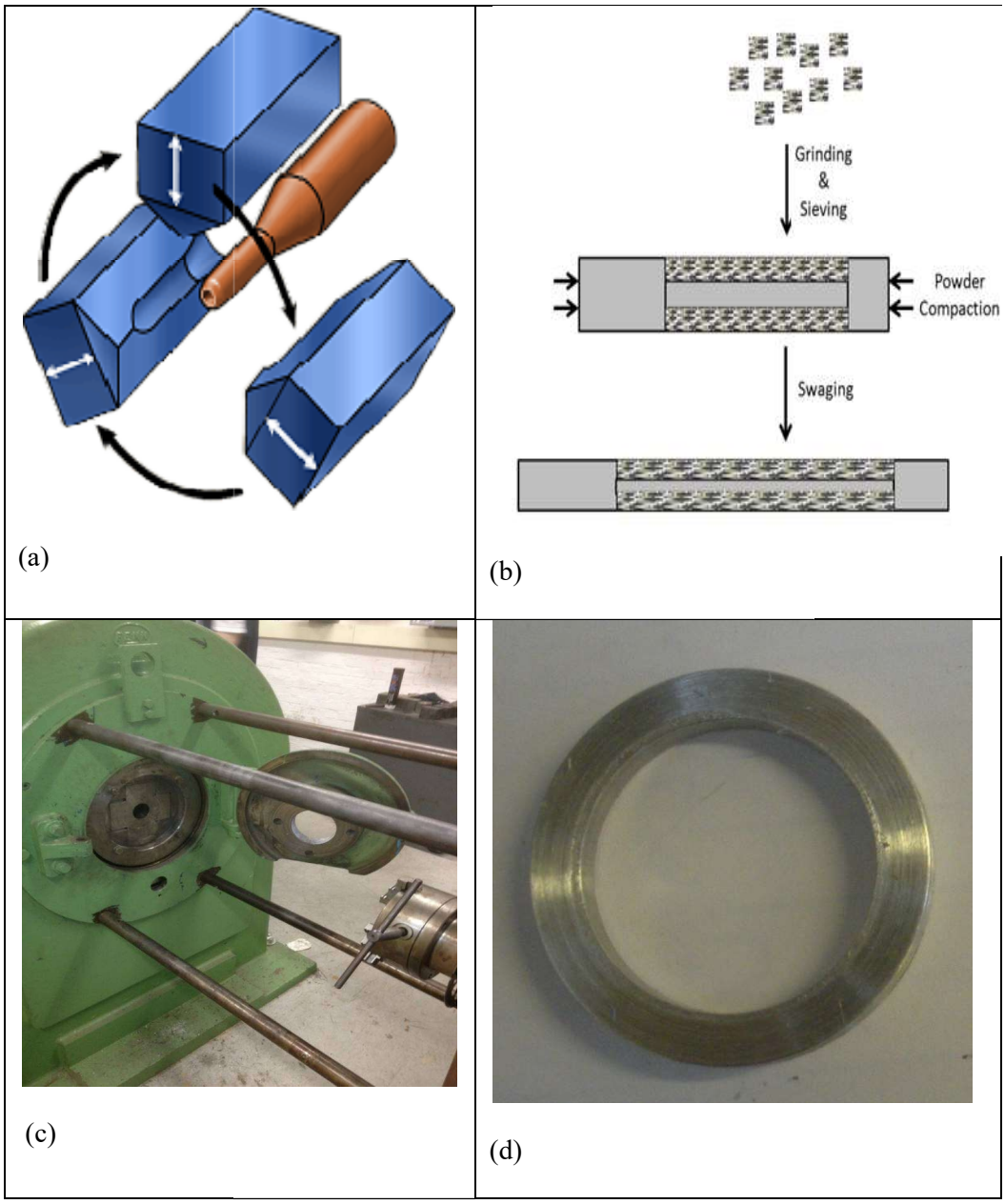

Figure 3.1: (a) Swaging method; (b) compaction and swaging procedure for powders; (c) swaging apparatus; and (d) machined disks.

3.2 Density and porosity analysis

In order to begin studying the effect of the different swaging processes on the aluminum and nickel-aluminum compacts, the percentage of densification was examined

along with the degree of porosity by utilizing ASTM standard C380. The procedure uses Archimedes' principle to analyze bulk density and apparent porosity through calculations involving dry weight, saturated weight, and suspended weight under vacuum in water. The test method is performed under the fundamental assumption that the open pores of the test specimens are completely permeated with liquid during the vacuum-pressure treatment.

The dry weight of the test specimens, *D*, is measured first by simply weighing the dry sample in grams to the nearest 0.1 g. Next the process of saturation is performed by soaking the test specimens in a beaker of water then placing them in a secure vacuum-pressure vessel and pumping the vessel down to an absolute pressure of approximately 6.4 kPa, where it is held for 30 minutes to allow the water to penetrate the pores of the specimens. Then the vacuum line is closed and the vessel is pressurized by means of a pressure pump to 30 psi or more for 60 minutes. Afterwards, the pressure is released and the saturated specimens are ready for weighing.

Next, the suspended weight, *S*, is determined by suspending the specimens in a loop or noose of AWG Gage-22 copper wire hung from one arm of the balance. Prior to this, the balance should be counter-balanced while the wire is in place and suspended in water. Once the suspended weight is determined, each specimen is blotted with a dampened soft linen or cotton cloth to remove all drops of water from the surface in order to determine the saturated weight, *W*, in grams to the nearest 0.1 g by weighing each specimen in air. The blotting process is conducted by rolling the specimen slightly on the dampened cloth, pressing just enough to remove all water droplets from the surface. Too much pressing could cause error by taking out water from the pores of the specimen.

The exterior volume of the test specimens, *V*, is determined in cubic centimeters by deducting the suspended weight from the saturated weight both in grams:

$$V, cm^3 = W - S \tag{76}$$

The exterior volume of the test specimens are equivalent to their bulk volume, consisting of all solid material, open pores, and impervious portions. The bulk density of the test specimens in grams over cubic centimeters is determined by dividing a specimen's dry weight by its bulk volume:

$$B, g/cm^3 = D/V \tag{77}$$

The percentage of densification is found by subtracting the bulk density from the theoretical density, dividing the result by the theoretical density, multiplying the quotient by 100 and deducting that result from 100 as follows:

$$\%\ Density = 100 - 100 * \left(\frac{\rho - B}{\rho}\right) \tag{78}$$

where ρ is the theoretical density.

The apparent porosity relates as a percentage the amount of the volume of open pores in the test specimen to its bulk volume. The apparent porosity is expressed by the following equation:

$$P\ , \% = \left[\frac{W - D}{V}\right] * 100 \tag{79}$$

Due to this expression involving the quotient of the volume of open pores, (*W-D)/*density of liquid, by the bulk volume, (*W-S*)/density of liquid, the correction factor being the density of liquid cancels out so that it does not appear in the equation at all. For each compact measurement a ring was broken into 2 smaller pieces and then another ring as well as the smaller pieces was measured using this procedure. Then the average of

these values was recorded in order to measure the entire surface porosity as well as internal porosity of all of the compacts.

3.3 Optical microscopy analysis

To continue studying the effect of the different swaging processes on the aluminum and nickel-aluminum compacts, their microstructures were analyzed with optical microscopy. Each of the compacts were sectioned into a small segment and embedded in epoxy. The surfaces were then grinded using silicon carbide (SiC) lapping discs in steps from 120 grit to 800 grit SiC disks. In order to obtain finer surface roughness and a smooth finish, polishing was also performed down to 0.5 μm using water based diamond suspensions with A-4 alpha polishing cloths. Once the surfaces of the samples were polished to a smooth finish in the epoxy, they were etched to further reveal the microstructures. The samples were etched to fully reveal their microstructure using Keller's etch. Keller's etch consists of 190 milliliters (ml) of distilled water, 5 ml of nitric acid, 3 ml of hydrochloric acid, and 2 ml of hydrofluoric acid. The etching process was performed by immersing the samples in the Keller's etch for 10 to 30 seconds. The samples were then examined with an Axio fluorescence optical microscope.

3.4 Quasi-static compression testing

A universal mechanical test machine was employed to characterize elastic and plastic behavior of materials. This basic mechanical test setup provided the essential information of micro- and macro-mechanical properties of materials. Elastic and plastic behaviors of materials related to a variety of factors such as manufacturing methods,

grain sizes, dislocations, etc. Hence the information from the quasi-static tests played a significant role in the practical point of view.

The universal test machine is shown in Figure 3.2. Cylindrical specimens that were 3 mm in diameter and 4 mm in height were cut from the swaged compacts using electrical discharge machining (EDM) in order to accurately section them close to these approximate dimensions. Then the cylindrical samples were stressed in the universal test machine through compression. In Figure 3.2, the upper part of the specimen is fixed on the crosshead of the machine. Two lateral screws control the movement of the upper load cell. Strains are measured by extensometers, strain gages, or from the indirect motion of the load cell. The machine is usually connected to a computer for recording the measurement and controlling the machine [76].

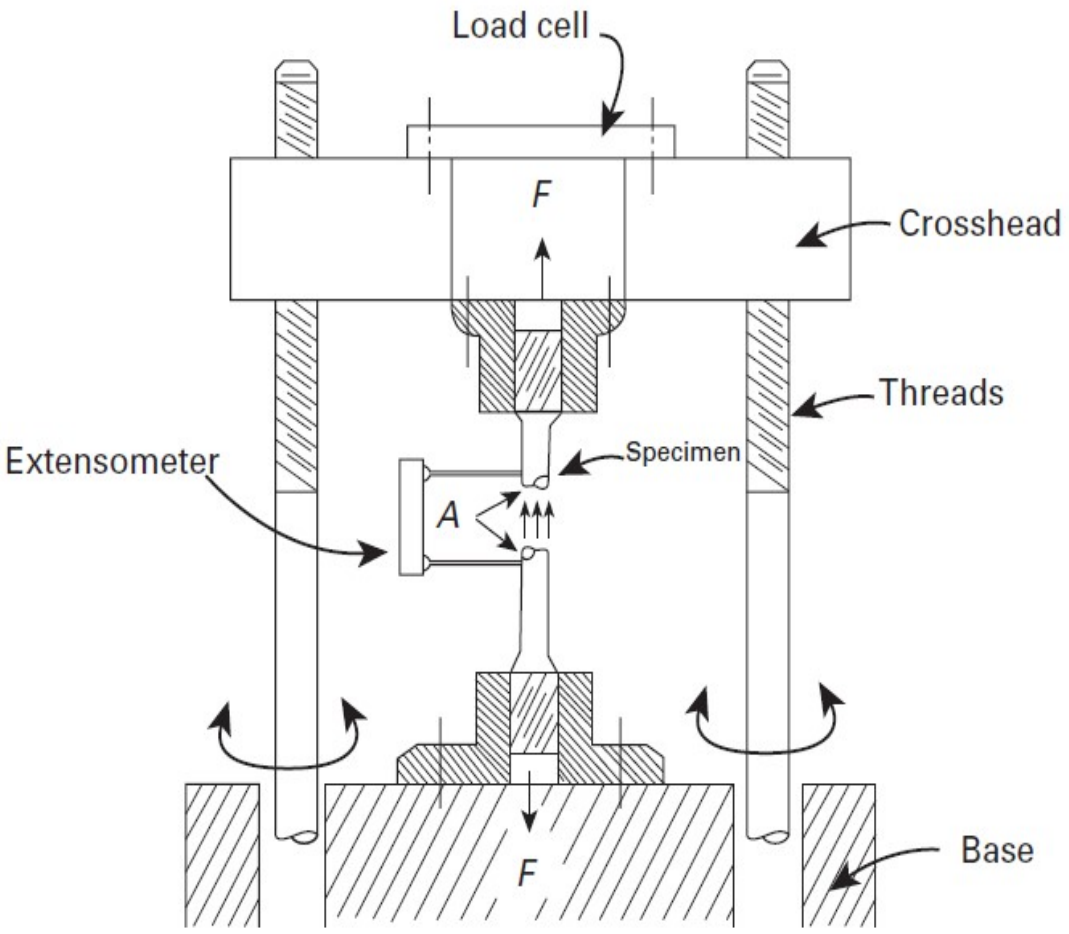

Figure 3.2: Sketch of a screw-driven tensile-strength testing machine [65].

The normal force applied on the sample can be qualitatively presented as engineering stress σ defined as resistance per unit area:

$$\sigma = \frac{F}{A_0} \tag{80}$$

where F is the normal force and A_o is the original area of cross-section. This force results in a corresponding deformation which can be presented as engineering strain ε:

$$\varepsilon = \frac{\Delta l}{l_0} \tag{81}$$

where Δl is the length change, and l_o is the original length. However these stress σ and strain ε cannot represent the real time deformation of materials while compressing or stretching due to a three dimensions deformation, hence the true stress σ_t and strain ε_t are employed in order to obtain more accurate values:

$$\sigma_t = \frac{F}{A} = \sigma \frac{A_0}{A} \tag{82}$$

$$\varepsilon_t = ln(1 + \varepsilon) \tag{83}$$

where A is the real time cross-sectional area. It should be noted that the elastic deformation in metals and ceramics rarely exceeds 0.005, therefore the differences between engineering and true stress and strain are neglected.

3.5 Split-Hopkinson pressure bar

The split Hopkinson pressure bar was employed to investigate dynamic behaviors of materials. An elastic shock-wave propagates through a cylindrical or rectangular sample and induces a corresponding dynamic process. The same cylindrical specimens used in the quasi-static testing that were EDM cut to 3 mm in diameter and 4 mm in height were tested by the split Hopkinson pressure bar. The five major parts are assembled to build a split Hopkinson pressure bar system is listed as follows [77]:

1. Two long, symmetrical bars
2. Bearing and alignment fixtures to allow the bars and striking projectile to move freely while retaining precise axial alignment
3. Compressed gas launcher/gun tube or alternate propulsion device for accelerating a projectile, termed the striker bar, to produce a controlled compressive pulse in the incident bar

4. Strain gages mounted on both bars to measure the stress-wave propagation
5. Associated instrumentation and data acquisition system to control, record, and analyze the stress-wave data in the bars.

Figure 3.3 presents the schematic plot of the split Hopkinson pressure bar. A striker bar is pushed by a compressed-air driven gas gun. The striker generates elastic shock-waves, which propagate through an incident bar and a sample, and then a transmitted bar. Two pairs of sensitive strain gages are attached on the transmitted and incident bar respectively. A momentum trap is placed and aligned after the rear end of the transmitted bar in order to stop the movement. All parts are fixed by a set of aligned fixtures. The pulse shape of transported shock waves is presented at the lower part of Figure 3.3. The shock wave ε_I propagates from the incident bar, and then reaches the cylindrical sample. Here a reflected wave ε_R forms due to the shock impedances corresponded to two different materials of the incident bar and the sample. This reflected shock wave can be measured by the strain gages attached on the incident bar and used for investigating the dynamic responses of the tested samples. After the shock wave ε_T propagates through the transmitted bar, the rest of the shock energy is trapped by a momentum trap usually made of Pb or other soft materials.

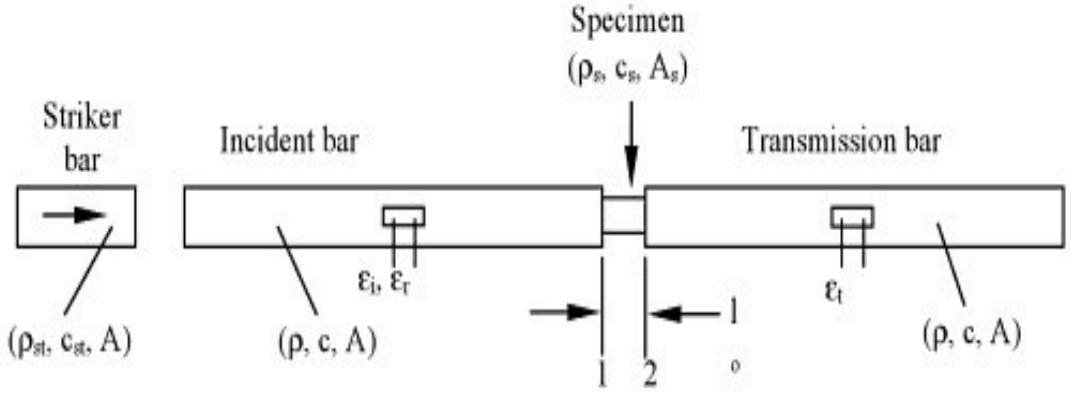

Figure 3.3: Diagram of Split-Hopkinson pressure bar [44].

The dynamic strain rate of the split Hopkinson pressure bar can reach several thousand per second [78]. The strain rate usually is not constant due to work hardening mechanisms of materials (see Figure 3.4) [79]. Figure 3.4 shows the NiTi superelastic alloy has undertaken a non-uniform stress while the shock wave propagates through the sample due to the strain hardening effect (see the reflected wave of Figure 3.4). This strain hardening phenomenon causes the strain rate vs. strain curves to decrease as well (Figure 3.5). Therefore it becomes a critical problem for researchers who use the split Hopkinson pressure bar to study the dynamic behaviors of materials. In order to obtain a constant strain rate during shock compression, a shaped incident shock wave is necessary.

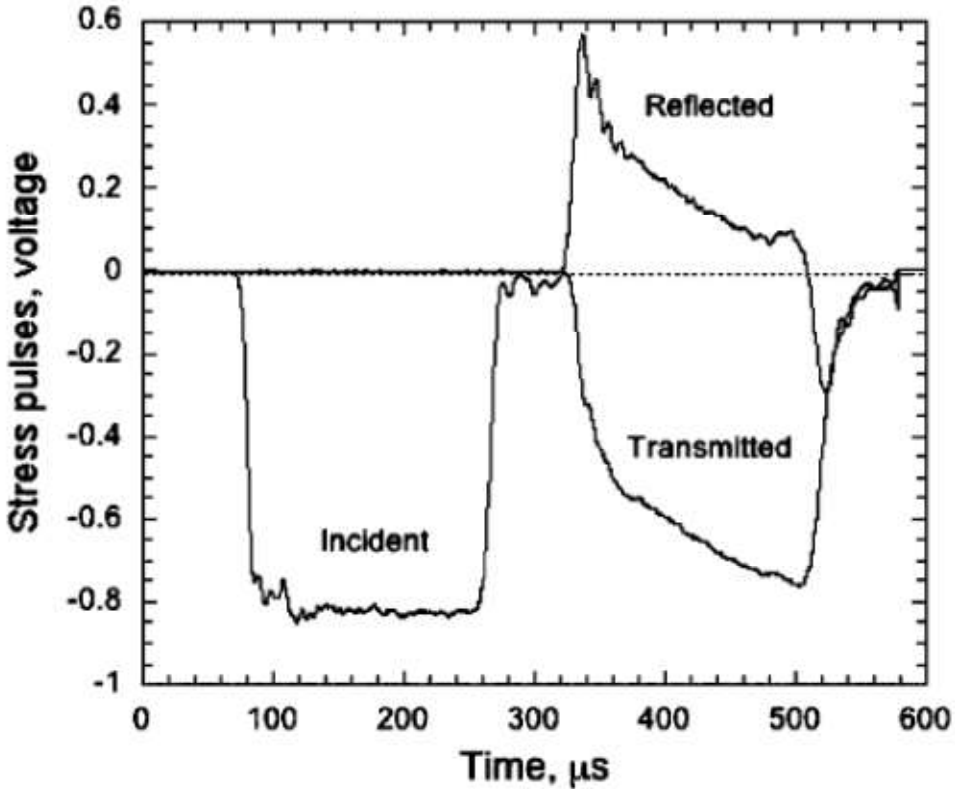

Figure 3.4: Stress vs. time plot of 50-50 NiTi super-elastic alloy at room temperature [54].

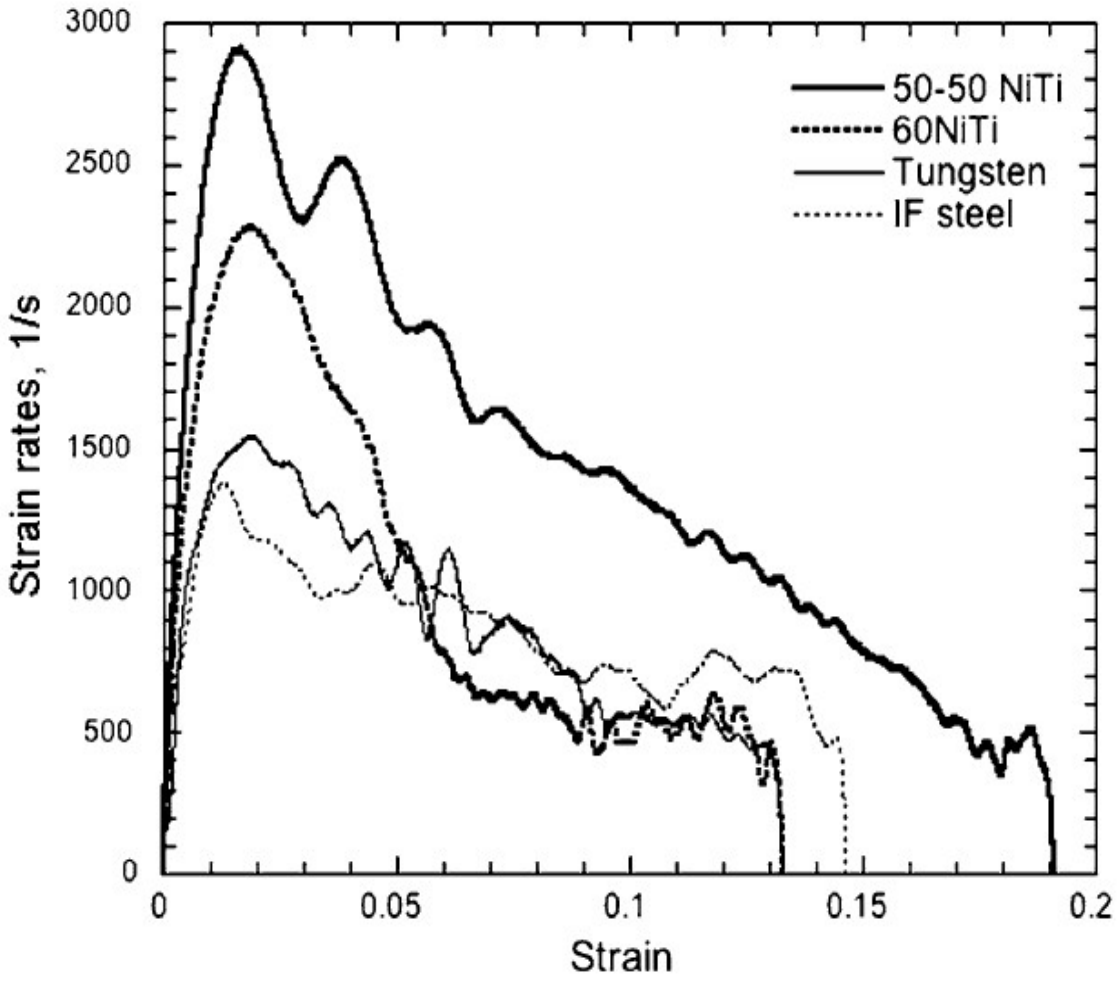

Figure 3.5: Strain rate vs. strain curves of metals show the strain hardening induced inhomogeneous strain rate.

Therefore a variety of pulse-shaping methods are proposed [79-89] in order to achieve a constant strain rate and dynamic stress equilibrium in samples to obtain reliable mechanical properties of the materials. By applying a pulse-shaped incident wave, the constant strain rate can be obtained. For example, Figure 3.6 presents incident and reflected waves after applied pulse shapers placed at the front end of the incident bar (transmitted pulse shaper) [79]. The pulse shaper alters the incident shock wave and

increases the rise time. These results in a flat and smooth reflected wave, demonstrating a constant strain rate is obtained.

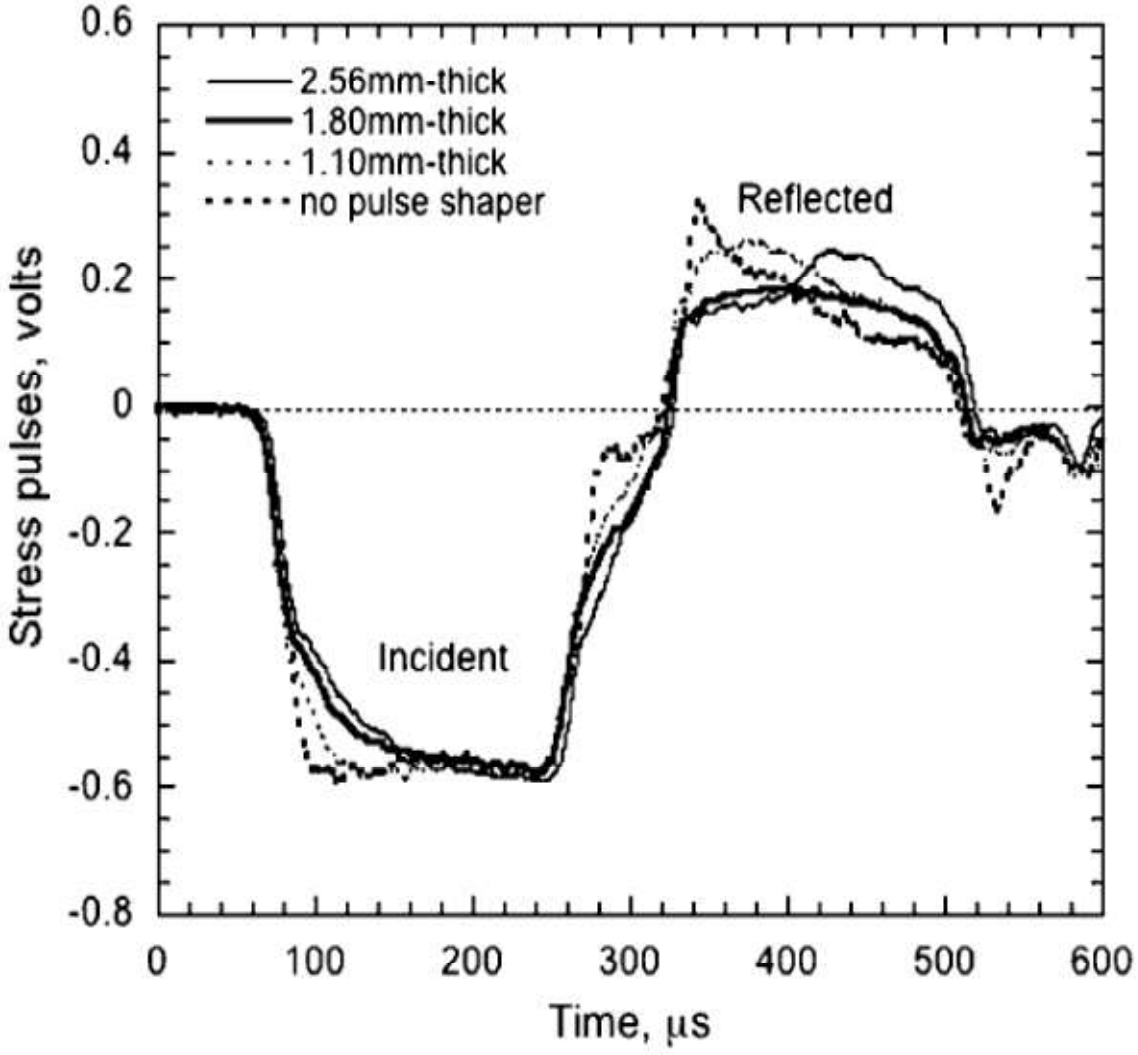

Figure 3.6: Incident and reflected waves with different thicknesses of pulse shapers [54].

The measured strains ε_I, ε_T, ε_R corresponding to incident, transmitted, and reflected waves can be written in an equation:

$$\varepsilon_T = \varepsilon_I - \varepsilon_R \tag{84}$$

due to the energy conservation. The dynamic stress $\sigma(t)$, strain $\varepsilon(t)$, and strain rate $\dot{\varepsilon}(t)$, are calculated based on one-dimensional stress wave theory [86]:

$$\sigma(t) = E\frac{A_o}{A}\varepsilon_T(t) \tag{85}$$

$$\varepsilon_T(t) = \frac{2C_o}{L_o}\int \varepsilon_R(t)dt \tag{86}$$

$$\dot{\varepsilon}(t) = \frac{2C_o}{L_o}\varepsilon_R(t) \tag{87}$$

where E is the Young's modulus of the pressure bars; A is the cross-sectional area of the bars; A_o and L_o are the initial cross-sectional area and length of the sample, respectively; C_o is the bulk sound speed of the bars. These equations provide the basic information obtained from the split Hopkinson pressure bar tests.

3.6 Fracture toughness determination

The standard test method for linear-elastic plane-strain fracture toughness (K_{Ic}) of metallic materials is called ASTM E399. This test method allows for the determination of fracture toughness of metallic materials under predominantly linear-elastic, plane-strain conditions using fatigue precracked specimens having a thickness of 1.6 mm (0.063 in.) or greater subjected to slowly, or in special (elective) cases rapidly, increasing crack-displacement force. The stress intensity factor (K_{Ic}) is measured using the operational procedure specified in Test Method E399, that provides for the measurement of crack-extension resistance at the onset (2% or less) of crack extension and provides operational definitions of crack-tip sharpness, onset of crack extension, and crack-tip plane strain.

Force is applied either in tension or three-point bending. Force versus crack-mouth opening displacement (CMOD) is recorded either autographically or digitally. The

force at a 5% secant offset from the initial slope (corresponding to about 2.0 % apparent crack extension) is established by a certain deviation from the linear portion of the record. The value of the stress intensity factor is calculated from this force using equations that have been established by elastic stress analysis of the specimen configurations related to this test method.

The validity of the stress intensity factor value determined by this test method depends upon the establishment of a sharp-crack condition at the tip of the fatigue crack in a specimen having an appropriate size to ensure predominantly linear-elastic, plane-strain conditions. To establish the suitable crack-tip condition, the stress intensity factor level at which specimen fatigue precracking is conducted is limited to a relatively low value. The specimen size required for test validity increases along with the square of the material's toughness-to-yield strength ratio. Thus there is a certain range of proportional specimens.

The test method serves several very important purposes. In research and development, this method helps to establish in quantitative terms relatable to service performance, the effects of metallurgical variables such as composition or heat treatment, or of fabricating operations such as welding or forming, on the fracture toughness of new or existing materials. In service evaluation, it is used to establish the suitability of a material for a certain application for which the stress conditions are prescribed and for which maximum flaw sizes can be established with certainty. Lastly it can be used for specifications of acceptance and manufacturing quality control, but only when there is a sound basis for specifying minimum stress intensity factor values, and then only if the

dimensions of the product are sufficient to provide specimens of the size required for valid stress intensity factor determination.

All specimens should be tested in their final heat-treated, mechanically-worked, and environmentally-conditioned state. The specimens should normally be machined in the final state. Nevertheless, for material that cannot be machined in the final state, the final treatment could be carried out after machining provided that the required dimensions and tolerances on specimen size, shape, and overall finish are still intact. For conventional quasi-static tests, the specimen should be loaded so that the increasing rate of stress-intensity factor is between 0.55 and 2.75 MPa√m/s during the initial elastic displacement. The test should be performed until the specimen can sustain no further increase in applied force. The maximum force must be noted and recorded. Three fatigue crack starter notch configurations are illustrated in Figure 3.7. In order to enable fatigue precracking at low stress intensity levels, the standard suggests that the root radius for a straight-through slot terminating in a V-notch is 0.08 mm (0.003 in) or less. While for the chevron form of the notch, it suggests that the root radius is 0.25 mm (0.010 in) or less. Lastly, for the slot ending in a drilled hole, it is essential to provide a sharp stress raiser at the end of the hole with care taken to make sure the stress raiser is located so that it meets the crack plane orientation requirements.

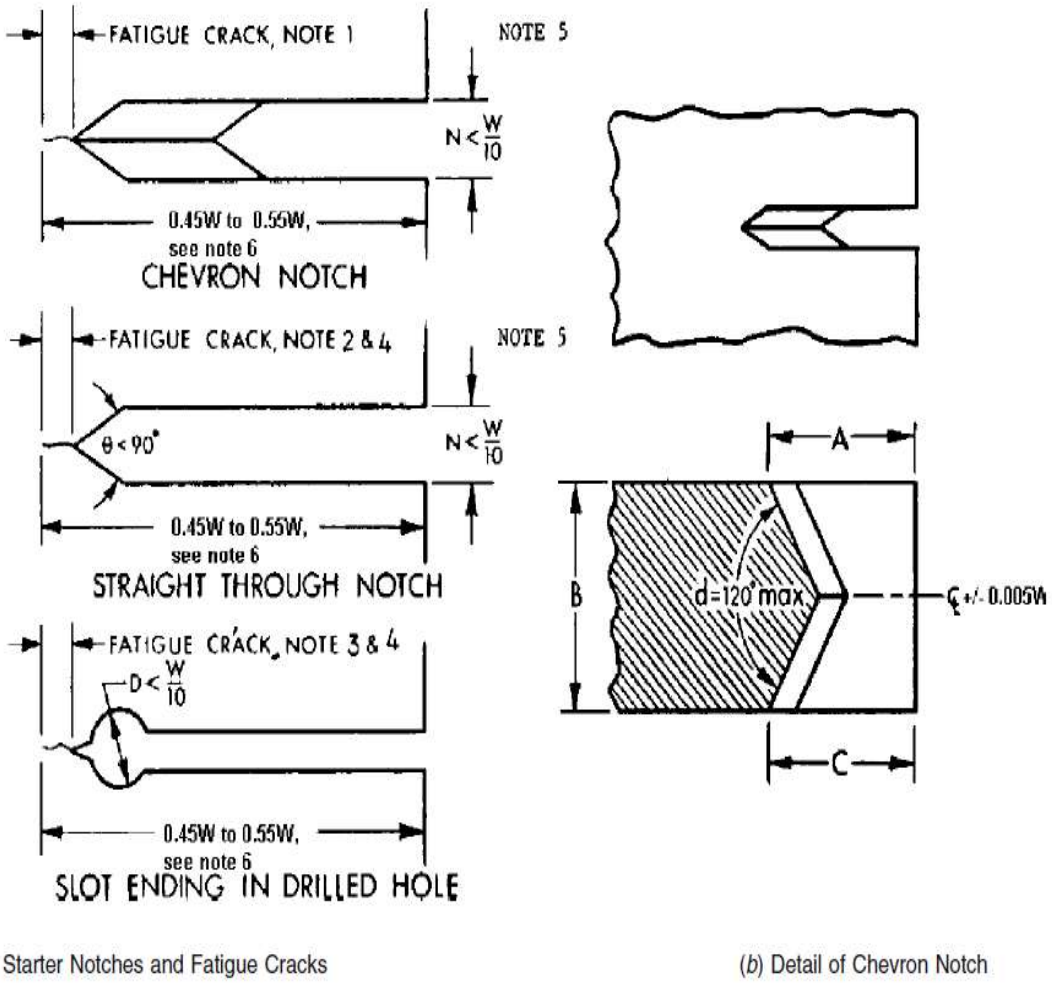

Figure 3.7: Crack starter notch and fatigue crack configurations. [90]

The most crucial measurements for the calculation of the fracture toughness are specimen thickness, *B*, crack size, *a*, and width, *W*. The specimen thickness should be measured before testing to the nearest 0.03 mm or to 0.01%, whichever is larger. The specimen width is also measured to the nearest 0.03 mm or 0.01%, depending on which is larger, at not less than three positions from the notch location then the average value will be recorded. The specimen crack size should be measured after fracture to the nearest 0.5% in the mid-thickness and the two quarter-thickness points. The average of those

three measurements is then taken as the crack size. The difference between any two of the three crack size measurements shouldn't be greater than ten percent of the average. The plane of the fatigue precrack in the central flat fracture area and the resulting two percent crack extension should be parallel to the plane of the starter notch within ten degrees.

The calculation of the fracture toughness begins with the calculation of the conditional result, K_Q, which involves the construction of the test record. Based on the test record, the conditional force P_Q is determined by drawing the secant line OP_5, as seen in Figure 3.8. The secant line is drawn through the origin (point *O*) of the test record with slope $(P/V)_5$ equal to $0.95(P/V)_o$, where $(P/V)_o$ is the slope of the tangent *OA* to the first linear portion of the record. However, in reality the origin (point *O*) is not automatically at the intersection of the displacement- and force-axes. The point *O* actually is found on the best fit line through the first linear portion of the record and at the intersection of the best fit line with the displacement-axis. So when calculating the secant line, the rotation point of the slope adjustment should be at the intersection of the line *OA* and the displacement-axis. Therefore the conditional force P_Q is defined as follows: if the force at every point on the record that precedes P_5 is less than P_5, then P_5 is P_Q; but if there is a maximum force preceding P_5 that is greater, then that maximum force is P_Q.

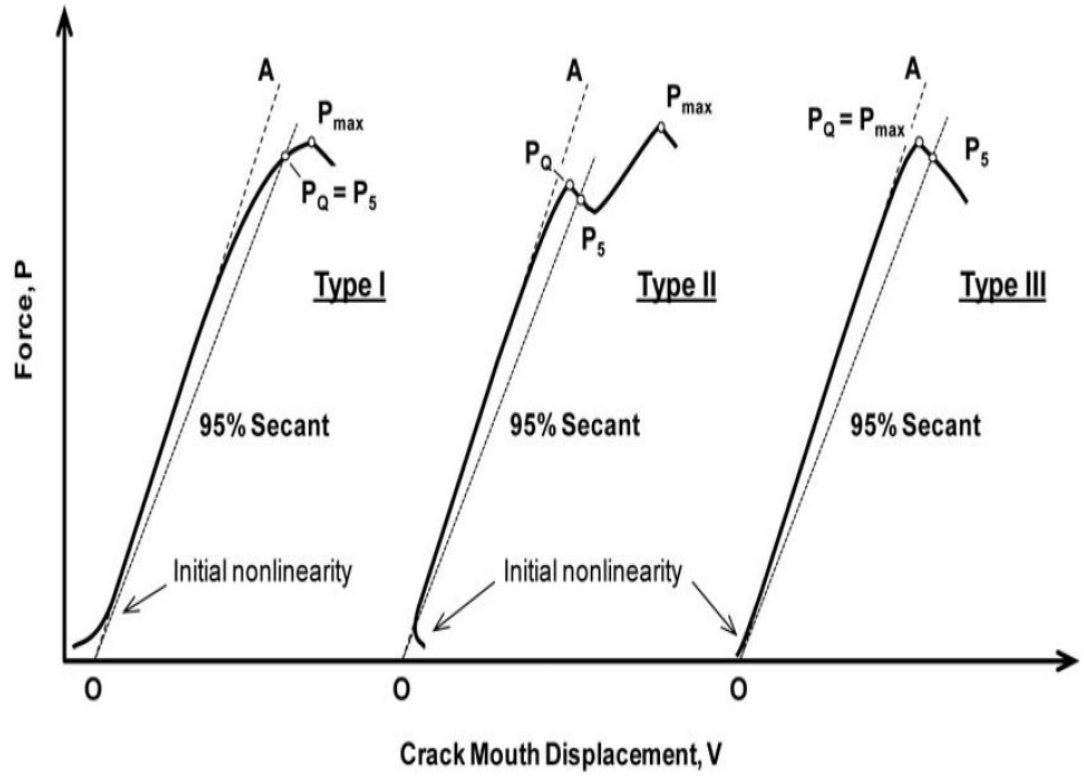

Figure 3.8: Principal types of Force-Displacement (CMOD) records. [90]

In order to predict fragment sizes using the modified Mott equation developed in this study, fracture toughness values must be determined for the various conditions of swaged Al and Ni-Al powder compacts. Experiments were conducted to obtain the fracture toughness values using ASTM E399 with some slight variations. Arc-shaped tension specimens were constructed from the swaged rings by sectioning them in half and cutting a starter notch in the center of the half-rings. However, instead of machining loading holes that could affect the behavior of the swaged materials, loading fixtures were constructed to allow for tensile testing without the necessity of holes in the

specimens. The modification of the supports from the ones recommended in ASTM E399 is not thought to alter the effectiveness of the testing procedure significantly.

During the tensile tests a high speed camera was used to measure the displacement of the crack mouth instead of displacement gages. The crack mouth opening displacement (CMOD) was measured frame by frame and compared to the force-time record to obtain a force-CMOD record. The conditional force is used to calculate the fracture toughness value by using the procedure detailed in ASTM E 399 and the following equation:

$$K_Q = \frac{P_Q}{B\sqrt{W}}\left(3\frac{X}{W} + 1.9 + 1.1\frac{a}{W}\right)\left[1 + 0.25\left(1 - \frac{a}{W}\right)^2\left(1 - \frac{r_1}{r_2}\right)\right] \cdot f\left(\frac{a}{W}\right) \qquad (88)$$

where:

$$f\left(\frac{a}{W}\right) = \frac{\sqrt{\frac{a}{W}}}{\left(1-\frac{a}{W}\right)^{3/2}}\left[3.74 - 6.30\frac{a}{W} + 6.32\left(\frac{a}{W}\right)^2 - 2.43\left(\frac{a}{W}\right)^3\right]$$

B is the specimen thickness, X is the loading offset, W is the width (depth) of the specimen, a is the crack size and r_1/r_2 is the ratio of inner-to-outer radii [27]. The measured fracture toughness values of the compacts are shown later and compared with the predicted fragment sizes calculated from these values.

3.7 Micro-hardness measurement

The Vickers hardness test was used to measure the hardness values of materials employed in this study. There are several types of hardness evaluating measurements, such as the Knoop test [91, 92] and the Rockwell test [93-98], commonly used because of their practical aspect. The Vickers hardness test is developed by Smith and Sandland [99]

from the United Kingdom. It has a square-based pyramidal-shaped indenter made from diamond. Figure 3.9 shows the indenter of the Vickers test which leaves an indented mark on the sample with the diagonal *D*. It should be noted that in the test, a known load is applied smoothly and has to hold in contact for about 15 seconds. After the load is removed, both diagonals are measured and the average is used to calculate the hardness value (HV) by using the equation:

$$HV = \frac{1854.4P}{d^2} \tag{89}$$

where *d* is the mean diagonal in μm, *P* is the applied load in gf.

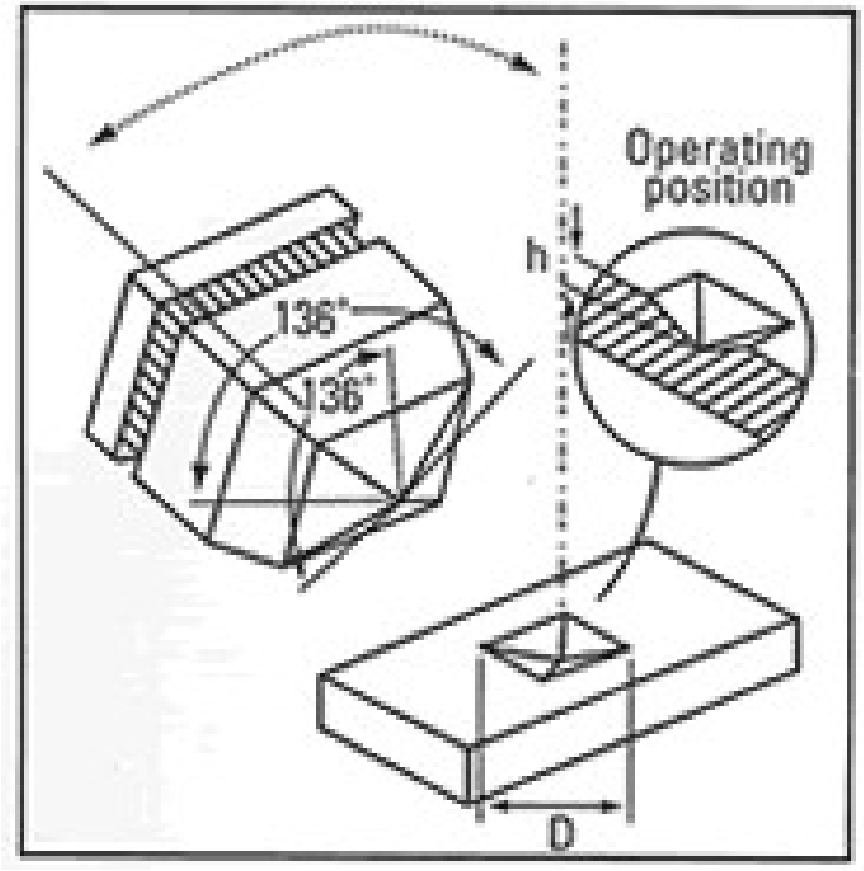

Figure 3.9: Schematic of the square-based diamond pyramidal indenter used for the Vickers hardness test and an example of the indentation that it produces.

The hardness values attained by microindentation hardness testing methods are related to various properties of a material such as the elastic modulus, compressive yield strength, or anisotropy. These types of material properties can alter the state of stress generated through an indenter. Thus, hardness values are not deemed central properties of a material, instead they specify the response of a particular material to stress states generated through a penetration experiment. There are benefits and shortcomings when using a Knoop indenter in comparison to a Vickers indenter when performing microindentation. Due to its more blunt profile, the Knoop indenter typically creates fewer cracks in the indentation of materials that are brittle (the depth of penetration is 0.635 times the depth of penetration for a Vickers indenter, with the assumptions of equivalent test force and hardness value). The impressions generated are lengthy and slim, which gives the Knoop indenter the ability to be utilized for hardness testing of small layers or of thin microstructural constituents. However, the reduced symmetry of a Knoop impression in contrast to impressions by a Vickers indenter, makes the Knoop indenter substantially more sensitive to crystallographic anisotropy in comparison to the Vickers indenter. For this reason the Vickers hardness test was used for this study.

The precision and consistency of the values attained when conducting microindentation hardness tests rely upon on three different facets: the microindentation machine, the person performing the tests, and also the characteristics of the material being tested. The microindentation hardness tester needs to be properly calibrated considering the applied force as well as the accuracy of optical measurement. The machine also needs to be isolated so that it does not experience any vibrations throughout testing. The fracture surfaces of the compacts were embedded in epoxy and grinded using

silicon carbide (SiC) lapping discs in steps from 120 grit to 800 grit. To obtain finer surface roughness and smooth finish, polishing was also performed down to 0.5 micron using water based diamond suspensions on A-4 alpha polishing cloths. The polished samples were tested for Vickers micro-hardness. Hardness testing was performed using a diamond indenter on microindentation tester (LM-810, Leco corporation, MI, USA). Loads of 500 and 1000gf were used with dwell time of 15 seconds to obtain coherent diamond shaped indents. Indent diagonals were measured using 50X magnification lens and a minimum of 6 readings were obtained over the sample length to provide average hardness values (HV number).

3.8 Expanding ring technique

The expanding ring technique was utilized to determine the fragmentation behavior using the experimental setup shown in Figure 3.10. The technique was introduced by Johnson et al [25]. This experimental setup provides high speed photography of the ring expansion, time resolved velocimetry of the radial expansion of the ring and soft capture of the ring fragments to allow for post fracture analysis. [100-102] The ring is loaded through the use of a column of explosives contained within a "transmitter" tube. A steel cylinder coated with approximately 20 mm of paraffin wax is placed around the specimen so that the fragments would slow to a stop before impinging on the steel. The explosives are detonated creating a shock wave that travels outward and enters the ring, propelling it in a trajectory with an expanding radius. High speed photography is conducted parallel to the cylinder axis through the setup shown if Figure 3.10. The radial expansion velocity of the ring is measured by a Photon Doppler

Velocimetry (PDV) system with a probe being a bare fiber placed approximately 3-5 mm from the ring.

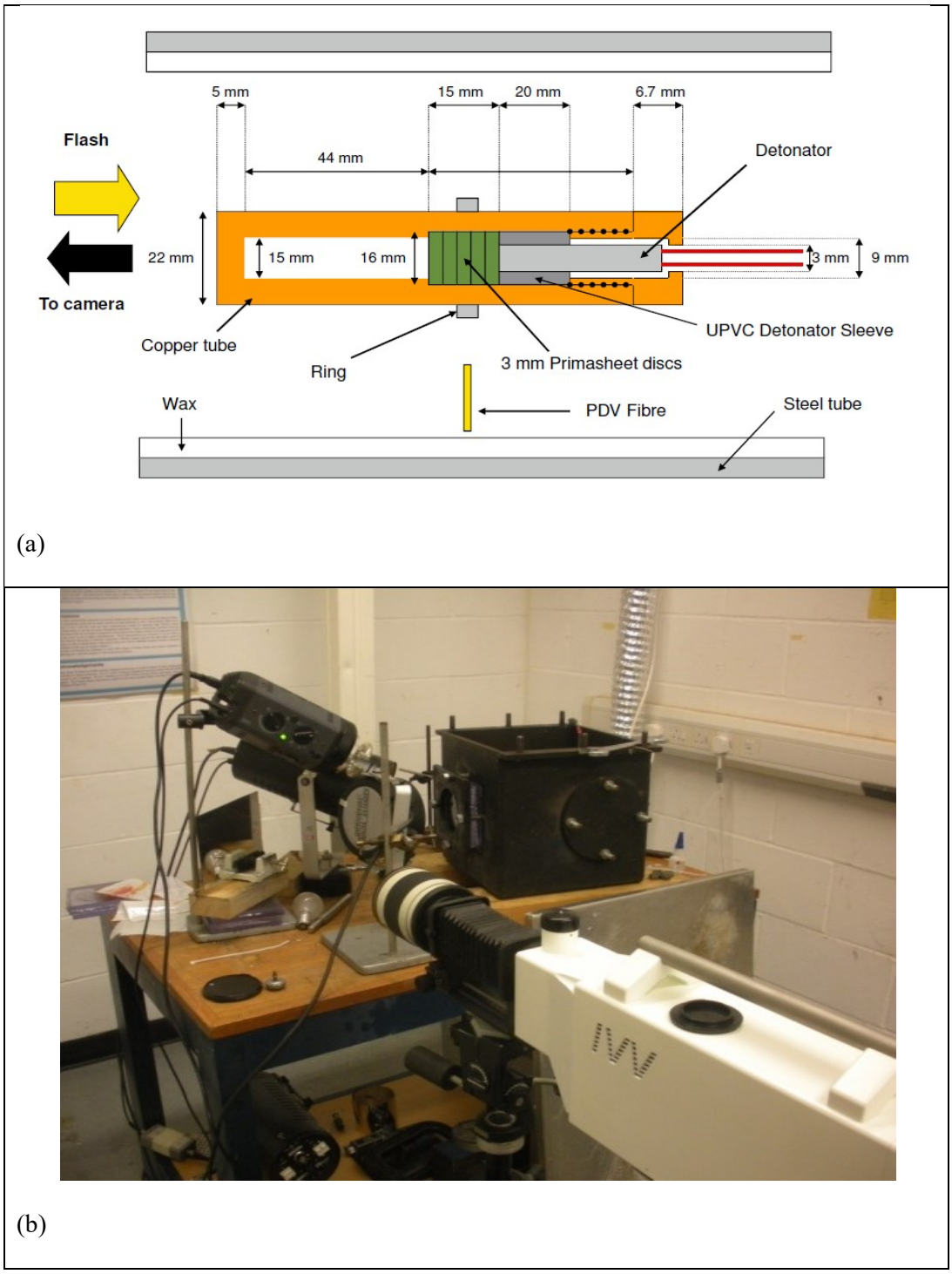

Figure 3.10: (a) Schematic of explosive ring setup; (b) Explosive ring apparatus and camera.

3.9 Photon Doppler Velocimetry

Photon Doppler Velocimetry (PDV) is a one-dimensional Fourier transform analysis of a heterodyne laser interferometry system, developed at Lawrence Livermore National Laboratory as an analytical tool for high explosive tests [103]. Initially PDV was created with hardware firstly constructed for the telecommunications industry. PDV is capable of measuring surface velocities ranging from centimeters per second to kilometers per second.

PDV is a very useful diagnostic tool for high explosives physics research. The frequency of the Doppler-shifted light gives an accurate quantification of the velocity of a swiftly travelling target by highlighting it with a laser. Light directed out of a multi-mode optical fiber highlights the target and a separate multi-mode fiber gathers the light that is Doppler-shifted, providing spatially-resolved velocimetry data. Prior to the creation of PDV researchers conducted surface velocity studies utilizing a method known as “Fabry-Perot Velocimetry.” This method used free-space Fabry-Perot interferometers and streak cameras for every particular data channel. The parts were expensive, intricate, needed constant upkeep or operator assistance, and also needed a custom manufactured optical table that took up a great deal of space. The Fabry-Perot method also utilized a huge laser whose output increased to 532 nanometers due to the fact that the streak camera photocathode is not sensitive enough in the infrared region of the spectrum. Even though the Fabry-Perot velocimeter provided exceptional information, the general channel count constantly stayed small because of its volume, price and intricacy. When modern high explosive facilities became accessible to researchers, it became increasingly

advantageous to have numerous velocimetry data channels offered without the price, convolution, and operator insensitive arrangement necessary for the diagnostic system.

The PDV method utilizes multi-mode fiber optics, an optical PIN detector, RF electronics, and moderate sample-rate A/D converter technology. The entire setup is contained within a little chassis. The benefit of utilizing multi-mode fiber is the considerable amplification of the optical light gathering from the target in contrast to that from a single-mode fiber. PDV also allows for the collection of many more additional data channels, significantly developing the spatial-temporal data attained at lower price, intricacy, and experimental cost.

Figure 3.11 illustrates an essential photonic Doppler velocimetry setup. At first a laser-generated optical carrier travels along a multi-mode fiber to a probe lens. The probe then highlights the target with the optical carrier. As the target travels in the direction of the lens, the reflected light is Doppler-shifted. The probe lens gathers a fraction of the Doppler-shifted light and the light returns through the multi-mode fiber. The Doppler-shifted light is combined with a portion of the initial optical carrier through a fiber-optic coupler and is measured by a "square-law" optical detector.

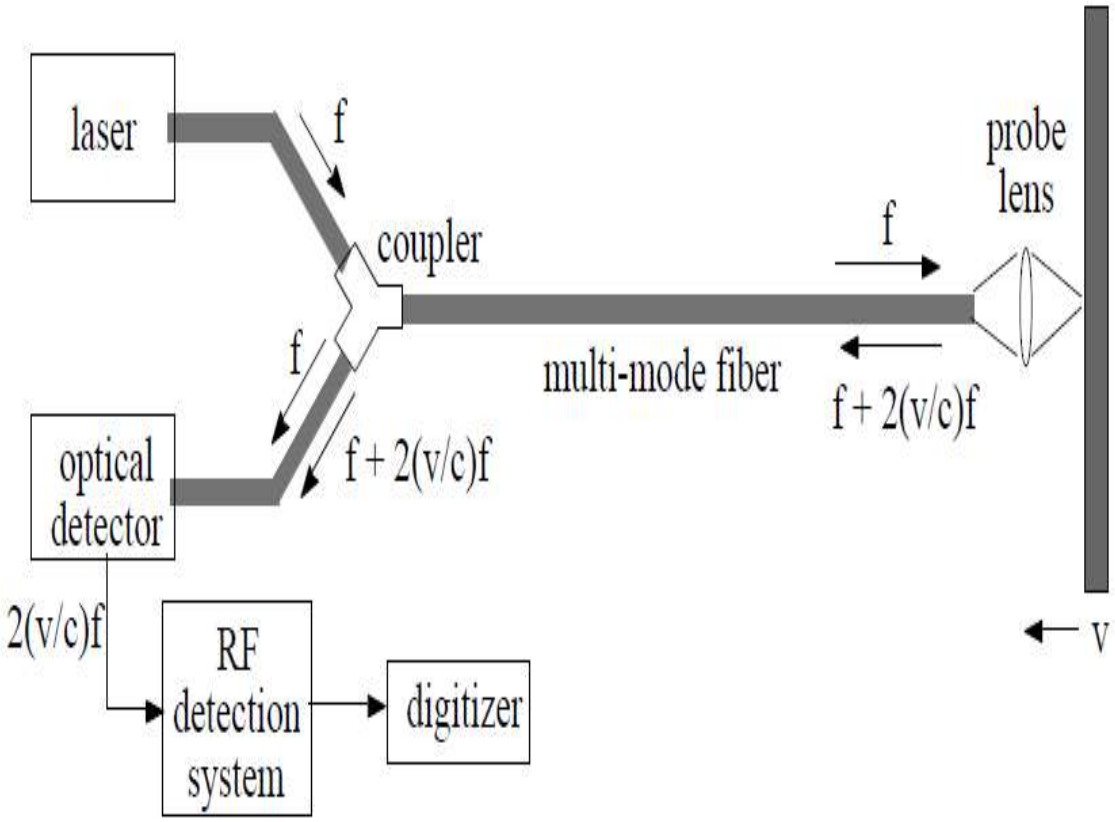

Figure 3.11: Basic block diagram of the photonic Doppler velocimetry system [103].

With suitable polarization and modal states, the "square-law" detector provides an electrical current equivalent to the square of the optical fields. For the Doppler-shifted light, this relates to a beat frequency equivalent to the instantaneous velocity of the target. At large velocities the beat frequency is excessive enough that is impossible to measure directly on a transient digitizer. To bypass this problem, a microwave phase discriminator was utilized to record the frequency-dependent phase shift generated by the Doppler signal. Measurement of the phase discriminator date is achieved by utilizing a digitizer with a moderate sampling rate.

The initial experiment for PDV took place on a shock-driven copper foil, along with the Fabry-Perot velocimeter acting as the evaluator. The study is illustrated in Figure 3.12, where it is shown that the copper foil was near a bridge wire, which was driven by a capacitance discharge unit (CDU). Green light from a frequency-doubled laser was focused onto a copper target with a probe lens. The Doppler-shifted light was reflected back through the probe lens and was concurrently processed by both the Fabry-Perot velocimeter and the PDV.

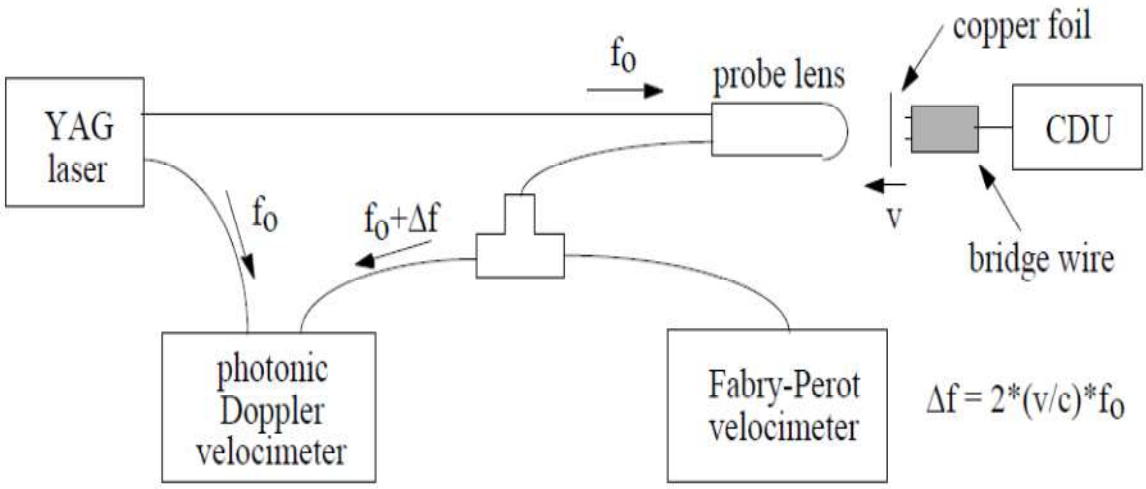

Figure 3.12: Block diagram of the copper foil velocity experiment, the first trial of the PDV [103].

The raw transient digitizer data from the PDV is shown in Figure 3.13(a), and the raw streak camera data from the Fabry-Perot system is shown in Figure 3.13(b). The Doppler beat frequency signal in Figure 3.13(a) was converted into frequency versus time, and then into velocity versus time as shown in Figure 3.14. Velocity measurements were hand-digitized from the Fabry-Perot data and then plotted on the same graph in Figure 3.14. The negative velocity at the conclusion of the data record is directly related to the rebounding of the copper foil after the shock event.

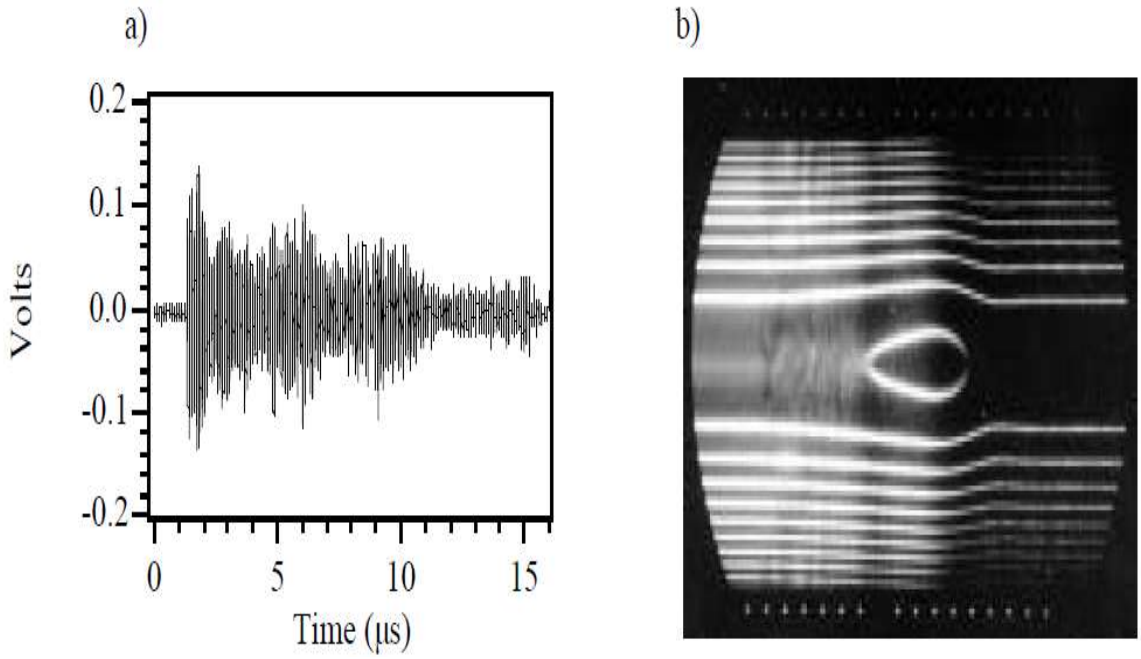

Figure 3.13: Raw data from the copper foil experiment: a) Photonic Doppler velocimeter, b) Fabry-Perot velocimeter [103].

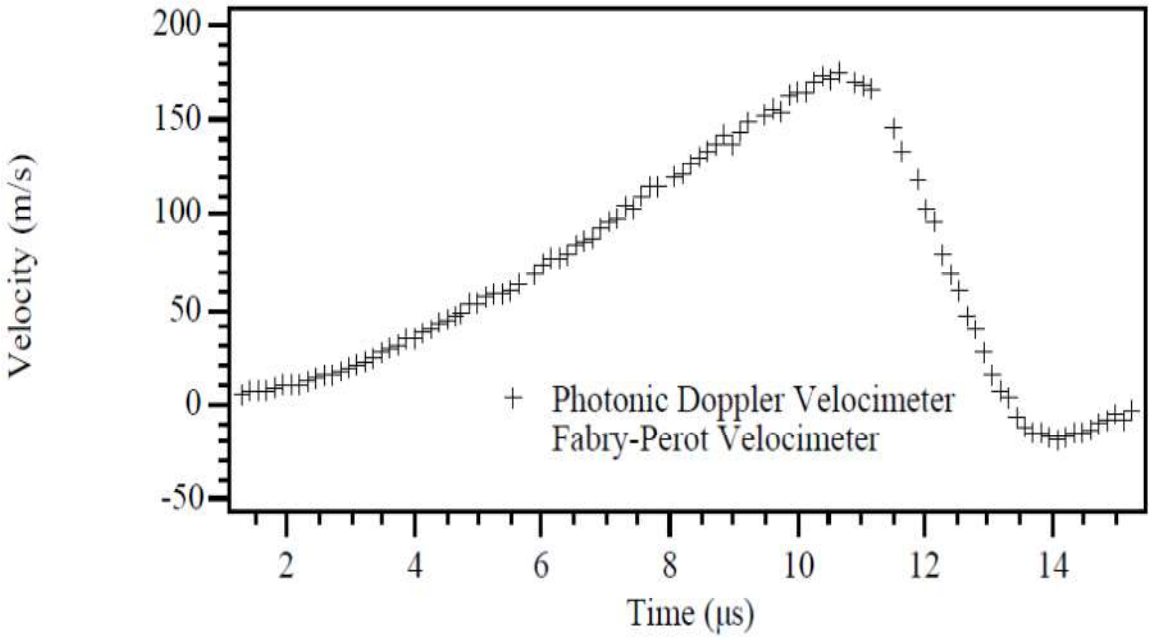

Figure 3.14: Processed data from the copper foil experiment [103].

3.10 Scanning electron microscopy

The scanning electron microscope (SEM) permits researchers to observe and investigate a huge variety of materials, such as metals, ceramics, or polymers on micrometer to nanometer scales. In 1935, Knoll proposed the concept of a scanning electron microscope [104]. Two years later (1938), van Ardenne constructed the first scanning electron microscope. Later on, lots of advances were developed and improved the capability of the SEM. The first commercial model was built by A.D.G. Stewart at Cambridge Scientific Instrument Co., and the components of this first generation SEM were applied and modified in the later commercial SEMs.

The scanning electron microscope (SEM) permits researchers to observe and investigate a huge variety of materials, such as metals, ceramics, or polymers on micrometer to nanometer scales. In 1935, Knoll proposed the concept of a scanning electron microscope [104]. Two years later (1938), van Ardenne constructed the first scanning electron microscope. Later on, lots of advances were developed and improved the capability of the SEM. The first commercial model was built by A.D.G. Stewart at Cambridge Scientific Instrument Co., and the components of this first generation SEM were applied and modified in the later commercial SEMs.

The basic components of modern SEMs are shown in Figure 3.15. Inside the microscope column, an electron gun provides electron beams which are used to scan the specimen. An electron beam passes through electron lenses made of magnetic materials and are controlled by the scan coils as shown in Figure 3.15. A computer system as shown in Figure 3.15 is used to acquire electron data and convert to SEM images is necessary, and recently, for all the modern SEM, the digitalized imaging system is

essential to the commercial model. The electron beam comes from the electron gun which is a LaB6 filament, or a file emission source as shown in Figure 3.15. The two electron lenses are made of magnetic materials used for focusing the electron beam. After focusing, the electron beam passes through an aperture, and then goes through the magnification controlled scan coils. The electron beam scans the specimen and generates several different types of electrons such as secondary electrons, backscattered electrons, and Auger electrons. The secondary (SE) and backscattered electrons (BSE) are utilized to generate SEM images. Due to their distinct electronic properties, the SEM images produced by secondary electrons are suitable for investigating the topography of the sample. However, the backscattered electrons show different gray levels of areas corresponding roughness and elemental differences as well.

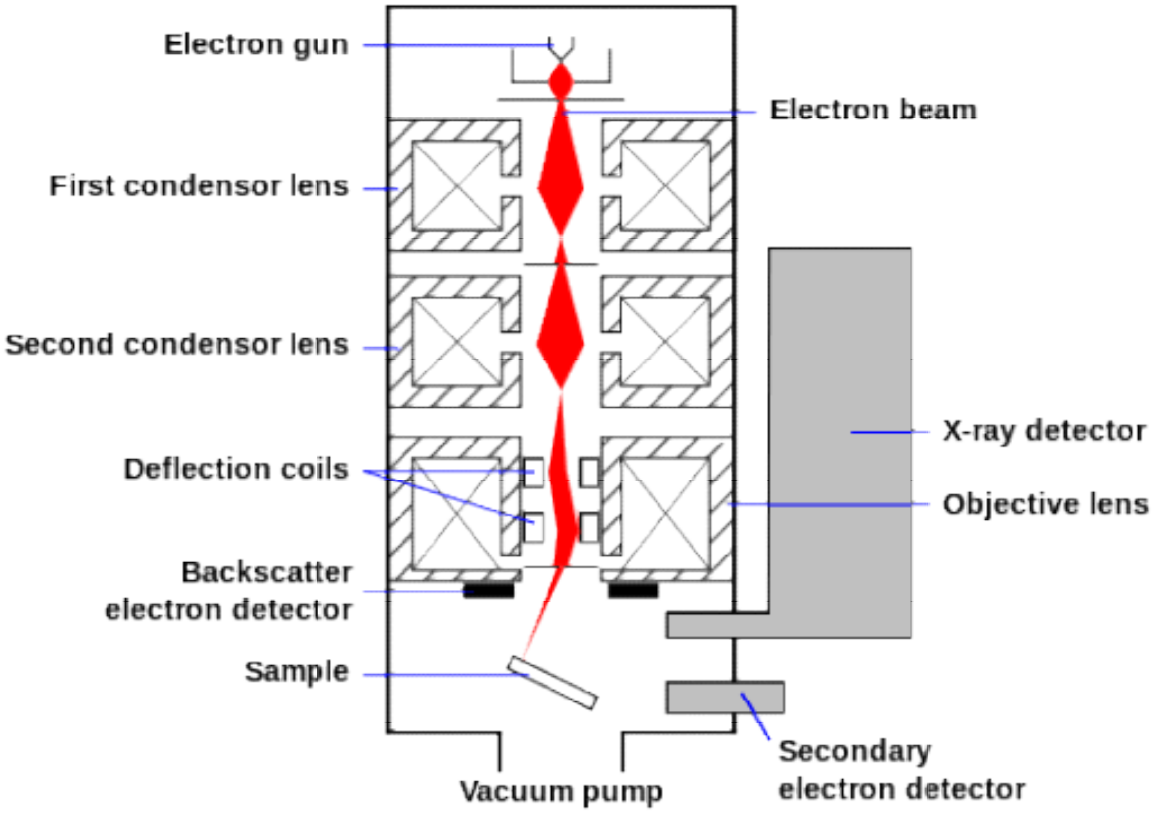

Figure 3.15: Diagram of Scanning Electron Microscope [104].

The chambers of the SEM always have to be underneath a vacuum otherwise it is possible for the electron beam to be dispersed by atoms of gas. Thus, it is essential that any specimen or mount utilized to secure the sample not have a large amount of vapor pressure. Vacuum pumps are usually set up to ensure that the electron column maintains a vacuum as a sample set up inside the SEM. The vacuum pump set up also allows for the electron gun to continue activity throughout switching of a sample, thereby speeding up the time it takes to change samples. Typically vacuum pumps are low pressure and are regular oil-diffusion pumps that generate levels of vacuum around 1.3×10^{-4} Pa. They are generally oil-diffusion pumps because if an electron beam hits a surface with even a

monolayer of oil, it will crack the oil, then a deposit of carbon will be left where the beam hit and reduce the quality of a SEM image.

A closely divergent beam of electrons is generated by the electron gun and sent through column's center. Figure 3.16 is a diagram of a typical tungsten gun. The source of electrons is a tungsten filament with a diameter of approximately 0.25 mm, which is raised in temperature to around 2500 °C. Thermionic emission occurs at the crooked end of the filament and the electrons that are released are pulled to an anode that is held at a positive voltage in relation to the filament, which is generally 5 to 30 kV in SEMs. The voltage is typically set to 20 kV, but some deviation is beneficial for different types of analyses.

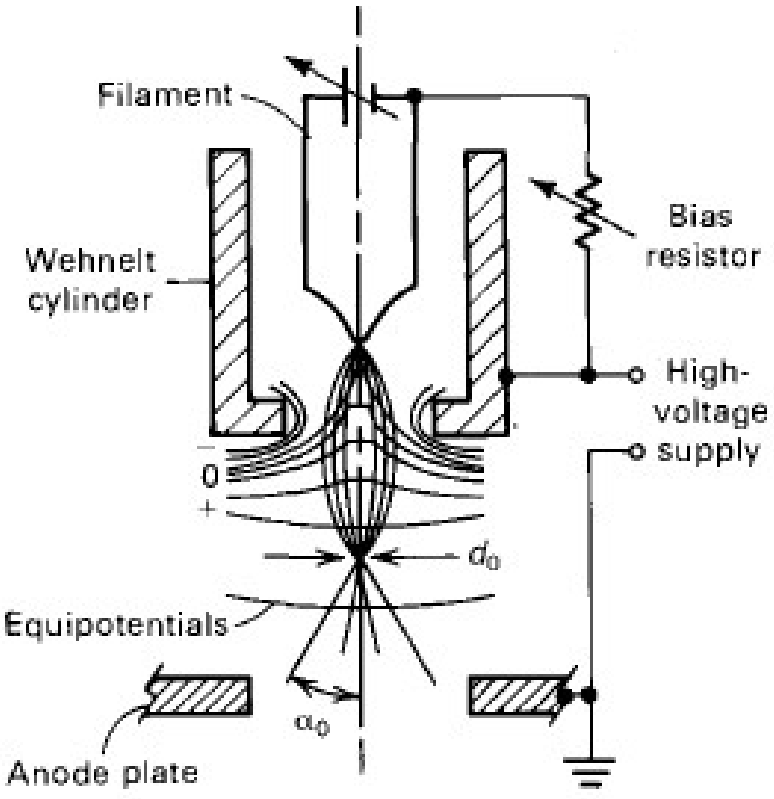

Figure 3.16: Typical tungsten hairpin filament electron gun [104].

There are magnetic lenses inside electron microscopes comparable to a typical solenoid coil. When an electron moves through a magnetic field, a radial force directed inward is applied upon the electron that is equivalent to the Lorentz force, $v \times B$, where v represents electron velocity, and B represents the magnetic flux density. The lensing operation is comparable to operations with an optical lens, whereby a ray parallel to the axis of the lens is directed to the lens axis relative to the focal length of the lens f. For optical lenses, the focal length is set through the lens surface curvature and is incapable of being altered. For electromagnetic lenses, the focal length is based upon two different features: voltage of the gun (which determines the electron velocity, v) and the current running along the coil (which determines the flux density, B). Thus, the focal lengths of the lenses can be set by changing the currents selected for them, by adding more current the radial force generated on the beam is enhanced thereby decreasing the focal length.

An SEM utilized the lenses it contains inside to decrease the electron beam diameter to a tiny spot along the surface of the specimen. Thus, a lens should be able to demagnify as illustrated in Figure 3.17. An arrow inside an object plane is replicated reversely inside an image plane, and the image of the arrow tip is found by tracing the rays designated by (1) and (2). Magnification is expressed by $M = S'/S$; when the focal length f is decreased, the value of S' is decreased, and magnification is reduced. Thus, if the arrow length is considered as diameter of the electron beam generated through the gun, d_o, the resulting beam diameter, d_1, once the beam has gone through an initial condenser lens relates to $d_1 = M_1 d_o$, where M_1 is the initial condenser lens magnification.

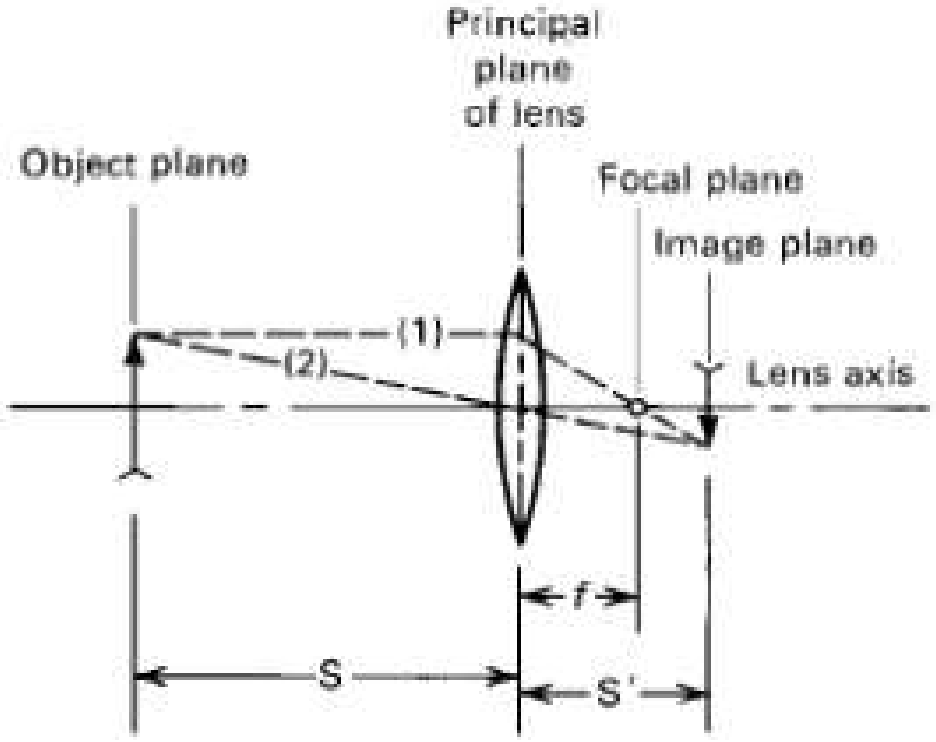

Figure 3.17: Ray schematic depicting lensing action [104].

Figure 3.18 is a diagram of how the three lenses are coupled; the objective for each of the lenses is the image from the lens on top of it. For a typical SEM, the two condenser lenses on top are coupled together so that the two lenses are concurrently controlled by one knob; changes to the knob are utilized to designate the final spot size d_3. The objective lens' focal length is controlled so that S'_3 lies upon the surface of the sample. The specimen can be set at different heights inside a specimen chamber. The working distance (WD) is the specimen's distance underneath objective lens. When the working distance is adjusted, the current through the objective lens needs to be changed so that S'_3 lies on the surface of the specimen thereby creating the lowest spot size on the surface of the specimen for the initial setup of C_1 and C_2. This fine-tuning is the operation by which

focusing is conducted; it is easily performed by changing the current through the objective lens, I_3, until the desired image is attained. Due to the fact that f_3 and thus S'_3 are dependent upon I_3, a distinctive value of the working distance relates to each value of I_3 once the operation by which the lens is focus is performed.

Once the image is in focus, the working distance value is calculated by the current through the objective lens, I_3. Modern SEMs show the working distance readily on the viewing screen. So the two condenser lenses can be changed to adjust the diameter of the beam on the sample surface, d_3, and although the working distance of the specimen can differ, the objective lens is controlled to reduce the size of the beam on the surface of the sample. A small d_3 is required for the highest magnification. But due to the fact that most analyses are conducted below the highest magnification, the optimal value of d_3 will generally be greater than its lowest value.

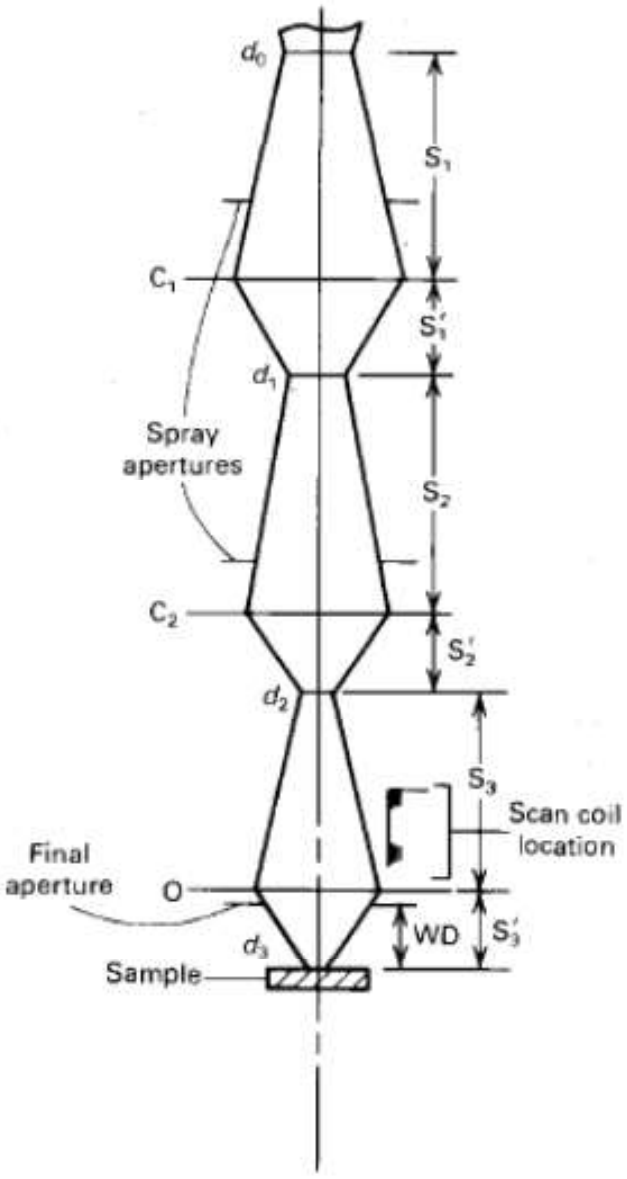

Figure 3.18: Illustration of the lensing action of the three lenses of a scanning electron microscope [104].

So the SEM has an electron beam scan the surface of a specimen. The twin sets of scan coils fixed in the middle of the objective lens cage illustrated in Figure 3.18 carry out the process of scanning. The scan coils (Fig. 3.18) direct the electron beam to scan a square area of size *r* x *r* on the surface of the specimen. The area being scanned is

typically known as the raster. Even though the electron beam is illustrated in Figure 3.19 as a line, in reality it is diverging as it goes through these coils. Nevertheless, due to the fact that divergence half-angle is about a milliradian, being depicted as a line is actually not far off. A system of double-deflection is utilized, wherein the electron beam is deflected through a Lorentz force generated by the magnetic fields of pairs of scan coils. The scan coil pairs on top, l_1-l_1, generate a magnetic field at time 1 that creates a Lorentz force on the beam, leading it to deflect to the right through an angle θ_{max} as illustrated. The scan coil pairs on the bottom l_2-l_2 deflect the beam back to the left through an angle $2\theta_{max}$ in order for it to strike the specimen as illustrated at the left edge of the raster. The voltage provided by the scan generator directs both coil pairs. The signal of the voltage experiences a linear decrease with time, as shown on the upper left of Figure 3.19. When it is decreasing from time 1 to time 5; the electron beam scans through the line of length *r* illustrated on the surface of the specimen in Figure 3.19. When it reaches time 5, the scanning voltage drops immediately to 1', directing the beam to come back suddenly to the left portion of the raster, depicted as position 1' inside Detail A of Figure 3.19.

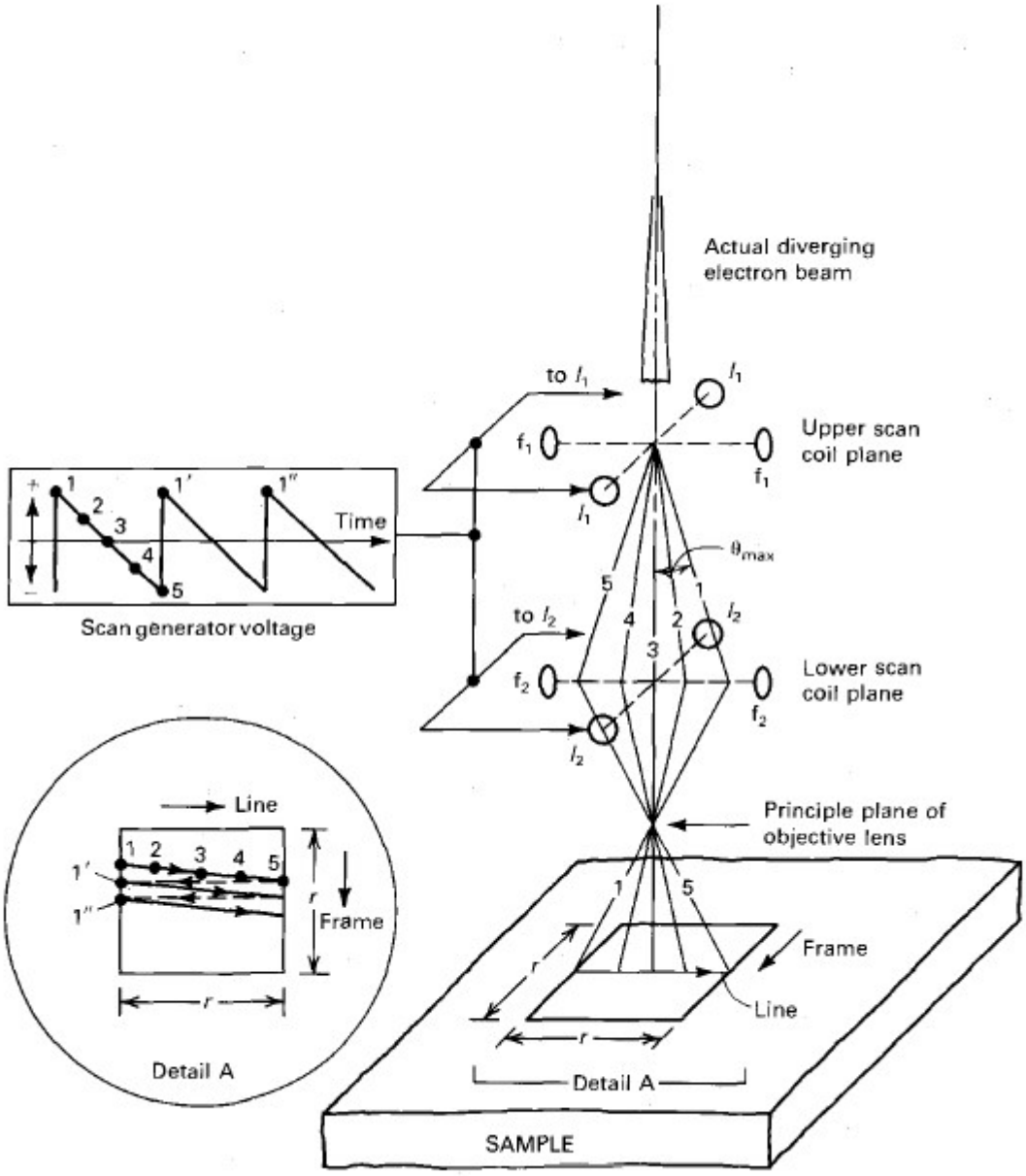

Figure 3.19: A schematic of a double-deflection scanning system showing a line scan with only the line coil pairs, l_1-l_1 and l_2-l_2, activated [104].

A SEM's depth of field is excellent when compared to an optical microscope. Typically, a SEM's depth of field is greater than that of an optical microscope by a factor of around 300. This is why SEMs have been used frequently for fracture surface studies

such as the ones performed here. However, the SEM is generally mediocre in comparison to the optical microscope for regular studies of samples created through customary metallographic methods when magnifications lower than 300 to 400x are used.

3.11 Energy Dispersive X-ray (EDX) analysis

Energy Dispersive X-ray (EDX) analysis is an emission spectroscopic technique that is widely used for elemental identification or chemical characterization. Its characterization potential comes from the principle that every element has a certain atomic structure that relays a particular set of peaks on its electromagnetic emission spectrum. It relies on the emission of characteristic x-radiation, typically in the 1- to 60-keVenergy range, subsequent to excitation of atomic energy levels by an outside energy source such as an electron beam, a charged particle beam, or an x-ray beam. EDX was used on fragments collected from the expanding ring tests to perform element content analysis as well as elemental mapping in order to see how these were affected throughout the explosive process.

3.12 Simulation tools (LS-DYNA)

The program LS-DYNA was used to simulate the results of the expanding ring experiments to compare to the actual experimental results. LS-DYNA is an advanced general-purpose multiphysics simulation software package distributed by the Livermore Software Technology Corporation (LSTC). LS-DYNA is used for failure analysis in many different industries. The model of the expanding ring experiments only considered a quarter of the aluminum ring being tested using specific boundary conditions to ensure

the plain strain rate. The inner layer of copper used in the expanding ring experiments was also present in the model as seen in Figure 3.20 as the blue inner layer of the simulation. The expansion was driven using prescribed displacement, in the radial direction, to the inner surface of the copper layer.

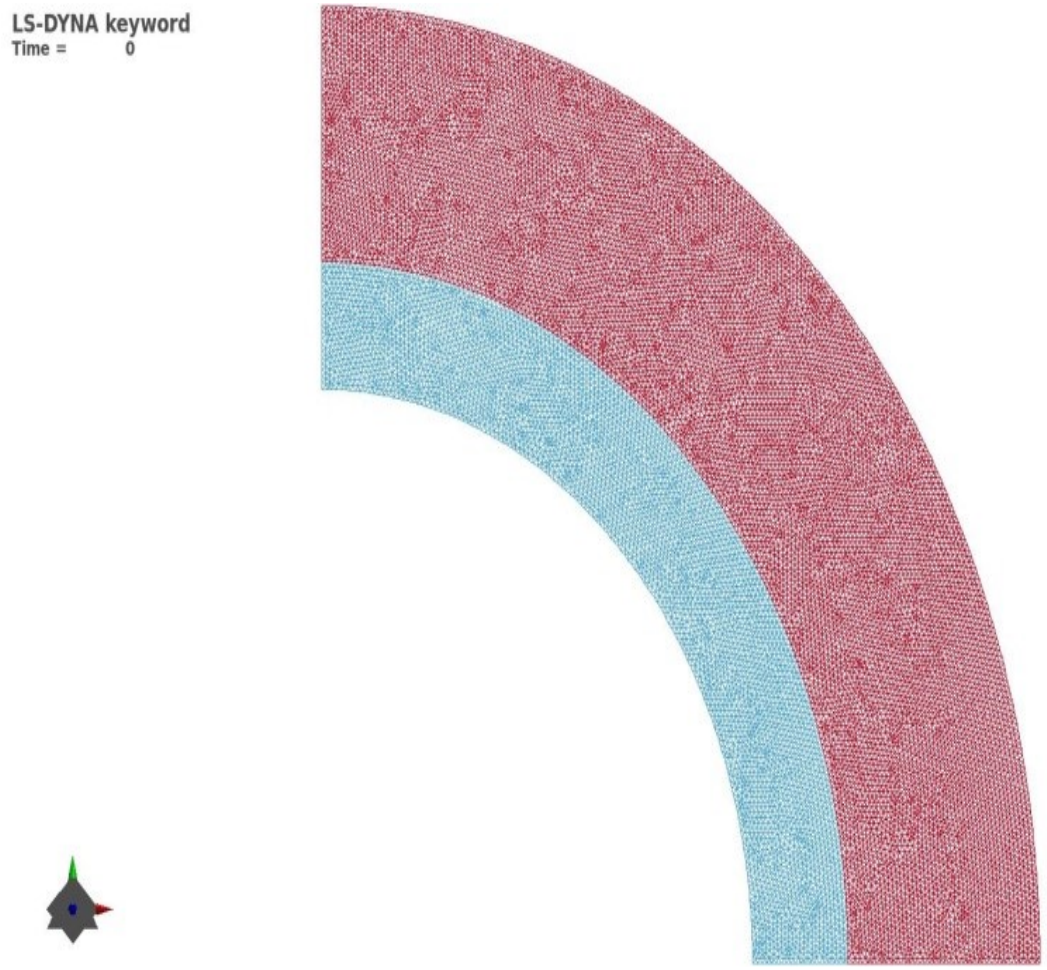

Figure 3.20: Setup of LS-DYNA Finite element simulation.

Chapter 3, in part, is published as “Fragmentation and constitutive response of tailored mesostructured aluminum compacts” Journal of Applied Physics, vol 119, p. 145903, 2016. A. Marquez, C. Braithwaite, T. Weihs, N. Krywopusk, D.

Gibbins, K. Vecchio, and M. Meyers. The dissertation author is the first author of this work.

CHAPTER 4: RESULTS AND DISCUSSION

4.1 Density and porosity analysis results

The results of the density and porosity analysis on each of the swaged aluminum compacts are shown in Table 4.1 and the results of the swaged nickel-aluminum compacts are shown in Table 4.2. Based on the results of these analyses, it appears that varying the particle and 6061 Al core size during swaging did not have a large effect on the density and porosity of the aluminum compacts as they both varied by less than 2% between each of the swaged aluminum compacts. However, there was still a trend of increasing density percentage between the swaged 100 micron aluminum particle compacts as the core size was increased while the apparent porosity decreased. Even though these trends were by a fraction of a percentage they were still evident. It is also important to note that all of the swaged aluminum compacts were over 94% fully dense and had less than 4% apparent porosity.

Varying the 6061 Al core size during the swaging process appeared to have a more significant effect on the swaged nickel-aluminum compacts. It is observed that there is a trend of increasing density percentage and decreasing apparent porosity by greater than 2% as the core size was increased. Unlike the swaged aluminum compacts, all of the swaged nickel-aluminum compacts were less than 87% fully dense and had an apparent porosity greater than 5%. The explanation for this contrast to the swaged aluminum compacts is further explored in the optical microscopy analysis in the next section.

Table 4.1: Density and porosity analyses results for the swaged aluminum compacts.

Compacts	40 µm Al (12.7 mm core)	100 µm Al (No core)	100 µm Al (12.7 mm core)	100 µm Al (18.8 mm core)	400 µm Al (18.8 mm core)
Average Density Percentage (%)	96.5 ± 0.36	94.7 ± 0.42	95.2 ± 0.16	95.7 ± 0.34	95.4 ± 0.49
Average apparent porosity (%)	2.14 ± 0.26	2.72± 0.21	2.49 ± 0.28	2.26 ± 0.38	3.25 ± 0.56

Table 4.2: Density and porosity analyses results for the swaged nickel-aluminum compacts.

Compacts	400 µm NiAl (No core)	400 µm NiAl (12.7 mm core)	400 µm NiAl (18.8 mm core)
Average Density Percentage (%)	80.5 ± 0.28	84.3 ± 1.3	86.2 ± 2.1
Average apparent porosity (%)	10.4 ± 0.14	8.37 ± 1.2	6.04 ± 0.8

4.2 Optical microscopy analysis results

The optical microscopy analysis helped greatly characterize the microstructure of most of the compacts and also explain the results of the density analysis in the previous section. The microstructures of the 40 micron and 400 micron swaged aluminum particle compacts were not able to be revealed even after several attempts of metallographic techniques, but the 100 micron swaged Al compacts with different core sizes showed

detailed results. The microstructure of the 100 micron Al swaged with an 18.8 mm core is shown in Figure 4.1 below.

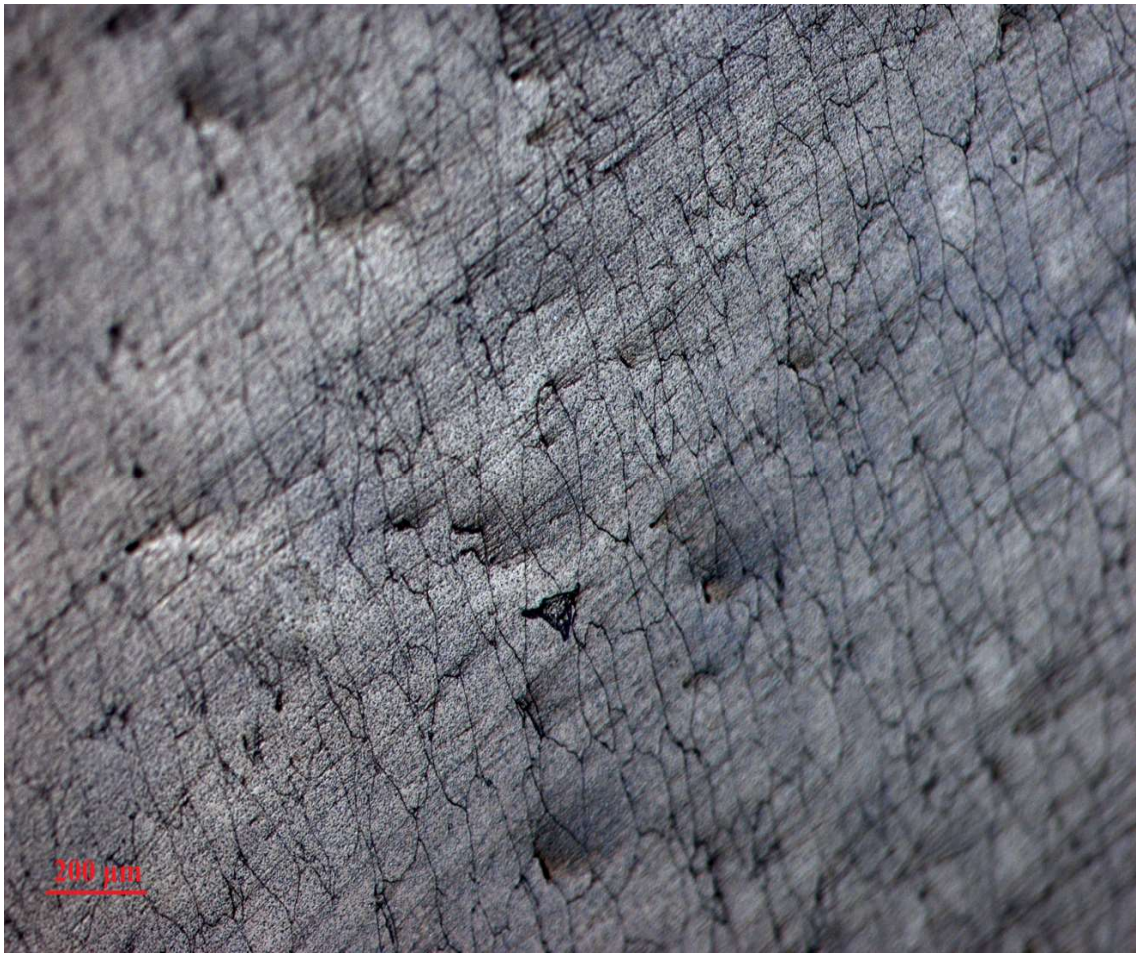

Figure 4.1: Microstructure of the 100 micron Al particles swaged with an 18.8 mm core.

The microstructure seen in Figure 4.1 reveals that when the 100 micron Al particles were swaged with an 18.8 mm core they were tightly compacted so that the grains of the material either maintained the 100 micron size of the particles or decreased considerably in size. This could likely be due to the greater degree of plastic deformation as predicted previously. There also appears to be little to no space between the grains in

contrast to the microstructure of the 100 micron particles swaged with a 12.7 mm core shown in Figure 4.2 below.

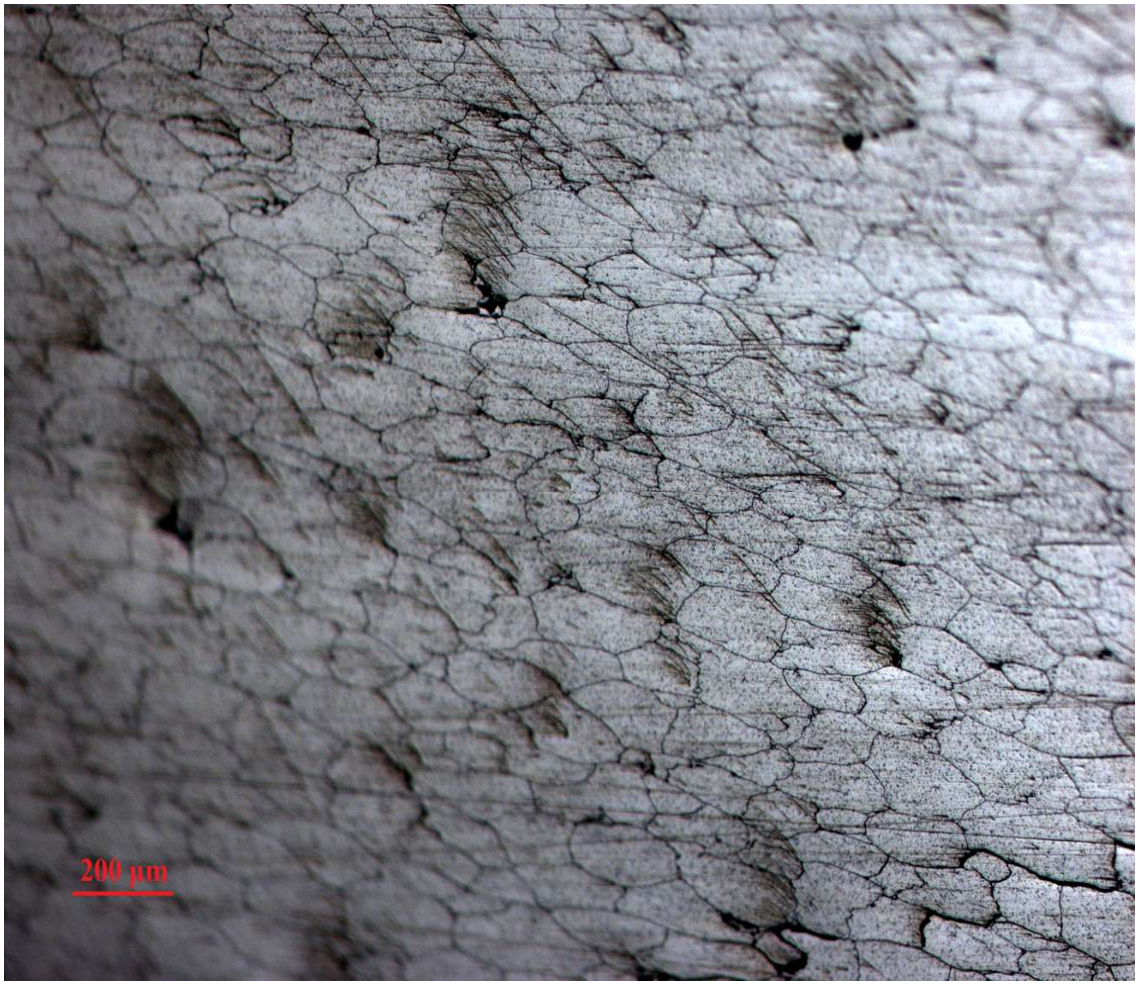

Figure 4.2: Microstructure of the 100 micron Al particles swaged with a 12.7 mm core.

There appears to be slightly more space or gaps between the grains of the microstructure of the 100 micron Al swaged with a 12.7 mm core seen in Figure 4.2, which could explain the relatively smaller average density percentage and greater average apparent porosity compared to the 100 micron Al swaged with an 18.8 mm core observed in the results of the previous section. Also, in comparison to the prior microstructure, it

appears that less of the grains tend to be smaller than 100 micron possibly because of the lower degree of plastic deformation associated with the smaller core size. Nevertheless, there are still a considerable amount of grains smaller than 100 micron especially compared to the microstructure of the 100 micron Al particles swaged with no core shown in Figure 4.3.

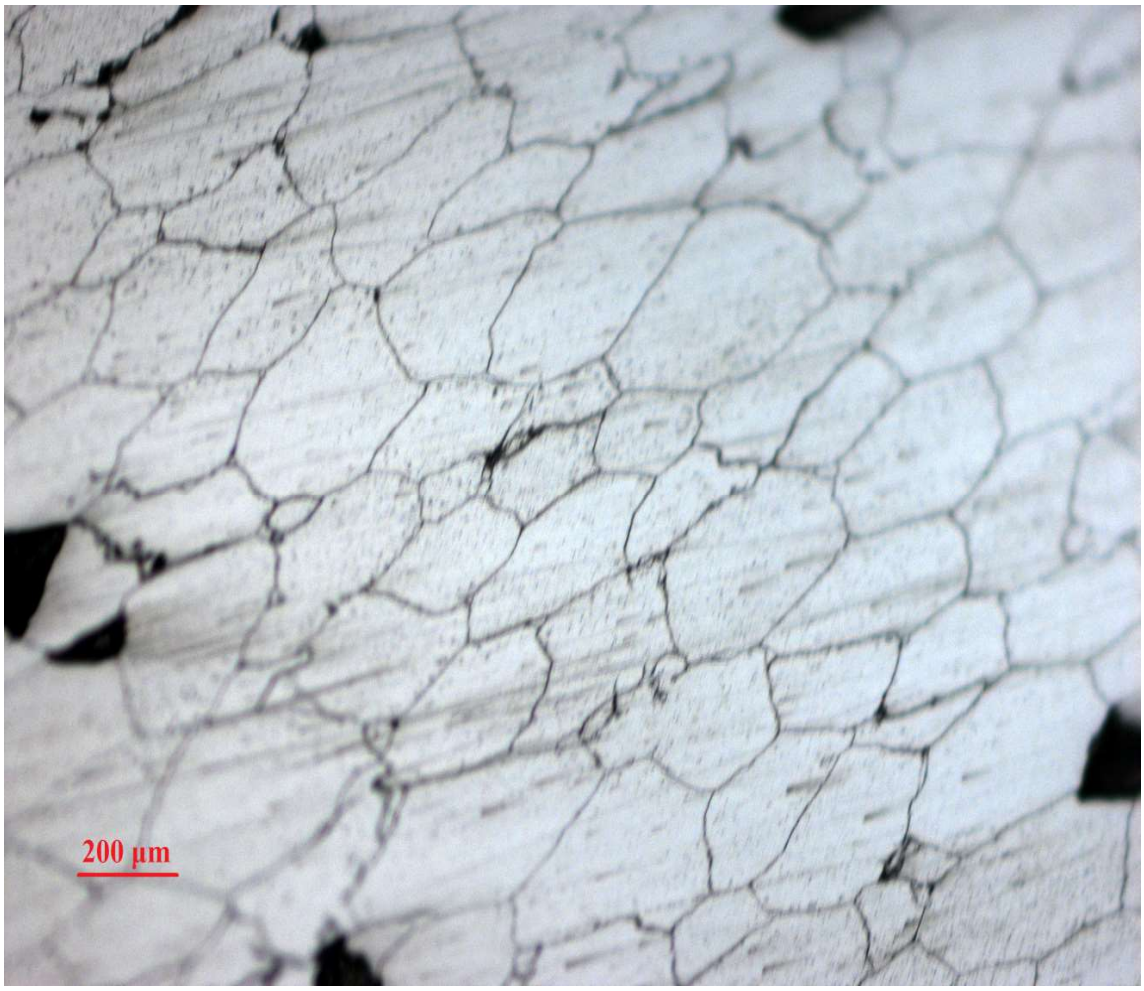

Figure 4.3: Microstructure of the 100 micron Al particles swaged with no core.

In the microstructure of the 100 micron Al swaged with no core in Figure 4.3 it appears that the grains of the material tended to vary more widely from smaller than 100

micron to even larger than 200 micron. There also appeared to be larger spaces or gaps between grains of the compact compared to Al compacts swaged with 6061 Al cores. This 100 micron Al compact swaged with no core had the lowest density percentage and highest apparent porosity of the 100 micron Al compacts so the trend of the greater degree of plastic deformation leading to these results could be repeating, although the gaps could also be due to the metallographic preparation of the samples. However, the microstructures of the swaged NiAl compacts also appear to significantly follow this trend. The microstructure of the NiAl particles swaged with no core is shown in Figure 4.4 below.

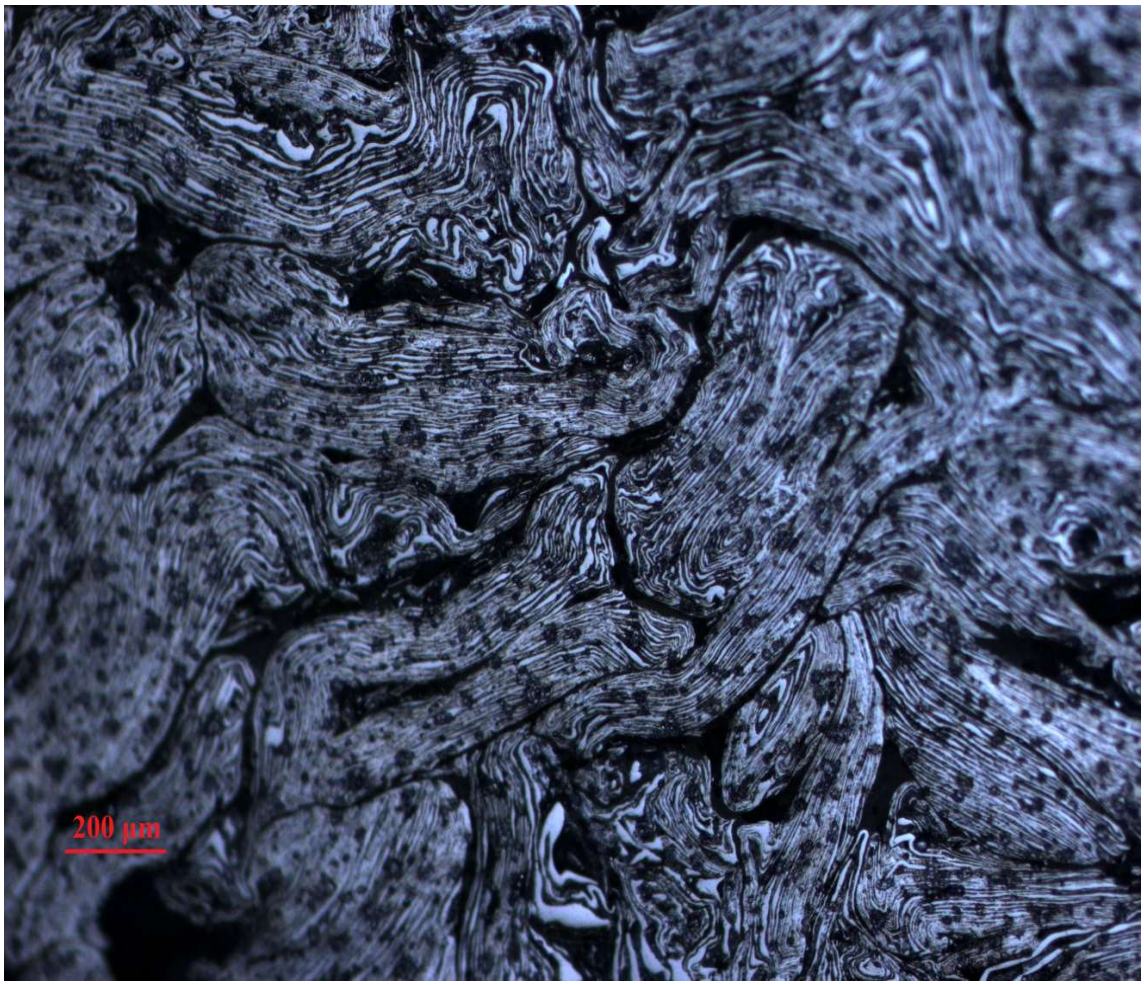

Figure 4.4: Microstructure of the 400 micron NiAl particles swaged with no core.

The microstructure of the swaged NiAl particles shown in Figure 4.4 is drastically different from the swaged Al compacts. The particles appear to have folded amongst each other into various sandwich formations during the swaging process with considerably large spaces between the particles especially compared to the almost fully dense swaged aluminum compacts. Supporting the trend of spaces or gaps in the microstructure resulting in lower density percentage and higher porosity, the 400 micron NiAl compact

swaged with no core had the lowest average density percentage of approximately 80% and the highest average apparent porosity of approximately 10%.

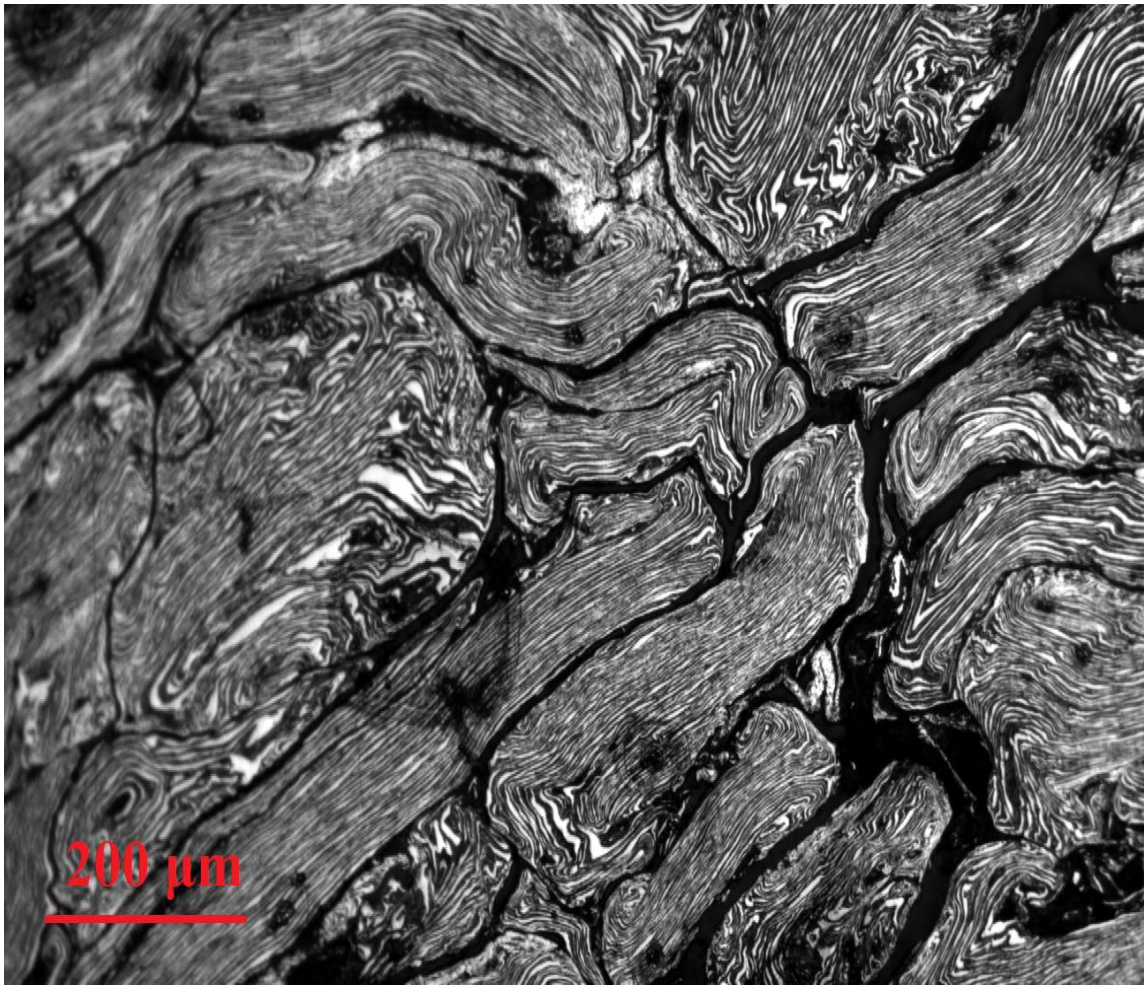

Figure 4.5: Microstructure of the 400 micron NiAl particles swaged with a 12.7 mm core.

The microstructure of NiAl particles swaged with a 12.7 mm core shown in Figure 4.5 has the same sandwiched formations of the NiAl compact swaged with no core but there are no gaps between the particles larger than 200 microns. This could explain why the average density percentage was approximately 4% higher than the compact swaged with no core and the average apparent porosity was about 2% lower. It is evident

that varying the core size has a more significant effect when swaging the NiAl particles compared to swaging compacts made of only Al particles.

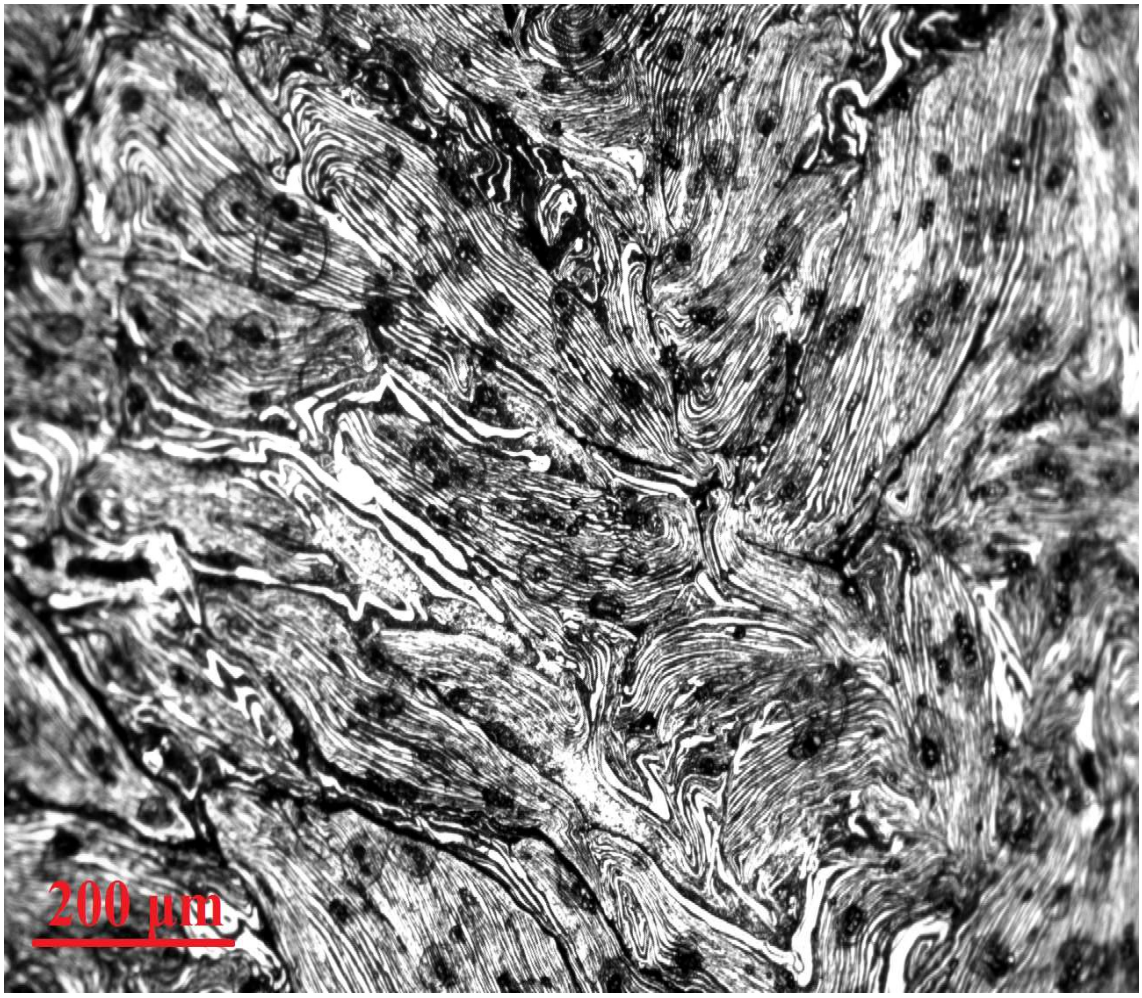

Figure 4.6: Microstructure of the 400 micron NiAl particles swaged with an 18.8 mm core.

The microstructure of NiAl particles swaged with an 18.8 mm core shown in Figure 4.6 maintains the sandwich formation of particles seen in the other NiAl compacts but the spaces observed between the compacted particles are the smallest of the swaged NiAl compacts. It also followed the trend of these smaller gaps resulting in higher density percentage and lower apparent porosity, as the average density percentage increased by

approximately 2% and the average apparent porosity decreased by approximately 2%. Therefore, it is evidenced in the results of the density and optical microscopy analyses that increasing the core size during swaging did indeed increase the degree of plastic deformation for a certain densification of the compacts, especially for the swaged NiAl compacts.

4.3 Sample characterization with SEM

The distinct powder morphology and size distribution of each of the different Al powders are shown in the scanning electron microscope images in Figure 4.7a-c. The ~40 μm size Al powder (Figure 4.7a) had moderately homogeneous shapes and particle sizes while the ~400 μm size Al powder (Figure 4.7c) had arbitrary shapes and a substantial variety of particle sizes (from 350 to 500 μm), so steel sieves were used to make sure they were in a close range of 400 μm. The ~100 μm size Al powder (Fig. 4.7b) also had arbitrary shapes but the particle size distribution (100 – 125 μm) was in a much closer range to 100 μm. The ~40 μm size Al powder are more clustered partly because of the large increases of surface area, which augment the effect of the van der Waals attraction forces that become gradually more relevant as the grain size is reduced. [105] As a result, the particles have a spongy arrangement.

Scanning electron microscopy was also used to characterize the failure morphology in fragments of the rings. The distinction between the fracture data of the rings is consistent with the failure morphologies seen in Figures 4.8 and 4.9. The outer deformed fracture surfaces of the 40 and 400 μm aluminum fragments (Figures 4.8a and b) exhibit rolling uneven surfaces that are typical of ductile deformation. The dimple morphology

demonstrated on the edges of these fragments is characteristic of ductile failure as well. In contrast, the fragments of the 100 μm aluminum rings, shown in Figure 4.9(a-c), demonstrate features that are indicative of a brittle failure such as interfacial cracking. The outer deformed fracture surfaces of the nickel-aluminum swaged with an 18.8 mm core (Figures 4.10a and b) exhibit undulating surfaces that are typical of ductile deformation. The dimple morphology observed on the edges of these fragments is characteristic of ductile failure as well. The fragments of the nickel-aluminum rings swaged with a center rod of 12.7 mm or no core at all, shown in Figures 4.11(a-c), demonstrate features that are indicative of a brittle failure such as intergranular cracking. The dissimilarity in the fracture surfaces indicates how a brittle failure induces the production of more fragments.

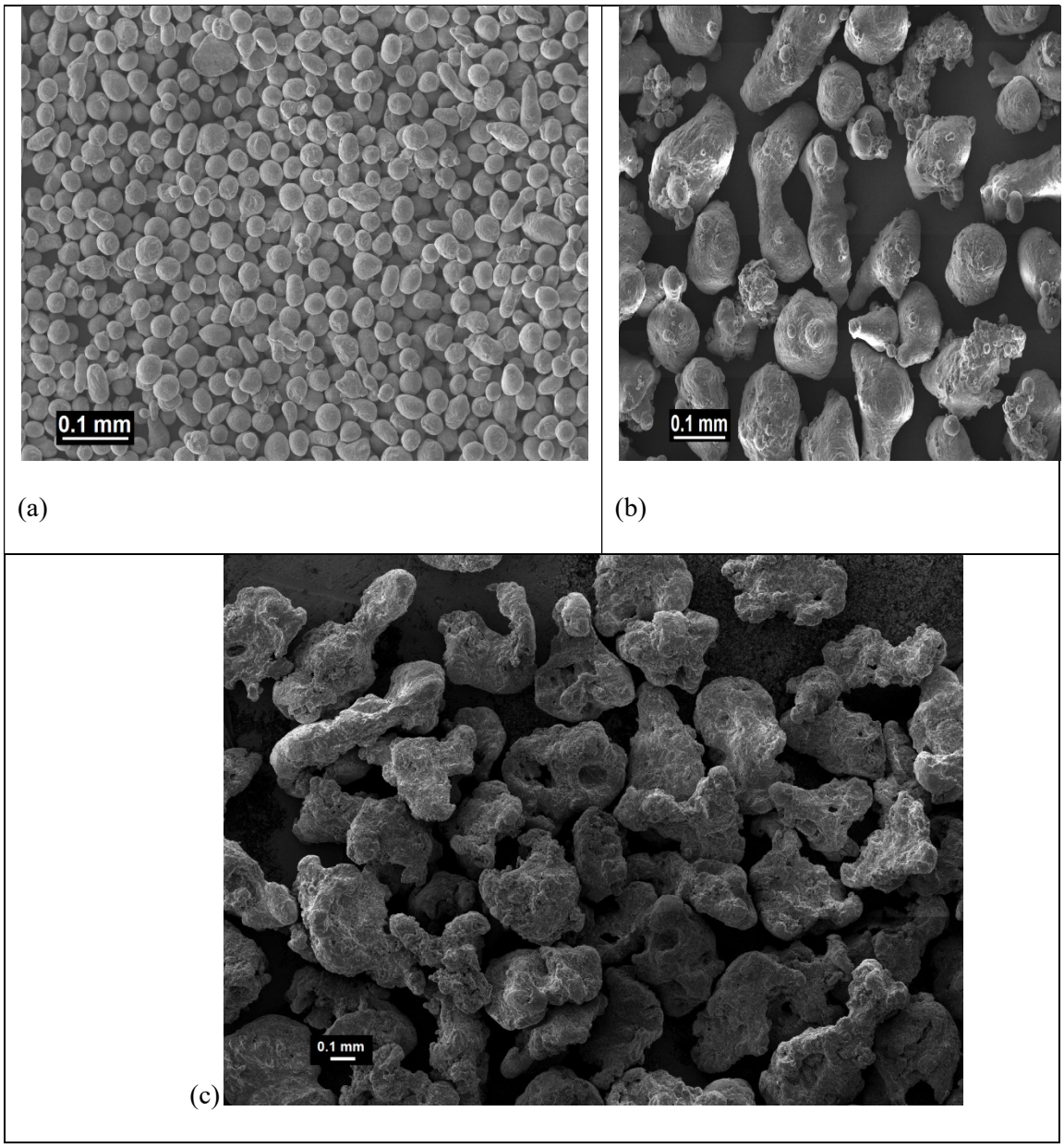

Figure 4.7: SEM micrographs of the different Al powder particle sizes: (a) 40 μm; (b) 100 μm; (c) 400 μm.

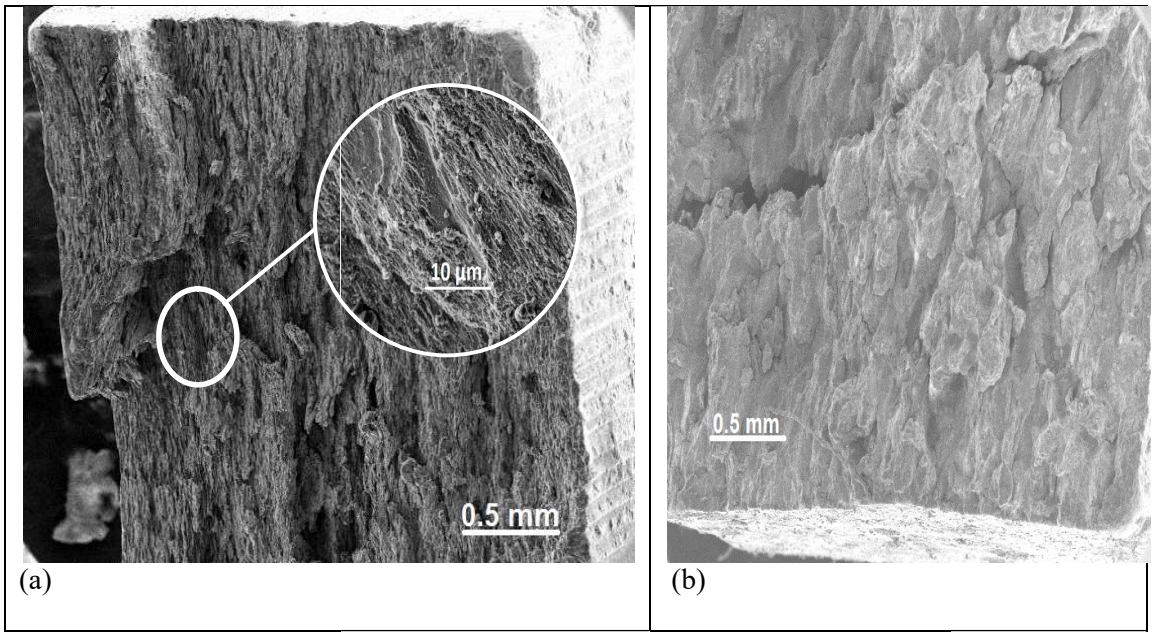

Figure 4.8: Fracture surfaces from expanding ring tests: (a) compact from 40 µm powder; (b) compact from 400 µm powder. Note the rolling uneven surfaces in both fractures that are indicative of ductile deformation and at a high magnification in the 40 µm fracture surface, shown by the inset image, there is visible elongated dimple morphology.

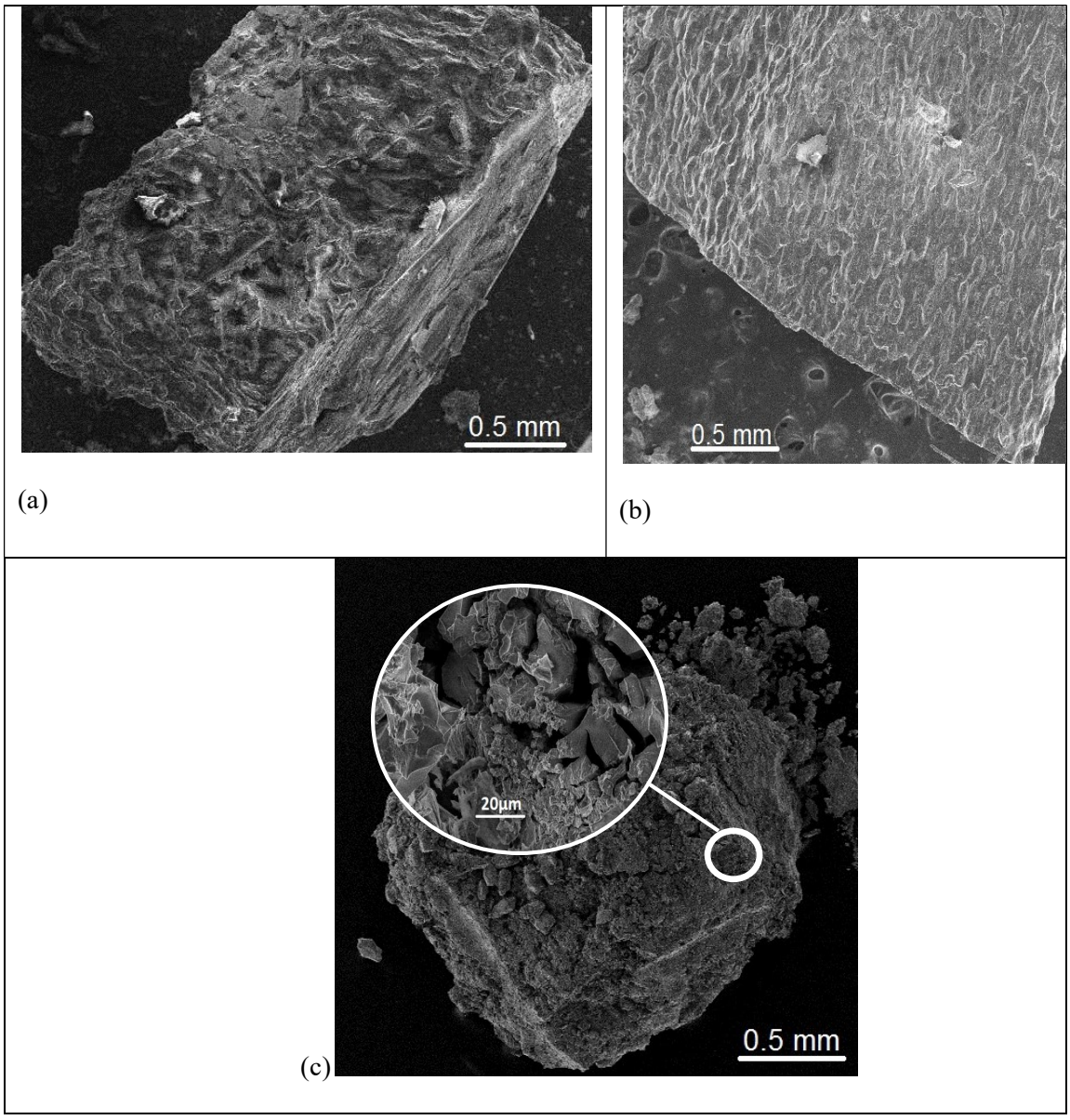

Figure 4.9: Fracture surfaces from expanding ring tests of compacts made from 100 μm powder: (a) 18.8 mm; (b) 12.7 mm; (c) no core. Note the interfacial cracking on these surfaces that are indicative of brittle failure, specifically in the high magnification inset of the fragment from the compact swaged with no core.

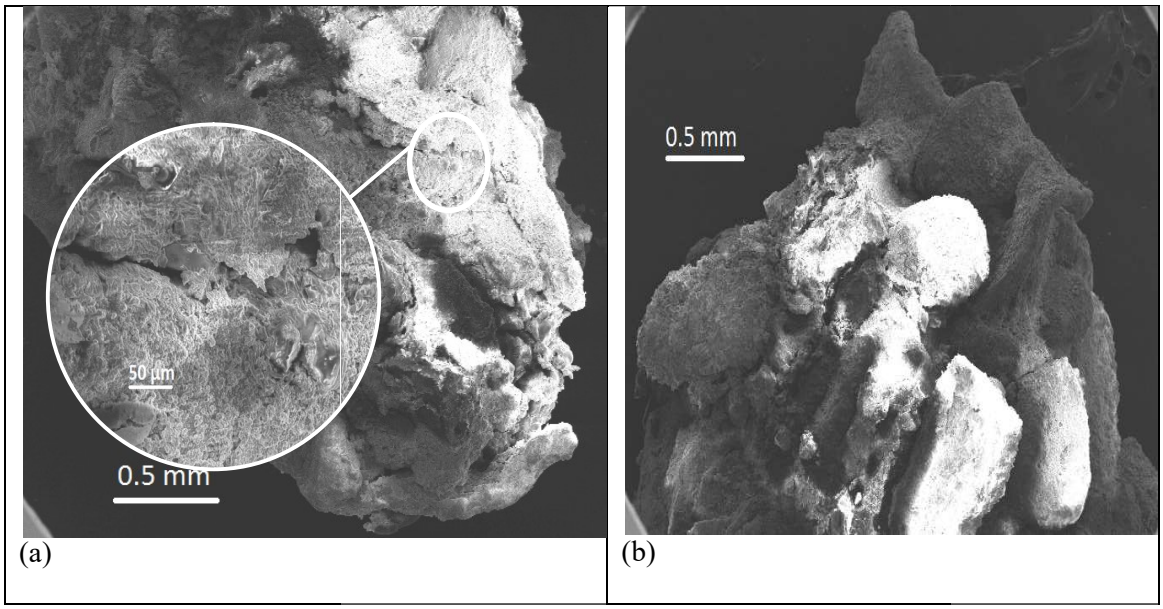

Figure 4.10: Fracture surfaces from expanding ring tests of the swaged ~400 µm NiAl compact made with an 18.8 mm core. Note the rolling uneven surfaces in both fractures that are indicative of ductile deformation and at a high magnification in the first image (a), shown by the inset image, this morphology is even more pronounced.

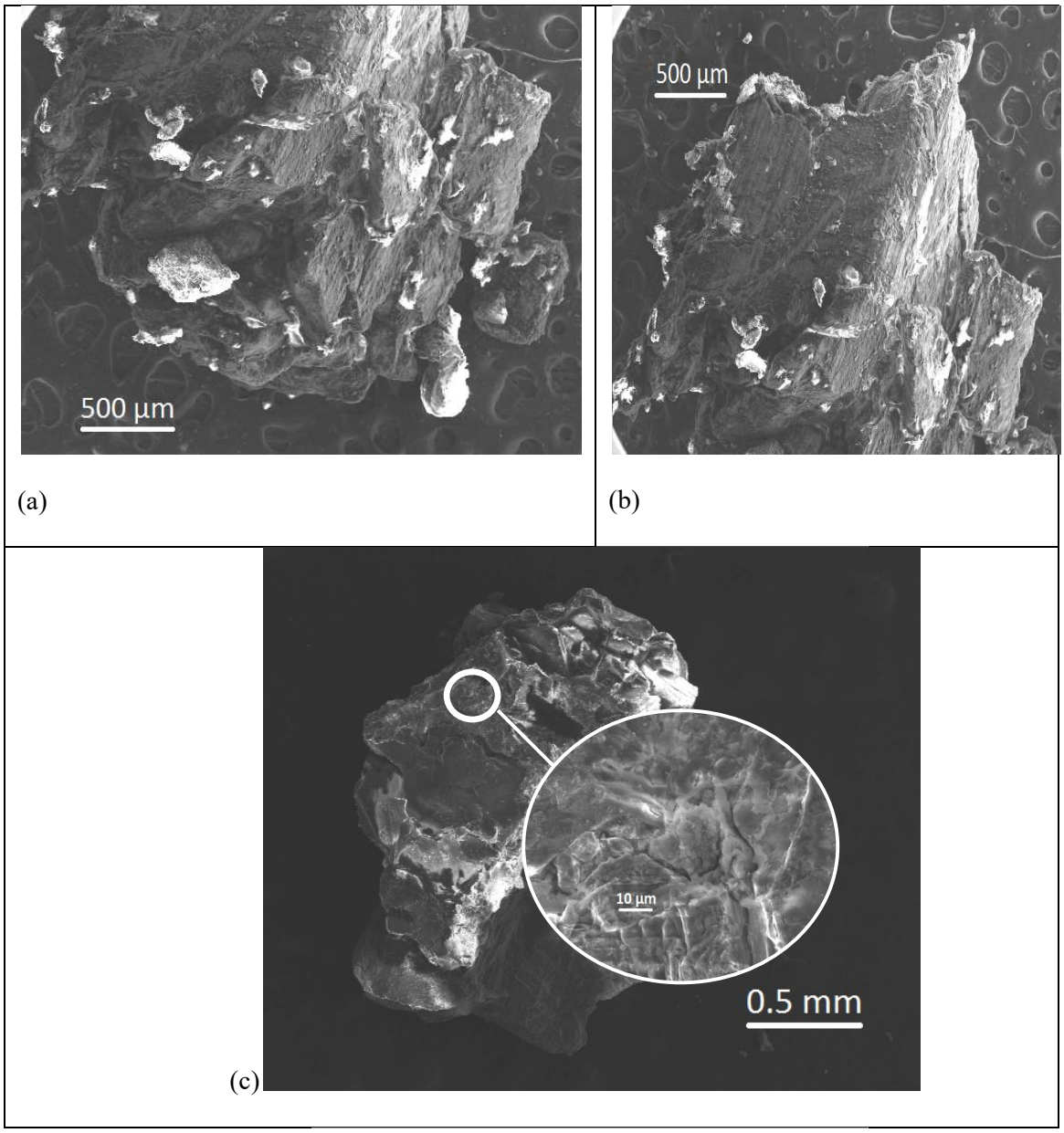

Figure 4.11: Fracture surfaces from expanding ring tests of the swaged ~400 µm NiAl compact made with a 12.7 mm core (a, b). Note the interfacial cracking on these surfaces that are indicative of brittle failure, specifically in the high magnification inset of the fragment from the compact swaged with no core (c).

4.4 Sample analysis with EDX

Energy-dispersive x-ray (EDX) analysis was also performed on the fragments of the nickel-aluminum compacts to study the elemental contents after the expanding ring

tests. It was observed that much of the fragments were covered in carbon and oxides likely from the Primasheet 1000 explosives. The largest fragments that resulted from tests of the NiAl compacts swaged with an 18.8 mm core were discovered to be the least problematic to for EDX analysis. Figure 4.12 is a color-coded result of the EDX analysis on a large segment of the fragment.

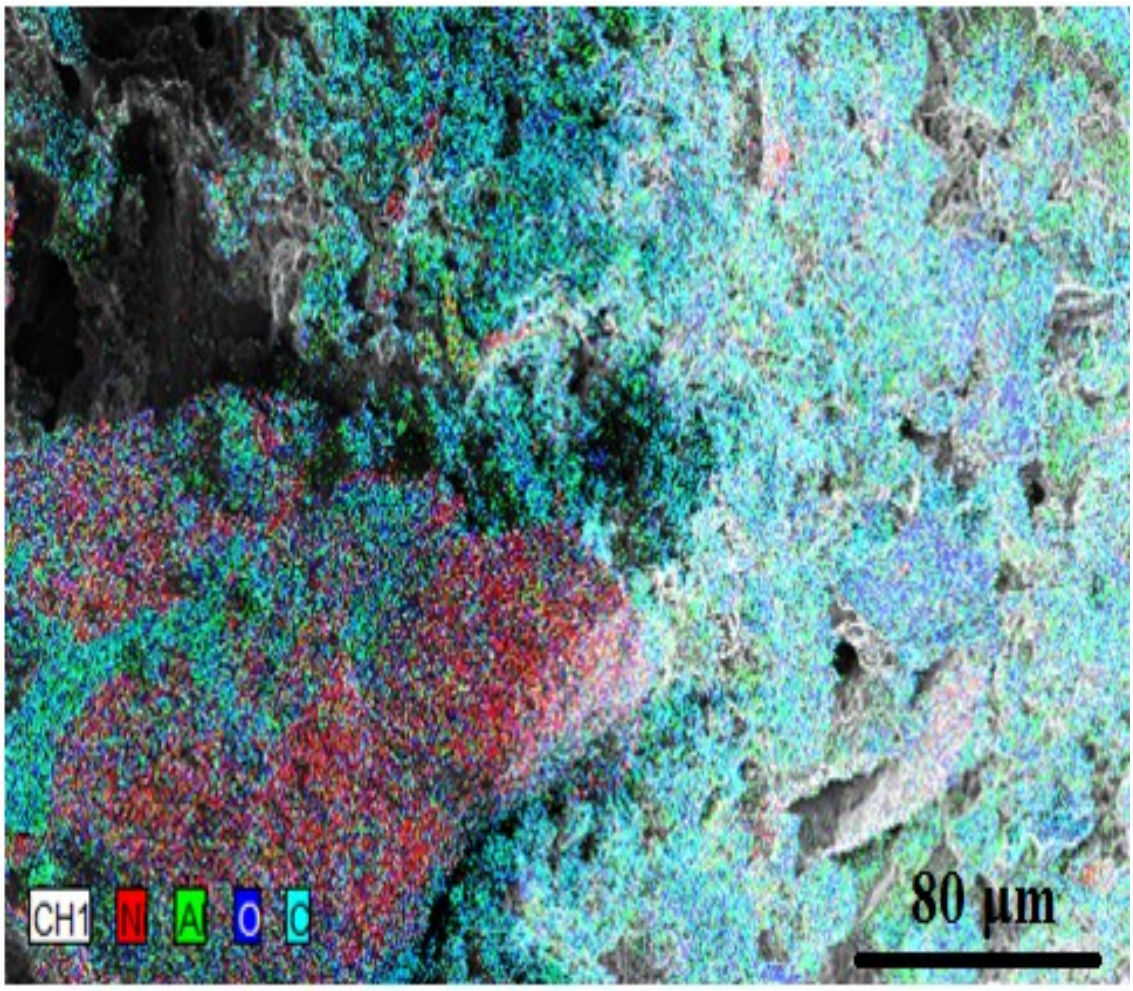

Figure 4.12: EDX of fracture surfaces from expanding ring tests of the swaged ~400 µm NiAl compact made with an 18.8 mm core.

The results of the elemental content analysis are shown in Figure 4.13. As stated previously, it appeared that a majority of the fragments were covered with residue from

the Primasheet 1000 explosive used in the expanding ring tests to exert the velocity outwards and this was confirmed with the results of this analysis. Primasheet 1000 is a rubberized sheet explosive and is pentaerythritrol tetranitrate (PETN) based. PETN is one of the most powerful explosive materials known and its chemical formula is $C_5H_8N_4O_{12}$. So after the explosive was detonated, at the end of the expanding ring test, it is apparent that much of the carbon and oxides from the PETN based explosive landed on the fragments collected around the edge of the steel cylinder in the layer of wax.

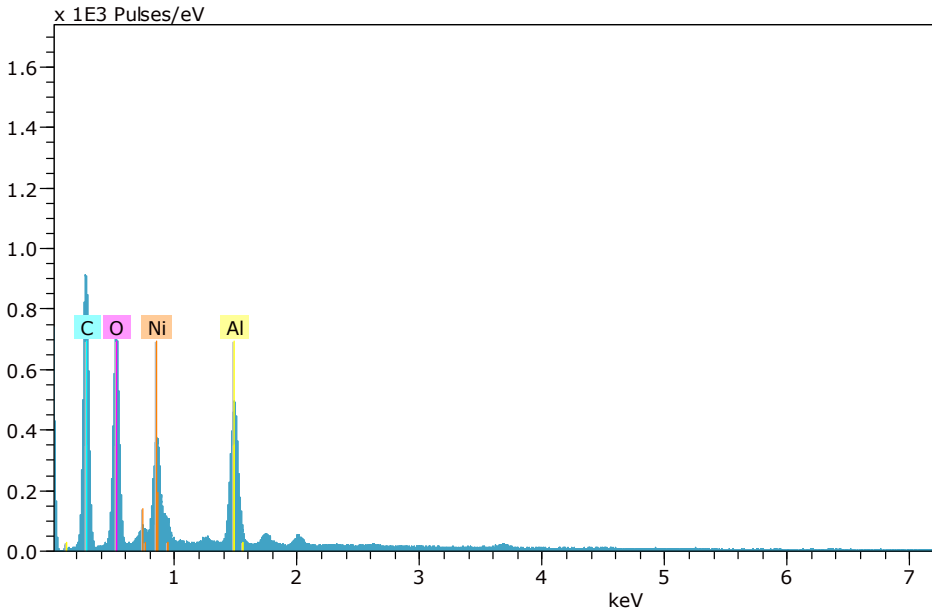

Area 284 Date:4/13/2017 1:25:48 PM HV:10.0kV Puls th.:3.62kcps

El	AN	Series	unn. C [wt.%]	norm. C [wt.%]	Atom. C [at.%]	Error (1 Sigma) [wt.%]
C	6	K-series	30.34	40.96	56.43	3.63
O	8	K-series	22.82	30.81	31.87	2.77
Al	13	K-series	8.36	11.28	6.92	0.40
Ni	28	L-series	12.56	16.95	4.78	1.58
		Total:	74.07	100.00	100.00	

Figure 4.13: EDX results of the elemental content analysis of fracture surfaces from expanding ring tests of the swaged ~400 μm NiAl compact made with an 18.8 mm core.

However, it also observed in these results that there is small but almost even percentage of nickel and aluminum in the large segment of the fragment. Thus, elemental mapping was also performed to characterize the distribution of the fragment. In Figure 4.14 it is shown through elemental mapping that the Ni was concentrated on the large portion of the fragment without many cracks while the Al seemed to have an even distribution throughout the entire fragment. It also helped to confirm that carbon and oxides were covering the entire surfaces of the fragment.

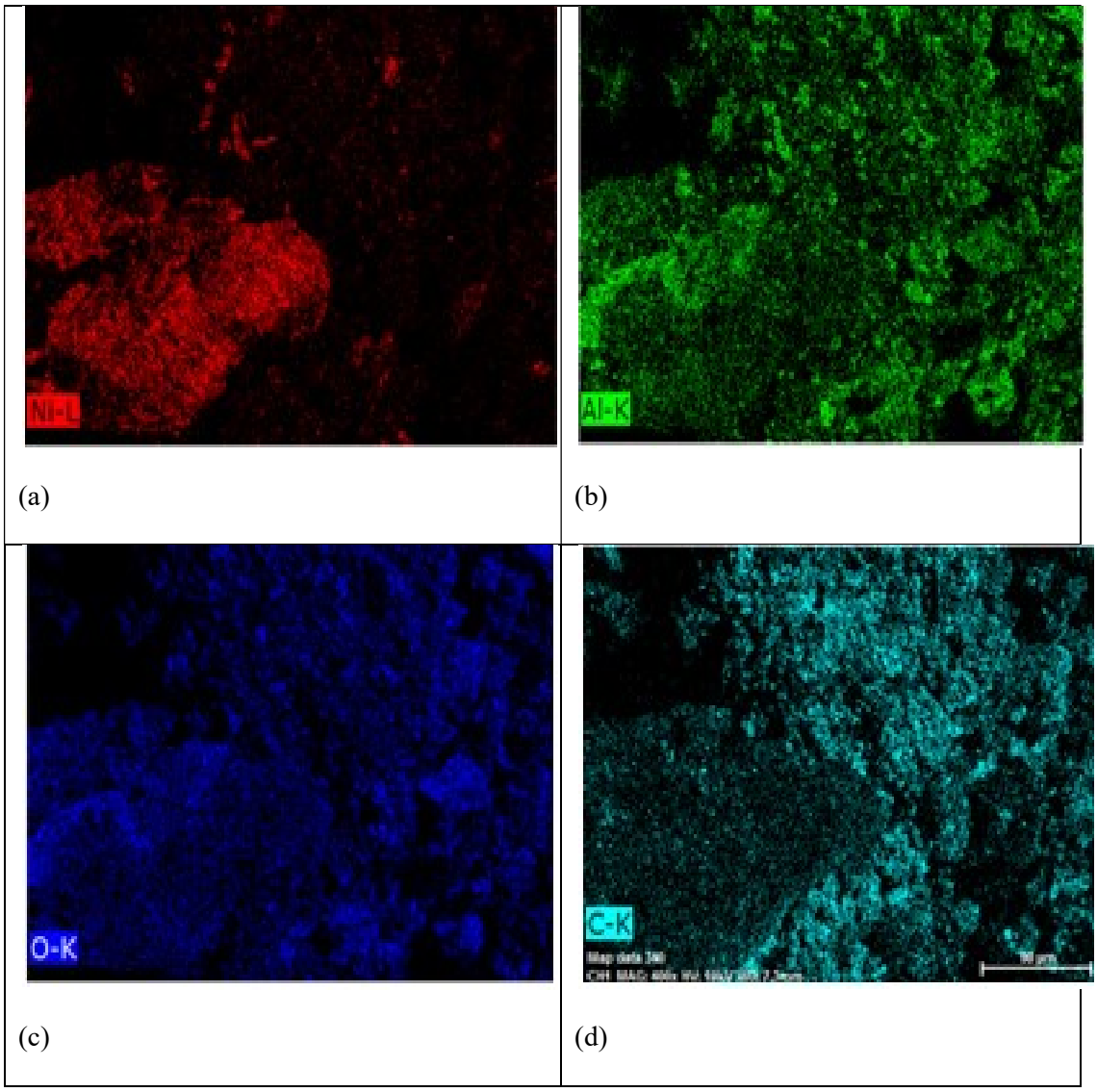

Figure 4.14: EDX mapping results of fracture surfaces from expanding ring tests of the swaged ~400 μm NiAl compact made with an 18.8 mm core.

Next EDX was performed on a small segment on the portion of the fragment without many cracks. The small segment that was analyzed is outlined by the yellow box seen in Figure 4.15. This was the area where the Ni was concentrated in the previous elemental mapping performed on the entire fragment.

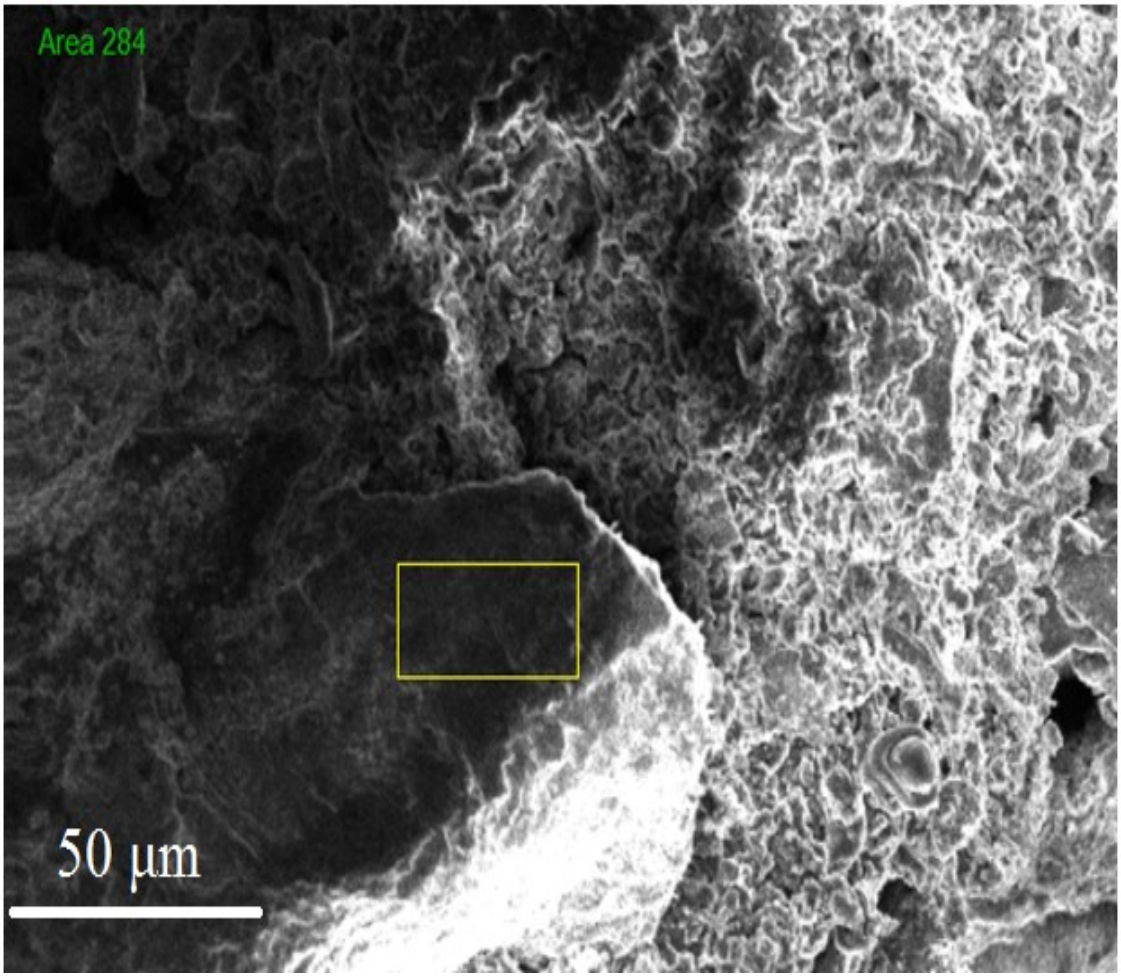

Figure 4.15: EDX of a small segment inside the fracture surfaces from expanding ring tests of the swaged ~400 µm NiAl compact made with an 18.8 mm core.

The results of the elemental content analysis on the small segment are shown in Figure 4.16. The results from this analysis of a smaller portion of a fragment show a much larger percentage of nickel in the area without cracking. This would be understandable as the portions where nickel interspersed more with aluminum should have higher strength and thus be more resistant to fracture. There were also considerable percentages of carbon and oxides as observed in the analysis of a larger portion of the fragment.

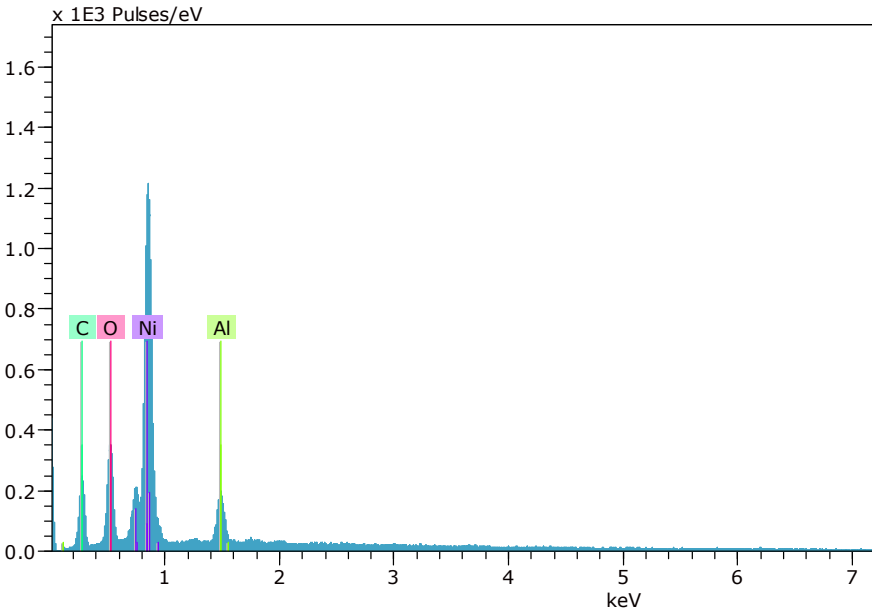

Area 284 Date:4/13/2017 1:34:54 PM HV:10.0kV Puls th.:6.73kcps

El	AN	Series	unn. C [wt.%]	norm. C [wt.%]	Atom. C [at.%]	Error (1 Sigma) [wt.%]
C	6	K-series	17.21	17.38	39.64	2.39
Ni	28	L-series	61.29	61.89	28.90	6.97
O	8	K-series	14.79	14.94	25.58	1.95
Al	13	K-series	5.74	5.80	5.89	0.29
		Total:	99.03	100.00	100.00	

Figure 4.16: EDX results of the elemental content analysis of a small segment inside the fracture surfaces from expanding ring tests of the swaged ~400 μm NiAl compact made with an 18.8 mm core.

Lastly, elemental mapping was also performed in this small segment through EDX. The results of the elemental mapping are shown in Figure 4.17. Aluminum appears to be concentrated in the center of this segment with nickel all around the outsides, in almost a reverse situation of the analysis of a large portion of the fragment. Then carbon and oxides cover the entirety of the segment, as observed with the rest of the fragment, but at least some portion of the fragment was clearly analyzed to give a better understanding of the elemental distribution of the nickel-aluminum fragments.

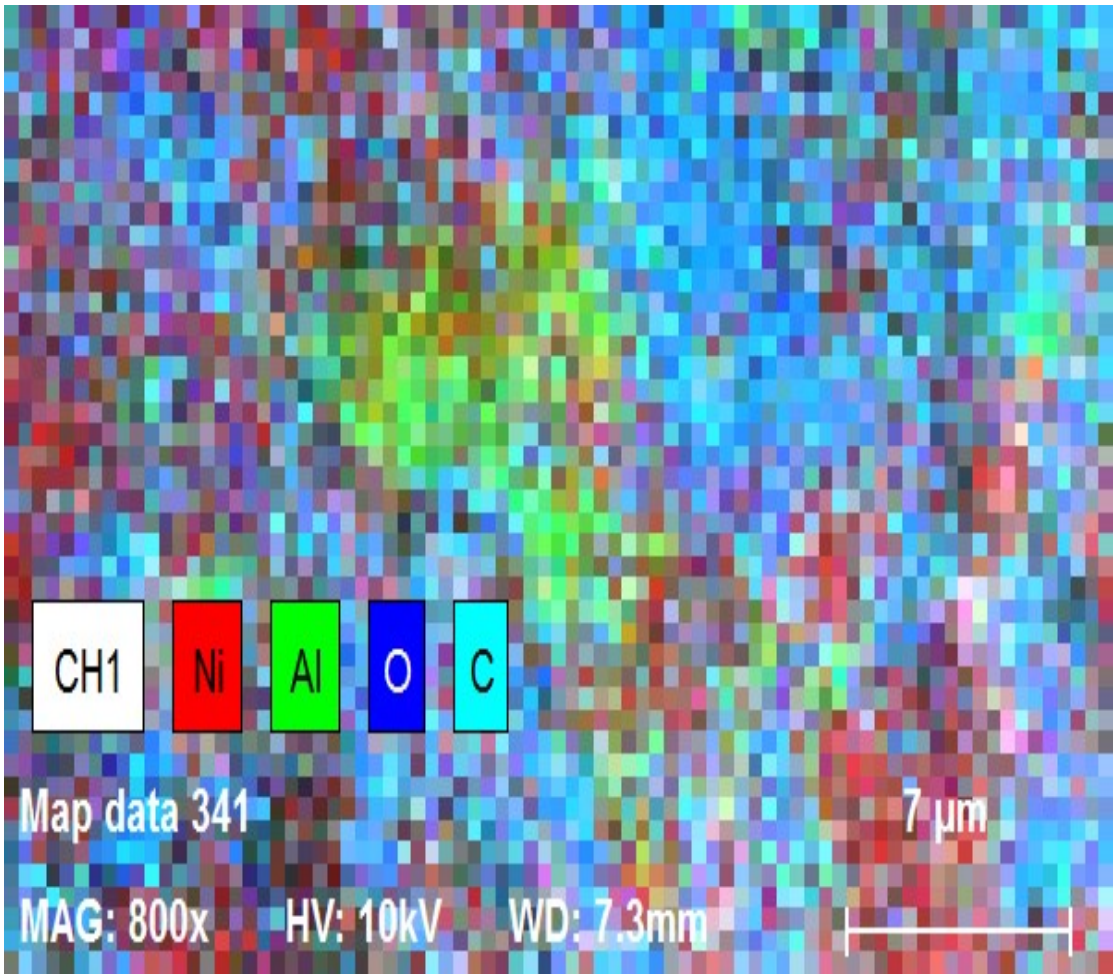

Figure 4.17: EDX mapping of a small segment inside the fracture surfaces from expanding ring tests of the swaged ~400 µm NiAl compact made with an 18.8 mm core.

4.5 Expanding ring experiments

As mentioned previously, there are a number of theories regarding fragmentation, but the two most relevant to this study are the classic Mott and Grady theories. Mott based his theory on the earlier work of Lineau who modeled fragmentation as the random geometric fracture of an infinite one-dimensional body. Mott and Linfoot took the same random geometric fragmentation idea and applied it to a two-dimensional geometric model. He then formulated the prominent fragment distribution law in the form:

$$N(m) = exp\left[-\left(\frac{m}{\mu}\right)^{\frac{1}{2}}\right] \quad (90)$$

where m is the mass and the characteristic mass μ is the distribution scale parameter.

Later Grady and Kipp suggested that if fragmentation can be represented by mechanism-independent statistical descriptions then fragment mass, as opposed to fragment size, is the more fitting random variable. Then they also suggested that the mass of the fragment is distributed over fragment number based on a Poisson process, or binomial if the fragment number is small, similar to the earlier developments of Lineau. From this suggestion they proposed the following linear exponential distribution:

$$N(m) = exp\left[-\left(\frac{m}{\mu}\right)\right] \quad (91)$$

The fragment mass distribution from each expanding ring experiment was analyzed. There are multiple fragment mass distribution laws, but for this analysis the classic Mott and Grady distributions were used. Figure 4.18(a-d) illustrates the comparison of cumulative fragment mass distributions. It is difficult to establish a relationship for the smaller distributions, such as in the case of the 40 and 400 μm aluminum fragments (Figure 4.18a and b), but it is evident in the 100 μm aluminum distributions (Figure 4.18c and d) that the Grady distribution provides a better description of the mass distribution of fragments generated in the expanding ring experiments.

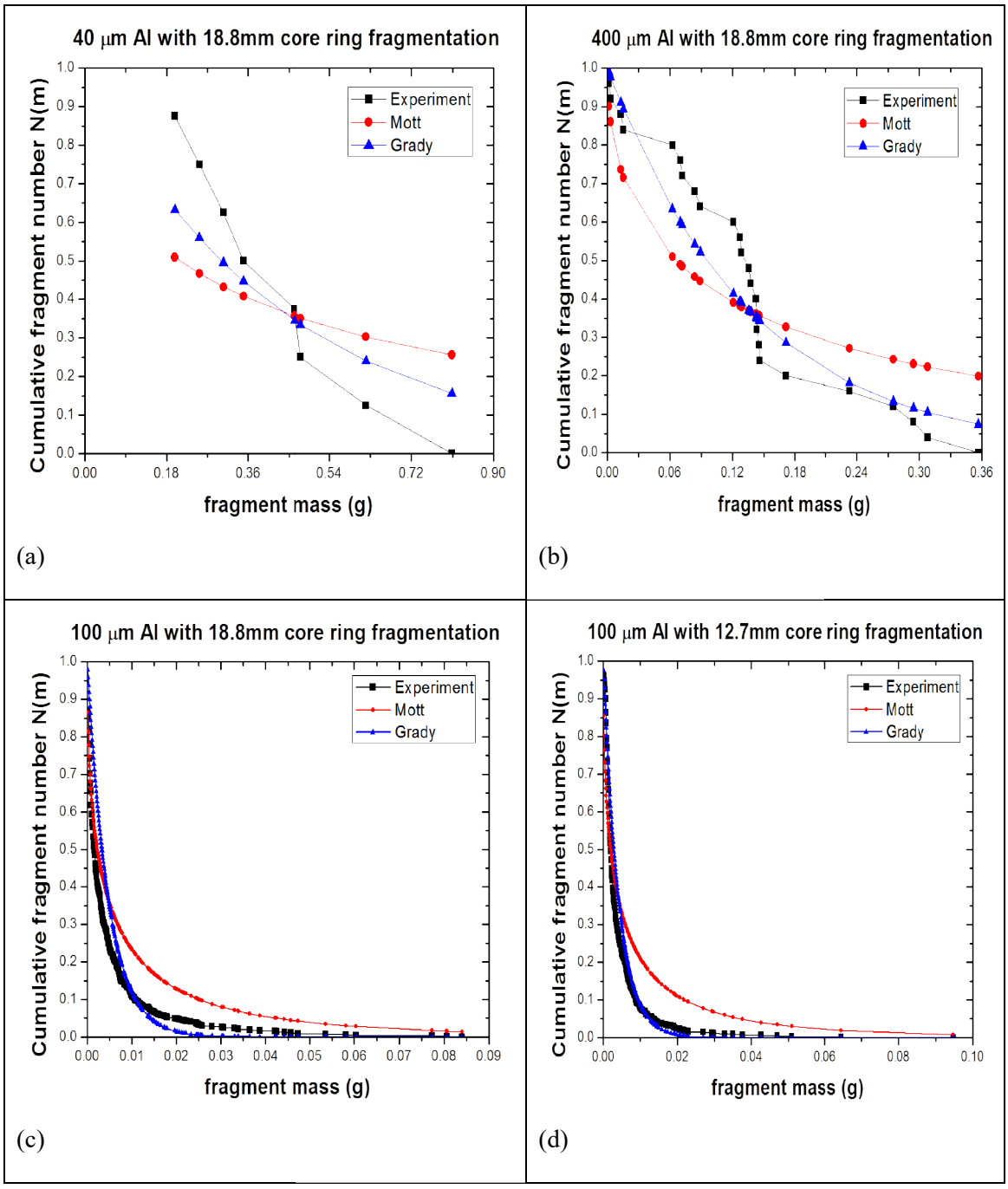

Figure 4.18: Cumulative distribution of fragment masses: comparison of experimental results and theories by Mott and Grady: (a) 40 μm particle compact; (b) 400 μm particle compact; (c) 100 μm with 18.8 mm core compact; (d) 100 μm particle with 12.7 mm core compact.

As described previously, the fragmentation of the rings in the expanding ring experiments was captured with a high speed photography system set up parallel to the cylinder axis. The photographs are shown in Figures 4.19-24. The 40 μm swaged Al powder ring shown fracturing in Figure 4.19 produced the smallest amount of fragments, 8 fragments, but they were the largest size fragments. The next largest size fragments came from the 400 μm swaged Al powder ring shown in Figure 4.20, which fractured into approximately 25 fragments. The 100 μm swaged Al powder ring with a 18.8 mm core fractured into approximately 600 fragments but the magnitude of fragment length was significantly smaller as shown in Figure 4.21(d). The 100 μm swaged Al powder ring with a smaller 12.7 mm core shown fracturing in Figure 4.22 generated almost a hundred more fragments than the ring with a 18.8 mm core, demonstrating an effect of the degree of compaction. Further illustrating this effect of the strength of the interface, the 100 μm swaged Al powder ring with no core shown fracturing in Figure 4.23 generated the most fragments with more than a thousand very small fragments. High speed photographs from an expanding ring experiment of the swaged Ni-Al rings are shown in Figure 4.24. The approximate numbers of fragments from the swaged aluminum experiments are shown in Table 4.1 and the approximate numbers of fragments from the swaged nickel-aluminum experiments are shown in Table 4.2.

Table 4.3: Number of fragments from expanding ring tests of swaged Al compacts.

Compacts	40 µm Al (12.7 mm core)	100 µm Al (No core)	100 µm Al (12.7 mm core)	100 µm Al (18.8 mm core)	400 µm Al (18.8 mm core)
Fragment number	8	~1000	~700	~600	25

Table 4.4: Number of fragments from expanding ring tests of swaged Ni-Al compacts.

Compacts	~400 µm NiAl (No core)	~400 µm NiAl (12.7 mm core)	~400 µm NiAl (18.8 mm core)
Fragment number	~4000	~2500	~1000

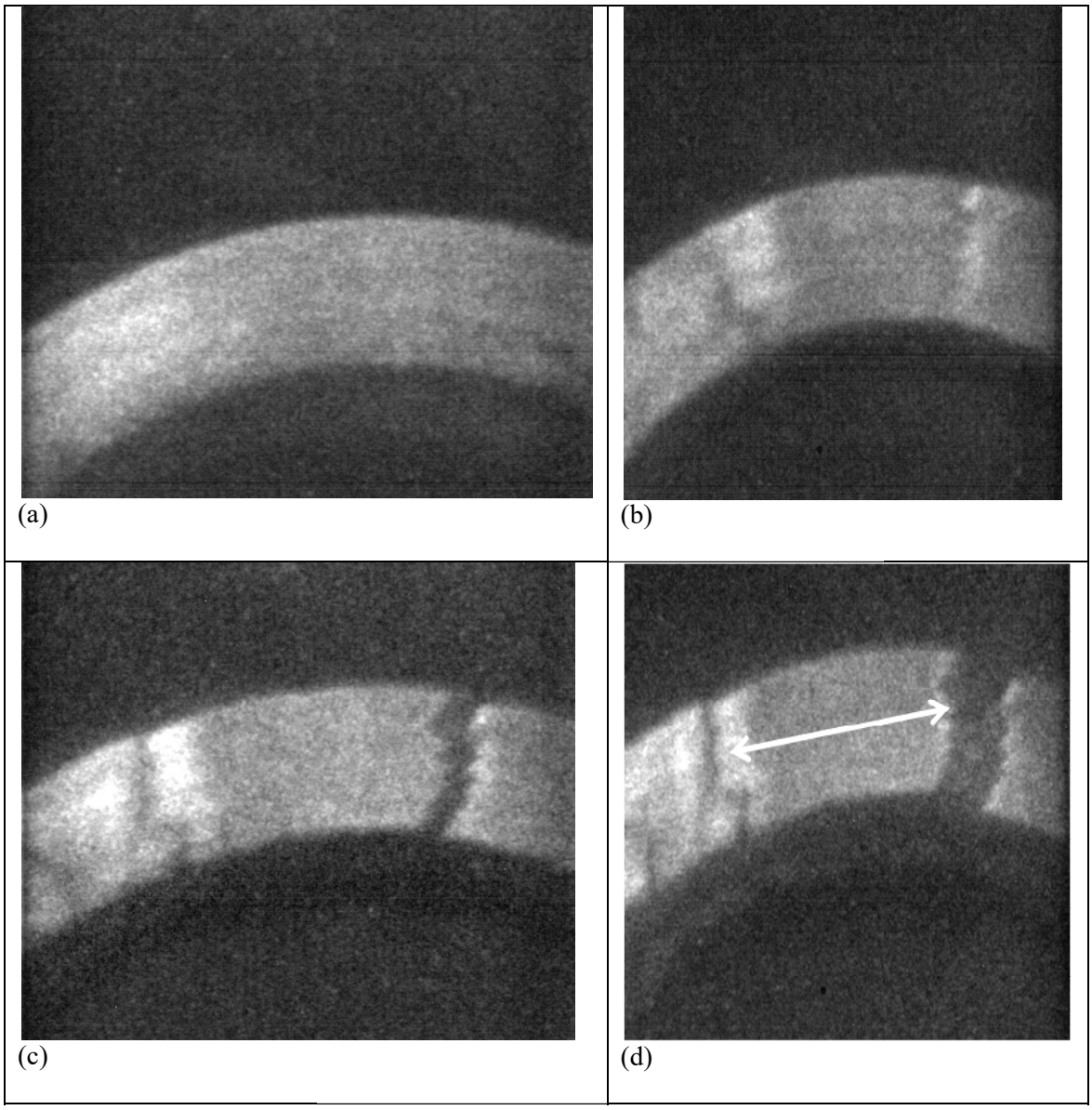

Figure 4.19: Sequence showing initiation of cracking and fragmentation in compact from 40 μm powder. Arrow in (d) provides approximate magnitude of fragment length.

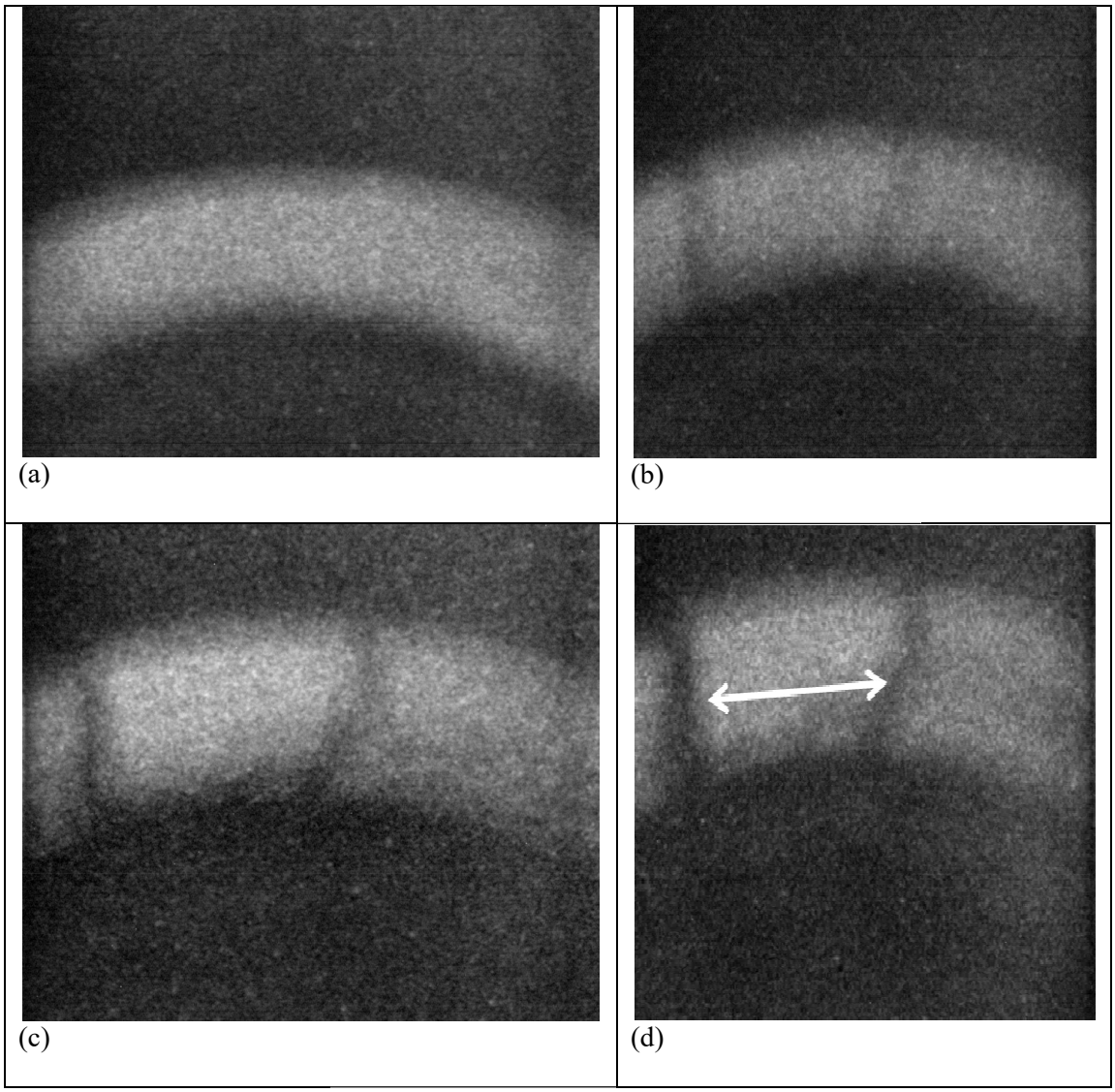

Figure 4.20: Sequence showing initiation of cracking and fragmentation in compact from 400 μm powder. Arrow in (d) provides approximate magnitude of fragment length.

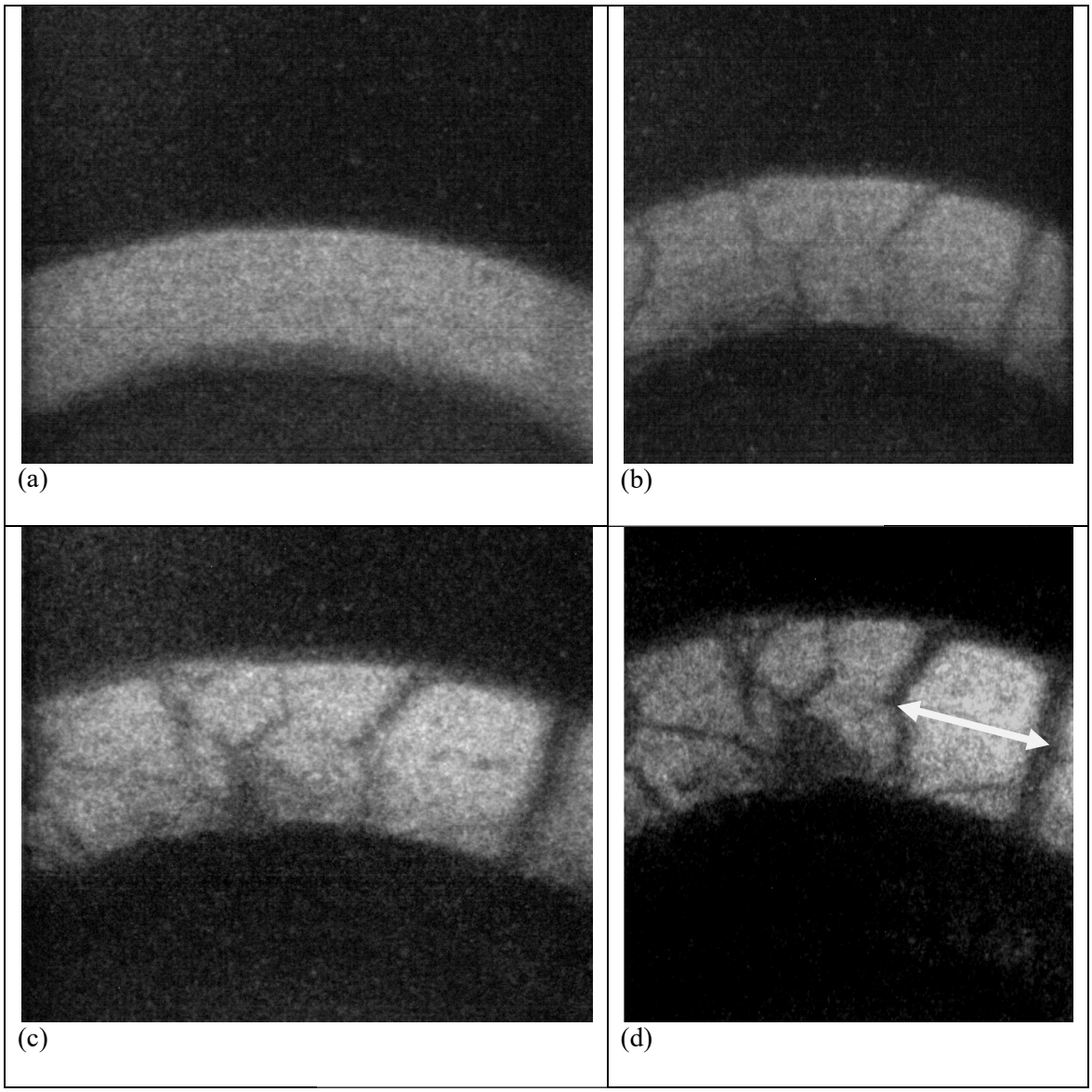

Figure 4.21: Sequence showing initiation of cracking and fragmentation in compact from 100 μm powder with a 18.8 mm core. Arrow in (d) provides approximate magnitude of fragment length.

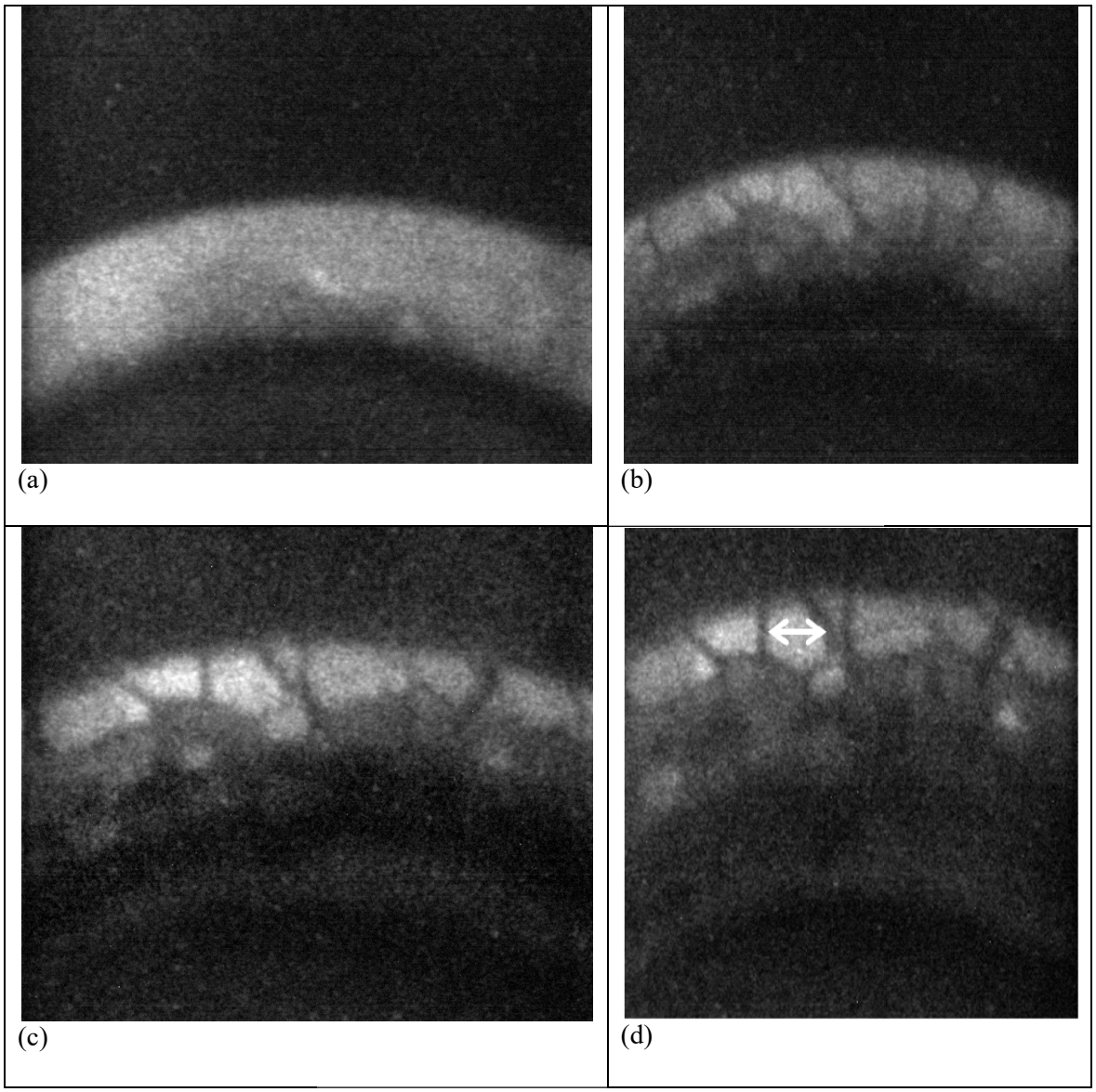

Figure 4.22: Sequence showing initiation of cracking and fragmentation in compact from 100 μm powder with a 12.7 mm core. Arrow in (d) provides approximate magnitude of fragment length.

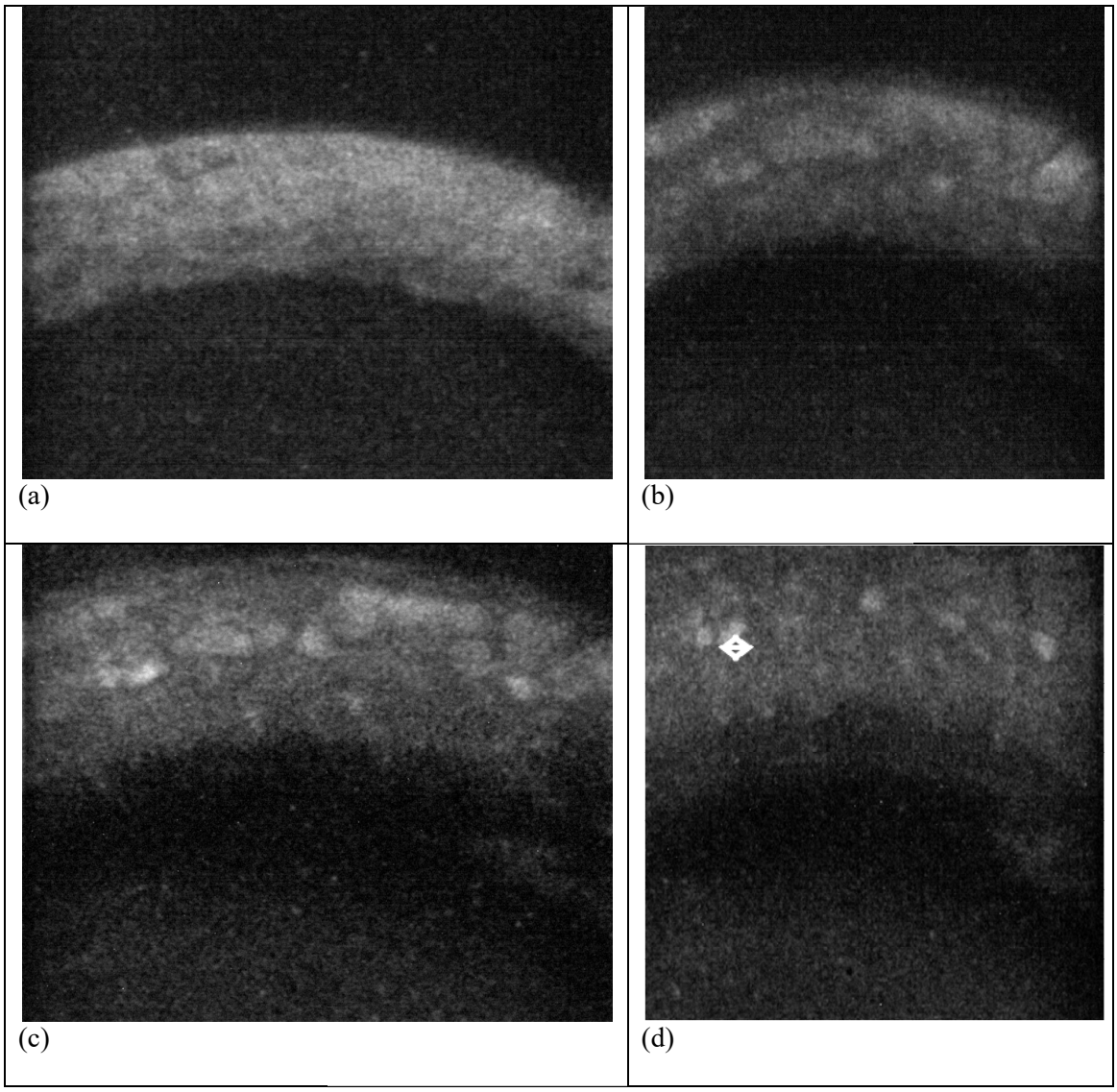

Figure 4.23: Sequence showing initiation of cracking and fragmentation in compact from 100 μm powder with no core. Arrow in (d) provides approximate magnitude of fragment length.

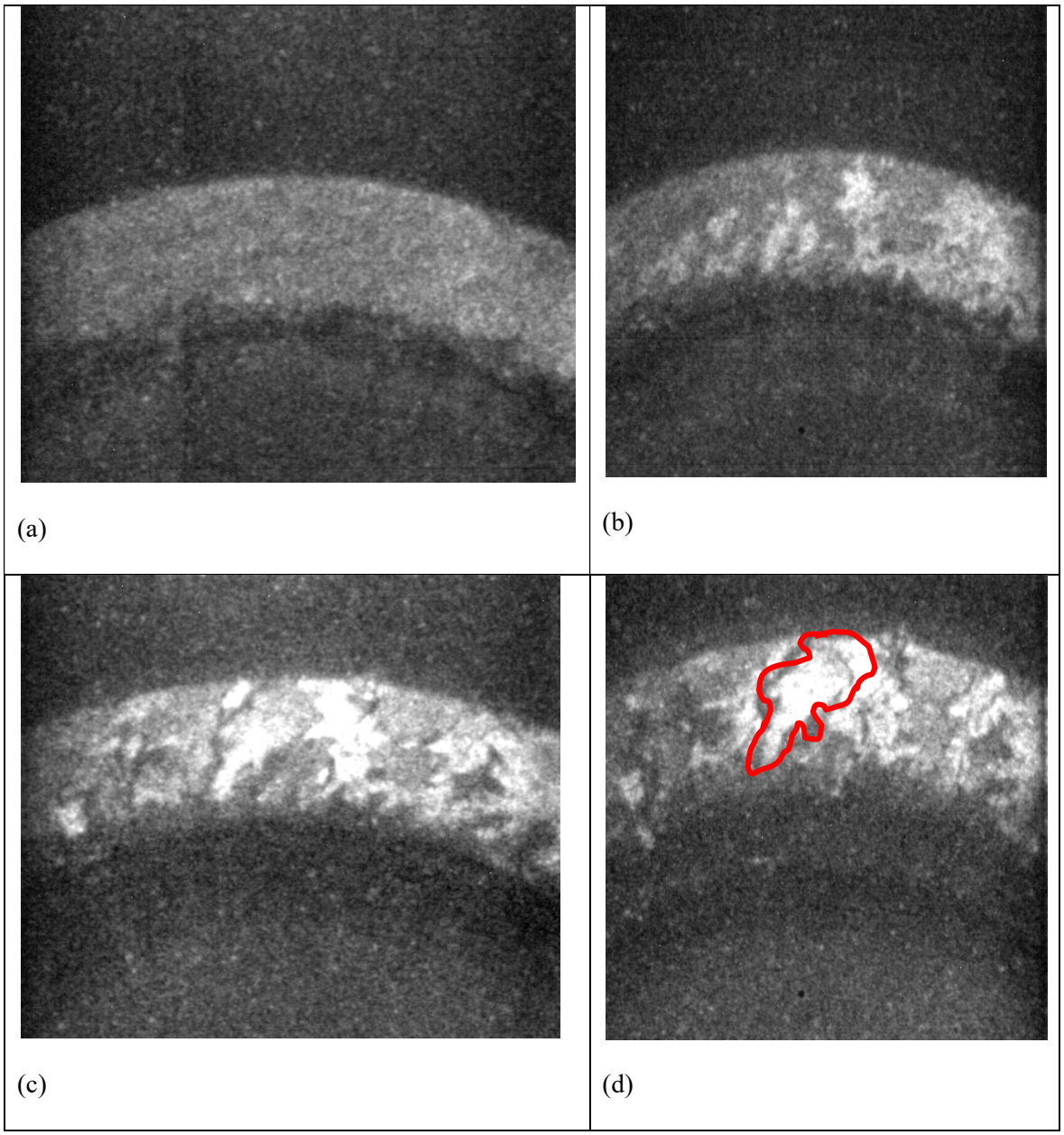

Figure 4.24: Sequence showing initiation of cracking and fragmentation in an expanding ring test of the swaged NiAl compact. One of the largest fragments that resulted from this test is outlined in the final photograph (d) of the sequence.

4.6 Fragmentation analysis

Mott and Linfoot [39] proposed, in 1943, a simple theory for the prediction of mean fragment sizes based on an energy balance, akin to the Griffith [106] theory for crack propagation. Although many more complex analyses have been developed since then, the Mott equation will be presented here, with a slight modification. The basic derivation of the Mott-Linfoot equation is presented first. Figure 4.25 shows an expanding ring expanding and fragmenting; a segment of size a just prior to fragmentation is shown in Figure 4.25(b). The radial velocity is V_l. Since the ring is expanding, the extremities also have a tangential velocity V_t. The arc has an angle α and therefore we have the following, after the arc has expanded to r+dr:

$$V_l = \frac{dr}{dt} \tag{92}$$

$$V_t = \frac{da}{2dt} \tag{93}$$

Thus:

$$V_t = \frac{daV_l}{2dr} \tag{94}$$

But:

$$a = \alpha r \tag{95}$$

$$da = \alpha dr \tag{96}$$

By substituting Equation 89 into Equation 87 we find:

$$V_t = \frac{\alpha V_l}{2} \tag{97}$$

These are the velocities of both the upper and lower edges of the segment of size a. The kinetic energy due to the expansion of the ring can be expressed, if one considers an origin moving with the fragment, can be calculated, per unit of length parallel to the axis

of the disk. We define an angle θ that is marked in Figure 4.25. The velocity varies with increasing θ as:

$$V_t = \frac{\theta V_l}{2} \tag{98}$$

The mass per unit of length along the axis of a sliver defined by dθ is expressed as:

$$dm = \rho t r d\theta \tag{99}$$

Where t is the thickness of the ring, rdθ is the length of the sliver, and ρ is the density of the material. Thus, the kinetic energy is:

$$dE_k = \frac{1}{2}\rho t r \frac{\theta^2 {V_l}^2}{4} d\theta \tag{100}$$

The total kinetic energy for the entire segment is obtained by integrating from –α/2 to +α/2:

$$E_k = \int_{-\alpha/2}^{+\alpha/2} dE_k = \int_{-\alpha/2}^{+\alpha/2} \frac{1}{2}\rho t r \frac{\theta^2 {V_l}^2}{4} d\theta = \frac{1}{24}\rho t r {V_l}^2 \alpha^3 \tag{101}$$

Mott [39] made the simple assumption that the kinetic energy was converted into the energy to generate two cracks at the extremities of the fragment. Since the number of cracks is equal to the number of fragments, only one crack has to be considered per fragment. Here we replace Mott and Linfoot's energy per unit area required to form a crack by the energy release rate, G, which expresses the same. For a thickness t:

$$\frac{1}{24}\rho t \quad {}_l{}^2 \alpha^3 = Gt \tag{102}$$

The fracture toughness, K_{Ic}, is introduced through the simple relationship:

$$G = \frac{K_{Ic}^2}{E} \tag{103}$$

Thus, the fragment size can be obtained, by substituting Equation 88 into Eqn. 95:

$$a = \left(\frac{24r^2K_{Ic}^2}{{V_l}^2\rho E}\right)^{1/3} \tag{104}$$

The introduction of the strain energy (a potential energy term) into the Mott theory can be simply effected through the addition of:

$$E_p = \left(\frac{1}{2}\sigma_y\varepsilon\right)at \tag{105}$$

By using Hooke's law, since the plastic energy is not recoverable:

$$E_p = \frac{{\sigma_y}^2}{2E}at \tag{106}$$

Adding Equation 99 to the first term of Equation 95 we arrive at:

$$a^3 + \frac{24r^2{\sigma_y}^2}{2{V_l}^2\rho E}a - \frac{24r^2K_{Ic}^2}{{V_l}^2\rho E} = 0 \tag{107}$$

The solution of this incomplete third order equation ($a^3 + pa + q = 0$) by Cardano's method gives the following only real root:

$$a = \left(-\frac{q}{2} + D^{1/2}\right)^{1/3} + \left(-\frac{q}{2} - D^{1/2}\right)^{1/3} \tag{108}$$

Where:

$$D = \left(\frac{p}{3}\right)^3 + \left(\frac{q}{2}\right)^2 \tag{109}$$

We apply Equation 101 to aluminum rings, keeping in mind that the tailored microstructures introduced by compaction and swaging of the powders reduces the fracture toughness significantly from the original value of` 60 MPam$^{1/2}$, which can be assumed for annealed 1100 aluminum. We take different values:

K_{Ic}: 100, 50, 10, 5, and 1 MPam$^{1/2}$.

V_l=100 and 500 m/s

E=70 GPa

$\rho=2.7\ x10^{3}\ kg/m^{3}$

$r=12x10^{-3}\ m$

One factor to consider is that, once the fragment size becomes smaller than t, the ring thickness, fragments tend to become equiaxed and the equations no longer apply. A conversion to fragment mass is in order at this point. One can set, to a first approximation, $mass=\rho a^{3}$.

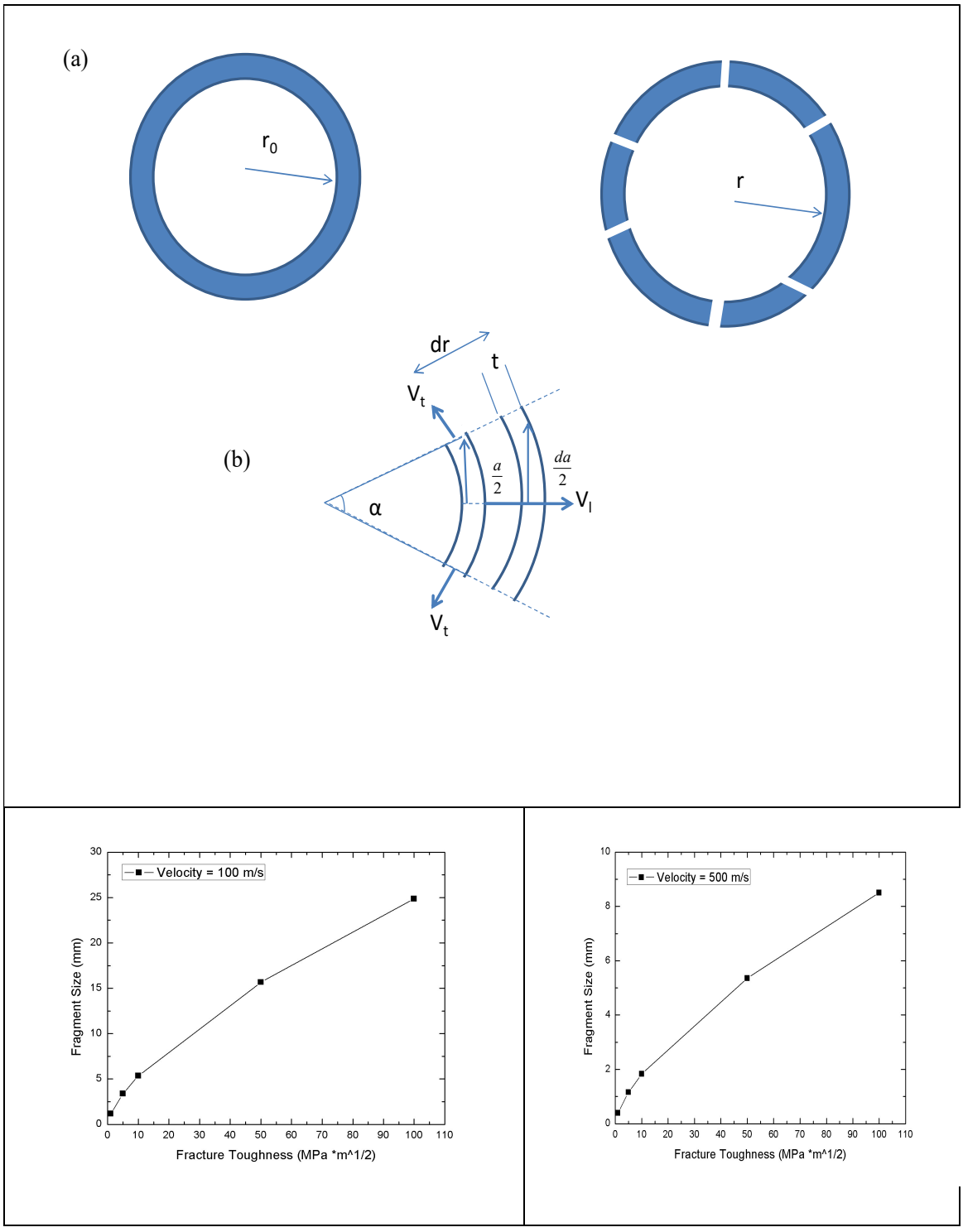

Figure 4.25: Analysis of fragmentation following Mott: (a) fragmentation of ring into segments; (b) segment of ring with parameters used in derivation; (c) predictions of modified Mott theory: fragment size as a function of fracture toughness for aluminum at two velocities: V_l=100 and 500m/s.

The fracture toughness for each of the swaged compacts was determined using the procedure described in section 3.4. Some of the high speed stills used to create the crack mouth opening displacement (CMOD) record are shown in Figures 4.26-31. The force-CMOD records from the fracture toughness tests are shown in Figure 4.32 and Figure 4.33. Thus once a fracture toughness value is attained it can be used with other experimentally determined values in Eqn. 101 to predict a mean fragment size. The calculated fracture toughness values and experimentally measured mean fragment sizes for each of the compacts are shown in Table 4.3 and Table 4.4.

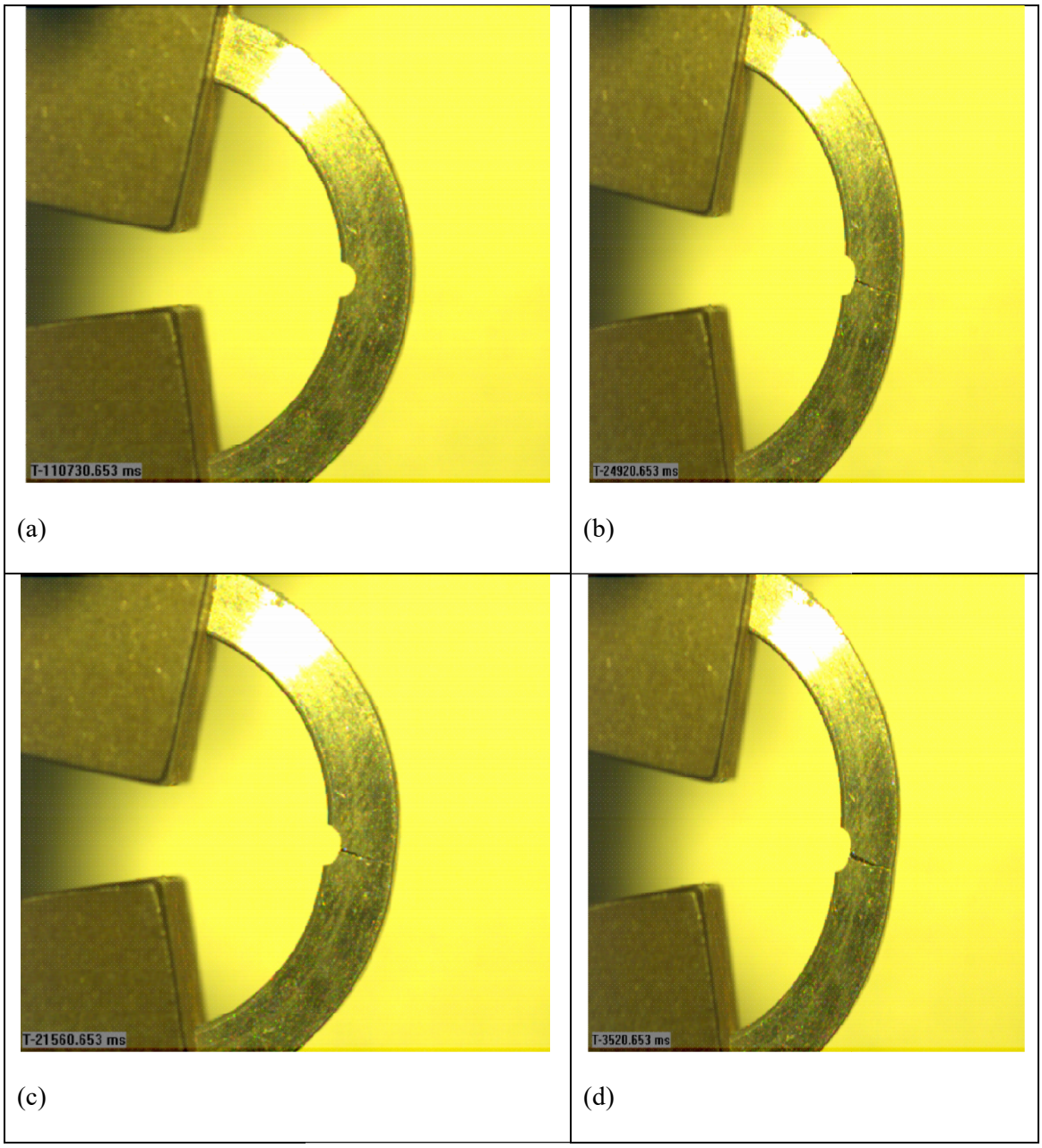

Figure 4.26: Several frames from the high-speed recording of the fracture toughness test of swaged ~40 micron powder aluminum ring with the loading fixtures attached at the top and bottom of the specimen: (a) frame captured from the beginning of the test; (b) frame captured at the onset of fracture; (c) frame captured just before complete fracture and failure; (d) frame showing the end of the test.

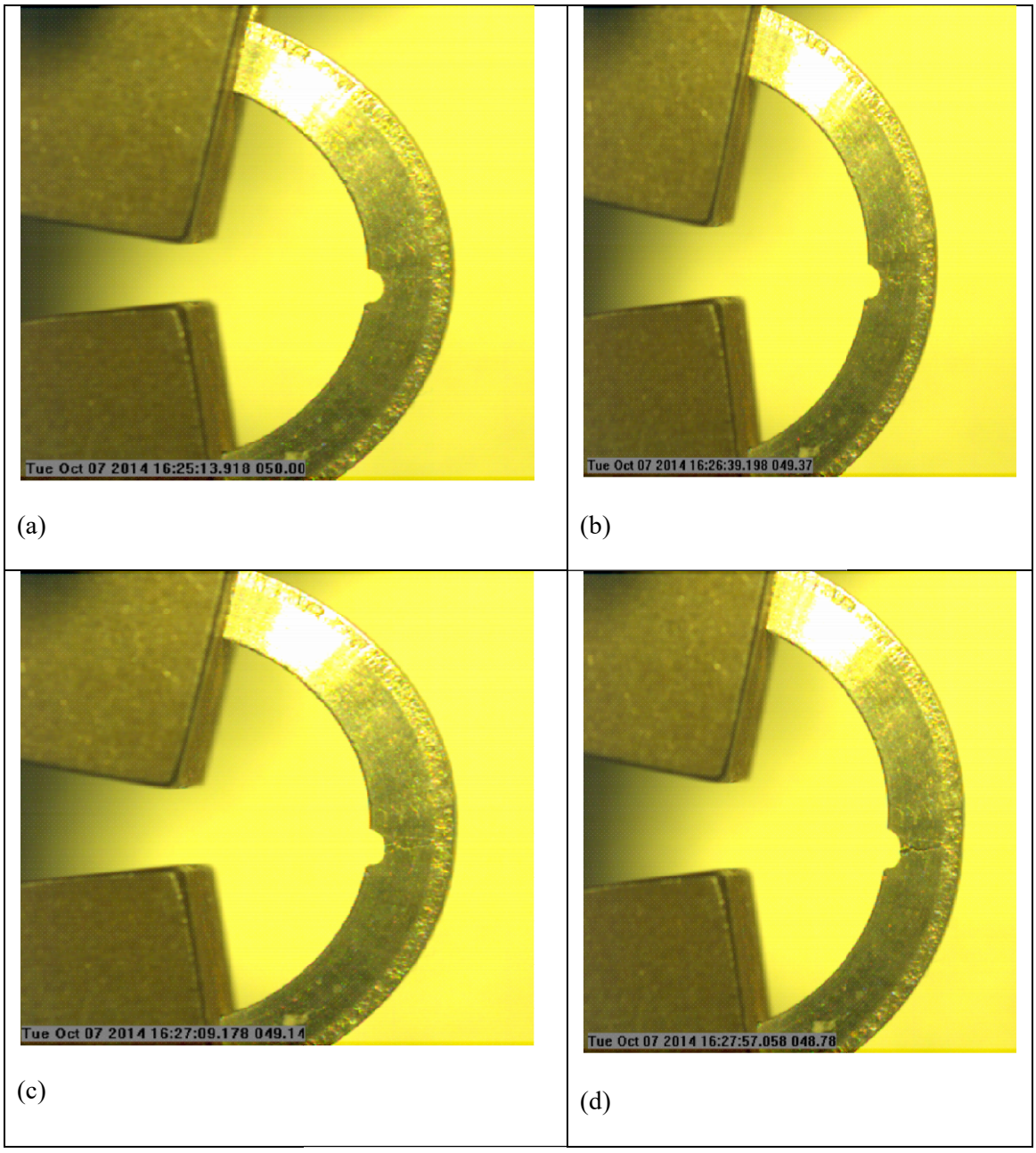

Figure 4.27: Several frames from the high-speed recording of the fracture toughness test of swaged ~400 micron powder aluminum ring with the loading fixtures attached at the top and bottom of the specimen: (a) frame captured from the beginning of the test; (b) frame captured at the onset of fracture; (c) frame captured just before complete fracture and failure; (d) frame showing the end of the test.

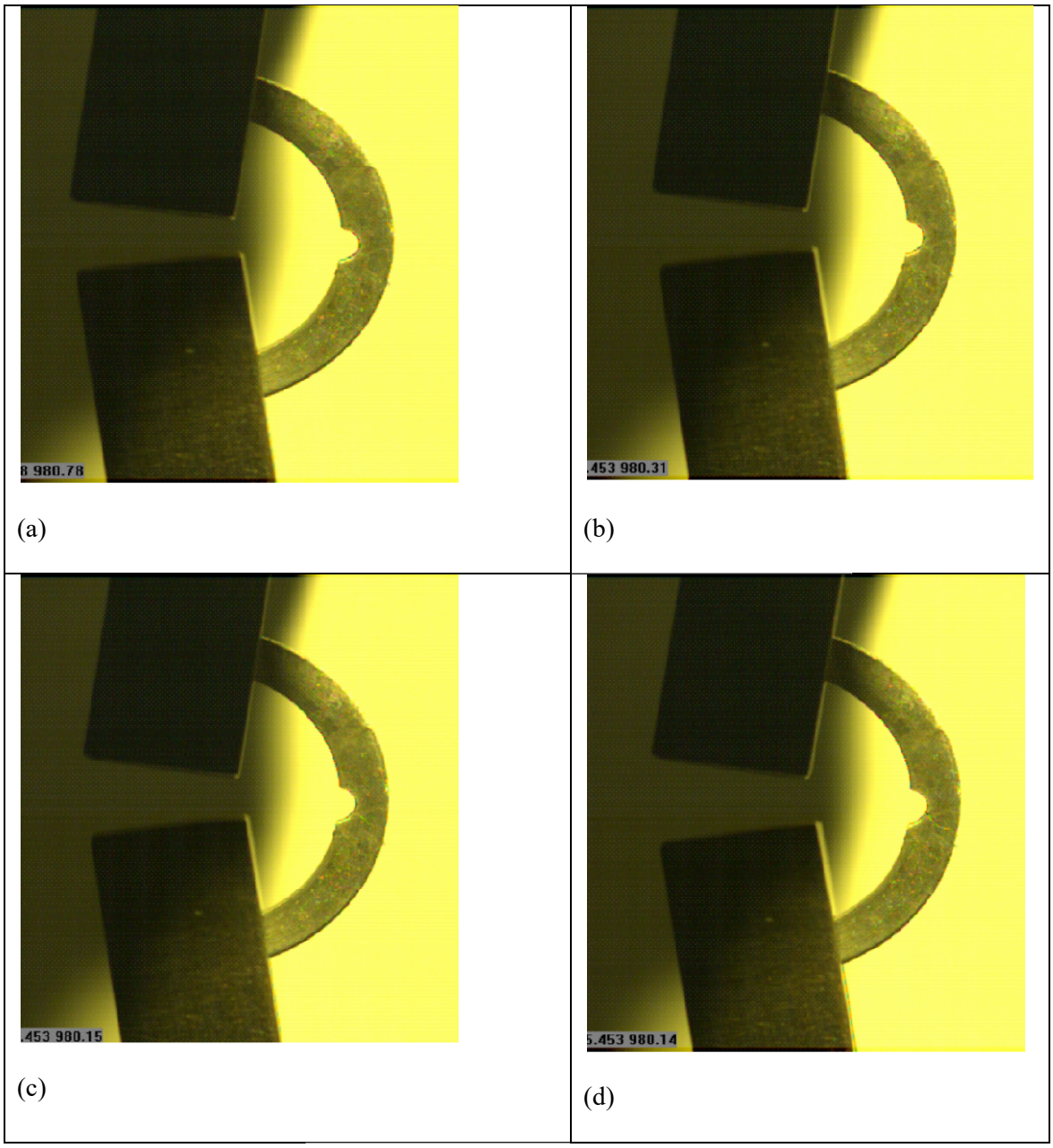

Figure 4.28: Several frames from the high-speed recording of the fracture toughness test of ~100 micron powder (swaged with no core) ring with the loading fixtures attached at the top and bottom of the specimen: (a) frame captured from the beginning of the test; (b) frame captured at the onset of fracture; (c) frame captured just before complete fracture and failure; (d) frame showing the end of the test.

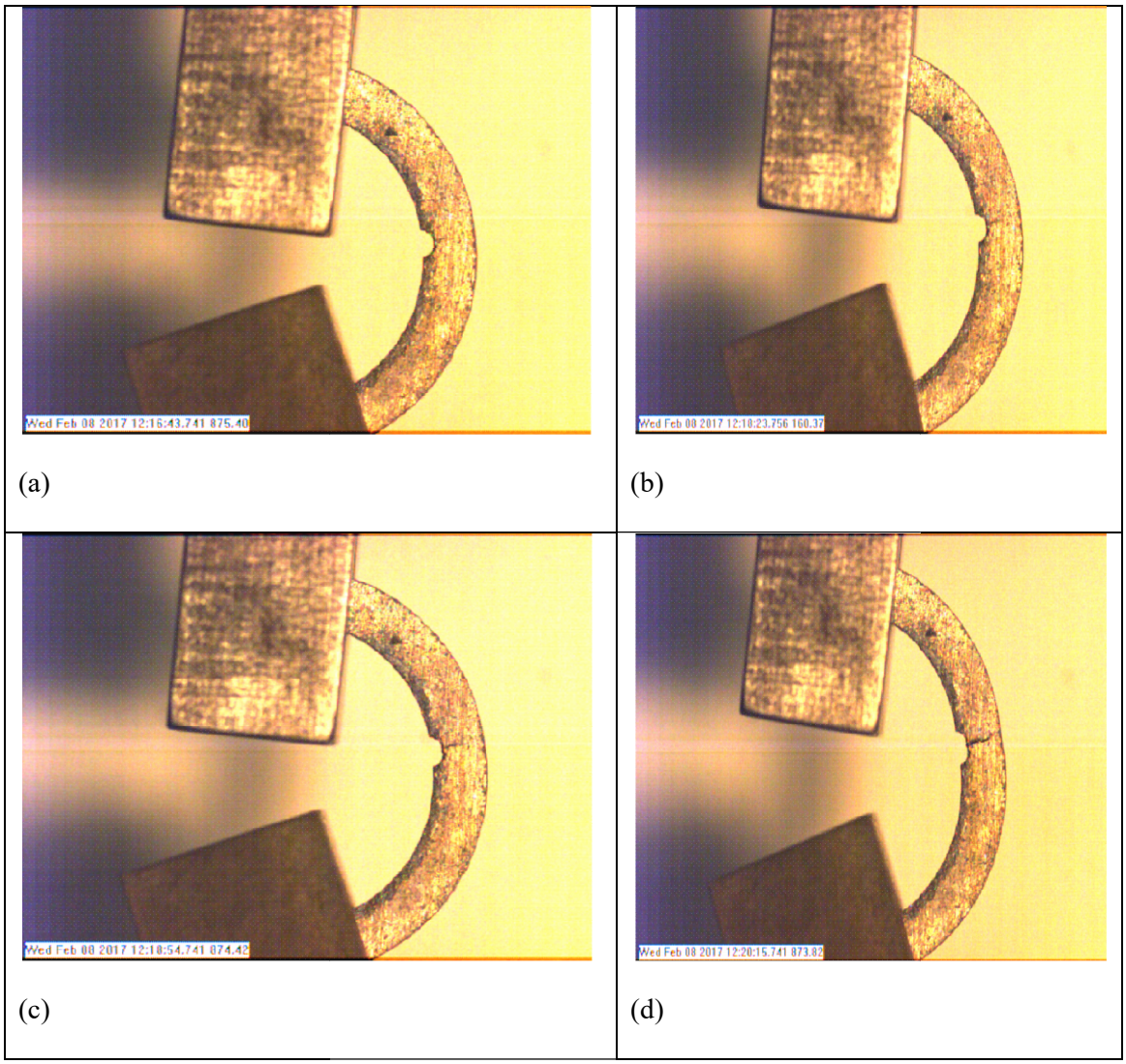

Figure 4.29: Several frames from the high-speed recording of the fracture toughness test of a ~400 micron nickel-aluminum powder (swaged with no core) ring with the loading fixtures attached at the top and bottom of the specimen: (a) frame captured from the beginning of the test; (b) frame captured at the onset of fracture; (c) frame captured just before complete fracture and failure; (d) frame showing the end of the test.

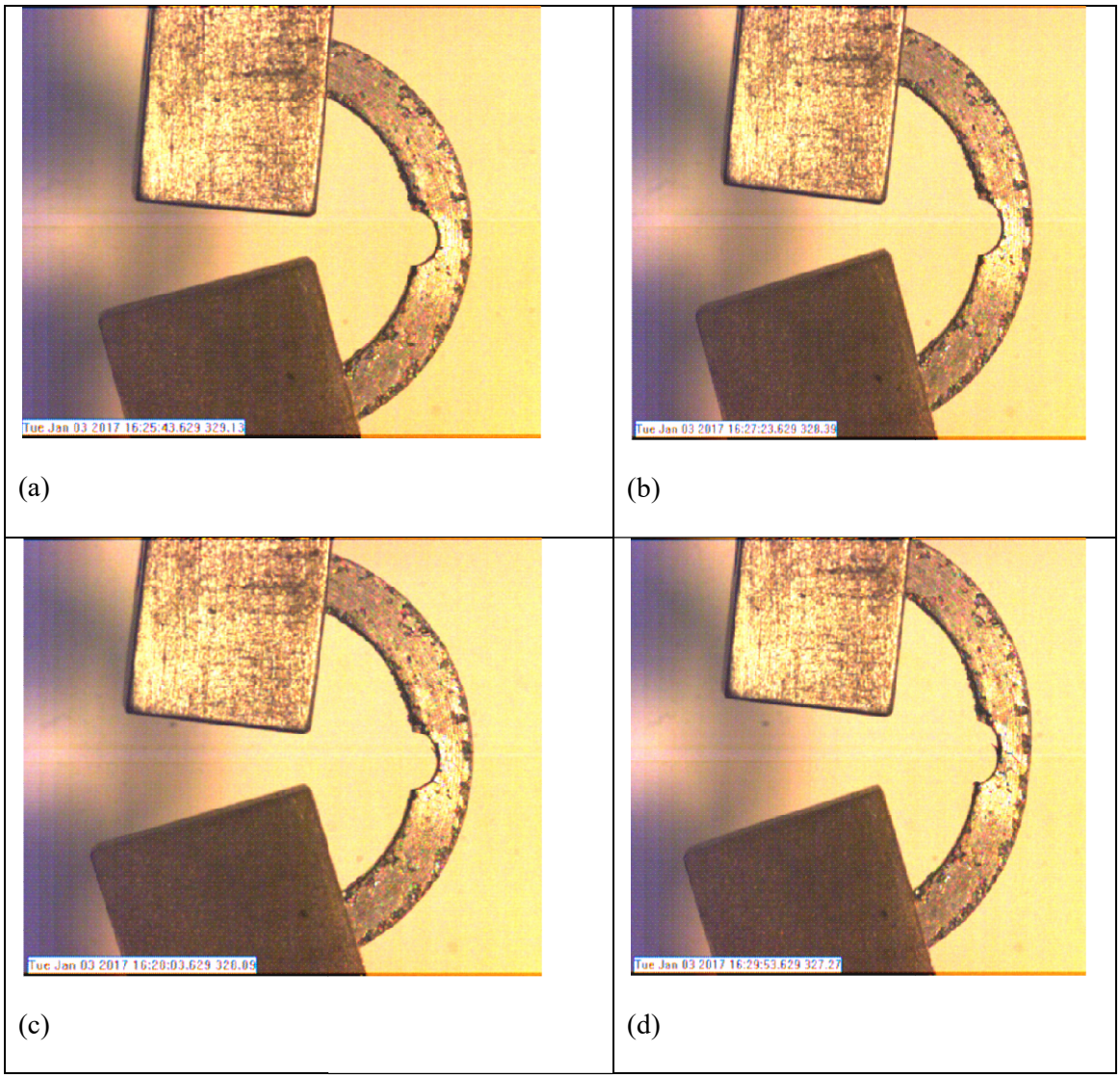

Figure 4.30: Several frames from the high-speed recording of the fracture toughness test of a ~400 micron nickel-aluminum powder (swaged with 12.7 mm core) ring with the loading fixtures attached at the top and bottom of the specimen: (a) frame captured from the beginning of the test; (b) frame captured at the onset of fracture; (c) frame captured just before complete fracture and failure; (d) frame showing the end of the test.

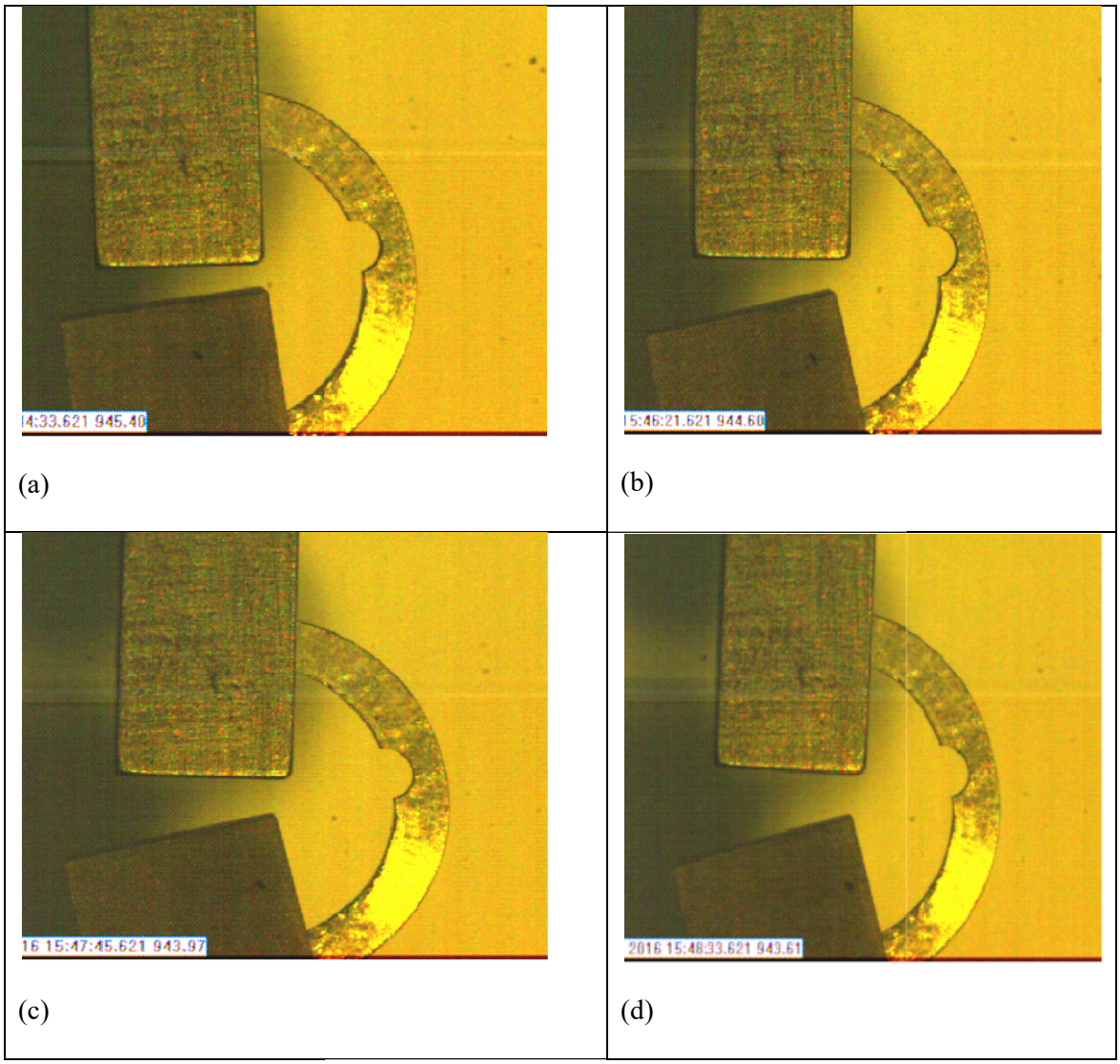

Figure 4.31: Several frames from the high-speed recording of the fracture toughness test of a ~400 micron nickel-aluminum powder (swaged with 18.8 mm core) ring with the loading fixtures attached at the top and bottom of the specimen: (a) frame captured from the beginning of the test; (b) frame captured at the onset of fracture; (c) frame captured just before complete fracture and failure; (d) frame showing the end of the test.

Table 4.5: Measured fracture toughness values and predicted and measured mean fragment sizes for the different compacts.

Compacts	40 μm Al (12.7 mm core)	100 μm Al (No core)	100 μm Al (12.7 mm core)	100 μm Al (18.8 mm core)	400 μm Al (18.8 mm core)
Fracture toughness value ($MPa*m^{1/2}$)	3.04	0.12	0.59	0.75	3.90
Predicted mean fragment size (mm)	2.10	0.01	0.30	0.40	2.70
Experimental mean fragment size (mm)	8.03	0.53	0.43	0.39	3.67

Table 4.6: Measured fracture toughness values and predicted and measured mean fragment sizes for the different Ni-Al compacts.

Compacts	~400 μm NiAl (No core)	~400 μm NiAl (12.7 mm core)	~400 μm NiAl (18.8 mm core)
Fracture toughness value ($MPa*m^{1/2}$)	0.17	0.39	0.67
Predicted mean fragment size (mm)	0.006	0.014	0.039
Experimental mean fragment size (mm)	0.01	0.02	0.04

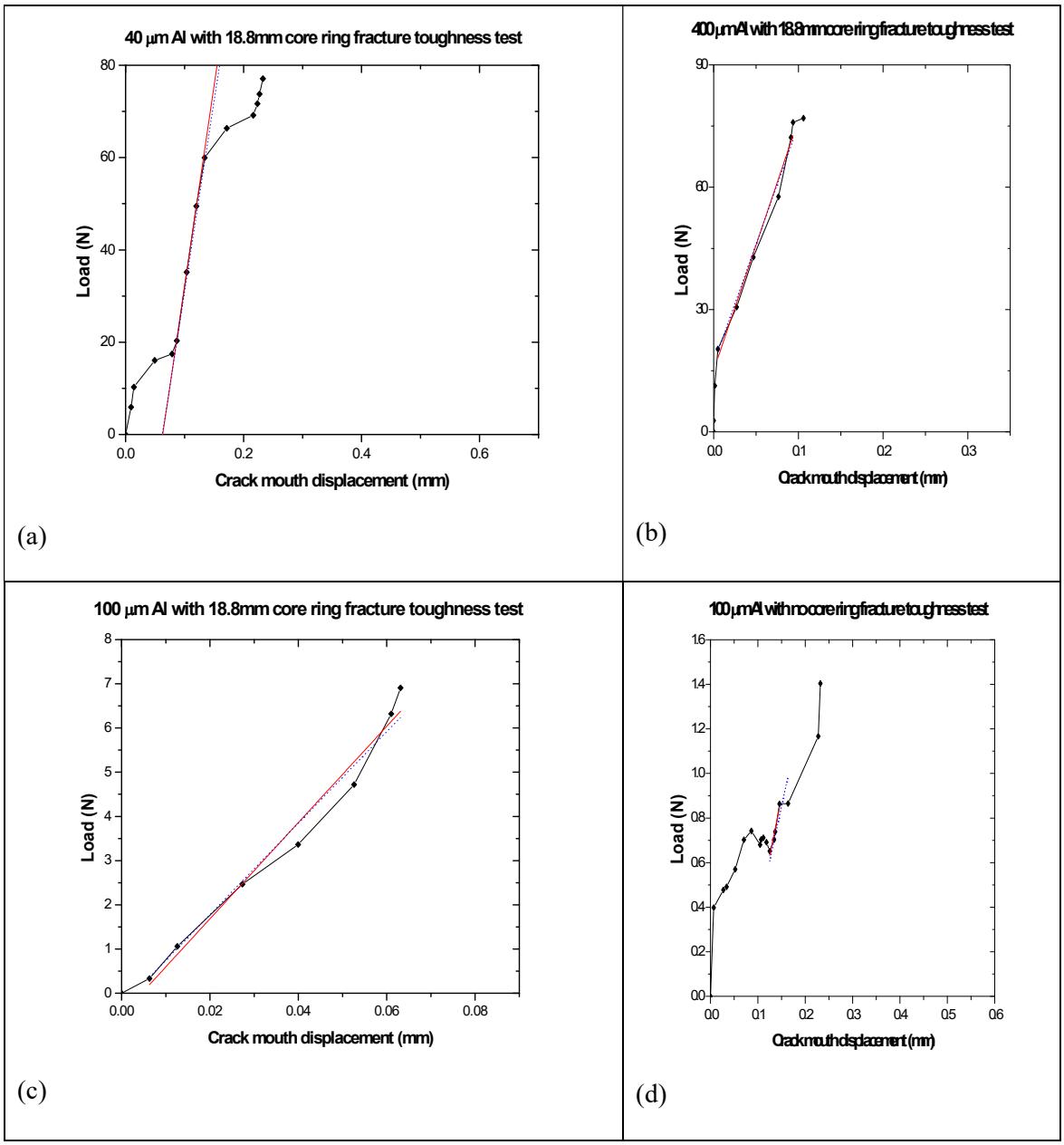

Figure 4.32: Force-Crack mouth opening displacement (CMOD) records from the fracture toughness tests with secant lines drawn to obtain the conditional fracture forces of various compacts: (a) 40 µm particle compact; (b) 400 µm particle compact; (c) 100 µm with18.8 mm core compact; (d) 100 µm particle with no core compact.

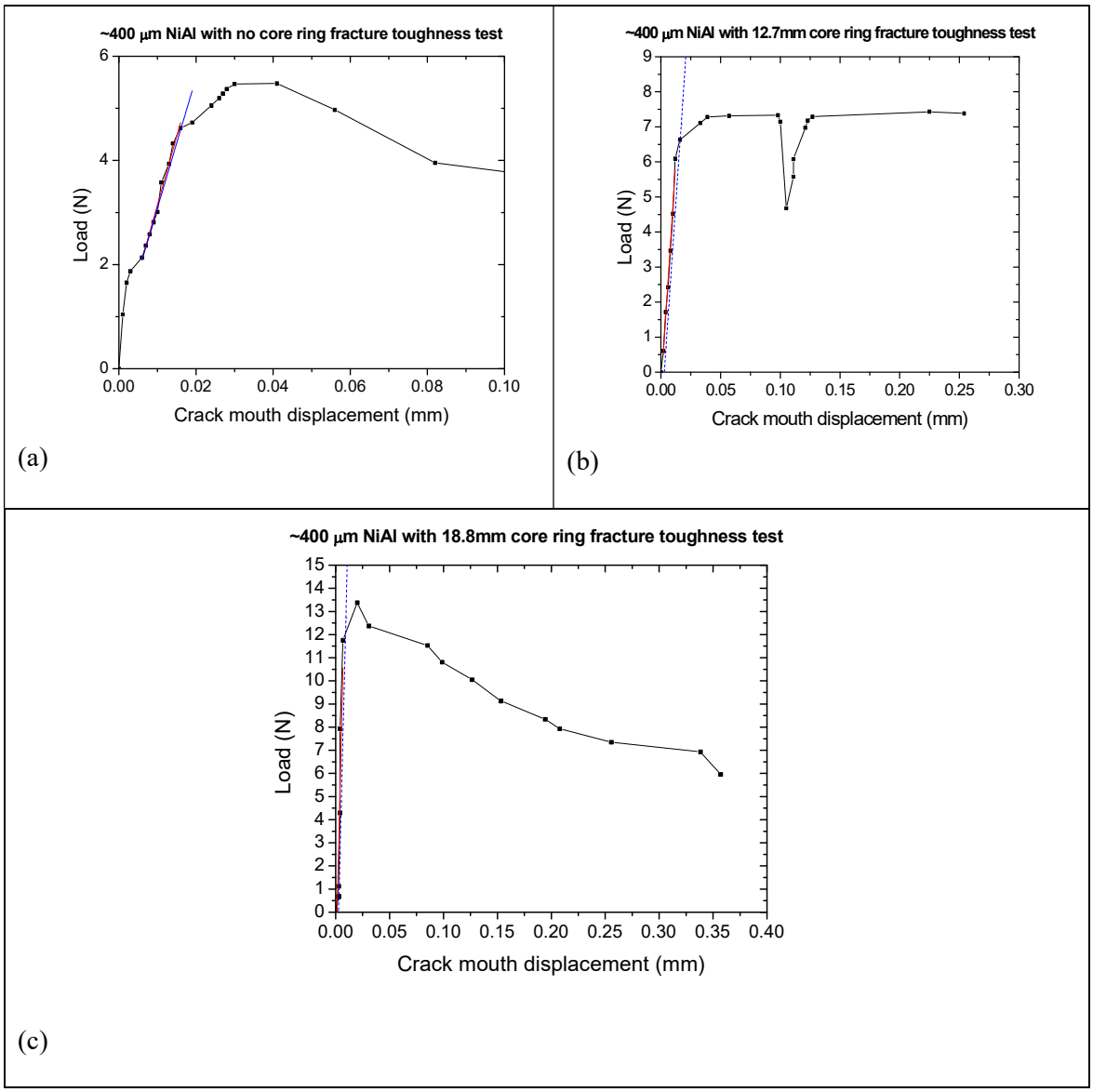

Figure 4.33: Force-Crack mouth opening displacement (CMOD) records from the fracture toughness tests with secant lines drawn to obtain the conditional fracture forces of various compacts: (a) ~400 μm NiAl particle compact swaged with no core; (b) ~400 μm NiAl particle compact swaged with 12.7 mm core; (c) ~400 μm NiAl particle compact swaged with 18.8 mm core.

The experimentally measured mean fragment sizes of the swaged aluminum are compared to the predicted values based on measured fracture toughness using the modified Mott theory (Eqn. 101) in Figure 4.34. The predicted response is given by the

dot dashed, dashed, and dotted lines for yield stresses of 50, 100, and 150 MPa, respectively; the experimentally measured fragment sizes are given by the solid line. The yield stress for each condition is marked in the plot. With the exception of the ~40 micron aluminum swaged with a 12.7 mm core (K_{Ic} = 3.04 $MPam^{1/2}$; σ_y=94 MPa) the experimentally measured mean fragment sizes correlate reasonably well with the predictions, being higher than the predicted in all cases. This can be due to fractures that did not open completely and therefore leading to two or more fragments being counted as one.

The aluminum with the lowest fracture toughness, the ~100 micron aluminum swaged with no core, could actually be closer to the predictions if not for the fact that the fragments were so small that they were compacted together during the explosion in the expanding ring experiment as shown in Figure 4.35. Therefore, the modified Mott theory could be used to predict fragment sizes for materials within ranges of yield stresses typical to that material.

The experimentally measured mean fragment sizes of the swaged nickel-aluminum are compared to the predicted values based on measured fracture toughness using the modified Mott theory (Eqn. 101) in Figure 4.36. The predicted responses are given by the blue, green and red lines for yield stresses of 100, 150, and 200 MPa, respectively; the experimentally measured fragment sizes are given by the black line. The yield stress for each condition is marked in the plot. The experimentally measured mean fragment sizes correlate reasonably well with the predictions, being only slightly higher than the predicted fragment sizes in all cases. This could be due to the fact that some fractures may not have opened completely, therefore leading to two or more fragments

being counted as one. But also the experimental mean fragment sizes lie along or in between the curves of predictions for yield stresses of 150 and 200 MPa, which were the yield stresses observed in the dynamic tests with the split-Hopkinson bar that use strain rates closer to those measured in the expanding ring tests. This is similar to the findings from the previous studies on swaged aluminum rings wherein the experimental fragment sizes were only slightly larger than the predictions from the modified Mott theory. Therefore, the modified Mott theory is shown to be able to predict fragment sizes for materials within ranges of yield stresses typical to that material for not only swaged aluminum rings like the previous study performed with this same process, but also with mixtures of aluminum such as the tailored swaged nickel-aluminum compacts.

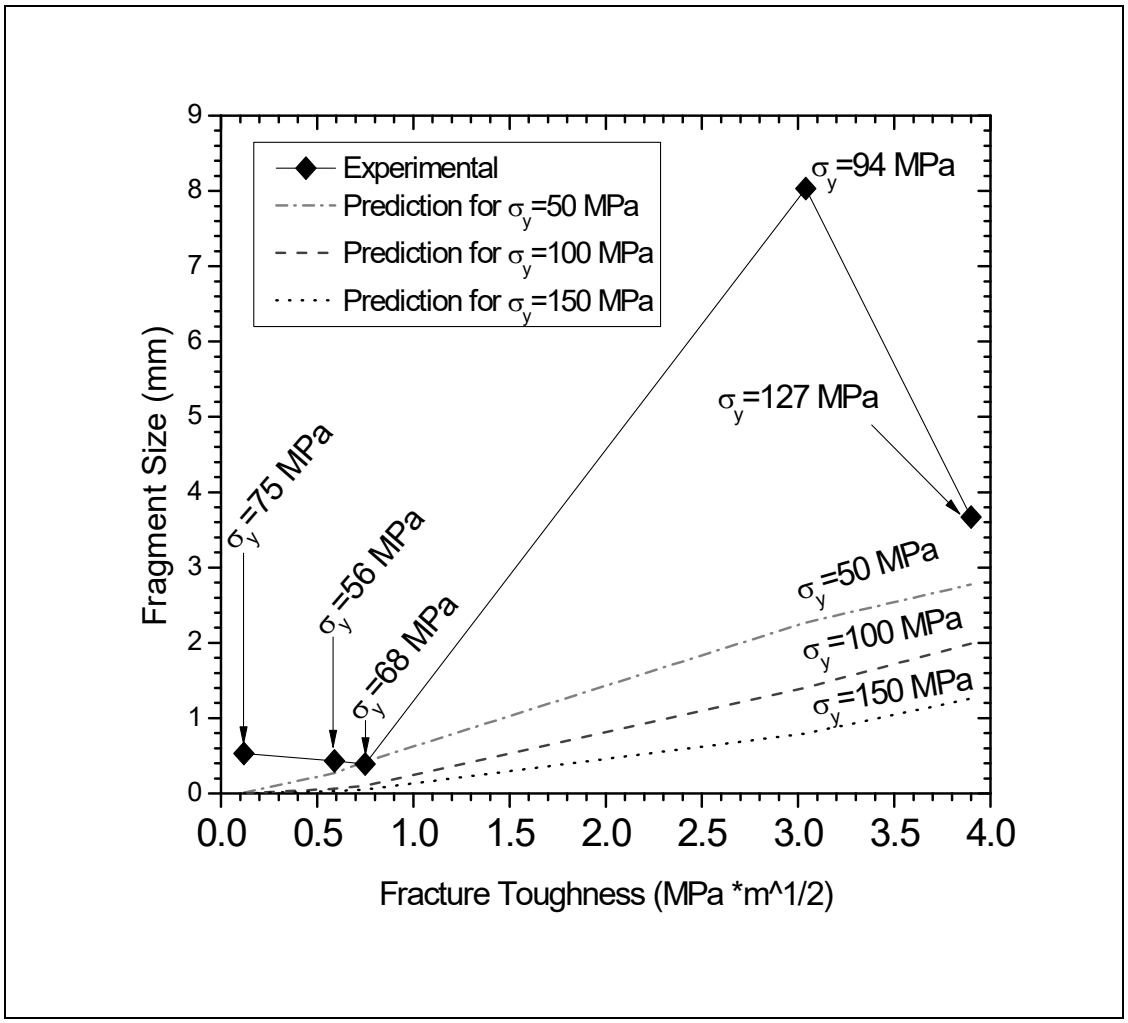

Figure 4.34: Experimentally measured mean fragment sizes (solid lines) of the swaged aluminum compared to the predictions for fragment sizes based on fracture toughness with the modified Mott theory within a range of yield stresses typical to the swaged aluminum (dotted, dash dotted, and dashed lines). The fragment size is dependent on yield stress, as shown by the three curves for 50, 100 and 150 MPa. The yield stresses of the experimental conditions are noted above each point.

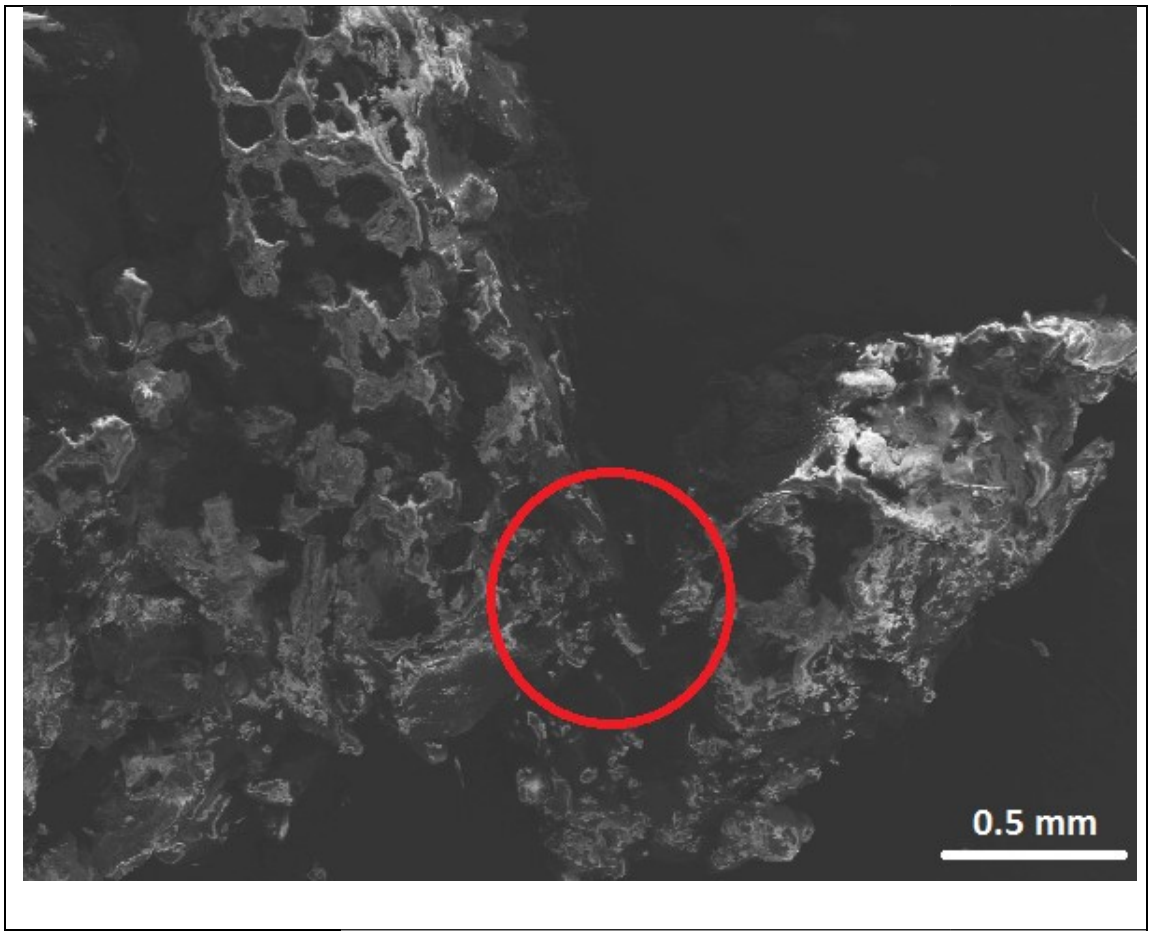

Figure 4.35: Scanning electron micrograph of fragments from the 100 micron aluminum ring, swaged with no core, compacted together at the edges as highlighted in the outlined area after an expanding ring test. The high contrast is due to the charge in the fragments being altered by wax also compacted with the fragments in the test.

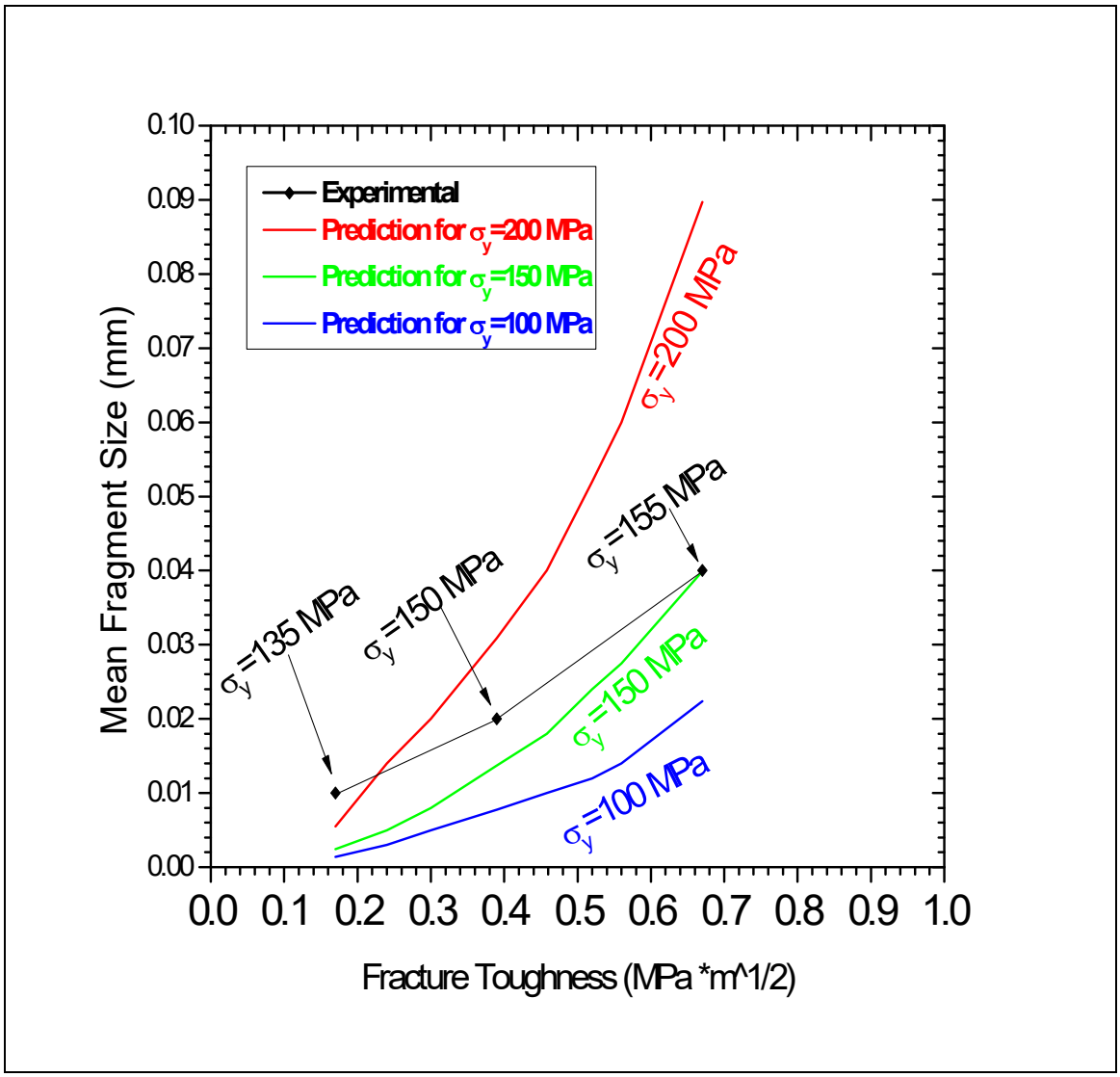

Figure 4.36: Experimentally measured mean fragment sizes (solid line) of the swaged nickel-aluminum compared to the predictions for fragment sizes based on fracture toughness with the modified Mott theory within a range of yield stresses typical to the swaged nickel-aluminum (blue, green, and red). The fragment size is dependent on yield stress, as shown by the three curves for 100, 150 and 200 MPa. The yield stresses of the experimental conditions are noted above each point.

4.7 Micro-hardness testing results of materials

The results of the micro-hardness tests on the swaged aluminum compacts are listed in Table 4.5 and the results of the swaged nickel-aluminum compacts are listed in Table 4.6. These results did not reveal many significant observations with the exception of the hardness being higher for the 100 micron Al swaged with an 18.8 mm core compared to the 100 micron Al swaged with no core, although the 100 micron Al swaged with a 12.7 mm core had a lower hardness than the 100 micron Al swaged with no core, and the 40 micron swaged Al having a higher hardness than the 100 micron Al compacts aside from the 100 micron Al swaged with an 18.8 mm core. However, for the swaged NiAl compacts the 400 micron NiAl swaged with no core had approximately the same hardness and even the same standard deviation as the 400 micron NiAl swaged with an 18.8 mm core, with the 400 micron NiAl swaged with a 12.7 mm core being slightly less than both. Thus, it is difficult to find considerable trends from the micro-hardness results, which were more prevalent in the analysis of the constitutive response discussed in the next section.

Table 4.7: Micro-hardness results for the different compacts.

Compacts	40 μm Al (12.7 mm core)	100 μm Al (No core)	100 μm Al (12.7 mm core)	100 μm Al (18.8 mm core)	400 μm Al (18.8 mm core)
Hardness (GPa)	0.43 ± 0.03	0.33 ± 0.02	0.28 ± 0.09	0.53 ± 0.06	0.68 ± 0.09

Table 4.8: Micro-hardness results for the swaged nickel-aluminum compacts.

Compacts	400 μm NiAl (No core)	400 μm NiAl (12.7 mm core)	400 μm NiAl (18.8 mm core)
Hardness (GPa)	1.2 ± 0.1	1.1 ± 0.04	1.2 ± 0.1

4.8 Constitutive response of materials

The quasi-static compression test results (Fig. 4.25a and b) revealed that the swaged 400 μm aluminum samples have the highest young's modulus (~22 GPa), followed by the swaged 40 μm aluminum samples(~17 GPa), and then the swaged 100 μm aluminum samples. Interestingly, the Young's modulus was higher in the swaged 100 μm aluminum samples with no core, which is ~13GPa, compared to that of the swaged 100 μm aluminum with a 12.7 mm core that is ~9 GPa. The yield stresses obtained from the measured quasi-static stress-strain curves followed the same trend. The swaged 400 μm aluminum had the highest yield stress, which is ~127 MPa. The yield stress of the swaged 40 μm aluminum is ~94 MPa. The yield stress of the swaged 100 μm aluminum with no core is ~75 MPa and the lowest yield stress is ~63 MPa for the swaged 100 μm aluminum with a 12.7 mm core. The dynamic yield stresses, shown in Figure 4.37(c),

varied from 75 to 150 MPa and are moderately higher than the quasi-static values. The order of highest yield stresses was consistent with the quasi-static results. The quasi-static and dynamic yield stresses are plotted as a function of strain rate in Figure 4.37(d).

The quasi-static compression test results Figures 4.38(a-c) revealed that the 355-500 μm nickel-aluminum samples swaged with an 18.8 mm core have the highest yield stresses (~155 MPa), followed by the nickel-aluminum samples swaged with a 12.7 mm core(~150 MPa), and then the nickel-aluminum samples swaged with no core (~135 MPa). The dynamic yield stresses, shown in Figure 4.38(d), varied from 140 to 180 MPa and are moderately higher than the quasi-static values. The order of highest dynamic yield stresses was consistent with the quasi-static results. The quasi-static and dynamic yield stresses are plotted as a function of strain rate in Figure 4.38(d). From that plot the strain-rate sensitivity, m, a parameter that measures how much a material's flow stress and work-hardening rate may be affected by strain rate, of the nickel-aluminum compacts can be determined. The strain-rate sensitivity is defined as $m = \partial \ln \sigma / \partial \ln \dot{\varepsilon}$. The low strain-rate sensitivity is expected with aluminum mixtures, as observed with previous studies[26].

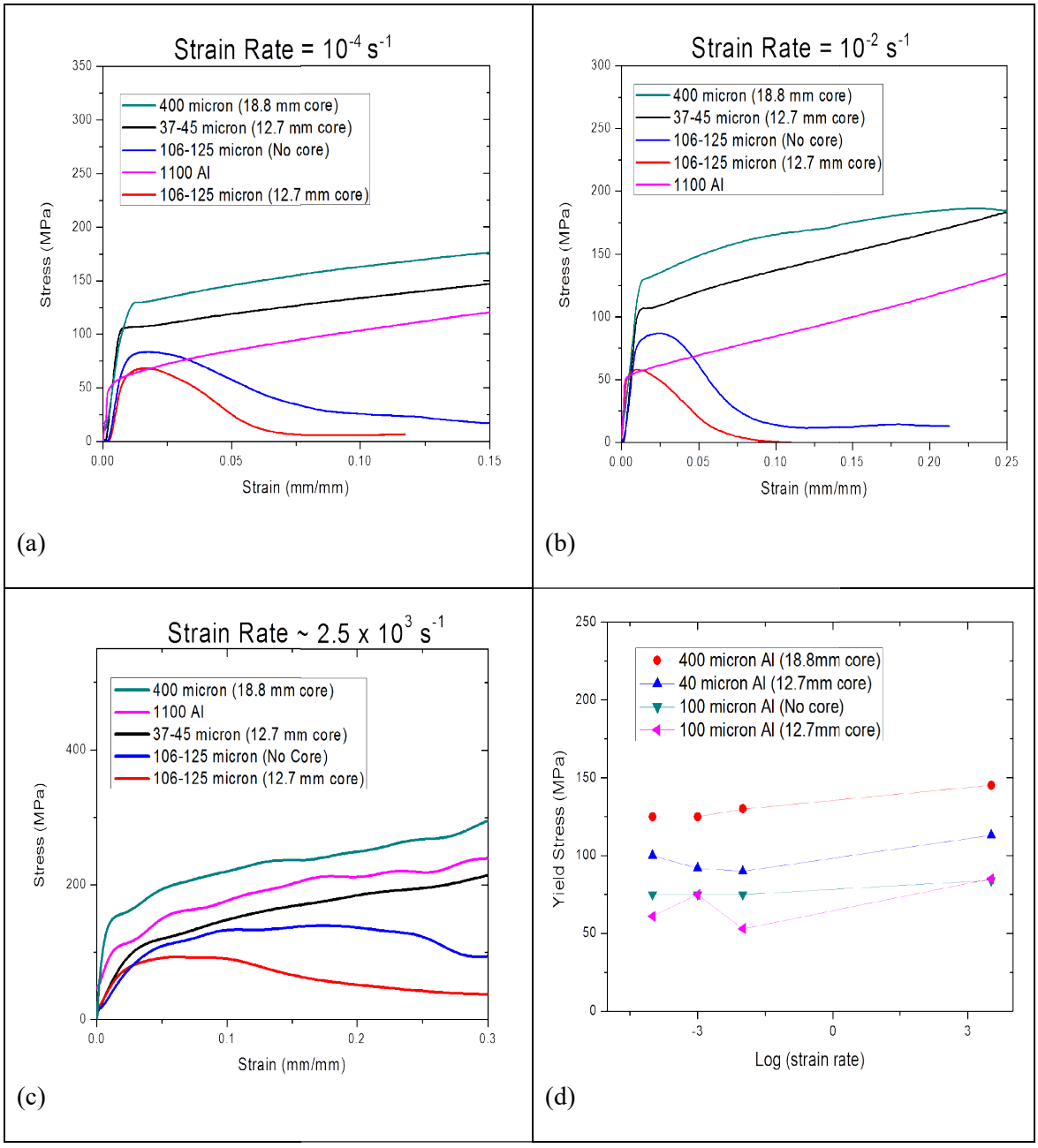

Figure 4.37: Constitutive response of compacts in compression: (a) 10^{-4} s^{-1}; (b) 10^{-2} s^{-1}; (c)2.5 x 10^{3} s^{-1}; (d) combined plot showing the yield stress as a function of strain rate.

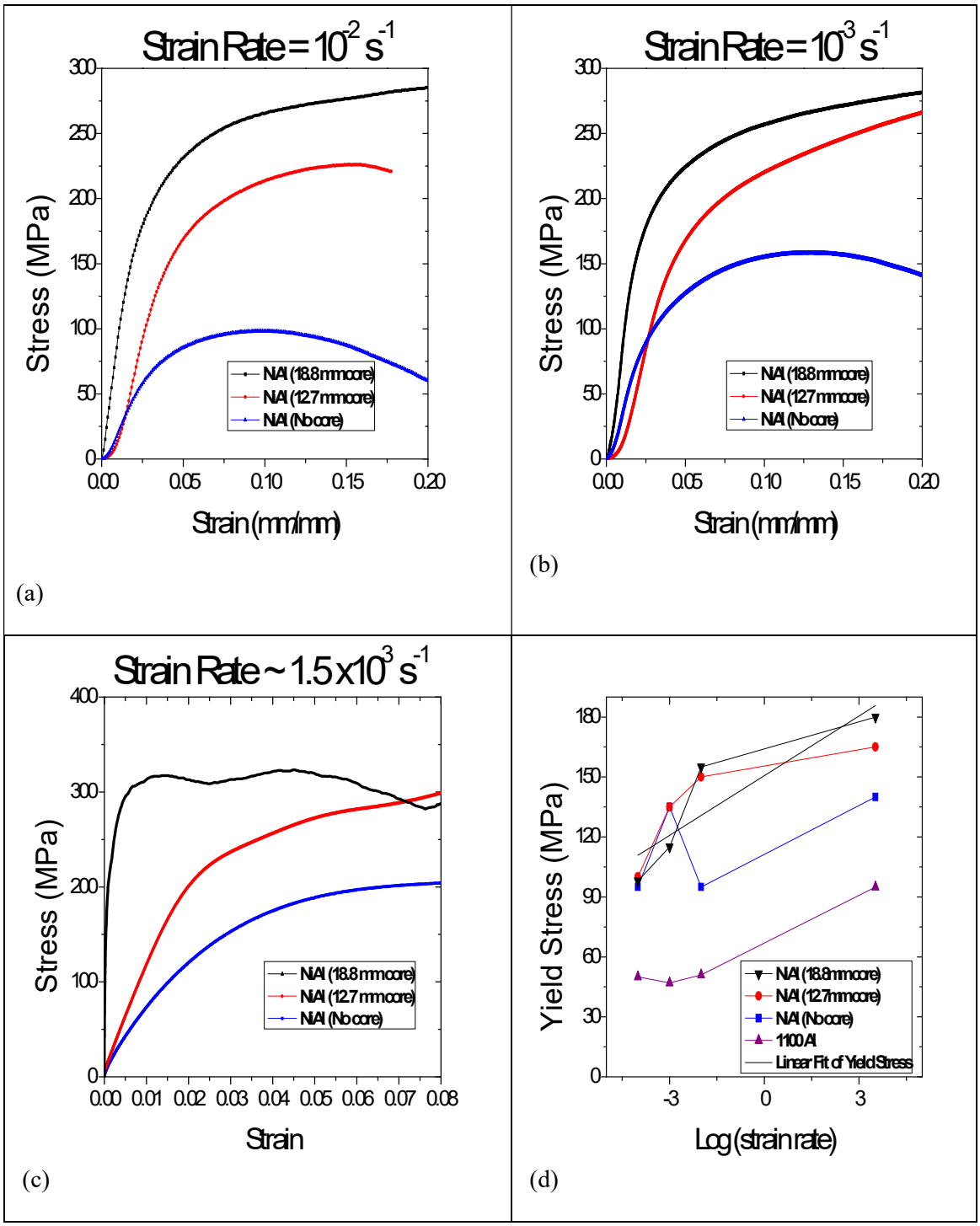

Figure 4.38: Constitutive response of compacts in compression: (a) 10^{-2} s^{-1}; (b) 10^{-3} s^{-1}; (c)10^{-4} s^{-1}; (d) combined plot showing the yield stress as a function of strain rate.

4.9 LS-DYNA simulations

The results of the numerical simulations are presented in Figures 4.39-42. For the aluminum rings, the Johnson-Cook[107] material model was used:

$$\sigma_y = \left(A + B\bar{\varepsilon}^{p^n}\right)(1 + C \ln \dot{\varepsilon}^*) \tag{110}$$

where A is the yield stress, B is the hardening modulus, C is the strain rate constant, $\bar{\varepsilon}^p$ is the effective plastic strain and $\dot{\varepsilon}^*$ is the normalized effective strain rate. The parameters for the Al rings in the simulations, shown in Table 4.1, were taken from the experimental results of the quasi-static and dynamic testing conducted on samples removed from the compacts.

The simulation of the 40 μm Al swaged powder ring (Fig. 4.27) was observed to fracture in two positions with a similar pattern as in the high speed photographs taken from the expanding ring tests (Fig. 4.13). When considering the quarter symmetry of the simulation mirrored over the entire ring, it would be observed to produce 8 fragments, as was collected from the experiment. The pattern of fracture observed in the simulation of the 400 μm Al swaged powder ring (Fig. 4.28) was also similar to the pattern seen in the high speed photographs from the actual experiment (Fig. 4.14). When the quarter symmetry of this simulation is considered over the entire ring it would be observed to produce approximately 32 fragments but as seen in the simulation some of the fragments were considerably small such that they could have reduced to powder by the end of the explosive experiment. The brittle fractures observed in the high speed photographs of the 100 μm Al swaged powder rings (Fig. 4.15-4.17) was seen in the simulations of those rings (Fig. 4.29-4.30).

Table 4.9: List of parameters taken from experimental results for LS-DYNA simulations.

Compacts	40 µm Al (12.7 mm core)	100 µm Al (No core)	100 µm Al (12.7 mm core)	400 µm Al (18.8 mm core)
Density	2.69 g/cm^3	2.69 g/cm^3	2.69 g/cm^3	2.67 g/cm^3
Young's modulus	0.197 Mbar	0.066 Mbar	0.131 Mbar	0.137 Mbar
Poisson's ratio	0.345	0.345	0.345	0.345
Yield stress (A)	8.40 x 10^{-4} Mbar	7.00 x 10^{-4}	6.00 x 10^{-4}	1.20 x 10^{-3}
Hardening modulus (B)	6.97 x 10^{-3} Mbar	3.32 x 10^{-4}	2.48 x 10^{-3}	2.40 x 10^{-3}
Strain rate constant (C)	0.007023	0.006516	0.007902	0.008517
Strain exponent (n)	1.320	0.123	0.835	0.800
Plastic strain of failure (PSFAIL)	0.220900	0.013916	0.029307	0.079440
Strain rate of reference (EPS0)	1 x 10^{-8} s^{-1}	1 x 10^{-8} s^{-1}	1 x 10^{-8} s^{-1}	1 x 10^{-8} s^{-1}

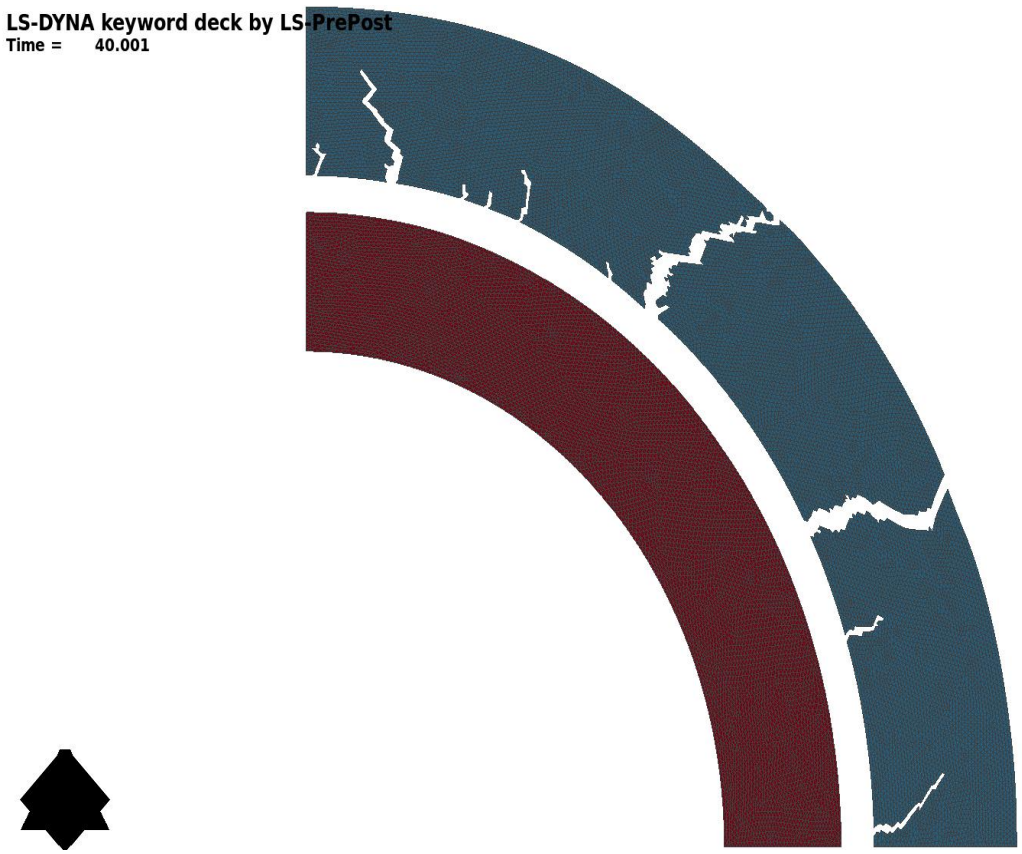

Figure 4.39: Fracture at the end of the expanding ring test simulation of 40 μm swaged Al powder ring.

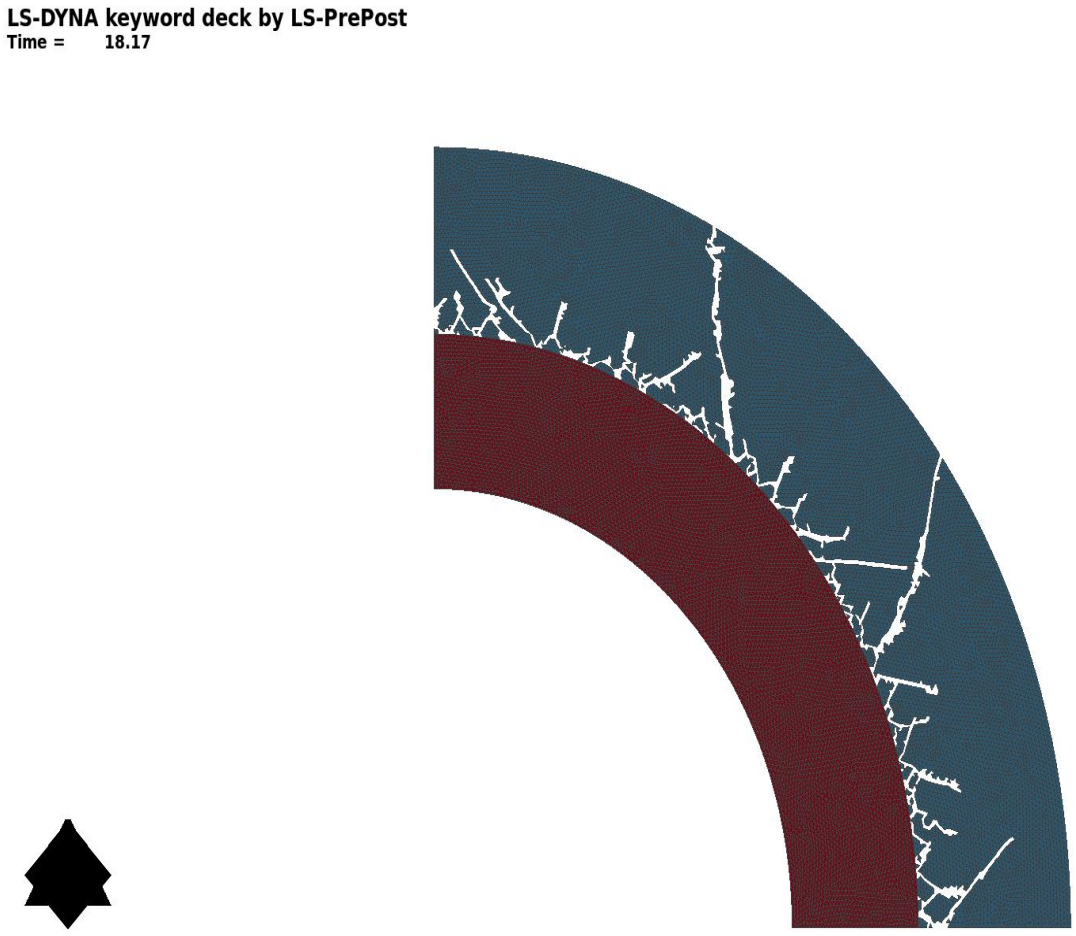

Figure 4.40: Fracture at the end of the expanding ring test simulation of 400 μm swaged Al powder ring.

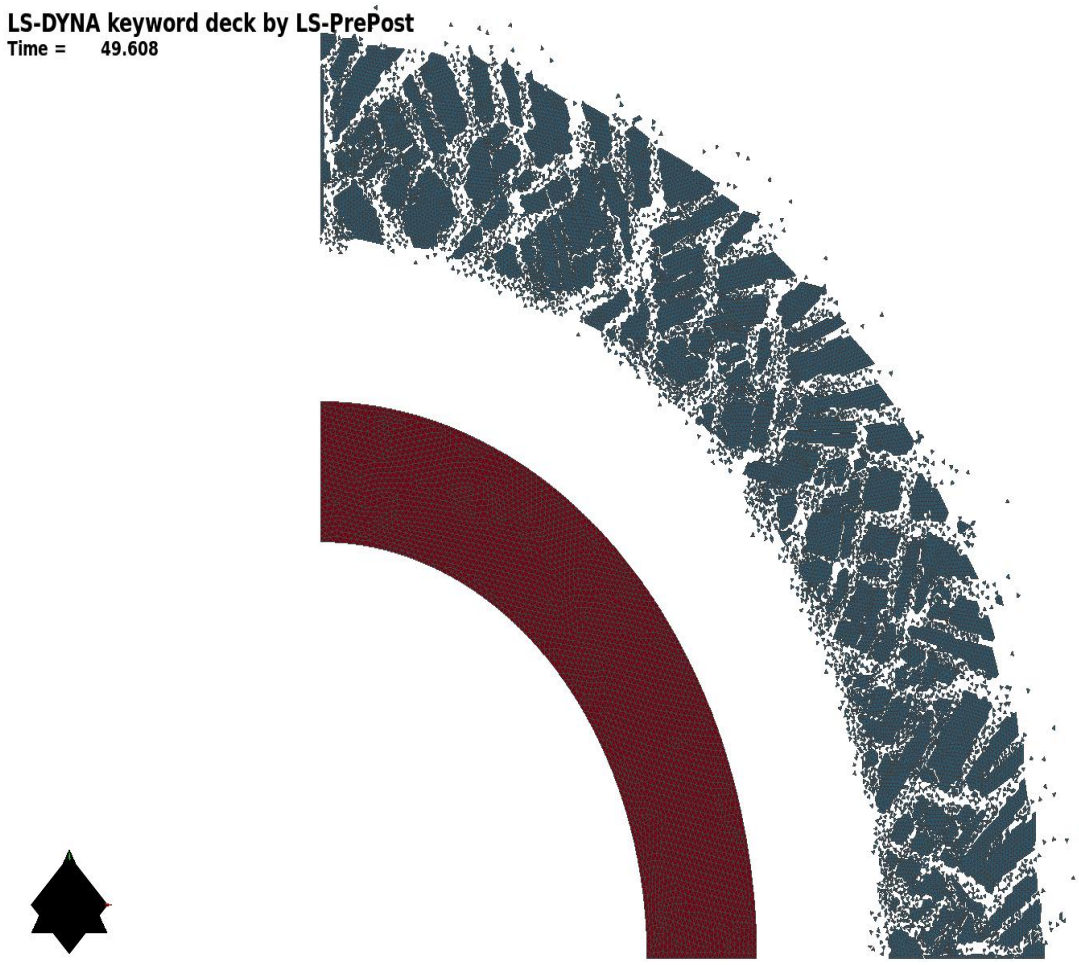

Figure 4.41: Fracture at the end of the expanding ring test simulation of 100 μm Al powder ring swaged with a 12.7 mm core.

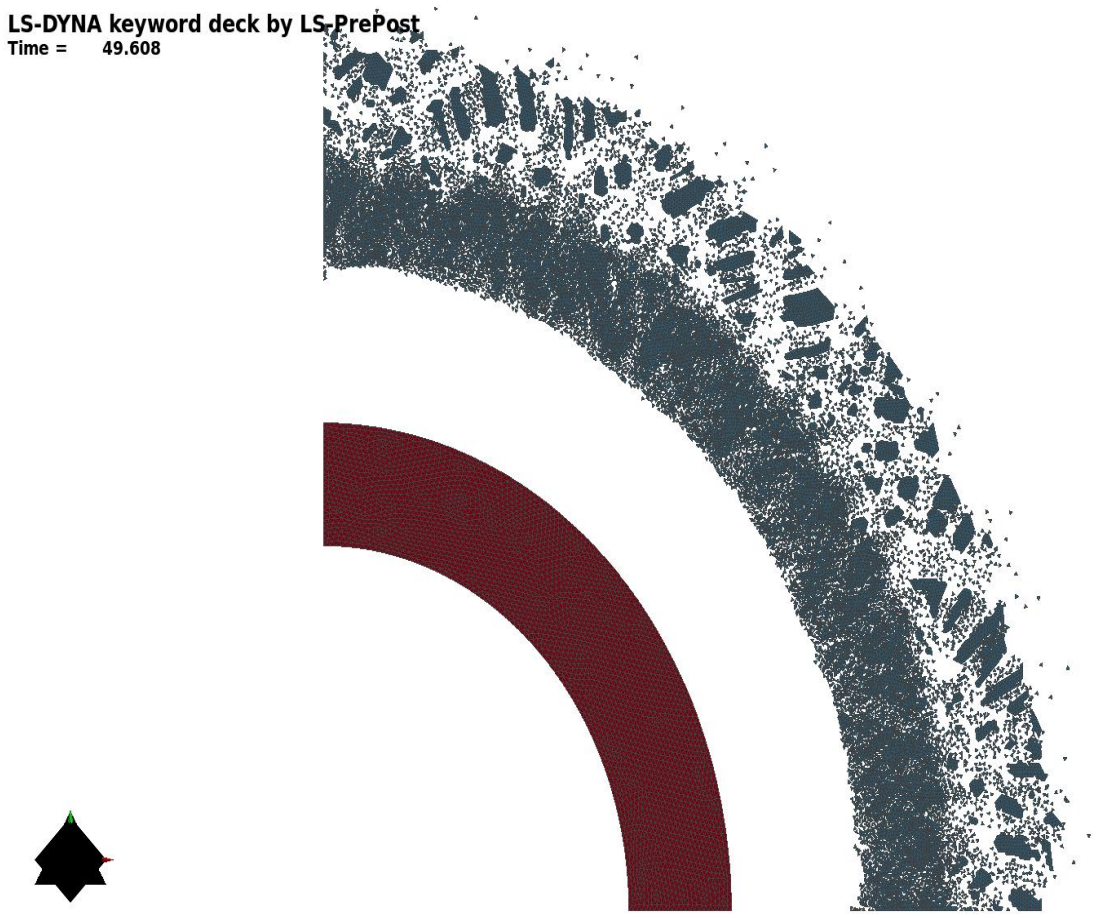

Figure 4.42: Fracture at the end of the expanding ring test simulation of 100 μm Al powder ring swaged with no core.

Chapter 4, in part, is published as "Fragmentation and constitutive response of tailored mesostructured aluminum compacts" Journal of Applied Physics, vol 119, p. 145903, 2016. A. Marquez, C. Braithwaite, T. Weihs, N. Krywopusk, D. Gibbins, K. Vecchio, and M. Meyers. The dissertation author is the first author of this work.

Chapter 4, in part, is submitted for publication as "Fragmentation and mechanical performance of tailored nickel-aluminum laminate compacts." A. Marquez, Z. Li, C. Braithwaite, T. Weihs, N. Krywopusk, D. Gibbins, and M. Meyers. The dissertation author is the first author of this work.

CHAPTER 5: CONCLUSIONS

5.1 Swaged aluminum compacts

Aluminum compacts of different particle sizes were processed through swaging. Quasi-static and dynamic compression tests were conducted to analyze the constitutive response of the compacts. Particle size and degree of compaction were determined to have a direct effect on constitutive response of the swaged aluminum. Fracture toughness values for the modified Mott equation were attained using the ASTM standard test method for linear-elastic plane-strain fracture toughness of metallic materials (ASTM E399) with some slight variations.

Expanding ring tests were also conducted on the compacts to examine the fragmentation behavior of the compacts. Scanning electron microscopy was utilized to investigate the fracture response of the swaged Al rings, the swaged 400 μm and 40 μm particle Al rings demonstrated ductile fracture behavior while the swaged 100 μm particle Al rings showed features indicative of a brittle material failure. The more ductile swaged 400 μm and 40 μm particle Al rings produced far fewer fragments than the more brittle swaged 100 μm particle Al rings.

A possible reason for the weaker compacts from 100 um particles is surface contamination of the powders which led to weaker interfaces. Fragmentation number statistics of the swaged aluminum tend to follow a Grady distribution more so than a Mott distribution. Fragment mean size predictions were attempted with a modified Mott equation similar to the Grady-Kipp theory. The experimentally measured mean fragment sizes were found to be close to the predictions of fragment size based on fracture

toughness by the modified Mott theory in all but one of the conditions of swaged aluminum. For this condition the particles were swaged most successfully producing a much higher fracture toughness than anticipated.

5.2 Swaged nickel-aluminum compacts

Nickel-aluminum compacts were processed through swaging to have varying degrees of compaction. Quasi-static and dynamic compression tests were conducted to analyze the mechanical performance of the compacts. The degree of compaction was determined to have a direct effect on constitutive response of the swaged nickel-aluminum. Fracture toughness values for the modified Mott equation were found using the ASTM standard test method for linear-elastic plane-strain fracture toughness of metallic materials (ASTM E399) with some minor variations.

Additionally, expanding ring tests were conducted on the compacts to study the fragmentation behavior of the compacts. Scanning electron microscopy used to examine the fracture response of the swaged Ni-Al rings, the Ni-Al rings swaged with an 18.8 mm core demonstrated ductile fracture behavior while the Ni-Al rings swaged with a 12.7 mm core or without any core showed brittle material fracture features. The more ductile Ni-Al rings swaged with an 18.8 mm core produced much fewer fragments than the more brittle Ni-Al rings swaged under different conditions.

Fragment mean size predictions were calculated with a modified Mott equation similar to the Grady-Kipp theory. The experimentally measured mean fragment sizes were found to be close to the predictions of fragment size based on fracture toughness by the modified Mott theory. This indicates that the modified Mott theory predicted the

fragment sizes for the swaged Ni-Al rings just as well as it did in the previous study performed under these conditions with swaged aluminum rings.

5.3 Finite element simulations

Finite element simulations of the expanding ring tests were also conducted to help better understand the influence of material properties on fragmentation. These numerical simulations utilized material parameters extracted from the experimental results of the quasi-static and dynamic testing conducted on samples removed from the compacts. Some of these material parameters, such as yield stress, are incorporated in the modified Mott theory developed in the experimental fragmentation studies. The simulations were performed in a quarter symmetry setup. Nevertheless, the fragmentation observed in these simulations is very similar to the type of fragmentation studied in high-speed photographs and post-fracture analysis of the actual expanding ring experiments. Therefore, the numerical simulations confirm that the modified Mott theory should accurately predict fragmentation, specifically fragment sizes, based upon material properties such as the fracture toughness and the yield stress.

REFERENCES

[1]L. Knapp, "Adding more bang to navy missiles", Web. (http://www.wired.com/science/discoveries/news/2002/12/56695), (2002.

[2] R.G. Ames. Energy release characteristics of impact-initiated energetic materials. Multifunctional Energetic Materials 2006; 896:123-132.

[3] J. Wang, E. Besnoin, A. Duckham, S. J. Spey, M. E. Reiss, O. M. Knio, T. P. Weihs. Joining of stainless-steel specimens with nanostructured Al/Ni foils. J Appl Phys 2004; 95:248-256.

[4] A.G. Merzhanov. Combustion processes that synthesize materials. J Mater Process Tech 1996; 56:222-241.

[5] K.S. Vecchio, L.H. Yu, M.A. Meyers. Shock synthesis of silicides .1. Experimentation and microstructural evolution. Acta Metall Mater 1994; 42:701-714.

[6] Wikipedia, Web. " Thermite", (Http://en.wikipedia.org/wiki/Thermite).

[7] J. Zhang, F.-S. Wu, J. Zou, B. An, H. Liu. Al/Ni multilayer used as a local heat source for mounting microelectronic components. ICEPT-HDP 2009; 838-842.

[8] J.C. LaSalvia, D.K. Kim, R.A. Lipsett, M.A. Meyers. Combustion synthesis in the Ti-C-Ni-Mo system .1. Micromechanisms. Metall Mater Trans A 1995; 26A:3001-3009.

[9] N.N.Thadhani. Shock-induced chemical-reactions and synthesis of materials. Progr Mater Sci 1993; 37:117-226.

[10] M.A. Meyers. Mechanics and Materials: Fundamentals and Linkages, John Wiley and Sons, New York, New York, 1999.

[11] B. Hopkinson. A method of measuring the pressure produced in the detonation of high explosives or by the impact of bullets. Philo Trans of the Royal Society of London 1914; 213:437-456.

[12] H. Kolsky. An investigation of the mechanical properties of materials at very high rates of loading. Proc Phys Soc B 1949; 62: 676-700.

[13] T. Kundu. Advanced Ultrasonic Methods for Material and Structure Inspection, John Wiley and Sons, New York, New York, 2007.

[14] M. A. Meyers. Dynamic Behavior of Materials, John Wiley and Sons, New York, New York, 1994.

[15] O.S. Lee, K.S. Cho, S.H. Kim, Y.H. Han. Dynamic deformation behavior of soft material using SHPB technique and pulse shaper. Inter J Mod Physics B 2006; 20: 3751-3756.

[16] O.S. Lee, S.H. Kim, Y.H. Han. Dynamic deformation behavior of soft materials at the low temperature using SHPB technique and pulse shaper. Exper Mech in Nano and Biotech 2006; 326:1577-1580.

[17] O.S. Lee, S.H. Kim, J.W. Lee. Thickness effect of pulse shaper on dynamic stress equilibrium in the NBR rubber specimen. Fracture and Strength of Solids 2006; 306: 1007-1012.

[18] O.S. Lee, Y.H. Han, D.H. Kim. Influence of temperature and heat-aged condition on the deformation behavior of rubber material using SHPB technique with a pulse shaper. Prog in Fracture and Strength of Materials and Structures 2007; 353:619-626.

[19] O.S. Lee, D.H. Kim, Y.H. Han, Y.C. Park. Dynamic deformation of hot temperature degraded POM and PP using a modified SHPB with pulse shaper technique. J Mech Sci Tech 2008; 22:1692-1698.

[20] J. Harding, E.O. Wood, J.D. Campbell. Tensile testing of materials at impact rates of strain. J Mech Eng Sci 1960; 2:88-96.

[21] T. Nicholas. Tensile testing of materials at high rates of strain. Exp Mech 1981; 21: 177-185.

[22] K. Ogawa. Impact-tension compression test by using a split-Hopkinson bar. Exp Mech 1984; 24:81-86.

[23] A. Gilat, Y.H. Pao. High-rate decremental-strain-rate test. Exp Mech 1988; 28:322-325.

[24] A. Gilat. Torsional Kolsky Bar Testing, in: H. Kuhn (Ed.), ASM Handbook, ASM International, Materials Park, Ohio, 2000, pp. 505-515.

[25] P.C. Johnson, B.A. Stein, R.S. Davis. Basic parameters of material behavior under high rate forming. 1962, U.S. Army Materials Research Agency: Watertown.

[26] R.M. Zoot. Laser Interferometry of Pentaprisms. Applied Optics 1964; 3:1187-1188.

[27] S. Walles. Laser Interferometry. Arkiv for Fysik 1965; 30:545-546.

[28] L.H. Tanner. Optics of Laser Streak Interferometry. J Scientific Instruments 1967; 44:725-730.

[29] D.L. Weisman. Laser Beam Shaping for Streak Interferometry. Applied Optics 1970; 9:1213.

[30] L.M. Barker. Laser Interferometry in Shock-Wave Research. Exp Mech 1972; 12:209-215.

[31] J.N. Gayles, W.L. Honzik, D.O. Wilson. On-Line Far-Infrared Michelson Interferometry in a Time-Shared Mode. IBM J Research and Development 1970; 14:25-32.

[32] L.W. Kunz, D. Goorvitc. Combined Effects of a Converging Beam of Light and Mirror Misalignment in Michelson Interferometry. Applied Optics 1974; 13:1077-1079.

[33] D. V. Bartlett, R.G.L. Hewitt, L.C. Robinson, G.D. Tait. Study of Far-Infrared Michelson Interferometry Based on Fast Plasma Scanning. Infrared Physics 1977; 17:89-103.

[34] A. J. Holloway, D.C. Emmony. Multiple-Pass Michelson Interferometry. J Physics E-Scientific Instruments 1988; 21:384-388.

[35] P.G. Vekilov, M. Ataka, T. Katsura. Growth-Processes of Protein Crystals Revealed by Laser Michelson Interferometry Investigation. Acta Crystallographica Section D-Biological Crystallography 1995; 51:207-219.

[36] C.R. Hoggatt, R.F. Recht. Stress-strain data obtained at high rates using an expanding ring Exp Mech 1969; 9:441-448.

[37] W.H. Gourdin, S.L. Weinland, R.M. Boling. Development of the electromagnetically launched expanding ring as a high-strain-rate test technique. Rev Sci Instrum 1989; 60:427-432.

[38] R.G. Ames. Energy release characteristics of impact-initiated energetic materials. Multifunctional Energetic Materials 2006; 896:123-132.

[39] N.F. Mott, E.H. Linfoot. A Theory of Fragmentation. Ministry of Supply 1943; A.C. 3348.

[40] N.F. Mott. Fragmentation of H.E. Shells: A Theoretical Formula for the Distribution of Weights of Fragments. Ministry of Supply 1943; A.C. 3642.

[41] N.F. Mott. A Theory of the Fragmentation of Shells and Bombs. Ministry of Supply 1943; A.C. 4035.

[42] N.F. Mott. Fragmentation of Shell Casings and the Theory of Rupture in Metals. Ministry of Supply 1943; A.C.4613.

[43] N.F. Mott. A Theory of Fragmentation Application to Wire Wound Bombs such as the American 20 lb, F. Ministry of Supply 1944; A.C. 6338.

[44] N.F. Mott, J.H. Wilkinson, T.H. Wise. Fragmentation of Service Projectiles. Ministry of Supply 1944; A.C. 6338.

[45] N.F. Mott. Fragmentation of Shell Cases. Proc Royal Soc 1947; A189:300-308.

[46] N.F. Mott. Fracture of Metals: Theoretical considerations. Engineering 1948; 165: 16-18.

[47] D. Grady. Fragmentation of Rings and Shells, Springer-Verlag, Berlin, Germany, 2006.

[48] C.C. Lineau. Random fracture of a brittle solid. J Franklin Inst 1936; 221:485-494, 674-686, 769-787.

[49] D.E. Grady. Particle size statistics in dynamic fragmentation. J Appl Phys 1990; 68:6099-6105.

[50] N.F. Mott. Mechanical Properties of Metals. Physica 1949; 15:119-134.

[51] Handbook of Mathematical Function, in: M. Abramowitz (Ed.), U.S. Government Printing Office, Washington, D.C., 1954.

[52] R.C. Buck. Advanced Calculus, McGraw-Hill, New York, New York, 1965.

[53] D.E. Grady, M.E. Kipp. Geometric statistics and dynamic fragmentation. J Appl Phys 1985; 58:1210-1222.

[54] P.S. Puri, C.M. Goldie. Poisson mixtures and quasi-infinite divisibility of distributions. J Appl Prob 1979; 16:138-153.

[55] B.N. Boots, D.J. Murdoch. The spatial arragnement of random voronoi polygons. Computers and Geosciences 1983; 9:351-365.

[56] V.A. Blatov, A.P. Shevchenko, V.N. Serezhkin. Crystal Space Analysis by Means of Voronoi-Dirichlet Polyhedra. Acta Crystallographica A 1995; 51:909-916.

[57] L. B. Serezhkina, V.N. Serezhkin. Voronoi-Dirichlet polyhedra of uranium atoms and 18-electron rule in carbonate-containing uranyl complexes. Radiochemistry 1996; 38: 110-117.

[58] O.A. Blatova, V.A. Blatov, V.N. Serezhkin. Study of rare-earth pi-complexes by means of Voronoi-Dirichlet polyhedra. Acta Crystallographica B 2001; 57:261-270.

[59] V.A. Blatov, O.A. Blatova, G.D. Ilyushin, L.N. Dem'Yanets. Analysis of microporous mineral phases with Voronoi-Dirichlet polyhedra. European J Mineralogy 2005; 17:819-827.

[60] V.N. Serezhkin, D.V. Pushkin, L.B. Serezhkina. Analysis of the Conformational Polymorph Crystal Structures by Means of Molecular Voronoi-Dirichlet Polyhedra. Crystallography Reports 2010; 55:554-562.

[61] T. Kiang. Mass distributions of asteroids, stars and galaxies. Zeitschrift fur Astrophysik 1966; 64:426-432.

[62] D. Weaire, N. Rivier. Soap, cells and statistics - random patterns in two dimensions. Contemp Phys 1984; 25:59-99.

[63] D.F. Watson. Computation the n-dimensional Delaunay tessellation with application to Voronoi polytopes. The Computer Journal 1981; 24:167-172.

[64] I.K. Crain. The Monte-Carlo generation of random polygons. Computers and Geosciences 1978; 4:131-141.

[65] M.A. Meyers, K.K. Chawla. Mechanical Behavior of Materials, Cambridge University Press, Cambridge, United Kingdom, 1994.

[66] J.B. Wachtman. Mechanical and Thermal Properties of Ceramics, in: J.B. Wachtman (Ed.), NBS, NBS Special Publication, Washington, D.C., 1963, p. 139.

[67] J.K. MacKenzie. The elastic constants of a solid containing spherical holes. Proc Phys Soc B 1950; 63:2-11.

[68] B. Budiansky, R.J. O'connell. Elastic moduli of a cracked solid. Intl J Solids Struct 1976; 12:81-97.

[69] F. Zerilli, R.W. Armstrong. Description of tantalum deformation behavior by dislocation mechanics based constitutive relations. J Appl Phys 1990; 68:1580-1591.

[70] D.S. Gianola, D.H. Warner, J.F. Molinari, K.J. Hemker. Increased strain rate sensitivity due to stress-coupled grain growth in nanocrystalline Al. Scripta Mater 2006; 55:649-652.

[71] R. Schwaiger, B. Moser, M. Dao, N. Chollacoop, S. Suresh. Some critical experiments on the strain-rate sensitivity of nanocrystalline nickel. Acta Mater 2003; 51:5159-5172.

[72] Y.M. Wang, E. Ma. Strain hardening, strain rate sensitivity, and ductility of nanostructured metals. Mater Sci Eng A 2004; 357:46-52.

[73] K.M. Lee, J.S. Lee, D.J. Lee, S.S. Kim, I.S. Ahn, M.W. Park. Effect of thermal treatment on the atomic ordering of mechanically alloyed Al3Nb. J Alloys Compounds 2000; 313:214-217.

[74] D.E. Eakins, N.N. Thadhani. The shock-densification behavior of three distinct Ni+Al powder mixtures. Appl Phys Lett 2008; 92:111903.

[75] A.K. Stover, N.M. Krywopusk, G.M. Fritz, S.C. Barron, J.D. Gibbins, T.P. Weihs. An analysis of the microstructure and properties of cold-rolled Ni:Al laminate foils. J Mat Sci 2013; 48:5917-5929.

[76] C.T. Wei, E. Vitali, F. Jiang, S.W. Du, D.J. Benson, K.S. Vecchio, N.N. Thadhani, M.A. Meyers. Quasi-static and dynamic response of explosively consolidated metal-aluminum powder mixtures. Acta Materialia 2012; 60:1418-1432.

[77] T. George. Mechanical Testing and Evaluation, in: H. Kuhn (Ed.), ASM Handbook, ASM International, Materials Park, Ohio, 2000, pp.488-496.

[78] P.H. Chiu, S. Wang, E. Vitali, E.B. Herbold, D.J. Benson, V.F. Nesterenko. Particle Size Effect in Granular Composite Aluminum/Tungsten. Shock Compression of Condensed Matter 2009; 1195:1345-1348.

[79] K.S. Vecchio, F.C. Jiang. Improved Pulse Shaping to Achieve Constant Strain Rate and Stress Equilibrium in Split-Hopkinson Pressure Bar Testing. Metall Mater Trans A 2007; 38:2655-2665.

[80] W. Chen, B. Song, D.J. Frew, M.J. Forrestal. Dynamic small strain measurements of a metal specimen with a split Hopkinson pressure bar. Exp Mech 2003; 43:20-23.

[81] D.J. Parry, A.G. Walker, P.R. Dixon. Hopkinson bar pulse smoothing. Measurement Sci Technol 1995; 6:443-446.

[82] S. Ellwood, L.J. Griffiths, D.J. Parry. Materials testing at high constant strain rates. J Phys E Sci Instrum 1982; 15:280-282.

[83] S. Nemat-Nasser, J.Y. Choi, W.G. Guo, J.B. Isaacs, M. Taya. High strain-rate, small strain response of a NiTi shape-memory alloy. J Eng Mater Technol 2005; 127:83-89.

[84] J. Duffy, J.D. Campbell, R.H. Hawley. Use of a Torsional Split Hopkinson Bar to Study Rate Effects in 1100-0 Aluminum. J Applied Mechanics 1971; 38:83-91.

[85] G.T. Gray. Mechanical Testing and Evaluation, in: H. Kuhn (Ed.), ASM Handbook, ASM International, Materials Park, Ohio, 2000, pp.462-476.

[86] C.E. Franz, P.S. Follanbee, W.J. Wright. New Experimental Techniques with the Split Hopkinson Pressure Bar. 8th Intern Conf on High Energy Rate Fabrication 1984; 1-18.

[87] P.S. Follansbee. The Hopkinson Bar, in: J.R. Newby (Ed.), Metals Handbook, American Society for Metals, Metals Park, Ohio, 1985, pp.198-217.

[88] S. Nemat-Nasser, J.B. Isaacs, J.E. Starrett. Hopkinson Techniques for Dynamic Recovery Experiments. Proceedings of the Royal Society of London Series A-Mathematical Physical and Engineering Sciences 1991; 435:371-391.

[89] D.J. Frew, M.J. Forrestal, W. Chen. Pulse shaping techniques for testing brittle materials with a split Hopkinson pressure bar. Exp Mech 2002; 42:93-106.

[90] ASTM E399, Standard Test Method for Linear-Elastic Plane-Strain Fracture Toughness K_{Ic} of Metallic Materials, ASTM International, West Conshohocken, PA, 2013.

[91] J.B. Haddow. A Study of Knoop Hardness Test. J Basic Engineering 1966; 88:682-683.

[92] K. Meyer. Optimum Illumination of Testing Station for Standard Evaluation of Hardness Test Impressions According to Brinell Vickers and Knoop. Microtecnic 1968; 22:57-58.

[93] J.E. Malam. The Rockwell hardness test. J Institute of Metals 1928; 40:375-394.

[94] D.K. Mackenzie, T.P. Newcomb. The Measurement of Meyer Hardness and Youngs Modulus on the Rockwell Test Machine. British J Appl Phys 1957; 8:398-399.

[95] J.T. Sidaway. Rockwell Hardness Test - Case History of a Design for a Standardizing Machine. Engineering Materials and Design 1968; 11:1788-1789.

[96] P. Mumford, G. Shaffer. Improving and Automating the Rockwell-Hardness Test through New Technology. 8th International Symposium : Hardness Testing in Theory and Practice 1990; 804:177-186.

[97] J. Gukhool. An Investigation of the Rockwell-C Hardness Test. Discovery and Innovation 1991; 3:37-51.

[98] G.L. Dai, K. Herrmann, F. Menelao. Two approaches for enhancing the accuracy of the Rockwell hardness test. Measurement Science & Technology 2009; 20:1-7.

[99] R.E. Smith, G.E. Sandland. An accurate method of determining the hardness testing of the materials with particular reference to those of high degree of hardness. Proc Inst Mechanical Engineers 1922:623-641.

[100] C.H. Braithwaite, B. Aydelotte, A.L. Collins, N.N. Thadhani, D.M. Williamson. Comparing Cth Simulations and Experiments on Explosively Loaded Rings. Shock Compression of Condensed Matter 2012; 1426:1049-1052.

[101] V.F. Nesterenko, P.H. Chiu, C. Braithwaite, A. Collins, D. Williamson, K.L. Olney, D.B. Benson, F. McKenzie. Dynamic Behavior of Particulate/Porous Energetic Materials. Shock Compression of Condensed Matter 2012; 1426:533-538.

[102] B. Aydelotte, C.H. Braithwaite, K. McNesby, R. Benjamin, N.N. Thadhani, D.M. Williamson, M. Trexler. A Study of Fragmentation in a Ni plus Al Structural Energetic Material. Shock Compression of Condensed Matter 2012; 1426:1097-1100.

[103] P.D. Sargis, N.E. Molau, D. Sweider, M.E. Lowry, O.T. Strand. Photonic Doppler Velocimetry. UCRL-ID-133075, Lawrence Livermore National Laboratory, Livermore, CA, 1999.

[104] J. Goldstein. Scanning Electron Microscopy and X-Ray Microanalysis, Kluwer Academic/Plenum Publishers, New York, New York, 2003.

[105] R.Y. Yang, A.B. Yu, S.K. Choi, M.S. Coates, H.K. Chan. Agglomeration of fine particles subjected to centripetal compaction. Powder Technology 2008; 184:122-129.

[106] A.A. Griffith. The Phenomena of Rupture and Flow in Solids. Philo Trans of the Royal Society of London 1921; 221:163-198.

[107] G.R. Johnson, W.H. Cook. Fracture Characteristics of 3 Metals Subjected to Various Strains, Strain Rates, Temperatures and Pressures. Engineering Fracture Mechanics 1985; 21:31-48.

[108] D.A. Hoke, D.K. Kim, J.C. La Salvia, M.A. Meyers. Combustion synthesis dynamic densification of a TiB2-SiC composite. J Am Ceram Soc 1996; 79:177-182.

[109] D.B. Miracle. Overview NO-104 - The physical and mechanical-properties of NiAl. Acta Metall Mater 1993; 41:649-684.

[110] H. Kolsky. An investigation of the mechanical properties of materials at very high rates of loading. Proc Phys Soc B 1949; 62: 676-700.

[111] J. Wang, E. Besnoin, O.M. Knio, T.P. Weihs. Investigating the effect of applied pressure on reactive multilayer foil joining. Acta Mater 2004; 52:5265-5274.

[112] A.J. Swiston, T.C. Hufnagel, T.P. Weihs. Joining bulk metallic glass using multilayer foils. Scripta Mater 2003; 48;1575-1580.

[113] D.E. Eakins, N.N.Thadhani. Shock compression of reactive powder mixtures. Intl Mater Rev 2009; 54:181-213.

[114] O.S. Lee, Y.H. Han, D.H. Kim. Influence of temperature and heat-aged condition on the deformation behavior of rubber material using SHPB technique with a pulse shaper. Prog in Fracture and Strength of Materials and Structures 2007; 353:619-626.

[115] M. A. Meyers. Dynamic Behavior of Materials, John Wiley and Sons, New York, New York, 1994.

[116] K.S. Vecchio, J.C. LaSalvia, M.A. Meyers, G.T. Gray III. Microstructural characterization of self-propagating high-temperature synthesis dynamically compacted and hot-pressed titanium carbides. Metal Trans A 1992; 23A:87-97.

[117] J.K. MacKenzie. The elastic constraints of a solid containing spherical holes. Proc Phys Soc B 1950; 63:2-11.

[118] R.J. Thompson, J.-C. Zhao, K.J. Hemker. Effect of ternary elements on a martensitic transformation in beta Ni-Al. Intermetallics 2010; 18:796-802.

[119] A. Mashreghi, M.M. Moshksar. Partial martensitic transformation of nanocrystalline NiAl intermetallic during mechanical alloying. J Alloy Compd 2009;482: 196-198.

[120] A.S. Murthy, E. Goo. Martensitic-transformation of the Ni2Al phase in 63.1 at.percent NiAl. Acta Metall Mater 1993; 41:2135-2142.

[121] A.G. Khachaturyan, S.M. Shapiro, S. Semenovskaya. Adaptive phase formation in martensitic-transformation. Phys Rev B 1991; 43:10832-10843.

[122] B.L. Eyre. Transmission electron-microscope studies of point-defect clusters in FCC and BCC metals. J Phys F: Metal Phys 1973; 3:422-470.

[123] R. Nakamura, K. Takasawa, Y. Yamazaki, Y. Iijima. Single-phase interdiffusion in the B2 type intermetallic compounds NiAl, CoAl and FeAl. Intermetallics 2002; 10:195-204.

[124] I.E. Gunduz, K. Fadenberger, M. Kokonou, C. Rebholz, C.C. Doumanidis. Investigations on the self propagating reactions of nickel and aluminum multilayered foils. Appl Phys Lett 2008; 93:134101.

[125] K. Morsi. Review: reaction synthesis processing of Ni-Al intermetallic materials. Mater Sci Eng A 2001; 299:1-15.

[126] T. Sano, K. Kato, H. Takeishi. Analysis of dynamic deformation mechanisms in powder metals. J Mater Process Tech 1995; 48:391-397.

[127] G.E. Duvall, R.A. Graham. Phase transitions under shock-wave loading. Rev Mod Phys 1977; 49:523-579.

[128] M.A. Meyers, G.T. Gray, N.N. Thadhani. The Dynamic Behavior of Materials: An Introduction. JOM 2010; 62:14-15.

[129] Y. Horie, R.A. Graham, I.K. Simonsen. Synthesis of nickel aluminides under high-pressure shock loading. Mater Lett 1985; 3:354-359.

[130] I.K. Simonsen, Y. Horie, R.A. Graham, M. Carr. Formation of amorphous nickel aluminides under shock-wave loading. Mater Lett 1987; 5:75-78.

[131] S.S. Batsanov. An additive method for calculation of the sound velocity in porous materials. Inorg Mater 2007; 43:1070-1072.

[132] S.P. Kiselev. On propagation of a shock wave in a porous material upon collision of plates. Combust Explo Shock 1995; 31:473-477.

[133] H. Sierber, J.S. Park, J. Weissmuller, J.H. Perepezko. Structural evolution and phase formation in cold-rolled aluminum-nickel multilayers. Acta Mater 2001; 49:1139-1151.

[134] A. Sagel, H. Siber, H.-J. Fecht, J. H. Perepezko. Synthesis of an amorphous Zr-Al-Ni-Cu alloy with a large supercooled liquid region by cold-rolling of elemental foils. Acta Mater 1998; 46:4233-4241.

[135] I.N. Qureshi, S. Rani, F. Yasmin, M. Farooque. TEM study for strengthening mechanisms in elgiloy. Key Eng Mater 2010; 442:268-274.

[136] X. Qiu, J.H. Graeter, L. Kecskes, J. Wang. Fabrication and characterization of cold rolled Ni/Al multilayer foils. Mater Res Soc Symp Proc 2007; 977:1-5.

[137] X. Qiu, J. Graeter, L. Kecskes, J. Wang. Exothermic reactions in cold-rolled Ni/Al reactive multilayer foils. J Mater Res 2008; 23:367-375.

[138] X. Qiu, R. Liu, S. Guo, J.H. Graeter, L. Kecskes, J. Wang. Combustion synthesis reactions in cold-rolled Ni/Al and Ti/Al multilayers. Metal Mater Trans A 2009; 40A:1541-1546.

[139] X. Qiu, J. Wang. Experimental evidence of two-stage formation of Al3Ni in reactive Ni/Al multilayer foils. Scripta Mater 2007; 56:1055-1058.

[140] L. Battezzati, P. Pappalepore, F. Purbiano, I. Gallino. Solid state reactions in Al Ni alternate foils induced by cold rolling and annealing. Acta Mater 1999; 47:1901-1914.

[141] T.P. Weihs and M. Reiss. Method of making reactive multilayer foil and resulting product, U.S. Patent No. 6 534 194, 2003.

[142] D.J. Steinberg, S.G. Coshran, M.W. Guinan. A constitutive model for metals applicable at high-strain rate. J Appl Phys 1980; 51:1498-1504.

[143] N. Tsuji, Y. Saito, S.-H. Lee, Y. Minamino. ARB (accumulative roll-bonding) and other new techniques to produce bulk ultrafine grained materials. Adv Eng Mater 2003; 5:338-344.

[144] S.W. Du, B. Aydelotte, D. Fondse, C.T. Wei, F. Jiang, E. Herbold, K. Vecchio, M.A. Meyers, N.N. Thadhani. Explosive compactions of intermetallic-forming powder mixtures for fabricating structural energetic materials. Shock Compression of Condensed Matter, AIP Conf Proc 2009; 1195:498-501.

[145] S.W. Du, N.N. Thadhani. Impact initiation of pressed Al-based intermetallic-forming powder mixture compacts. Shock Compression of Condensed Matter, AIP Conf Proc 2009; 1195:470-473.

[146] J.R. Asay. The use of shock-structure methods for evaluating high-pressure material properties. Int J Impact Engng 1997; 20:27-61.

[147] M.A. Meyers, S.L. Wang. An improved method for shock consolidation of powders. Acta Metall 1988; 36:925-936.

[148] W. H. Zhu, M. Yoshida, H. Tamura, K. Kondo, S. Tanimura. Multiple spalling of aluminum subjected to a picosecond stress pulse. J Mater Sci Lett 2001; 20:961-963.

[149] R. Boehler, M. Ross. Melting curve of aluminum in a diamond cell to 0.8 Mbar: implications for iron. Earth Planet Sc Lett 1997; 153:223-227.

[150] G.X. Li, C.S. Liu, Z.G. Zhu. Scaling law for diffusion coefficients in simple melts. Phy Rev Lett 2005; 71:1-7.

[151] H. Okamoto. Al-Ni (Aluminum-Nickel). J Phase Equilib 1993; 14:257-259.

[152] J. Cai, V.F. Nesterenko, K.S. Vecchio, F. Jiang, E.B. Herbold, D.J. Benson, J.W. Addiss, S.M. Walley, W.G. Proud. The influence of metallic particle size on the

mechanical properties of polytetrafluoroethylene-Al-W granular composite materials. Appl Phys Lett 2008; 92:1-3.

[153] J. Cai, F. Jiang, K.S. Vecchio, M.A. Meyers, V.F. Nesterenko. Mechanical and microstructural properties of PTFE/Al/W system. AIP Conf Proc 2007; 955:723-726.

[154] C.L. Yeh, H.J. Wang. Effects of sample stoichiometry of thermite-based SHS reactions on formation of Nb-Al intermetallics. J Alloy Compd 2009: 485:280-284.

[155] C.T. Wei, B.R. Maddox, T.P. Weihs, A.K. Stover, V.F. Nesterenko, M.A. Meyers. Laser shock compression and spalling of reactive Ni-Al laminate composites. Shock Compression of Condensed Matter 2009; 1195:305-308.

[156] U. Gosele, K.N. Tu. Growth-kinetics of planar binary diffusion couples - thin-film case versus bulk cases. J App Phys 1982; 53:3252-3260.

[157] C. Wagner. The evaluation of data obtained with diffusion couples of binary single-phase and multiphase systems. Acta Metall 1969; 17:99-107.

[158] M.M.P. Janssen, G.D. Riecks. Reaction diffusion and Kirkendall-effect in the nickel-aluminum system. Trans Met Soc AIME 1967; 239:1372-1385.

[159] S.P. Garg, G.B. Kale, R.V. Patil, T. Kundu. Thermodynamic interdiffusion coefficient in binary systems with intermediate phases. Intermetallics 1999; 7:901-908.

[160] E. Arzt. Overview no. 130 - Size effects in materials due to microstructural and dimensional constraints: A comparative review. Acta Mater 1998; 46:5611-5626.

[161] M. Taya. Strengthening mechanisms of metal matrix composites. Mater T JIM 1991; 32:1-19.

[162] P. Kasiraj, T. Vreeland, Jr. R.B. Schwarz, T.J. Ahrens. Mechanical properties of a shock consolidated steel powder. Shock Waves in Condensed Matter 1983; 10:439-442.

[163] C.T. Wei, B.R. Maddox, A.K. Stover, T.P. Weihs, V.F. Nesterenko, M.A. Meyers. Reaction in Ni-Al laminates by laser-shock compression and spalling. Acta Mater 2011; 59:5276-5287.

[164] Z. Hashin. The elastic moduli of heterogeneous materials. J Appl Mech 1962; 29:143-150.

[165] R.L. Suffredini. How swaging affects mechanical properties of steel. Metal Progress 1963; 109-120.

[166] R.L. Kegg. Mechanics of the rotary swaging process. J Eng Ind Trans 1964; 86:317-325.

[167] S. Kalpakjian. Dimensional changes in tube swaging. J Eng Ind Trans 1966; 88:147-150.

[168] W.G. Ovens, E.L. Bartholomew, R.R. Biederman. Metal flow two-die swaging. J Eng Ind Trans 1976; 98:1121-1124.

[169] T. Nakagawa, T. Amano. Compacting of high density P/M bars by rotary swaging. JSTP 1976; 17:209-215.

[170] J. Schrank, B. Ortner, H.P. Stuwe, A. Grabianowski. Work softening and work hardening during rotary swaging of copper. Mater Sci Technol 1985; 1:544-549.

[171] L.A. Glenn, A. Chudnovsky. Strain-energy effects on dynamic fragmentation. J Appl Phys 1986; 59:1379-1380.

[172] A.M. Lennon, K.T. Ramesh. A technique for measuring the dynamic behavior of materials at high temperatures. Int J Plast 1998; 14:1279-1292.

[173] A. Piela. Analysis of the metal flow in swaging-numerical modeling and experimental verification. Int J Mech Sci 1997; 39:221-231.

[174] ASM. Rotary swaging of bars and tubes. ASM Metals Handbook 1969; 4:333-346.

[175] R.J. Wright, R.E. Anderson Jr., Z.R. Waltz. Single-crystal alumina/aluminum alloy composite structure fabrication by RF-coupled plasma spray processing. J Therm Spray Techn 1994; 3:292-294.

[176] ASTM E399, Standard Test Method for Linear-Elastic Plane-Strain Fracture Toughness K_{Ic} of Metallic Materials, ASTM International, West Conshohocken, PA, 2013.

[177] M.A. Meyers. Mechanics and Materials: Fundamentals and Linkages, John Wiley and Sons, New York, New York, 1999.

[178] O.S. Lee, K.S. Cho, S.H. Kim, Y.H. Han. Dynamic deformation behavior of soft material using SHPB technique and pulse shaper. Inter J Mod Physics B 2006; 20: 3751-3756.

[179] L.M. Barker. The development of VISAR, and its use in shock compression science. Shock Compression of Condensed Matter 2000; 505:11-17.

[180] E. Dunbar, N.N. Thadhani, R.A.Graham. High-pressure shock activation and mixing of nickel-aluminum powder mixtures. J Mater Sci 1993; 28:2903-2914.

[181] N. N. Thadhani, S. Work, R. A. Graham, W. F. Hammetter. Shock-induced reaction synthesis (SRS) of nickel aluminides. J Mater Res 1992; 7:1063-1075.

[182] K.A. Philpot, Z.A. Munir, J.B. Holt. An investigation of the synthesis of nickel aluminides through gasless combustion. J Mater Sci 1987; 22:159-169.

[183] O.S. Lee, S.H. Kim, Y.H. Han. Dynamic deformation behavior of soft materials at the low temperature using SHPB technique and pulse shaper. Exper Mech in Nano and Biotech 2006; 326:1577-1580.

[184] A.G. Merzhanov, B.I. Khaikin. Theory of combustion waves in homogeneous media. Prog Energy Combust Sci 1988; 14:1-98.

[185] J.C. LaSalvia, D.K. Kim, R.A. Lipsett, M.A. Meyers. Combustion synthesis in the Ti-C-Ni-Mo System: Part I. Micromechanisms. Metall Mater Trans A 1995; 26A:3001-3009.

[186] M.A. Meyers, C.T. Aimone. Dynamic fracture (spalling) of metals. Prog Mater Sci 1983; 28:1-96.

[187] D.E. Grady. Local inertial effects in dynamic fragmentation. J Appl Phys 1982; 53:322-325.

[188] M.E. Kipp, D.E. Grady. Dynamic fracture growth and interaction in one dimension. J Mech Phys Solids 1985; 33:399-415.

[189] D.E. Grady. The spall strength of condensed matter. J Mech Phys Solids 1988; 36:353-384.

[190] L.M. Barker, R.E. Hollenbach. Laser interferometer for measuring high velocities of any reflecting surface. J Appl Phys 1972; 43:4669-4675.

[191] M.E. Kipp, D.E. Grady, J.W. Swegle. Numerical and experimental studies of high-velocity impact fragmentation. Int J Impact Eng 1993; 14:427-438.

[192] D.E. Leyden. X-Ray Spectrometry, in: R.E. Wahn (Ed.), ASM Handbook, ASM International, Materials Park, Ohio, 2000, pp. 82-101.

[193] D.E. Grady, M.L. Kipp. Dynamic fracture and fragmentation, in: J.R. Asay (Ed.), High-Pressure Shock Compression of Solids, Springer, New York, NY, 1993, pp. 265-322.

[194] F. Zhou, J.F. Molinari, K.T. Ramesh. Analysis of the brittle fragmentation of an expanding ring. Comput Mater Sci 2006; 37:74-85.

[195] M.A. Meyers, B.B. Gupta, L.E. Murr. Shock-wave consolidation of rapidly solidified super-alloy powders. J Metals 1981; 33:21-26.

[196] H.L. Coker, M.A. Meyers, J.F. Wessels. Dynamic consolidation of rapidly solidified titanium-alloy powders by explosives. J Mater Sci 1991; 26:1277-1286.

[197] S.L. Wang, M.A. Meyers, A. Szecket. Warm shock consolidation of IN 718 powder. J Mater Sci 1988; 23:1786-1804.

[198] L.H. Yu, M.A. Meyers, T.C. Peng. Shock consolidation of Al-Li alloy powders. Mater Sci Eng A 1991; 132:257-265.

[199] L.H. Yu, M.A. Meyers. Shock synthesis and synthesis-assisted shock consolidation of silicides. J Mater Sci 1991; 26:601-611.

[200] S. Shang, K. Hokamoto, M.A. Meyers. Hot dynamic consolidation of hard ceramics. J Mater Sci 1992; 27:5470-5476.